Quantum Memories for Continuous Variable States of Light in Atomic Ensembles

Gabriel Hétet

A thesis submitted for the degree of
Doctor of Philosophy at
The Australian National University

ANU
THE AUSTRALIAN NATIONAL UNIVERSITY

October, 2008

Declaration

This thesis is an account of research undertaken between March 2005 and June 2008 at the Department of Physics, Faculty of Science, Australian National University (ANU), Canberra, Australia. This research was supervised by Prof. Ping Koy Lam (ANU), Prof. Hans-Albert Bachor (ANU), Dr. Ben Buchler (ANU) and Dr. Joseph Hope (ANU). Unless otherwise indicated, the work present herein is my own.

None of the work presented here has ever been submitted for any degree at this or any other institution of learning.

Gabriel Hétet
October 2008

Acknowledgments

I would naturally like to start by thanking my principal supervisors. Ping Koy Lam is the person I owe the most. I really appreciated his approachability, tolerance, intuition, knowledge, enthusiasm and many other qualities that made these three years at the ANU a great time. Hans Bachor, for helping making this PhD in Canberra possible and giving me the opportunity to work in this dynamic research environment. I always enjoyed his friendliness and general views and interpretations of physics. Thanks also to both of you for the opportunity you gave me to travel and present my work to international conferences.

This thesis has been a rich experience thanks to my other two supervisors : Joseph Hope and Ben Buchler. I would like to thank Joe for invaluable help on the theory and computer side and Ben for the efficient moments he spent improving the set-up and other innumerable tips that polished up the work presented here, including proof reading this thesis.

When I arrived here, the ALE project had just started. I had the pleasure to share a few months in the lab with Katie Pylipas and Charles Harb. I then had the luck to learn how to handle lasers with Oliver Gloeckl. I am really grateful to Oliver for his deep involvement in the project and his rigor all the way through. I gained a great deal from his expertise. Thanks also goes to Magnus Hsu for the knowledge and experimental skills he transmitted to me on the atom side of the experiment. I am also indebted to Amy Peng, Mattias Johnson, Alexander Akulshin, Kirk McKenzie, and also the LKB team in Paris for invaluable help and discussions all along this project. These were really fruitful and enjoyable years, thanks again to all of you. I would like to wish luck to Mahdi and Ben for the rest of their PhD/Honours and thank them for their help during my last months here.

I had the opportunity to work with two great researchers, Matt Sellars and Jevon Longdell, from the Research School of Physical Sciences, during my PhD. I want to thank them deeply for allowing me and the group to partake in this awesome work they are doing. This was a truly interesting and really pleasant collaboration. Good continuation with your work.

I would certainly not forget to thank Paul Tant, Paul MacNamarra, Neil Devlin, Shane Grieves, and Neil Hinchey for their help with the mechanics and electronics involved in the experimental work.

Merci aussi à Robin Kaiser et les gens du INLN pour leur accueil super sympa à Nice. J'y ai passé un mois très agréable et très enrichissant.

A big collective thanks goes to all the people that have contributed to the work presented here, from the office at the faculties, to my family and my friends in France and here in Australia. Last but certainly not least, to Violaine, for giving me support and happiness during these years.

Abstract

The field of quantum information science holds great promise for enhancing computing speed and secure communication. In this thesis, we present theoretical studies and experiments that aim to develop a key component of quantum communication systems : quantum memories. Specifically, we examine the potential of continuous variable quantum memories for light using large ensemble of atoms.

It is important to compare the performance of light storage experiments against relevant benchmarks. We propose to benchmark efficacies using the classical teleporter. We investigate theoretically the propagation of quantum states through lossy and noisy quantum channels and use the *T-V diagram* to quantify quantum memory performances. As most experimental demonstrations are performed with rubidium atoms, we built a squeezed light source operating at rubidium wavelengths. We achieved 5.2 dB of squeezing using PPKTP in an optical parametric oscillator and pushed the bandwidth suppression down to 200 Hz, well within the transmission of Electromagnetically Induced Transparency (EIT) based quantum memories. A study of EIT is presented theoretically and experimentally. We discovered theoretically that population exchange between the ground states is responsible for excess noise on the output field due to phase-insensitive amplification of the probe in the medium. Phase space numerical models were developed to calculate the efficiency of information storage and retrieval. We use this code and our benchmarks to calculate the parameter regimes that would enable EIT to act as a quantum memory. Experiments performed in a warm rubidium vapour cell showed transmission of 2 dB of squeezed light through an EIT feature. Using the same squeezed source, biased entanglement was used to show quantum state delay of 2 μs while also preserving state inseparability. We show that the presence of buffer gas eliminates the excess noise observed in samples containing natural mixtures of rubidium. Using a similar set-up, we demonstrate the writing and read-out of a classical pulse to and from the ground states of rubidium atoms using EIT and examine the limitations of the technique.

Alternative quantum memories for light using photon echo techniques are also proposed. After analyzing the standard photon echoes techniques and controlled reversible inhomogeneous broadening (CRIB) for quantum state storage, we discovered an efficient quantum memory protocol. The Gradient Echo Memory (GEM) uses two-level atoms and a reversible detuning that varies linearly with propagation distance across the atomic sample. Using numerical simulations, we show that GEM is perfectly efficient in the limit of a large number of atoms. We compare our results with experimental demonstrations performed in solid state systems. The memory dynamics are interpreted as the formation of polaritonic modes that can be controlled by the detuning slope. We found that, as GEM stores information in the Fourier domain, it can store signals that have a large time-bandwidth product, an important feature for quantum memories. We propose a direct extension of the GEM protocol using three-level atoms in an off-resonant Raman configuration and present proof of principle demonstrations of this Λ-GEM memory scheme in a rubidium vapour by controlling a linear Zeeman shift.

Contents

Introduction

This thesis investigates, both experimentally and theoretically, the potential of quantum memories for light using atomic ensembles.

Quantum memories are devices that allow the storage and retrieval of quantum states of light. Storing information carried by light, apart from a fundamental interest, represents an important step towards realizing efficient quantum information protocols. Quantum memories form the building block of quantum repeaters [Briegel et al., 1998], that allow long distance communication with quantum states [Duan et al., 2001]. They are also a key ingredient of quantum information protocols that need synchronization of quantum gates [Knill et al., 2001].

The Heisenberg uncertainty principle sets a limit on the efficacy of memories that depends on "classical" measurement and subsequent reconstruction. Classical storage techniques can not be used to store two conjugate observables simultaneously without paying a quanta of duty [Wootters and Zurek, 1982]. Unless some extra quantum resources are used, excess noise will then mask the quantum statistics of the light field to be stored. Much experimental and theoretical research has been directed towards memories that surpass this Heisenberg limit.

To interact efficiently with the material storing the quantum information, the "effective coupling" with the photons must be as close as possible to unity. Methods using an ultra-high finesse cavity [Parkins et al., 1993] and a single atom were proposed to achieve such strong coupling but are experimentally quite challenging. Other promising methods were put forward using large number of atoms. The coupling strength between one photon to N atoms can be extremely large provided the medium is optically thick and schemes were then proposed to efficiently map information onto atoms [Kozhekin et al., 2000]. The challenge is to find schemes that allow one to retrieve on demand the full quantum state that was mapped onto the atoms. Controlling dynamically the properties of Electromagnetically Induced Transparency (EIT) was demonstrated an efficient way to store and retrieve classical [Fleischhauer and Lukin, 2000, Liu et al., 2001, Phillips et al., 2001] and quantum [Honda et al., 2008, Appel et al., 2008, Laurat et al., 2006, Eisaman et al., 2005, Chanelière et al., 2005] information encoded onto light fields in rubidium gases. Other methods were also investigated to reversibly map photons onto large atomic ensembles by projective measurement of the atomic ensemble collective state [Felinto et al., 2006, Kuzmich et al., 2003] or using controlled reversible inhomogeneous broadening (CRIB) [Moiseev and Kröll, 2001, Kraus et al., 2006, Nilsson and Kröll, 2005, Sangouard et al., 2007, Alexander et al., 2006].

Efficient storage and retrieval of non-classical light provides direct evidence of the quantum nature of the resource used for the memory. Squeezed light or single photon states are therefore valuable tools for probing the performance of potential quantum memories. Such non-classical states belong to the continuous variable and discrete variable regimes respectively and are nowadays produced at various wavelengths. Large degrees of squeezing have recently been produced at 860 nm [Takeno et al., 2007] and 1064 nm [Vahlbruch et al., 2008]. Most quantum memory experiments in atomic vapours are performed in rubidium at 795 nm where squeezing technology is still in its infancy. Controlling efficiently the storage and retrieval of continuous variable Gaussian states is of particular interest, as the technology for CV-quantum cryptography [Grosshans and Grangier, 2002a, Lance et al., 2005] is already well-established, but the communication distance is limited. A useful quantum memory would help to overcome this distance limitation.

In this thesis, we concentrated on the study of two quantum memories for light using large atomic ensembles: EIT and CRIB based memories. The work presented here is divided in three parts.

Part I presents the theoretical and experimental background required to appreciate the workings of the two quantum memories. In **chapter 1**, we introduce the quantum atom-optics concepts and theoretical framework. In **chapter 2** we define benchmarks for quantum memories. It is important to specify the experimental regimes where the memories operate better than classical devices so we provide answers to these questions in this chapter. In **chapter 3**, we demonstrate the production of a squeezed light source at 795 nm. The squeezed light source was designed to probe the efficiency of quantum memories for light at rubidium wavelengths and can generate noise suppression in sideband frequencies as low as 200 Hz.

Part II is a study of quantum memories based on *Electromagnetically Induced Transparency*, (EIT). The first chapter (**chapter 4**) presents a theoretical analysis of the memory. We perform a quantum analysis of EIT as a delay line and storage device including sources of decoherence present in current experiments. We identify a source of excess noise and then define the parameter regimes where EIT is able to store information in the quantum regime. In the second chapter of this part, **chapter 5**, we experimentally demonstrate the delay of entanglement and squeezed light through an EIT quantum channel and the storage and retrieval of a classical pulse on and from the rubidium Zeeman ground states.

Part III presents theoretical and experimental studies of a quantum memory scheme based on the idea of photon echoes. **Chapter 6** describes the theoretical and experimental state of the art in the field of information storage using photon echoes and *controlled reversible inhomogeneous broadening* (CRIB). This background information allows us to introduce (in **chapter 7**) a new scheme for quantum information storage using an ensemble of two level atoms, the Gradient Echo Memory (GEM). We describe the memory performance and dynamics by solving the problem numerically and identify freely evolving polariton modes. Our numerical model is found to be in good agreement with an experiment performed in a solid state system. In **chapter 8**, we propose a variant of GEM using three atomic levels, the Λ-GEM memory. We demonstrate a proof of principle of this scheme in warm rubidium vapour cell and again demonstrate good agreement with the theory.

List of publications

Most of the work covered in this thesis was published in international peer reviewed journals

1. Hétet G., Longdell J. J., Sellars M. J., Lam P. K. and Buchler B. C. *Multimode properties and dynamics of the gradient echo quantum memory*, to appear in Phys. Rev. Lett.

2. Hétet G., Hosseini M., Sparkes B., Oblak D., Lam P. K. and Buchler B. C. *Photon echoes generated by reversing magnetic field gradients in a rubidium vapour*, Optics Letters. **33**, 20 pp 2323-2325 (2008).

3. Longdell J. J., Hétet G., Lam P. K. and Sellars M. J. *Analytic treatment of controlled reversible inhomogeneous broadening quantum memories for light using two-level atoms*, Phys. Rev. A, **78** 032337 (2008)

4. Hétet G., Buchler B. C., Glöckl O., Hsu M. T. L., Akulshin A. M., Bachor H.-A. and Lam P. K., *Delay of squeezing and entanglement using electromagnetically induced transparency in a vapour cell*, Optics Express, Vol. **16**, Issue 10, pp. 7369-7394 (2008).

5. Hétet G., Peng A., Johnson M. T., Hope J. J. and Lam P. K., *Characterisation of EIT based continuous variables quantum memories*, Phys. Rev. A, **77** 012323 (2008).

6. Hétet G., Longdell J. J., Alexander A. L., Lam P. K., and Sellars M. J. *Electro-Optics quantum memory for light using two level atoms*, Phys. Rev. Lett., **100** 23601, (2008).

7. Hétet G., Glöckl O., Pilypas K. A., Harb C. C., Buchler B. C., Bachor H.-A. and Lam P. K., *Squeezed light for bandwidth limited experiments at rubidium wavelengths*, J. Phys. B, **40**, 221 (2006).

8. Hétet G., Peng A., Johnsson M. T., Hsu M. T. L., Glockl O., Lam P. K., Bachor H. -A., and Hope J. J., *Erratum : Squeezing and entanglement delay using slow light,* Phys. Rev. A **74**, 059902 (2006).

9. Hsu M. T. L., Hétet G., Glöckl O., Longdell J. J., Buchler B. C., Bachor H.-A., and Lam P. K., *Quantum study of information delay with electromagnetically induced transparency*, Phys. Rev. Lett. **97**, 18601 (2006).

10. Hsu M. T. L., Hétet G., Peng A., Harb C. C., Bachor H.-A., Johnsson M. T., Hope J. J., Lam P. K., Dantan A., Cviklinski J., Bramati A., and Pinard M., *Effect of atomic noise on squeezing via self-rotation*, Phys. Rev. A **73**, 023806 (2006).

Contributed papers at conferences

1- Hétet G., Hsu M. T. L., Glockl O., Buchler B. C., Longdell J. J., Peng A., Johnsson M. T., Hope J. J., Bachor H.-A. and Lam P. K. , *Slowing and storing quantum information with EIT.* Proceedings of the 8th International Conference on Quantum Communication, Measurement and Computing, 497-500 (2007).

2- Longdell J. J., Hétet G., Alexander A. L., Lam P. K., and Sellars M. J. *Gradient echo quantum memory for light using two-level atoms.* Proc. SPIE 6710, 67100X (Sep. 25, 2007).

Part I

Tools for quantum memory characterisation

Chapter 1

Elements of quantum-atom-optics theory

In this chapter, we introduce the formalism necessary to understand atomic quantum memories and their applications. The formalism and concepts introduced here will be used in both the experimental and theoretical parts of this work.

The interaction between two-level atoms and a multimode quantized field will be the main focus of this chapter. The theoretical background of the first four sections will be especially relevant to the chapters on quantum memory benchmarks, Electromagnetically Induced Transparency (EIT) and Gradient Echo Memories (GEM). The last section is devoted to the detection and production of Gaussian quantum states which will be of interest for chapters 2, 3 and 5.

1.1 Quantum states of light for storage

In this section, we present quantum states of light that we will manipulate throughout this thesis. We also calculate their probability distribution using the *Wigner function*.

1.1.1 Heisenberg uncertainty principle

One cannot measure with arbitrary precision two non-commuting (or conjugate) observables. In other words, there is a fundamental limit to how well we can measure two variables related by Fourier transform. This *uncertainty principle* has dramatic consequences when one measures the position $\hat{X}$, and the momentum $\hat{P}$ of particles such as photons or electrons. The uncertainty principle can be formally quantified by

$$\Delta\hat{X}\Delta\hat{P} \geq \hbar/2, \tag{1.1}$$

where $\hbar$ is the normalized Planck constant ($h/2\pi$). Eq.(1.1) is known as the Heisenberg uncertainty relation, where Δ represents the standard deviation of the fluctuations due to the measurement of $\hat{X}$ or $\hat{P}$. The standard deviation of an observable $\hat{A}$ is defined as

$$\Delta\hat{A} = \sqrt{\langle\psi|\hat{A}^2|\psi\rangle - |\langle\psi|\hat{A}|\psi\rangle|^2}, \tag{1.2}$$

where $|\psi\rangle$ is the state vector over which the projective measurement is performed.
It can be shown that Eq.(1.1) follows from the canonical commutation relations between $\hat{X}$ and $\hat{P}$

$$[\hat{X}, \hat{P}] = i\hbar. \tag{1.3}$$

Although the quanta $\hbar$ gives rise to a fundamental noise source that is a problem for a number of precision measurements, the field of quantum information takes advantage of it.

For quantum information processing, light states are the most common objects. They travel with very little loss in free space and over a few kms in optical fibres whilst retaining their quantum statistics. In this thesis, we will concentrate on the evolution of observables describing the state of *light fields*, with the aim of coherently controlling their velocity using large atomic ensembles.

1.1.2 Experimental observables

Quantization of the radiation field can be done by associating operators with the potential vector, and its derivative for freely propagating photons. The complete derivation can for example be found in [Cohen-Tannoudji et al., 1993]. The solution of the Maxwell equation for these newly defined field operators is, in the Coulomb gauge,

$$\hat{E}(\mathbf{r},t) = \int_{-\infty}^{\infty} dk \sqrt{\frac{\hbar\omega_k}{2\epsilon_0}} [\hat{a}_k u_k(\mathbf{r}) e^{-i\omega_k t} - \hat{a}_k^\dagger u_k^*(\mathbf{r}) e^{i\omega_k t}], \tag{1.4}$$

where $\omega_k = kc$, with c the speed of light in vacuum, ϵ_0 the permittivity in vacuum and $u_k(\mathbf{r})$ transverse spatial modes[1] . The optical modes $\hat{a}_k$ satisfy the commutation relation

$$[\hat{a}_k, \hat{a}_{k'}^\dagger] = \delta(k - k'). \tag{1.5}$$

We will consider the decomposition of the transverses modes in terms of plane waves satisfying periodic boundary conditions inside a volume V, and write

$$u_k(\mathbf{r}) = \frac{e^{ik\mathbf{r}}}{\sqrt{V}}, \tag{1.6}$$

where the orthonormality of the mode functions $u_k(\mathbf{r})$ allowed us to scale them by $\sqrt{V}$.

If we assume the optical wavelength $\lambda = 2\pi/k$ to be much smaller than L, where L is the length of the volume V in the direction of the light field propagation, we can rewrite Eq. (1.4) as

$$\hat{E}(\mathbf{r},t) = \sqrt{\frac{\hbar\omega_0}{2\epsilon_0 V}} [\hat{\mathcal{E}}(z,t) e^{ik_0(z-ct)} - \hat{\mathcal{E}}^\dagger(z,t) e^{-ik_0(z-ct)}], \tag{1.7}$$

where $\hat{\mathcal{E}}(z,t)$ is a *multimode* slowly varying envelope operator and ω_0, k_0 are the carrier frequency and wave-vector in free space respectively. $\hat{\mathcal{E}}(z,t)$ satisfies the commutation relation

$$[\hat{\mathcal{E}}(z,t), \hat{\mathcal{E}}^\dagger(z',t')] = \frac{L}{c}\delta(t - z/c - (t' - z'/c)). \tag{1.8}$$

Because the carrier wave oscillates too quickly to be detected in any standard detection scheme[2], the quantum states will be modelled by this slowly varying quantity. The information will be encoded onto the amplitude and momentum (or phase) operators defined as

$$\hat{X} \ = \ \frac{1}{2}(\hat{\mathcal{E}} + \hat{\mathcal{E}}^\dagger) \ \text{ and } \ \hat{P} = -\frac{i}{2}(\hat{\mathcal{E}} - \hat{\mathcal{E}}^\dagger), \tag{1.9}$$

---

[1] We ignored the polarisation modes here.

[2] For example, it oscillates at $\omega_0 = 0.4 \times 10^{15}$ Hz at a wavelength of 795 nm.

respectively, in analogy with the harmonic oscillator normal variables. $\hat{X}$ and $\hat{P}$ are two conjugate quantities, and therefore obey a commutation relation like Eq. (1.3). They are often called the *quadratures* of the electromagnetic field.

For a given problem, one can derive equations of motion for the slowly varying quadrature operators in the *Heisenberg* picture. Another approach is to let the states evolve in time, in the *Schrödinger* picture, and project these operators onto the appropriate detection basis. Both approaches will be used in this thesis depending on the context. We will specifically mention which approach will be followed before each section.

1.1.3 The density matrix

A convenient mathematical object for solving a problem in the Schrödinger picture is the density matrix. We will use it here to present the properties of entangled states, to introduce mixed states and define quantum characteristic functions.

Let us write $|\psi(t)\rangle$, a state vector evolving in a closed Hilbert space $\mathcal{S}$. The density matrix $\hat{\rho}$ of $|\psi(t)\rangle$ is defined as

$$\hat{\rho} = |\psi(t)\rangle\langle\psi(t)|, \tag{1.10}$$

where we submit $\hat{\rho}$ to the constraint $\mathrm{Tr}\hat{\rho} = 1$. By decomposing the vector $|\psi(t)\rangle$ in a basis $\{|\psi_a\rangle\}$ of $\mathcal{S}$ we find

$$\hat{\rho} = \sum_{a,b} c_a(t) c_b^*(t) |\psi_a\rangle\langle\psi_b|. \tag{1.11}$$

The diagonal elements $|c_a|^2$ of the density matrix are called the *populations* and the off-diagonal elements $c_a^* c_b$ the *coherences.*

To understand the usefulness of the density matrix, let us separate $\mathcal{S}$ into two subsystems $\mathcal{S}_1$ and $\mathcal{S}_2$. The expectation value of an observable $\mathcal{A}$ acting on the subsystem $\mathcal{S}_1$ can be found to be

$$\langle\psi(t)|\mathcal{A}|\psi(t)\rangle = \mathrm{Tr}_{\mathcal{S}_1}(\hat{\rho}_{\mathcal{S}_1}\mathcal{A}), \tag{1.12}$$

where $\hat{\rho}_{\mathcal{S}_1} = \mathrm{Tr}_{\mathcal{S}_2}(\hat{\rho})$. The measurement of an observable acting on a subspace $\mathcal{S}_1$ is obtained by taking the partial trace of the product between the density matrix reduced to $\mathcal{S}_1$, and $\mathcal{A}$. This property will be used extensively in the next section.

Entangled states

If the two subsystems $\mathcal{S}_1$ and $\mathcal{S}_2$ are coupled by some interaction, quantum correlations are established between them. Let us now write $\{|\phi_i\rangle\}$ and $\{|\theta_j\rangle\}$ the orthonormal bases of $\mathcal{S}_1$ and $\mathcal{S}_2$. When the two subsystems are coupled at $t = 0$, an initially factorized state $|\psi(0)\rangle = |\phi_0\rangle|\theta_0\rangle$ from $\mathcal{S}$, will evolve to

$$|\psi(t)\rangle \;=\; \mathcal{U}(0,t)|\psi(0)\rangle = \sum_{i,j} \lambda_{ij}(t)|\phi_i\rangle|\theta_j\rangle, \tag{1.13}$$

where $\mathcal{U}(0,t)$ describes a unitary evolution from $t = 0$ to t, and $\lambda_{ij}(t)$ are coefficients quantifying the strength of the interaction at a time t. This state is, in general, inseparable or *entangled.* One intriguing feature of entangled states is that quantum correlations can exist between two spatially separated systems, Einstein describing this feature as “spooky interactions at a distance”. If we note $\hat{\rho}_{\mathcal{S}_{1,2}} = \mathrm{Tr}_{\mathcal{S}_{2,1}}(\hat{\rho})$ the reduced density matrix to $\mathcal{S}_{1,2}$, we then have $\hat{\rho}_{\mathcal{S}} \neq \hat{\rho}_{\mathcal{S}_2} \otimes \hat{\rho}_{\mathcal{S}_1}$. A quantum state comprised of two modes is separable if and only if its density matrix can be written $\hat{\rho} = \hat{\rho}_{\mathcal{S}_1} \otimes \hat{\rho}_{\mathcal{S}_2}$. Such entangled states will be described in chapter 2 and produced chapter 5.

Mixed states

An important property of the density matrix is that it allows one to define statistical mixtures of quantum states. By definition, a state is *pure* if and only if the purity parameter $p = \mathrm{Tr}(\hat{\rho}^2) = 1$ (a definition that does not depend on the chosen basis), if not the state is *mixed.* For Gaussian states, this definition is equivalent to[3] $V^+V^- = 1$. Any state $|\psi(t)\rangle$ from $\mathcal{S}$ is pure because $\mathcal{S}$ is a closed Hilbert space[4]. However, when the two subsystems $\mathcal{S}_1$ and $\mathcal{S}_2$ are coupled, the purity parameter for their *reduced* density matrices can be below one. Each state of the subsystems is then not pure.

The density matrix will be used in the next section to describe the evolution of a small Hilbert space interacting with a another much bigger space (containing many modes), which will allow us to present the concept of *decoherence.*

Using the density matrix, we will now introduce another important mathematical tool, the characteristic function.

The characteristic function

Characteristic functions ϕ_X are normally used to evaluate the moments of random variables X, in standard probability theory. They are defined by the following formula

$$\phi_X(t) = \langle \exp(itX) \rangle, \tag{1.14}$$

where t is a real number and $\langle . \rangle$ represents ensemble statistical average. Owing to the non-commuting properties of quantum observables, canonical distributions for quantum statistical ensembles can be defined in various ways. The *symmetric* quantum characteristic function of a density operator $\hat{\rho}$ is defined by the expectation value of the *unitary displacement operator* $\hat{D}(\lambda) = \exp(\lambda \hat{a}^\dagger - \lambda^* \hat{a})$ where λ is a complex scalar. We then have

$$\chi(\lambda) = \langle \hat{D}(\lambda) \rangle = \mathrm{Tr}(\hat{\rho} e^{\lambda \hat{a}^\dagger - \lambda^* \hat{a}}). \tag{1.15}$$

It characterizes the probability density of finding a system in a certain state, with the moments calculated from derivatives of this function, as we will see later on. One can also define normally and anti-normally ordered characteristic functions

$$\chi_N(\lambda) \quad = \quad \mathrm{Tr}(\rho e^{\lambda a^\dagger} e^{-\lambda^* a}) \;\; \text{and} \;\; \chi_A(\lambda) = \mathrm{Tr}(\rho e^{-\lambda^* a} e^{\lambda a^\dagger}). \tag{1.16}$$

The above functions are defined for a single operator, but can be generalized to N operators $\hat{O}_j$ by writing

$$\chi(\lambda) = \mathrm{Tr}(\hat{\rho} \hat{\Xi}(\underline{\lambda})), \tag{1.17}$$

---

[3] We write $V^{\pm}$ the variances of the amplitude/phase quadratures defined as the square of the standard deviation in Eq. (1.2).

[4] It is straightforward to show that $p = 1$ using Eq.(1.10).

where the kernel $\hat{\Xi}(\underline{\lambda})$ is, for example, given by

$$\hat{\Xi}(\underline{\lambda}) = \prod_{k=1}^{N} e^{i\lambda_{N-k}\hat{O}^{\dagger}_{N-k}} \prod_{j=1}^{N} e^{i\lambda_{j*}\hat{O}_j}, \tag{1.18}$$

for the normally ordered characteristic function. We can use the characteristic function to define several probability distributions. For Gaussian states, the most convenient distribution is the Wigner function.

1.1.4 Wigner function

The density matrix often describes the evolution of a large number of modes (like optical traveling waves) and is therefore hard to manipulate. In quantum optics, probability distributions are often used to reduce the size of the problem to solve. The *Wigner function*, W, was originally introduced for studying quantum corrections to statistical mechanics. One way to define it, is via a Fourier transform of the symmetrically ordered characteristic function

$$W(\alpha) = \frac{1}{\pi^2}\int d^2\lambda e^{\lambda\alpha^* - \lambda^*\alpha}\chi(\lambda). \tag{1.19}$$

The Wigner function always exists, but is not always positive. It is therefore not a genuine probability distribution (it is often called a *quasi-probability distribution*) but it is however well suited to the description of Gaussian states, as will be shown.

1.1.5 Quantum states of light

In this thesis, we will be manipulating continuous variable Gaussian states. We present here coherent states, thermal states and squeezed states.

The coherent state

One of the most commonly used states is the coherent state $|\alpha\rangle$, satisfying the relation

$$\hat{a}|\alpha\rangle = \alpha|\alpha\rangle, \tag{1.20}$$

that is, it is an eigenstate of the annihilation operator [Glauber, 1963]. The square of the absolute value of α, represents the mean number of photons in the beam and its argument the phase of the field. The coherent state can be decomposed as a superposition of Fock states $|n\rangle$

$$|\alpha\rangle = e^{-|\alpha|^2/2}\sum_{n=0}^{\infty}\frac{\alpha^n}{\sqrt{n!}}|n\rangle. \tag{1.21}$$

This expression shows that the photon number probability of the coherent state is Poissonian. The state is composed of photons arriving at statistically independent times with a mean number of photons equal to $|\alpha|^2$. From this formula, we can also show that $\langle\alpha|\alpha'\rangle = e^{-|\alpha-\alpha'|^2}$, so the coherent states are not orthogonal and form an over-complete basis.

Using Eq. (1.5), we find that the standard deviation in the measurements of both the amplitude and phase quadratures of the single mode $\hat{a}$ is 1 in the coherent state basis. The result implies that $\Delta\hat{X}\Delta\hat{P} = L/c$ for the slowly varying envelope operator. The

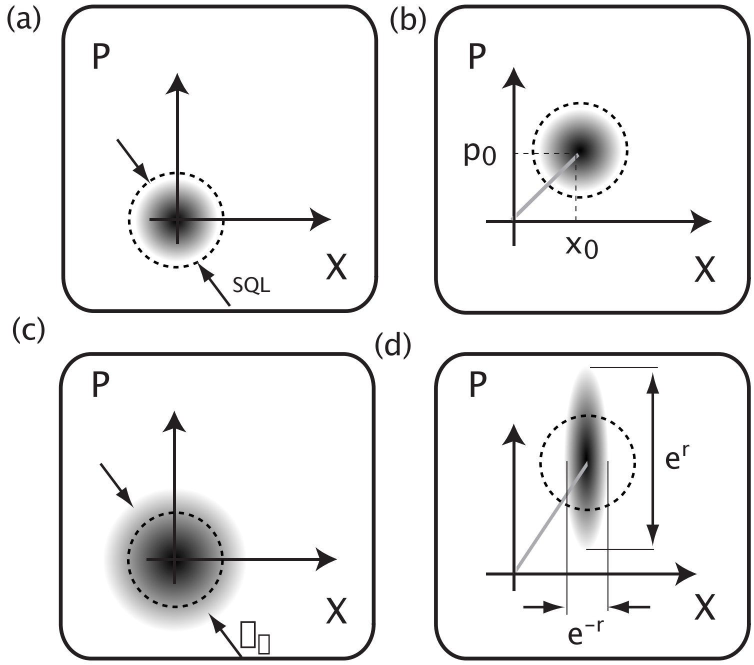

Figure 1.1: Wigner function on the (x, p) coordinates for different states : (a) for a vacuum state, (b) a coherent state, (c) a thermal state and (d) an amplitude squeezed state. The dashed line corresponds to the shot-noise limit.

Heisenberg uncertainty principle is satisfied exactly because we are describing a system prepared in a single eigenstate $|\alpha\rangle$. We can also see this from the purity parameter, which equals 1, implying that there is a minimum uncertainty relation between the two field quadratures[5]. The value of the product $\Delta\hat{X}\Delta\hat{P}$ for coherent states, defines the standard quantum limit, or shot-noise. We note that the standard quantum limit does not depend on the intensity $|\alpha|^2$ of the beam. Even in the limit where there are no actual photons (the state is then in the ground state of the harmonic oscillator, the vacuum state $|0\rangle$), this shot-noise is still present[6].

For a given coherent state $|\alpha_0\rangle$, $\rho = |\alpha_0\rangle\langle\alpha_0|$. The characteristic function is then

$$\chi(\lambda) = e^{\lambda\alpha_0^* - \lambda^*\alpha_0}. \tag{1.22}$$

Changing variables from (α, α^*) to $(x = 1/2(\alpha + \alpha^*), p = -i/2(\alpha - \alpha^*))$ in Eq. (1.19), we get the Wigner function of the coherent state

$$W(x, p) = \frac{2}{\pi}\exp\Big(-\frac{1}{2}(x - x_0)^2 - \frac{1}{2}(p - p_0)^2\Big). \tag{1.23}$$

This corresponds to a symmetric Gaussian profile in phase space whose width is the standard quantum limit. This is depicted Fig. 1.1 (a-b), for a vacuum state where

---

[5] There is equivalence between pure and minimum uncertainty states for Gaussian states.

[6] The coherent state can be obtained mathematically from the *displacement operator* $\hat{D}(\alpha)$ applied to the vacuum state $|0\rangle$ so that $|\alpha\rangle = \hat{D}(\alpha)|0\rangle$. This definition will be used to introduce squeezed states later in the section.

$(x_0, p_0) = (0, 0)$, and for a bright coherent state respectively.

Thermal states

The density matrix for a thermal state can be written in the Fock state basis. Using Boltzmann law to find the probability for the light field at energy $\hbar\omega$ to be in a certain Fock state given the temperature of a bath T, we obtain

$$\hat{\rho} = (1 - e^{\hbar\omega/kT}) \sum_n |n\rangle\langle n| e^{-n\hbar\omega/kT}. \tag{1.24}$$

From this expression, the characteristic function of the thermal state is found to be

$$\chi(\lambda) = \exp\Big[- \frac{|\lambda|^2}{e^{\hbar\omega/kT} - 1} \Big]. \tag{1.25}$$

After changing variables to (x, p) again, and introducing the quantity $\Gamma_T = \tanh(\hbar\omega/2kT)^{-1}$, we find the Wigner function

$$W(x, p) = \frac{2}{\Gamma_T \pi} \exp\big(- \frac{x^2 + p^2}{2\Gamma_T} \big). \tag{1.26}$$

This thermal state distribution is also symmetric in phase space but its width larger than the standard quantum limit when $T > 0$, as shown Fig. 1.1-(c). The photons emitted from the bath tend to broaden the distribution. This can be understood from the fact that the photons created in the beam mode are not randomly separated anymore, like for a Poissonian distribution, but rather arrive in clumps[7].

Squeezed states

A squeezed state $|\alpha, \xi\rangle$ may be obtained from the following mathematical transformation

$$|\alpha, \xi\rangle = \hat{D}(\alpha)\hat{S}(\xi)|0\rangle, \tag{1.27}$$

where $\hat{S}(\xi) = \exp\big(\frac{1}{2}\xi^* \hat{a}^2 - \frac{1}{2}\xi \hat{a}^{\dagger 2}\big)$, and ξ is the squeezing parameter. Unitary input-output relations can be obtained from the operator $S(\xi)$

$$\begin{aligned} \hat{S}^\dagger(\xi)\hat{a}\hat{S}(\xi) &= \hat{a}\cosh(r) + \hat{a}^\dagger e^{-2i\phi}\sinh(r) & (1.28) \\ \hat{S}^\dagger(\xi)\hat{a}^\dagger S(\xi) &= \hat{a}^\dagger \cosh(r) + \hat{a} e^{2i\phi}\sinh(r), & (1.29) \end{aligned}$$

where we write $r = \xi e^{-2i\phi}$. These transformations are "Local Linear Unitary Bogolioubov Operations" (LLUBO)[8]. We will come back to these expressions in section 1.4.4 and calculate ξ for the parametric oscillator.

Using the same procedure as for the coherent and thermal states, we obtain the Wigner function for the squeezed state

$$W(x, p) = \frac{2}{\pi} \exp\Big(- \frac{1}{2} e^{-2r}(x - x_0)^2 - \frac{1}{2} e^{2r}(p - p_0)^2 \Big). \tag{1.30}$$

---

[7] In the discrete variable "community" this effect is termed bunching.

[8] These transformations belong to the *simplectic* group. They preserve the commutation relations and can be realized from a Hamiltonian that is bilinear with respect to the field operators, like $\frac{1}{2}\xi^* \hat{a}^2 - \frac{1}{2}\xi \hat{a}^{\dagger 2}$. The second order non-linear interactions perform such operations, as will be shown.

The fluctuations in the $\hat{X}$ quadrature are reduced below the shot-noise level at the expense of an increase in the fluctuations in the quadrature $\hat{P}$, as can be seen Fig.1.1-(d). The state introduced here is pure ($e^{2r}e^{-2r} = 1$). Any loss mechanism will however transform the squeezed state into a mixed state. The formalism to describe such losses will be presented in the next section and are crucial to find ways to efficiently transfer continuous variable light states onto and from atoms.

1.1.6 Other quasi-probability distributions

We have already introduced the Wigner function to represent light states. Other probability distributions, well suited to the study of Gaussian states, were also introduced by Glauber [1963] and Sudarshan [1963] and then by Drummond and Gardiner [1980].

The P representation

When the state is composed of a statistical ensemble of coherent states, we may write

$$\hat{\rho} = \int d^2\alpha P(\alpha,\alpha^*)|\alpha\rangle\langle\alpha|. \tag{1.31}$$

This expression introduces a distribution P which represents the probability density to find a state $|\alpha\rangle$[9]. It was introduced independently by Glauber [1963] and Sudarshan [1963]. Because the coherent state basis is not orthogonal, the so-defined P function is also not a genuine probability distribution.

An expression for P can nevertheless be found. If $\hat{\rho}$ has a such a P representation, we can show that the normally ordered characteristic function $\chi_N(\lambda)$, is the two dimensional Fourier transform of $P(\alpha,\alpha^*)$. Taking the inverse Fourier transform, we then obtain

$$P(\alpha,\alpha^*) = \frac{1}{\pi^2}\int d^2\lambda e^{\lambda\alpha^*-\lambda^*\alpha}\chi_N(\lambda), \tag{1.32}$$

similarly to the definition of the Wigner function.

The Generalized P representations

As discussed, the P and Wigner representations are not genuine probability distributions. An alternative solution was formulated by Drummond and Gardiner [1980], who introduced generalized P-representations as expansions of the density matrix in non-diagonal coherent state projection operators.

The generalized P-representations are defined as

$$\hat{\rho} = \int \hat{\Lambda}(\alpha,\beta)P(\alpha,\beta)d\mu(\alpha,\beta), \tag{1.33}$$

where

$$\hat{\Lambda}(\alpha,\beta) = \frac{|\alpha\rangle\langle\beta^*|}{\langle\beta^*|\alpha\rangle}. \tag{1.34}$$

The integration measure $d\mu(\alpha,\beta)$ is applicable to different representations. For the *Glauber-Sudarshan-P* function defined Eq. (1.31) we see that $d\mu(\alpha,\beta) = \delta^2(\alpha^*-\beta)d^2\alpha d^2\beta$.

---

[9] For the coherent state, the P function is then a Dirac delta function.

A *complex-P* representation can also be defined as $d\mu(\alpha,\beta) = d\alpha d\beta$, so that (α,β) vary over complex conjugate contours. Because α and β are complex numbers the complex-P function does not have any equivalence in terms of probability distributions.

The *positive-P* representation uses $d\mu(\alpha,\beta) = d^2\alpha d^2\beta$ as integration measure and allows (α,β) to vary *independently* over the complex plane. This is the representation chosen to derive equations that model the EIT quantum memory in chapter 4.

All these representations were shown to exist mathematically for any density operator and we show how to obtain equations of motion for these probability distributions in Appendix B.

1.2 Interaction between a single mode light field and a single atom

The equation of motion for the reduced density matrix of a system interacting with a reservoir, the master equation, is derived Appendix A. In this section, we focus on the particular case of two-level atoms (as the system) interacting with laser modes $\hat{a}_k$ (reservoirs), the aim being again to present the tools and notations used in the next chapters. We present the damping and resulting atomic noise of the two-level atom and derive the Maxwell equation for a multimode laser field propagating in a non-linear atomic medium from the Heisenberg equation of motion of each mode $\hat{a}_k$. The equations will be described here in the Schrödinger picture until section 1.2.4 where we introduce the Heisenberg-Langevin equations.

1.2.1 Description of the model

The evolution of the reduced density matrix is given by

$$\frac{d}{dt}\hat{\rho} = \frac{1}{i\hbar}[\hat{\mathcal{H}}, \rho] + \mathcal{L}[\hat{\rho}], \tag{1.35}$$

where the so-called *Liouvillian* $\mathcal{L}[\hat{\rho}]$ is given by Eq. (A.15) in the Schrödinger picture, and the total Hamiltonian is $\hat{\mathcal{H}} = \hat{\mathcal{H}}_{\rm R} + \hat{\mathcal{H}}_{\rm at} + \hat{\mathcal{H}}_{\rm int}$. The free space Hamiltonian $\hat{\mathcal{H}}_{\rm R}$ for the light field is

$$\hat{\mathcal{H}}_{\rm R} = \sum_k \hbar\omega_k(\hat{a}_k^\dagger \hat{a}_k + \frac{1}{2}), \tag{1.36}$$

and the rest atomic energy $\mathcal{H}_{\rm at}$ is

$$\hat{\mathcal{H}}_{\rm at} = \hbar\omega_{\rm at}\hat{\sigma}^\dagger\hat{\sigma}. \tag{1.37}$$

For neutral atoms, the coupling between light and atoms can be modelled by the Hamiltonian $\hat{\mathcal{H}}_{\rm int} = -\hat{d}.\hat{E}$ (the dipolar approximation). The interaction Hamiltonian coupling the atomic mode with the laser modes k is

$$\hat{\mathcal{H}}_{int} = \hbar(\hat{\sigma} + \hat{\sigma}^\dagger)(\hat{\Gamma} + \hat{\Gamma}^\dagger), \tag{1.38}$$

where $\hat{\Gamma} = \sum_k g_k \hat{a}_k$ and g_k is the vacuum Rabi frequency given by

$$g_k = d_k \sqrt{\frac{\omega_k}{2\epsilon_0 V \hbar}}. \tag{1.39}$$

ϵ_0 is the permeability of the vacuum, V the quantized volume considered, ω_k the frequency of the transition and d_k the dipole moment of the atomic transition k. The operator products $\hat{\sigma}\hat{\Gamma}$ and $\hat{\sigma}^\dagger\Gamma^\dagger$ give rise to oscillations that are two times faster than the atomic transition frequency. They then correspond to far off-resonant excitations and will be neglected. After doing this *rotating wave approximation* we obtain the so-called *Jaynes-Cummings* Hamiltonian

$$\hat{\mathcal{H}}_{int} = \hbar(\hat{\sigma}\hat{\Gamma}^\dagger + \hat{\sigma}^\dagger\hat{\Gamma}). \tag{1.40}$$

which describes both the stimulated emission and the absorption of photons.

1.2.2 Reversible evolution of the density matrix

In this section, we focus on the physics of the reversible interaction of light with a two-level atom. The damping and noise arising from the coupling of the atom with the bath will be described in the next subsection. We assume here that the atom is driven by coherent radiation modes, and write $g\langle\hat{\mathcal{E}}\rangle = \langle\hat{\Gamma}\rangle$.

The evolution of the averaged atomic modes can be found by tracing over the atomic variables

$$\langle\hat{\sigma}_{12}\rangle = \mathrm{Tr}_{\mathrm{at}}(\hat{\rho}\hat{\sigma}) \ ; \ \langle\hat{\sigma}_{11}\rangle = \mathrm{Tr}_{\mathrm{at}}(\hat{\rho}\hat{\sigma}^\dagger\hat{\sigma}) \ \text{ and } \ \langle\hat{\sigma}_{22}\rangle = \mathrm{Tr}_{\mathrm{at}}(\hat{\rho}\hat{\sigma}\hat{\sigma}^\dagger), \tag{1.41}$$

which are the respective atomic coherences and populations in the ground/excited state of the atom. Using the cyclic properties of the trace and Eq.(1.35), excluding the Liouvillian for now, we get the equations of motion

$$\begin{aligned} \frac{d}{dt}\langle\hat{\sigma}_{12}\rangle &= -i\omega_{\mathrm{at}}\langle\hat{\sigma}_{12}\rangle + ig\langle\hat{\mathcal{E}}\rangle(\langle\hat{\sigma}_{11}\rangle - \langle\hat{\sigma}_{22}\rangle) \\ \frac{d}{dt}\langle\hat{\sigma}_{11}\rangle &= +ig(\langle\hat{\mathcal{E}}\rangle^*\langle\hat{\sigma}_{12}\rangle - \langle\hat{\mathcal{E}}\rangle\langle\hat{\sigma}_{21}\rangle). \end{aligned} \tag{1.42}$$

They describe how the light field creates coherences and distributes atomic population via *Rabi flopping*. We will find solutions to this equation by introducing the Bloch-sphere in chapter 6.

The evolution of the atoms in a quantum memory is often well described in the weak probe regime. The Rabi frequency of the laser field that is to be stored is assumed to be much less than g so that the population in the excited state $\langle\hat{\sigma}_{22}\rangle$ is negligible. Using population preservation, we are only left with a single linear equation for the optical coherence

$$\frac{d}{dt}\langle\hat{\sigma}_{12}\rangle \simeq -i\omega_{\mathrm{at}}\langle\hat{\sigma}_{12}\rangle + ig\langle\hat{\mathcal{E}}\rangle, \tag{1.43}$$

which we will use extensively throughout this thesis.

1.2.3 Damping of the coherences and populations

We now turn to the (irreversible) damping of the two-level atom. To describe damping, we need to consider the interaction of a single atomic mode σ, with a reservoir of light modes. The damping of the harmonic oscillator will be derived from the master equation (A.15). We will first be using a Jaynes-Cummings interaction with the bath. This will lead to a damping of both the populations and the coherences. Then, we use a phase-damping Hamiltonian, which will only lead to a decay of the coherences.

Damping affecting populations and coherences

The first form of coupling between the two-level atom and the bath that we use is the Jaynes-Cummings Hamiltonian

$$\hat{V} = \hbar\hat{\sigma}^\dagger\hat{\Gamma}_b + h.c., \tag{1.44}$$

where $\hat{\Gamma}_b = \sum_i g_i\hat{a}_i$. We will compute the equation of motion describing the evolution of the atom in the presence of such a coupling with the radiation bath. By inserting this interaction Hamiltonian in the master equation (A.15), we obtain the equation for the reduced density matrix $\tilde{\rho}$

$$\begin{aligned} \frac{d\tilde{\rho}}{dt} &= \frac{-1}{\hbar^2}(\sigma^\dagger\sigma\tilde{\rho} - \sigma\tilde{\rho}\sigma^\dagger)\int_0^\infty \mathrm{d}(t'-t'')\langle\tilde{\Gamma}_b(t')\tilde{\Gamma}_b^\dagger(t'')\rangle_B e^{i\omega_0(t'-t'')} \\ &+ \frac{-1}{\hbar^2}(\tilde{\rho}\sigma\sigma^\dagger - \tilde{\rho}\sigma\sigma^\dagger)\int_0^\infty \mathrm{d}(t'-t'')\langle\tilde{\Gamma}_b^\dagger(t')\tilde{\Gamma}_b(t'')\rangle_B e^{i\omega_0(t'-t'')} \\ &+ h.c. \end{aligned} \tag{1.45}$$

Doing a spectral decomposition of $\tilde{\Gamma}_b$ in the Fock state basis using Eq. (1.24) we get

$$\langle\tilde{\Gamma}_b(t')\tilde{\Gamma}_b^\dagger(t'')\rangle_B = \sum_i |g_i|^2(\langle n_i\rangle + 1)e^{-i\omega_i(t'-t'')} \tag{1.46}$$

$$\langle\tilde{\Gamma}_b^\dagger(t')\tilde{\Gamma}_b(t'')\rangle_B = \sum_i |g_i|^2\langle n_i\rangle e^{-i\omega_i(t'-t'')}, \tag{1.47}$$

where $\langle n_i\rangle$ represents the average number of excitation quanta in the mode i. We note that the normally ordered correlation Eq. (1.47) contribute to the evolution of the density matrix only when the bath contains photons ($\langle n_i\rangle \neq 0$), which occurs for temperatures larger than $\hbar\omega/k_B$. The anti-normally ordered correlation (1.46) however always contribute to the dynamics of $\tilde{\rho}$, even at zero Kelvin, and gives rise to zero-point fluctuations of the two level atom.

We can now perform the integration in equation (1.45), and go back to the Schrödinger representation for the reduced density matrix. We obtain

$$\begin{aligned} \frac{d}{dt}\hat{\rho} &= -i(\omega_{\mathrm{at}} + \Delta_L)[\hat{\sigma}^\dagger\hat{\sigma}, \hat{\rho}] + \gamma(\hat{\sigma}\hat{\rho}\hat{\sigma}^\dagger - \frac{1}{2}\hat{\sigma}^\dagger\hat{\sigma}\hat{\rho} - \frac{1}{2}\hat{\rho}\hat{\sigma}^\dagger\hat{\sigma}) \\ &+ \gamma'(\hat{\sigma}\hat{\rho}\hat{\sigma}^\dagger + \hat{\sigma}^\dagger\hat{\rho}\hat{\sigma} - \hat{\rho}), \end{aligned} \tag{1.48}$$

where we introduced

$$\begin{aligned}\gamma &= \frac{2\pi}{\hbar}\sum_i |g_i|^2\delta(\hbar\omega-\hbar\omega_i)\ ;\ \gamma' = \frac{2\pi}{\hbar}\sum_i |g_i|^2\langle n_i\rangle\delta(\hbar\omega-\hbar\omega_i) \\ \hbar\Delta_L &= \mathcal{P}\sum_i \frac{|g_i|^2}{\hbar\omega-\hbar\omega_i}\ ;\ \hbar\Delta_L' = \mathcal{P}\sum_i \frac{|g_i|^2\langle n_i\rangle}{\hbar\omega-\hbar\omega_i}. \end{aligned} \tag{1.49}$$

The δ and $\mathcal{P}$, are the Kronecker symbol and principal Cauchy integral respectively. They arise from the integration of the exponential. The quantities γ, γ' will be crucial for the performance of the quantum memories and will be used many times in the next chapters. To understand their physical meanings, we will calculate the evolution of the averaged atomic variables. Using Eq. (1.41), we find

$$\frac{d}{dt}\langle\hat{\sigma}_{12}\rangle = -\big(i(\omega_{\text{at}}+\Delta_L)+\frac{\gamma}{2}\big)\langle\hat{\sigma}_{12}\rangle \tag{1.50}$$

$$\frac{d}{dt}\langle\hat{\sigma}_{22}\rangle = -\gamma\langle\hat{\sigma}_{22}\rangle+\gamma'. \tag{1.51}$$

The significance of the terms of Eq. (1.49) is now evident. γ induces a decay of the coherences and excited state atomic population. It is therefore an inelastic process. A photon is given to the bath during this spontaneous decay, the origin of which can be interpreted as a coupling of the atomic modes to the vacuum modes of the reservoir. $\hbar\Delta_L$ is a radiative frequency shift of the atom resulting from this spontaneously emitted photon (the Lamb shift). Both these terms have a pure quantum origin.

γ' on the other hand does not affect the coherence but only the populations. It corresponds to a stimulated emission and absorption of photon in/from the reservoir. Indeed, this term allows an atom initially in the ground state, to reach the excited state when $\langle n_i\rangle \neq 0$, i.e at temperatures $T > \hbar\omega/k_B$. This is not true for optical transitions[10] but might be reached for RF-transitions. We note that the associated frequency shift $\hbar\Delta_L'$ does not appear in the evolution of the atom. This is because the radiative shift caused by the absorption is equal and opposite to the shift caused by stimulated emission.

The damping term $2/\gamma$ affecting the coherence is called the longitudinal decoherence time T_1, and the damping affecting the populations $(1/\gamma)$ is called the transverse decoherence time T_2, because of their roots in nuclear magnetic resonance, where the atomic evolution is represented on a Bloch-sphere. (We will come back to the Bloch-sphere when presenting photon echo memories in chapter 6.) Here we have $T_1 = 2T_2$, but generally we would have $T_1 < 2T_2$ due to processes that only cause a loss of coherence.

Phase-damping

The previous Jaynes-Cummings type coupling term leads to damping of both the populations and the coherences. If we now have a system where the populations are preserved, but not the coherences, another form of Hamiltonian coupling with the bath must be used. This is the case when random frequency splittings between the two levels happen, due to elastic collisions or inhomogeneous magnetic fields. Such a “scattering Hamiltonian” may be found by considering an atom interacting off-resonance with a light field and adiabatically eliminating the light field fluctuations. This kind of interaction involves

---

[10] We will therefore set γ' to zero in this thesis.

loss-less scattering of the atom in a different mode, which is the kind of dynamics we need to describe the phase damping [Walls and Milburn, 1985]. The Hamiltonian is of the form

$$\hat{V} = \hbar\hat{\sigma}_z\hat{\Gamma}_b + h.c, \tag{1.52}$$

where we introduced $\hat{\sigma}_z = \hat{\sigma}^\dagger\hat{\sigma}$. It can be shown using Eq.(A.15) that the master equation describing such a phase damping of the two-level atom is now

$$\frac{d}{dt}\hat{\rho} \;=\; -i(\omega_{\text{at}} + \Delta_L)[\hat{\sigma}_z, \hat{\rho}] + \gamma_0(\hat{\sigma}_z\hat{\rho}\hat{\sigma}_z - \frac{1}{2}\hat{\sigma}_z\hat{\rho} - \frac{1}{2}\hat{\rho}\hat{\sigma}_z). \tag{1.53}$$

where γ_0 is the decay term associated with this new coupling. Using Eq.(1.41) again, we now obtain

$$\begin{aligned} \frac{d}{dt}\langle\hat{\sigma}_{12}\rangle &= -\big(i(\omega_{\text{at}} + \Delta_L) + \frac{\gamma_0}{2}\big)\langle\hat{\sigma}_{12}\rangle & (1.54) \\ \frac{d}{dt}\langle\hat{\sigma}_{22}\rangle &= 0, & (1.55) \end{aligned}$$

so that only the coherences decay, at a rate given by $\gamma_0/2$. This phase damping term is also widely used to describe the loss of coherence in the ground states of three-level systems.

1.2.4 Heisenberg-Langevin equations

We used a Schrödinger approach to derive equations modelling a reversible, or unitary, atomic evolution with a coherent radiation field. From the master equation, we then derived damping terms giving rise, for example, to spontaneous emission. We showed the physical significance of those terms in the mean atomic evolution. We will go a bit further in chapter 4, and instead of tracing over the atomic degrees of freedom and assuming a classical laser field, we will unravel the master equation to obtain a set of Itô quantum stochastic differential equations. The steps to be taken using such an approach are detailed in Appendix A and B.

As briefly mentioned earlier, another way to solve the problem is to let the operators evolve in time in the Heisenberg picture. The Heisenberg equation for a time dependent operator $\hat{O}(t)$ is

$$\frac{d}{dt}\hat{O}(t) = -\frac{1}{i\hbar}[\hat{\mathcal{H}}, \hat{O}(t)], \tag{1.56}$$

where $\hat{\mathcal{H}}$ describes the total energy of the universe (system plus reservoir)[11].

To preserve the commutation relations of the system variables in the presence of damping in a full quantum model, one includes the coupling with the modes of a reservoir. This of course gives the same decay terms found above plus "stochastic terms" containing the reservoir operators called *Langevin* noise.

Rather than deriving the *Heisenberg-Langevin* equations here, we will follow a slightly different route. We find the reversible equation of motion for the operators using the Heisenberg equations (so without the coupling to a bath). Then, we "add" the decay terms resulting from the coupling with the reservoir found in the Schrödinger approach

---

[11] Mind the difference in the sign for the Heisenberg equation of motion and the Von-Neuman equation for $\hat{\rho}$.

together with the stochastic Langevin terms. We do not give the formal expressions of the Langevin terms but we show in Appendix A how to obtain a correlation relation (the *generalized Einstein relations*) between them from the commutation properties of the system variables.

Incorporating the damping terms from Eqs. (1.50-1.51) and Eqs. (1.54-1.55), and including their associated Langevin operator $\hat{F}_{ij}$, we find

$$\begin{aligned}
\frac{d}{dt}\hat{\sigma}_{12} &= -\big(i\omega_{\text{at}} + \frac{\gamma+\gamma_0}{2}\big)\hat{\sigma}_{12} + ig\hat{a}_k(\hat{\sigma}_{11} - \hat{\sigma}_{22}) + \hat{F}_{12} \\
\frac{d}{dt}\hat{\sigma}_{11} &= \gamma\hat{\sigma}_{22} + ig(\hat{a}_k^{\dagger}\hat{\sigma}_{12} - \hat{a}_k\hat{\sigma}_{12}^{\dagger}) + \hat{F}_{11} \\
\frac{d}{dt}\hat{\sigma}_{22} &= -\gamma\hat{\sigma}_{22} - ig(\hat{a}_k^{\dagger}\hat{\sigma}_{12} - \hat{a}_k\hat{\sigma}_{12}^{\dagger}) + \hat{F}_{22}. \qquad (1.57)
\end{aligned}$$

They are the *Heisenberg-Langevin* equations. We here inserted the light shifts Δ_L into ω_{at} and disregarded the decay γ'. These equations describe the interaction between an optical quantized field mode $\hat{a}_k$ and the two-level atom. We introduced the fluctuating forces $\hat{F}_q(t)$ with zero mean, responsible for a random walk of the $\hat{\sigma}_q$s due to "collisions" with the bath's modes. These terms are necessary to preserve the commutation relations of the system observables during the interaction. This will become apparent in chapter 4. The mean of the $\hat{F}_q(t)$'s is zero but their fluctuations are macroscopic and can give rise to measurable noise.

The Heisenberg-Langevin equations are a "quantum analog" to the classical Brownian motion of a small particule colliding with heavy particules. They provide a means for calculating the noise added to the system. Compared with the Schrödinger approach based on the unravelling of the master equation, it is useful in situations where analytical expressions can be found, and gives another insight on the mechanisms giving noise. Historically, it was also the first stochastic equation where a fluctuating term was used to derive macroscopic quantities, allowing a clear link to be made between dissipation and fluctuation.

1.3 Interaction of quantum states of light with atomic ensembles

We now present a model describing the interaction of quantum states of light with a collection of N atoms in the Heisenberg picture. The state basis over which the measurement is done is supposed to be the state, $|\text{All the atoms in the ground state}\rangle \otimes |\text{n photons}\rangle$.

1.3.1 The Maxwell equation

We will be interested in studying the propagation of a multimode quantum state of light travelling through an ensemble of atoms. Due to the coupling with the atoms, the light field might be absorbed throughout its propagation in the medium. It is then important to include its dependence with propagation distance. The total Hamiltonian $\hat{\mathcal{H}}$ of the system can again be decomposed into three parts defining the free space energy of the light field $\hat{\mathcal{H}}_R$, the atom rest energy $\hat{\mathcal{H}}_{at}$ and the above interaction potential $\hat{\mathcal{H}}_{int}$.

To get an equation of motion for the envelope operator introduced in section (1.1), we can write the Heisenberg equation of motion for a mode $\hat{a}_k$ and Fourier transform it over k to obtain an equation of motion for the collective evolution of all the optical modes

$\hat{\mathcal{E}}(z,t) = \int dk \hat{a}_k \exp(ikz)$. Using the fact that $[\hat{\mathcal{H}}_R, \hat{\mathcal{H}}_{at}] = 0$, we have

$$\frac{1}{\sqrt{2\pi}} \int dk \frac{1}{i\hbar} \big[\hat{a}_k(t), \hat{\mathcal{H}}_R + \hat{\mathcal{H}}_{int}\big] e^{ikz} = \frac{1}{\sqrt{2\pi}} \int dk \frac{\partial}{\partial t} \hat{a}_k(t) e^{ikz} \tag{1.58}$$

$$= \frac{\partial}{\partial t} \hat{\mathcal{E}}(z,t), \tag{1.59}$$

and since $[\hat{a}_k(t), \hat{\mathcal{H}}_R] = \hbar c k \hat{a}_k(t)$, in the interaction picture[12], we get

$$\Big(\frac{\partial}{\partial t} + c\frac{\partial}{\partial z}\Big)\hat{\mathcal{E}}(z,t) = \frac{1}{i\hbar}\big[\hat{\mathcal{E}}(z,t), \hat{\mathcal{H}}_{int}\big]. \tag{1.60}$$

This is the *Maxwell equation* for the slowly varying quantum envelope. The right hand side is often called the source term. It will be responsible for the absorption and phase shifts imposed on the light field by the atoms. When this term is negligible, the light propagates freely at the speed of light c.

We now turn to the modelling of the atomic ensemble operators.

1.3.2 Local averaging

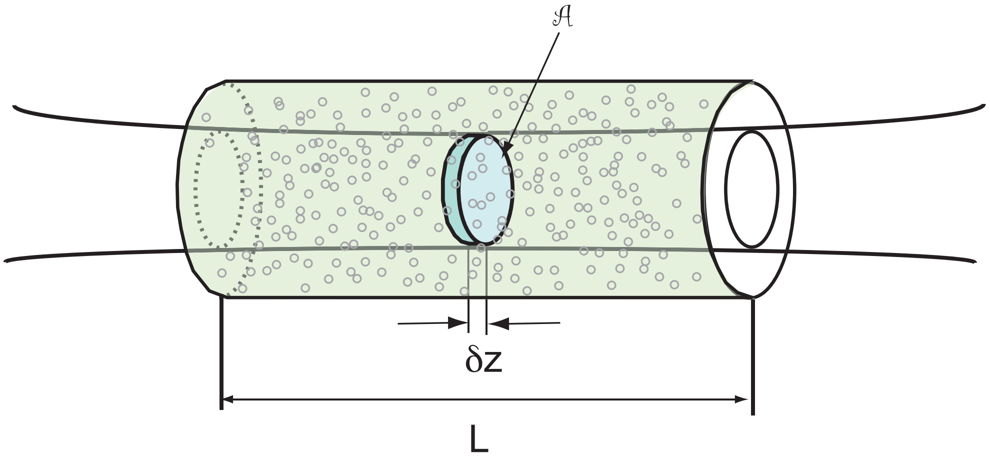

Figure 1.2: Schematic of an ensemble of atoms interacting with a laser beam. $\mathcal{A}$ is the cross section area of the beam inside the medium, δz a infinitesimal slice long the propagation direction.

We define locally averaged atomic dipole operators $\hat{\sigma}_{ij}(z,t)$ for the $|i\rangle - |j\rangle$ transition given by (see for example [Fleischhauer and Lukin, 2000, Peng et al., 2005])

$$\hat{\sigma}_{ij}(z,t) = \frac{1}{n\mathcal{A}\delta z} \sum_{z_k \in \delta z} \hat{\sigma}^k_{ij}(z,t), \tag{1.61}$$

where $\mathcal{A}$ is the cross-sectional area of the beam, n the atomic density and δz an infinitesimal slice of the medium containing N identical atoms, as depicted Fig. (1.2). The averaged dipole operators commute when they belong to a different slice δz. The linearity of equations (1.57) for the single atoms $\hat{\sigma}^k_{ij}(z,t)$ ensures that the averaged atomic

---

[12] k is then the momentum *relative* to $k_0 = 2\pi/\lambda$.

operators defined by Eq.(1.61) obey the same Heisenberg-Langevin equations. Going to the continuum limit, Fourier transforming over k and integrating over z, the interaction Hamiltonian can be written in terms of the locally-averaged atomic operators as

$$\hat{\mathcal{H}}_{\text{int}} = \int \frac{N\hbar}{L}[g\hat{\sigma}^{\dagger}(z,t)\hat{\mathcal{E}}(z,t) + h.c.]dz. \tag{1.62}$$

Using Eq.(1.62) and Eq.(1.60), we get

$$(\frac{\partial}{\partial t} + c\frac{\partial}{\partial z})\hat{\mathcal{E}}(z,t) = igN\hat{\sigma}(z,t). \tag{1.63}$$

This expression can be simplified by moving into a frame at the speed of light and performing the transformation $z \to z - \tau/c$, where $t = \tau$. We obtain

$$\frac{\partial}{\partial z}\hat{\mathcal{E}}(z,\tau) = \frac{igN}{c}\hat{\sigma}(z,\tau). \tag{1.64}$$

As the time and space evolution is decoupled in the Heisenberg equation for the atomic evolution and the Maxwell equations, self-consistent solutions are easily found numerically. In this thesis, we will often use XMDS to solve this system of equations. XMDS is the acronym for eXtensible Multi-Dimensional Simulator. The equations are written in a high level form in XML (extensible markup language) and XMDS generates the low level code in C which can then be run. The documentation and source code are available from http://www.xmds.org.

The analyses presented in these first sections concentrated on the interaction between light and atomic modes at the quantum level. We also defined specific quantum states of light. We now need to study how to produce and detect such states.

1.4 Detection and production of Gaussian states

This section is devoted to the detection of continuous variable Gaussian states and their production. We will focus on phase-insensitive detection and balanced homodyne detection. Then, we introduce Fabry-Perot cavities as tools for spectral and spatial filtering of light beams, allowing one to improve the efficiency of homodyne measurements. Squeezed light generation from a parametric amplifier is then presented. A linearized approach is finally used to explain squeezed states of light, entangled states and classical information from a sideband picture. This section is especially relevant to chapter 2, 3 and 5. All the results will be presented in the Heisenberg picture here.

1.4.1 Phase-insensitive photodetection

Direct photodetection

Let us consider the simple case of photo-detection first. We will calculate the evolution of the measured noise power with the mean number of photons hitting the detector. We will show that while the noise power of a classical (thermal) source shows a quadratic dependence with the mean photon number, the noise power of a Poissonian source varies linearly, as expected from a Poissonian distribution of photons.

Using the photoionization process, photomultipliers or semiconductor diodes transform a stream of photons to a stream of electrons. The quantum theory of photodetection was

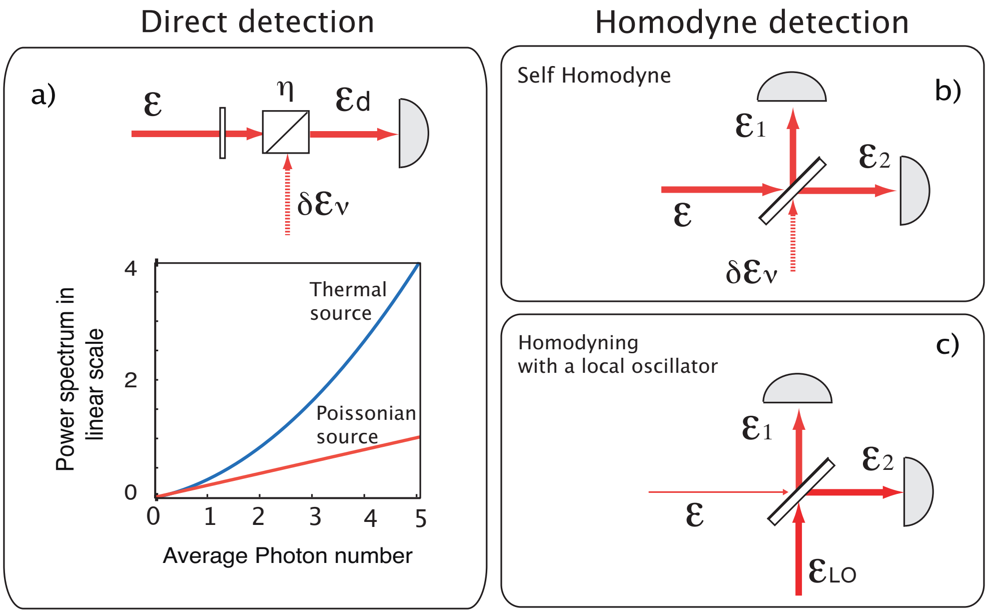

Figure 1.3: Homodyne and direct detection. (a) Calibration of shot-noise using a single detector. (b) Self homodyne measurement. (c) Homodyne measurement.

developed by Glauber [1963]. It was shown that when a detector absorbs all the photons from a field $\hat{\mathcal{E}}_d$, one can define a photocurrent operator

$$\hat{i}(t) = \hat{\mathcal{E}}_d^\dagger(t)\hat{\mathcal{E}}_d(t). \tag{1.65}$$

This photocurrent is then usually amplified and analyzed to yield information about the statistics of the light field. As will be seen in chapters 3 and 5, the noise spectrum of this photocurrent is often not white, and the detection not broadband. The photocurrent is then measured within a certain frequency bandwidth. To do such a measurement, one can use a spectrum analyzer that measures the power spectral density directly. The acquisition can also be done in the time domain. After down sampling the acquired photocurrent to DC, one can calculate its standard deviation around the mean value, which squared also gives the power spectral density.

The power spectral density[13] $S_d(\omega)$ of the operator $\hat{i}(t)$ measured during a time T, is the Fourier transform of its autocorrelation function $g(\tau) = \langle\psi|\hat{i}^\dagger(t)\hat{i}(t-\tau)|\psi\rangle$[14], where $|\psi\rangle$ is the state of the light field over which the measurement is done (we do not write it explicitly from now on). We then have

$$S_d(\omega) = \int_T d\tau g(\tau) e^{-i\omega\tau}. \tag{1.66}$$

When normalized to the detection bandwidth B, chosen to be much smaller than the frequency range of interest, we can show that the measured power spectrum is

$$S_d(\omega) = B\langle\hat{i}(\omega)\hat{i}(-\omega)\rangle, \tag{1.67}$$

---

[13] At some RF frequency ω in a rotating frame at the carrier frequency.
[14] Wiener-Kintchine theorem.

that is the correlation between signals oscillating at ω and $-\omega$ with respect to the carrier frequency. The power spectral density $S_d(\omega)$ is then directly related to the variance $V(\omega) = \langle|\hat{i}(\omega)|^2\rangle$ in the measurement of the observable $\hat{i}(\omega)$.

Mean field approximation

For Gaussian states, we can always write $\hat{\mathcal{E}}_d(t) = \langle\hat{\mathcal{E}}_d(t)\rangle + \delta\hat{\mathcal{E}}_d(t)$, that is we can decompose the light state into a mean value plus a fluctuating term with zero mean value. Provided the light field intensity is much larger than the amplitude of the fluctuations, one can perform a so-called *mean-field approximation.* We neglect second order terms like $\delta\hat{\mathcal{E}}_d^\dagger(t)\delta\hat{\mathcal{E}}_d(t)$ compared to $\langle\hat{\mathcal{E}}_d(t)\rangle^2$. This allows us to obtain

$$\hat{i}(t) = \alpha_d^2 + \alpha_d\delta\hat{X}_d(t), \tag{1.68}$$

where $\hat{X}_d(t)$ is the amplitude quadrature. We assumed the mean-field amplitude $\langle\hat{\mathcal{E}}_d(t)\rangle = \alpha_d$ to be real. We see that a single detector can only ever measure the amplitude quadrature fluctuations of the light field. A homodyne detection is necessary to measure the phase quadrature. We will come to this in the next subsection.

Dependence between noise power and mean number of photons

It is instructive to consider the evolution of the power spectrum of an optical signal being attenuated by a passive absorber, like a beam splitter, before the detection. We consider the situation depicted in Fig. 1.3-(a). The beam splitter introduces some loss $\sqrt{\eta}$ on the laser mode $\hat{\mathcal{E}}(t)$. The output of this beam splitter obeys the canonical relation

$$\hat{\mathcal{E}}_d(t) = \sqrt{\eta}\hat{\mathcal{E}}(t) + \sqrt{1-\eta}\delta\hat{\mathcal{E}}_\nu(t), \tag{1.69}$$

where we added a vacuum term $\delta\hat{\mathcal{E}}_\nu(t)$ to preserve the commutation relations of the field $\hat{\mathcal{E}}_d$. Doing a mean-field approximation, we can obtain a simple expression for the photocurrent

$$\hat{\mathcal{E}}_d^\dagger(t)\hat{\mathcal{E}}_d(t) = \alpha(\eta\alpha + \eta\delta\hat{X}(t) + \sqrt{\eta(1-\eta)}\delta\hat{X}_\nu(t)), \tag{1.70}$$

where $\delta\hat{X}(t)$ is the fluctuating part of the amplitude quadrature of the field before the beam splitter. We can now get a relation between the autocorrelation function of the photocurrent $g(\tau)$, and the autocorrelation function of the vacuum and input field amplitude quadratures

$$\langle\hat{i}(t)\hat{i}(t-\tau)\rangle = \alpha^2\left[\eta^2\alpha^2 + \eta^2\langle\delta\hat{X}(t)\delta\hat{X}(t-\tau)\rangle + \eta(1-\eta)\langle\delta\hat{X}_\nu(t)\delta\hat{X}_\nu(t-\tau)\rangle\right]. \tag{1.71}$$

The power spectral density of the photocurrent $\hat{i}(t)$ can be found by taking the Fourier transform of this equation. Disregarding the time independent term, we obtain

$$S_d(\omega) = \alpha^2\left[\eta^2 V(\omega) + \eta(1-\eta)\right], \tag{1.72}$$

where $V(\omega)$ is the variance of the amplitude quadrature that would be measured before the beam splitter. We also set $V_\nu(\omega)$, the variance of the vacuum coupled via the "empty" port of the attenuator, to unity.

Let us now decompose the time-varying part of the light field before the beam splitter into the sum of two uncorrelated signals, a shot-noise limited signal $\delta\hat{X}'_\nu$ and a classical signal $\delta\hat{X}_s$. We then have $V(\omega) = V_s(\omega) + 1$. Substituting it in the above expression and replacing η by α_d^2/α^2, we finally obtain the relation

$$S_d(\omega) \propto N^2 V_s(\omega) + N V_\nu(\omega). \tag{1.73}$$

As V_s and V_ν do not depend on α_d, the evolution of the power spectrum is quadratic as a function of mean number of photons $N = \alpha_d^2$ impinging on the detector for a classical source, and linear for a Poissonian source as indicated Fig.1.3-(a). This is a signature of the statistics of a thermal state and a coherent state[15] respectively.

This method then provides a way to experimentally determine if a laser is shot-noise limited.

1.4.2 Balanced detection

The above method gives an insight on the statistics of the photons involved in the measurements outcomes. However, when two similar detectors are available, a more direct calibration of the shot-noise may be performed, using a so-called *homodyne* method.

Self-homodyne detection

Let us first introduce the self-homodyne method, depicted Fig.1.3-(b). By splitting the signal beam into two even parts and measuring the sum and difference of the photocurrents one can get a direct calibration of the shot-noise.

The sum and difference photocurrents can easily be found to be

$$\begin{aligned} \hat{i}_s(t) &= \alpha^2 + \alpha\delta\hat{X}(t) && (1.74) \\ \hat{i}_d(t) &= \alpha\delta\hat{X}_\nu(t), && (1.75) \end{aligned}$$

respectively, where we kept the same notations as above. The power spectra of the difference and sum signals at a given sideband frequency are then (disregarding the constant terms again)

$$S_s(\omega) = \alpha^2 V_{\rm in}(\omega) \text{ and } S_d(\omega) = \alpha^2 V_\nu(\omega). \tag{1.76}$$

The power spectra are therefore identical if the amplitude quadrature of the input state reaches the shot-noise limit, which allows one to conclude as to whether the laser source is at the shot-noise or not.

Homodyne detection

The above measurements do not allow one to get information about the phase quadrature. In quantum information science, one needs to perform measurements of both the amplitude and phase observables as we will discuss next. Also, as the detected signal power is proportional to the mean-field amplitude, these techniques do not allow the detection of too weak beams. We describe here a method that solves these two problems. It is based on the mixing of the signal beam with a strong *local oscillator* in the same mode, on a beam splitter and doing a subtraction of the two photocurrents. This method, called a *homodyne* detection, is sketched Fig.1.3-(c).

---

[15] The standard deviation in the number of photons is $\sqrt{N}$ for a Poissonian source so the variance scales linearly with N.

Let us write $\hat{\mathcal{E}}_{\rm LO}$ the local oscillator light mode and $\hat{\mathcal{E}}$ the signal. After efficient mixing of the two modes on a 50/50 beam splitter, the output of the two ports can be written

$$\hat{\mathcal{E}}_1 = \frac{1}{\sqrt{2}}(\hat{\mathcal{E}} - \hat{\mathcal{E}}_{\rm LO}) \text{ and } \hat{\mathcal{E}}_2 = \frac{1}{\sqrt{2}}(\hat{\mathcal{E}} + \hat{\mathcal{E}}_{\rm LO}), \tag{1.77}$$

where we recognize the π phase shift due do the hard reflection on the beam splitter. The two photocurrents are then subtracted electronically. One can easily show after a mean-field approximation and assuming the local oscillator to be much larger than the signal, that the subtracted signal equals

$$i_d(t) = \alpha_{\rm LO}\delta\hat{X}^\theta(t), \tag{1.78}$$

where θ is the phase difference between the local oscillator and the signal and $\alpha_{\rm LO}$ the mean amplitude of the local oscillator. We also introduced

$$\hat{X}^\theta = \hat{\mathcal{E}}e^{-i\theta} + \hat{\mathcal{E}}^\dagger e^{i\theta}. \tag{1.79}$$

One of the main features of this technique is that the local oscillator noise is subtracted away. We also note that the power spectrum of the subtracted signal is proportional to the local oscillator strength only. The fluctuations of the phase or amplitude quadratures of a signal, no matter how weak, can be measured. The homodyne technique will be used extensively in the experiments chapter 3 and 5 to measure squeezed vacuum states.

As quantum states of light are extremely sensitive to loss, it is important to minimize the possible sources of inefficiencies in their measurements. We list here three of the most important requirements for an efficient homodyne measurement.

Detectors inefficiencies Depending on the wavelength, different materials will be chosen to enhance the photon-photocurrent conversion at the detection. The quantum efficiency is extremely close to 100% nowadays, in Silicon substrates at a wavelength 860 nm for example.

Mode matching The signal and local oscillator need to perfectly interfere at the beam splitter. Any mode matching inefficiency can be modelled easily by including a finite interference contrast V. The net result is to decrease the detection efficiency by a factor of V^2.

Dark noise clearance The local oscillator power has to be large enough for the noise floor to be far above the thermal noise of the electronics used to amplify the photocurrent. It also has to be much larger than the power of the signal beam to minimize errors on the shot-noise level. We note that the splitting ratio of the beam splitter does not have to be 50%. If one can measure signals far above the dark noise of each detector and compensate the unbalance with electronic gains, this is not required.

1.4.3 Fabry-Perot cavity

Getting a pure transverse mode is crucial to ensure optimum efficiency of quantum-optics experiments, for example for a good mode matching between the local oscillator and the light beam to be measured in homodyne detection. Also a large cancellation of the local

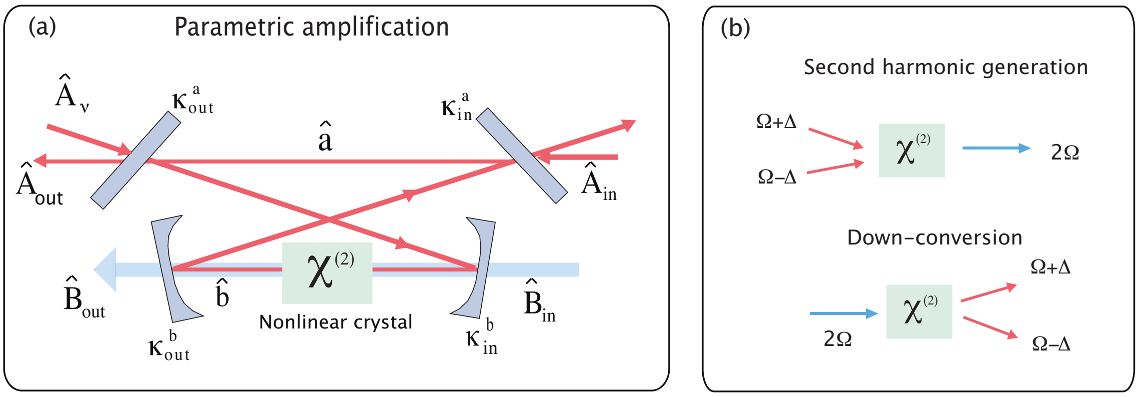

Figure 1.4: (a) The non-linear material inside the cavity, forming an optical parametric oscillator. (b) Second harmonic generation and downconversion processes.

oscillator noise is necessary to measure shot-noise, so minimizing the noise on the local oscillator is still important. Fabry-Perot cavities are useful resources as they allow to reach a good transverse mode quality (defined by the geometry of the cavity) and a noise filtering outside its linewidth.

A Fabry-Perot cavity is a resonator for the electromagnetic field. It consists of an ensemble of mirrors with various reflectivities that induce multiple interferences of the light with itself as depicted Fig.1.4-(a) (let us ignore the crystal and the pump field $\hat{B}$ in this subsection).

Input-output approach to cavities

In a closed system (without loss) described by a Hamiltonian $\hat{H}_{\text{rev}}$, the Heisenberg equation of motion for a single electromagnetic field mode $\hat{a}$ inside the cavity is

$$\dot{\hat{a}} = -\frac{1}{i\hbar}[\hat{H}_{\text{rev}}, \hat{a}], \tag{1.80}$$

where $\hat{H}_{\text{rev}} = \hbar\Omega\hat{a}^\dagger\hat{a}$ and Ω is the resonance frequency of the cavity. When the cavity comprises mirrors with finite reflectivities, one again has to consider the interaction of the cavity mode with a reservoir. We will follow the theory developed in [Collett and Gardiner, 1984].

The free Hamiltonian of the reservoir is the sum over the energies of each harmonic oscillator mode $\hat{\mathcal{E}}_b(\omega)$. The interaction of the reservoir modes with $\hat{a}$, is naturally given by

$$\hat{H}_{\text{irrev}} = \hbar\int\sqrt{2\kappa}(\hat{\mathcal{E}}_b^\dagger(\omega)\hat{a} + \hat{a}^\dagger\hat{\mathcal{E}}_b(\omega))d\omega, \tag{1.81}$$

where $\sqrt{2\kappa}$ is a constant coupling term in the Markov approximation. We can write $\kappa_i = \epsilon_i/2\tau$ where ϵ_i is the transmissivity of the mirror i and τ the round trip time, that is the time it takes for the field to travel the length of the cavity. The Hamiltonian $\hat{H}_{\text{irrev}}$ is then added to the reversible Hamiltonian in equation (1.80). After some algebra we are left with a simple equation of motion for the cavity mode $\hat{a}$

$$\dot{\hat{a}} = \frac{1}{i\hbar}[\hat{H}_{\text{rev}}, \hat{a}] - \kappa\hat{a} + \sqrt{2\kappa}\hat{\Sigma}(t), \tag{1.82}$$

where $\sqrt{2\kappa}\hat{\Sigma}(t)$ corresponds to vacuum noise from the reservoir modes and κ appears simply as the decay rate of the field in the cavity due to losses. When there are various loss sources κ_i inside the cavity, terms like $\sqrt{2\kappa_i}\hat{\Sigma}_i(t)$ are added sequentially to Eq.(1.82).

The relation between the output and input cavity fields can be found using *input-output relations* described in [Collett and Gardiner, 1984]. They are "beam-splitter relations" applied to the circulating intra-cavity mode $\hat{a}_c$, and the input/output fields as can be seen Fig. 1.4-(a). For the output field $\hat{A}_{\text{out}}$, we have

$$\hat{A}_{\text{out}} = \sqrt{\epsilon_{\text{out}}}\hat{a}_c - \sqrt{1-\epsilon_{\text{out}}}\hat{A}_{\nu}, \tag{1.83}$$

where ϵ_{out} is the transmissivity of the output mirror. In the case where $\epsilon_{\text{out}} \ll 1$, so that the light field undergoes many interferences before leaving the cavity, and writing $\hat{a} = \sqrt{\tau}\hat{a}_c$, we find

$$\hat{A}_{\text{out}} = \sqrt{2\kappa^a_{\text{out}}}\hat{a} - \hat{A}_{\nu}. \tag{1.84}$$

From this equation, we now derive a simple relation between the input and output fields. This will allow to introduce the idea of impedance matching.

Impedance matching

To calculate the equation of motion for $\hat{a}$, we move in a rotating frame at the field carrier frequency Ω_0 (making the substitution $\hat{a} \to \hat{a}e^{i\Omega_0 t}$) and get

$$\dot{\hat{a}} = -(\kappa_a + i\Delta_c)\hat{a} + \sqrt{2\kappa^a_{\text{in}}}\hat{A}_{in} + \sqrt{2\kappa^a_{\text{out}}}\delta\hat{A}_{\nu}(t), \tag{1.85}$$

where $\Delta_c = \Omega - \Omega_0$, is the cavity detuning from the carrier frequency and $\kappa_a = \kappa^a_{\text{out}} + \kappa^a_{\text{in}}$.

Assuming the cavity is hold on resonance ($\Delta_c = 0$), and looking at the classical mean field in steady state ($\dot{\hat{a}} = 0$, $\langle\hat{a}\rangle = \alpha$ and $\langle\hat{A}_{\text{in}}\rangle = \alpha_{\text{in}}$), we reach

$$\alpha_{\text{out}} = \frac{2\sqrt{\kappa^a_{\text{in}}\kappa^a_{\text{out}}}}{\kappa^a_{\text{in}} + \kappa^a_{\text{out}}}\alpha_{\text{in}}, \tag{1.86}$$

where we used Eq. (1.84). From this result we see that when the input and output mirrors are identical, the output power is the same as the input power. We have an *impedance matched* cavity. When the input coupler is smaller than the output coupler, the cavity is impedance mismatched (or over-coupled) and the output power drops. In the presence of losses in the cavity, impedance matching can be obtained by increasing the output coupler transmissivity.

Cavity locking

In most situations the cavity size is adjusted so that the input laser frequency is resonant with the cavity mode to ensure maximum coupling. Any small temperature fluctuations of the mirrors or acoustic noise will cause the cavity to drift. To achieve a stable *locking* of the cavity on resonance, the solution is to generate an *error signal* that can be fed back to an actuator of the cavity size. The actuator is usually a piezoelectric crystal attached to one of the mirrors. The most precise cavity locking is achieved from a Pound Drever Hall error signal [Drever et al., 1983] and the technique called *PDH-locking.*

One can see from Eq.(1.85) that the cavity amplitude response is a Lorentzian function of detuning. The associated phase response is then linear for small detunings and constant for large detunings with respect to κ_a (from the Kramers-Krönig relations).

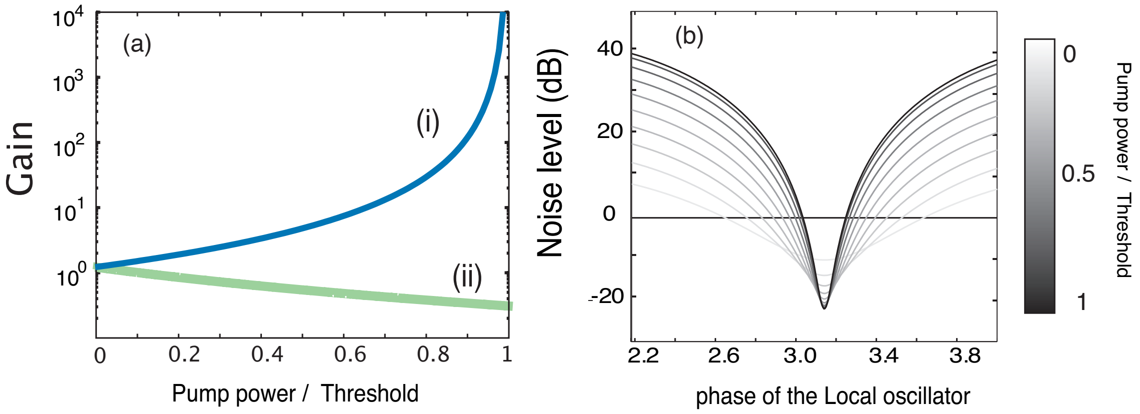

Figure 1.5: (a) Evolution of the parametric gain with pump power normalized to threshold in the amplification (i) and the de-amplification regimes (ii). (b) Noise power as a function of the local oscillator phase, 0 dB corresponding to the shot-noise level.

Let us now assume that the input field is phase modulated at a frequency where the phase response is constant. If the cavity is resonant with the incident optical field carrier, there is no phase rotation of the carrier and the phase modulation stays phase modulation for the outgoing mode. If the cavity drifts away from resonance, the carrier phase rotates so the phase modulation is transformed into amplitude modulation. The amplitude modulation can be detected (in this case, in transmission), mixed down at the phase modulation frequency and low pass filtered to give a *PDH-error signal*.

After appropriate amplification and filtering of the error signal, it can be used to actively control the cavity size. The bandwidth over which one can control the cavity usually depends on the actuator response. The filtering has to select the frequency range over which the phase response of the whole feedback loop is flat. The technique will be used in chapters 3 and 5.

1.4.4 The parametric amplifier

To produce non-classical states of light, for instance for quantum memories characterisations, one needs non-linear effects. One non-linear effect uses the $\chi^{(2)}$ susceptibility, present in most (non-symmetric) crystals. It allows frequency conversion from a laser beam at a frequency 2Ω to Ω and vice versa as depicted Fig. 1.4-(b). For the *down-conversion* process, pairs of photons are spontaneously created at frequencies $\Omega \pm \Delta$ where Δ varies within by the bandwidth of the non-linear crystal. This is commonly referred to as non-degenerate down conversion. This process creates entangled pairs of photons at frequency modes Δ and $-\Delta$ with respect to the carrier. As we saw earlier, the degree of correlation between sidebands ($V_\nu(\omega)$ in Eq.(1.73)) defines the noise level. The shot-noise was defined by a Poissonian source, where the two sidebands are completely uncorrelated. In the presence of quantum correlations between two sidebands, the quantum noise drops below the shot-noise level and we obtain squeezed light.

The details on how an efficient non-linear medium can be engineered is described in chapter 3, devoted to the squeezing generation. As we will discuss chapter 3, 100% conversion efficiency from Ω to 2Ω and vice-versa, is never reached. One solution to enhance the pair production efficiency is to place the crystal in a cavity (see Fig. 1.4-(a)). We will present now how this allows a high degree of squeezing to be obtained.

Equations of motion

A laser mode $\hat{B}_{\text{in}}$ at a frequency Ω_2 (called the second-harmonic field from here on) "pumps" the crystal placed in the cavity mode resonant for a fundamental mode $\hat{A}_{\text{in}}$ at a frequency $\Omega_1 = \Omega_2/2$. When the fundamental field $\hat{A}_{\text{in}}$ enters the cavity, quantum correlations between photons at frequencies symmetrically placed around Ω arise thanks to the second order nonlinearity, as we will show. The pair production grows exponentially with time thanks to the cavity build up. The best squeezing is in fact achieved from the vacuum mode $\hat{A}_\nu$, as the output mode $\hat{A}_{\text{out}}$ is necessarily impedance matched with it when intra-cavity losses are negligible.

The Hamiltonian describing a $\chi^{(2)}$ interaction inside a cavity is

$$\hat{H}_{\text{rev}} = \hbar\Omega_1 \hat{a}^\dagger \hat{a} + \hbar\Omega_2 \hat{b}^\dagger \hat{b} + \frac{i\hbar\chi^{(2)}}{2}(\hat{b}^\dagger \hat{a}^2 - \hat{a}^{\dagger 2}\hat{b}). \tag{1.87}$$

The last term of this equation describes the $\chi^{(2)}$ non-linear interaction, where either two photons from the fundamental field are annihilated and one from the second harmonic field is created (this is described by $\hat{b}^\dagger \hat{a}^2$, giving second harmonic generation) or the reverse ($\hat{a}^{\dagger 2}\hat{b}$ giving down-conversion). As we will see, the down-conversion process can give rise to phase-sensitive gain and squeezing of the fundamental mode.

Assuming zero detuning for both the fundamental and second harmonic from the cavity eigenmode frequency, their equations of motion in their respective moving frames are found to be

$$\begin{aligned}
\dot{\hat{a}} &= -\kappa_a \hat{a} + \chi^{(2)} \hat{a}^\dagger \hat{b} + \sqrt{2\kappa^a_{\text{in}}}\hat{A}_{\text{in}} + \sqrt{2\kappa^a_l}\delta\hat{A}_{\text{l}}(t) + \sqrt{2\kappa^a_{\text{out}}}\delta\hat{A}_\nu(t) && (1.88)\\
\dot{\hat{b}} &= -\kappa_{\text{b}} \hat{b} - \frac{1}{2}\chi^{(2)} \hat{a}^2 + \sqrt{2\kappa^{\text{b}}_{\text{in}}}\hat{B}_{\text{in}} + \sqrt{2\kappa^b_{\text{l}}}\delta\hat{B}_{\text{l}}(t) + \sqrt{2\kappa^b_{\text{out}}}\delta\hat{B}_\nu(t), && (1.89)
\end{aligned}$$

where $\kappa^{a,b}_{\text{in,out}}$ are the losses at the input/output mirrors on the fundamental/second harmonic fields respectively. $\kappa^{a,b}_{\text{l}}$ are the losses inside the crystal. We will now calculate the pair production efficiency, assuming that the second harmonic field is larger than the fundamental field.

Linear analysis of the OPO

A full quantum analysis can be carried out using the above equations, as in [Chaturvedi et al., 2002] but simplified solutions can also be found far from the oscillation threshold of the OPO, which we will define soon. We here assume that the second harmonic field is much stronger than the fundamental so that it is not depleted by the down conversion process and it can be treated as a classical field. We then write $\hat{b} = \beta$ and $\hat{B}_{in} = \beta_{\text{in}}$. This is an assumption only valid far from threshold, which allows one to linearize the problem and get simple analytical solutions[16]. Let us also assume that $\kappa_a \ll \kappa_b$, i.e the cavity is only resonant for the fundamental mode and the dynamics of the harmonic field can be neglected. We also assume $\kappa^b_{\text{in}} \gg (\kappa^b_{\text{out}}, \kappa^b_\nu, \kappa^b_{\text{l}})$, so $\kappa_b = \kappa^b_{\text{in}}$ and Eq. (1.89) yields

$$\beta = \frac{\sqrt{2\kappa_b}\beta_{\text{in}}}{\kappa_b}. \tag{1.90}$$

---

[16] One can also keep the second harmonic field as an operator and linearize the equations in the pump-depleted regime making sure that the second harmonic losses are treated as a self-consistent perturbation, far enough from threshold [Grosse et al., 2006].

Replacing $\hat{b}$ by β in Eq.(1.88) gives the linear equation

$$\dot{\hat{a}} = -\kappa_a \hat{a} + \chi \hat{a}^\dagger + \sqrt{2\kappa^a_{\mathrm{in}}}\hat{A}_{\mathrm{in}} + \sqrt{2\kappa^a_{\mathrm{l}}}\delta\hat{A}_{\mathrm{l}}(t) + \sqrt{2\kappa^a_{\mathrm{out}}}\delta\hat{A}_\nu(t), \tag{1.91}$$

where $\chi = \chi^{(2)}\beta$. It is interesting to calculate the evolution of $\hat{A}_{\mathrm{out}}$ as a function of $\hat{A}_{\mathrm{in}}$. We will first solve it classically in steady states to calculate the down-conversion efficiency, and then quantum mechanically.

Classical amplification

We will assume the crystal to be lossless for the fundamental field to simplify the equations. Let us look at the evolution of the output fundamental, as a function of the input power classically, setting $\dot{\hat{a}} = 0$, $\langle \hat{a} \rangle = \alpha$, and $\langle \hat{A}_{\mathrm{in}} \rangle = \alpha_{\mathrm{in}}$. Let us also assume the second harmonic field to be in the real plane, that is χ is either positive or negative. From Eq. (1.91), we obtain the two relations

$$\kappa_a \alpha - \chi \alpha^\star = \sqrt{2\kappa^a_{\mathrm{in}}}\alpha_{\mathrm{in}} \tag{1.92}$$

$$\kappa_a \alpha^\star - \chi \alpha = \sqrt{2\kappa^a_{\mathrm{in}}}\alpha^\star_{\mathrm{in}}. \tag{1.93}$$

Using Eq. (1.84), we now get a relation between the input and output field amplitudes

$$\alpha_{\mathrm{out}} = \frac{2\sqrt{\kappa^a_{\mathrm{in}}\kappa^a_{\mathrm{out}}}(1-\chi/\kappa_a)}{\kappa_a(1-\chi^2/\kappa_a^2)}\alpha_{\mathrm{in}}. \tag{1.94}$$

Finally, in terms of optical intensity ($P_{\mathrm{out}} = |\alpha_{\mathrm{out}}|^2$) we have

$$G = \frac{P_{\mathrm{out}}}{P_{\mathrm{out}/\chi=0}} = \frac{(1-\chi/\kappa_a)^2}{(1-\chi^2/\kappa_a^2)^2}. \tag{1.95}$$

This describes the gain G of the parametric process. Close to the threshold, defined by $\chi = \kappa_a$, the output field is amplified maximally. At threshold, the equations have to be corrected to account for pump depletion, but they are valid when $\chi \ll \kappa_a$ where we find two regimes. For a negative and real β_{in}, ($\chi < 0$) there is amplification of the fundamental, whereas for a positive β_{in}, which means that the pump is in phase with the fundamental input, we have deamplification. This can be seen Fig.1.5-(a) where we plot the evolution of the fundamental power with the pump power normalized to threshold. Fig. 1.5-(a), trace (i) corresponds to amplification and trace (ii) corresponds to deamplification of the input fundamental field.

Squeezing below threshold

We now turn to the quantum noise behavior of the amplified and deamplified signals below threshold and assume the intra-cavity losses to be negligible for now. Eq. (1.91) and its conjugate give in the Fourier domain[17]

$$i\omega\tilde{a}(\omega) = -\,\kappa_a\tilde{a}(\omega) + \chi\tilde{a}^\dagger(-\omega) + \sqrt{2\kappa^a_{\mathrm{in}}}\tilde{A}_{\mathrm{in}}(\omega) + \sqrt{2\kappa^a_{\mathrm{out}}}\delta\hat{A}_\nu(\omega) \tag{1.96}$$

$$i\omega\tilde{a}^\dagger(-\omega) = -\,\kappa_a\tilde{a}^\dagger(-\omega) + \chi\tilde{a}(\omega) + \sqrt{2\kappa^a_{\mathrm{in}}}\tilde{A}^\dagger_{\mathrm{in}}(-\omega) + \sqrt{2\kappa^a_{\mathrm{out}}}\delta\hat{A}^\dagger_\nu(-\omega). \tag{1.97}$$

---

[17] Mind the change of sign when Fourier transforming : $[\tilde{a}(\omega)]^\dagger = \tilde{a}^\dagger(-\omega)$.

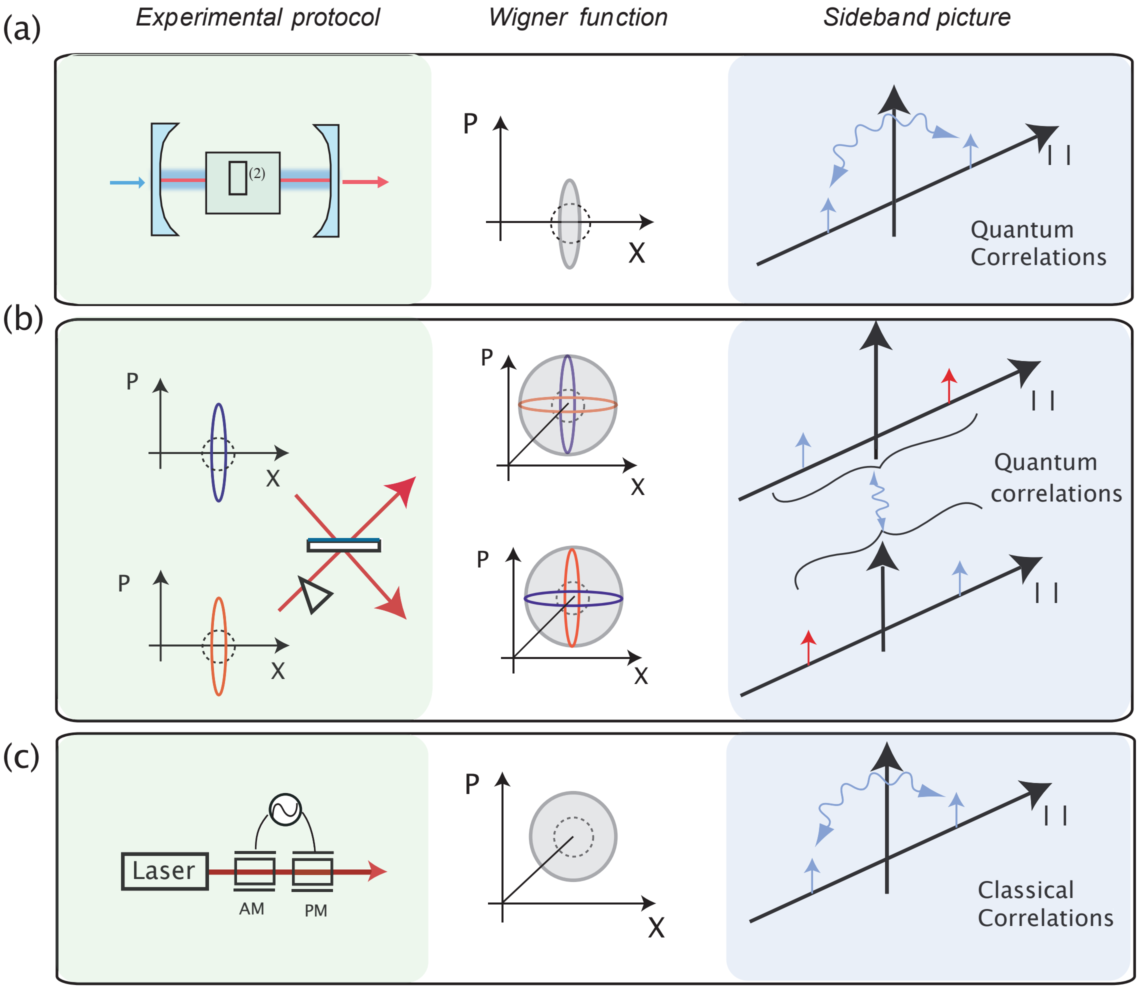

Figure 1.6: Wigner representation and sideband picture for three different Gaussian states, (a) a phase squeezed state, (b) entangled states obtained by mixing two squeezed light sources on a beam splitter (c) amplitude and phase modulated coherent state. We show the experimental protocol, the Wigner representation (dotted lines are the Wigner representations for coherent states) and the sideband pictures.

Using Eq.(1.84) and assuming a small input coupler ($\kappa^a_{\text{in}}/\kappa^a_{\text{out}} \ll 1$; $\kappa_a \simeq \kappa^a_{\text{out}}$), we then have

$$\tilde{A}_{\text{out}}(\omega) = \frac{\chi^2 + \kappa_a^2 + \omega^2}{(\kappa_a + i\omega)^2 - \chi^2}\tilde{A}_\nu(\omega) + \frac{2\chi\kappa_a}{(\kappa_a + i\omega)^2 - \chi^2}\tilde{A}^\dagger_\nu(-\omega), \tag{1.98}$$

which at low sideband frequencies gives

$$\tilde{A}_{\text{out}}(\omega) = \sqrt{G}\tilde{A}_\nu(\omega) + \sqrt{G-1}\tilde{A}^\dagger_\nu(-\omega). \tag{1.99}$$

This is similar to the behavior of phase insensitive amplifiers [Caves, 1982] where $\tilde{A}_{\text{out}} = \sqrt{G}\tilde{A}_\nu + \sqrt{G-1}\tilde{A}^\dagger_\mu$ and ν,μ are uncorrelated modes, but here the non-linear interaction acts on two frequency modes from the same spatial mode $\tilde{A}_\nu$ whilst preserving the commutation relations. This expression is a Local Linear Bogolioubov Transformation like the one presented Eq.(1.28) so we already know that it gives rise to pure squeezed states.

We now calculate the OPO spectrum of the fluctuations for the amplitude (denoted

+) and phase quadratures (denoted -). Using Eq.(1.98), we find

$$V_{\text{out}}^{\pm}(\omega) \quad = \quad 1 \pm \frac{4\kappa_a \chi}{(\chi \mp \kappa_a)^2 + \omega^2}. \tag{1.100}$$

The amplitude quadrature uncertainty can then drop below the shot-noise limit while the amplitude quadrature noise is above the shot-noise. At threshold and $\omega \approx 0$, the squeezing is ideal.

A general expression can easily be found when other sources of loss are present. It can be shown that

$$V_{\text{out}}^{\pm}(\omega) \quad = \quad 1 \pm \eta\eta_{\text{esc}} \frac{4\chi/\kappa_a}{(\chi/\kappa_a \mp 1)^2 + \omega^2/\kappa_a^2}, \tag{1.101}$$

where $\eta = \kappa_{\text{out}}^a/(\kappa_{\text{out}}^a + \kappa_l^a)$ is the *escape efficiency* of the OPO and κ_l^a are losses inside the cavity. η represents other losses after the OPO cavity. Experimentally, the difficulty is to maximize the escape efficiency and lower the threshold to obtain a strong squeezing with achievable pump power.

To detect such a squeezed state of light, we can use homodyne detection. By changing the local oscillator phase, we can move continuously from the measurement of the amplitude to the measurement of the phase quadratures. The plot of the variance as a function of local oscillator phase gives the curves shown Fig.1.5-(b) plotted for different pump powers. As the pump power gets closer and closer to threshold, both the squeezing and the anti-squeezing level increase.

1.4.5 Classical and quantum correlations

As we discussed in the section about photodetection, the variance $V^{\pm}$ in the measurement of continuous variable states is related to the two-time correlation function between two signals oscillating at ω and $-\omega$. Squeezing is then the result of quantum correlations between two frequency modes, two *sidebands*, as depicted Fig. 1.6-(a). The two frequency modes connected via the non-linear interaction belong to the same spatial mode at the output of an OPO. Squeezing has many applications in precision measurement but in order to take advantage of the *entangled state* produced by the OPO for quantum information applications, one needs to *separate* the sidebands spatially. This can be done using a cavity reflecting the upper sideband and transmitting the lower sidebands [Huntington et al., 2005]. Building such a cavity is however not trivial and is often accompanied with losses.

To generate large continuous variable entanglement between two spatially separated modes, one can also mix two squeezed states on a 50/50 beam splitter with one of the beams phase shifted by $\pi/2$ as shown Fig. 1.6-(b). The correlation is established between opposite pairs of sidebands modes that are then spatially separated. We will come back to this entangled state in the next chapter and characterize it using the EPR and inseparability criteria.

In quantum cryptography classical states are sufficient to ensure the security for the exchange of messages between two parties. In continuous variable quantum cryptography, classical information is encoded on a laser beam by means of amplitude and phase modulations at the same frequency as is shown Fig. 1.6-(c). This technique create sidebands that are classically correlated. Contrary to entangled states, the knowledge of one of the signals at ω given knowledge of the other signal at $-\omega$ can not exceed the shot-noise limit.

The security of quantum key distribution is guaranteed by the fact that the amplitude and phase quadratures are two conjugate observables.

Chapter 2

Benchmarks for continuous variable quantum memories

The Heisenberg Uncertainty Principle (HUP) sets a limit on the quality of information storage that depends on direct measurement and subsequent reconstruction. As a consequence, *classical* storage devices cannot store two conjugate observables simultaneously without paying a quanta of duty. To allow long distance communication and the synchronization of gates in quantum computing, one important step is the realization of a device that allows the coherent storage of information. Much experimental and theoretical research is then directed towards *quantum memories for light*.

This chapter presents benchmarks that quantum memories have to beat to outperform classical means of storage. Before describing the details of our proposed benchmarks, we will present two areas of quantum information research for which a quantum memory is required : quantum cryptography and quantum computing. To realize quantum memories, methods that provide a coherent interface between light fields and large atomic ensembles are promising. We also summarize the proposed and currently studied memories.

Continuous variable information in the form of amplitude and phase modulations, squeezing or entanglement are the main focus of this thesis. In the next section, we present the theoretical background necessary to study the preservation of coherent and entangled states. We then present our theoretical benchmarks for continuous variable quantum memories. We finally discuss how the measurement of the memory output state can be done and also introduce a measure similar to the time-bandwidth product to quantify the preservation of the input pulse shape after storage and retrieval from a quantum memory. Part of this work was published in [Hétet et al., 2008a] and [Hétet et al., 2008].

2.1 Why use quantum memories ?

A memory that can store quantum states is becoming a necessity in quantum information science. We will here give the examples of quantum cryptography and quantum computing wherein the use of quantum memory is crucial to their optimum functioning.

2.1.1 Quantum key distribution

The work of Bennett and Brassard introduced quantum cryptography and the BB84 protocol [Bennett and Brassard, 1984]. They showed that the security in the exchange of messages was perfect when taking advantage of the properties of quantum states. The idea is that two parties share a private key comprising a sequence of quantum states from an orthogonal basis. Then, they communicate on a public channel sending messages encrypted with this private key. It is impossible for anyone to intercept the private key and resend it without leaving a trace, because the measurement of the state will introduce excess noise. This is known as the "no-cloning theorem" [Wootters and Zurek, 1982]. This excess noise can give a hint to the receiver of the private key that someone is listening. In that case they do not communicate. Otherwise, the two parties can exchange their signal on a public channel and decrypt it using the private key, being sure that the latter has not been intercepted by an eavesdropper. A large research community is now working on improving Quantum Key Distribution (QKD) protocols.

Most demonstrations of QKD have used fibre optics to send the quantum states. There is however an exponential loss of signal with distance in the fibrEs (0.2 dB/km) which limits the communication distance [Stucki et al., 2002]. In free space the maximum distance of transmission is limited to line of sight links and depends critically on the weather [Jacobs and Franson, 1996]. When the communication line is on the order of the attenuation length, the security is not guaranteed anymore. An eavesdropper intercepting the private key and then resending it would "look" the same for Bob and he cannot know if someone was listening on the line or not. The use of a quantum repeater [Briegel et al., 1998] gives an unlimited increase to this transmission distance whilst ensuring unconditional security. A quantum repeater is the quantum analogy of the classical repeater. The classical repeater overcomes the losses along the line by measuring the signal, amplifying it, and recreate it as many times as required. For quantum information to be transmitted over greater distances one cannot use this technique. The noise added by the amplification process will be too large to guarantee the security (this will be shown in the next sections). A quantum repeater rather relies on entanglement swapping [Bennett et al., 1993], entanglement purification [Bennett et al., 1996], and quantum memories [Duan et al., 2001].

The idea of a quantum repeater is as follows. The total channel is divided into N short channels, and N+1 nodes in between which losses are negligible. Entangled states are shared between each node and acquired from stations situated nearby. When the private key is input to the first node, the entanglement is purified and the adjacent nodes subsequently connected via a Bell measurement. The operation is repeated between the newly connected nodes via entanglement swapping, and re-purified until the key is transfered to the end of the line. The purification process has to be done between each Bell measurement because of the noise and loss it will introduce, causing the entanglement to vanish before the end of the process. As noted in [Duan et al., 2001], as the purification protocols are probabilistic, memories are needed to keep the state if the purification succeeded. A memory that preserves the quantum characteristic of the state is necessary here. If there were no available quantum memory then the purifications at each section would have to succeed at the same time, the probability of this occurring decreases exponentially with the transmission channel length.

2.1.2 Quantum computing

In parallel with the development of quantum cryptography, theoretical proposals demonstrated that quantum mechanics would allow more efficient computation. The first ideas came from David Deutsch in 1985, when was proposed the idea of a *Universal Quantum Computer* [Deutsch, 1985]. After this proposal, other quantum algorithms followed aiming to solve various problems demanding in computer power [Abrams and Lloyd, 1997, Grover, 1997]. Shor proposed in 1994 a quantum algorithm that factorises large numbers into two prime numbers [Shor, 1994]. Factorisation is at the core of the RSA[1] public key encryption which relies on the fact that classical computers take a long time to find the prime factors of large numbers. Information coded by the RSA would no longer be secure against a quantum computer using Shor's algorithm. This realization increased further the interest in quantum computing.

A lot of experimental work aiming towards building a quantum computer were made in many different systems, including trapped ions [Barrett et al., 2004, Monroe et al., 1995, Riebe et al., 2004], solid state systems [Fraval et al., 2005], linear optics and liquid state NMR [Nielsen and Chuang, 2000]. A scheme using only linear elements[2] and photon detectors was proposed by Knill, Laflamme and Milburn (KLM) [Knill et al., 2001]. This scheme works using three ideas, the first is to create a non-deterministic gate using single photons and post-selection. In the proposed arrangement, the probability of success of the operation is 1/16 and the result is known. This non-deterministic gate is then combined with quantum teleportation to increase the probability of success. Depending on the outcome of the measurement after these operations, it can be concluded if the gate operation succeeded. Whilst these measurements are carried out, the information must be stored in a quantum memory until the gate has been determined to have succeeded and the photon can then continue on to the next stage.

2.1.3 Current quantum memories

As we discussed, a quantum memory would allow longer communication distances for QKD, and the synchronization of entangling gates in quantum computation. How efficient must a quantum memory be for these protocols to work ? Any leak of the quantum signal from the memory before it is stored is, for example, a potential source of information for an eavesdropper when the memory is used on a quantum cryptography line. How much can two parties that want to exchange secure messages tolerate ? We answer these questions in the next sections, but first give a brief overview of the current quantum memories for light.

To interact efficiently with the material system storing the information, the effective coupling strength from one photon to one atom must be as close as possible to unity. It was shown in [Parkins et al., 1993] that a photon can almost completely be mapped onto a single atom inside ultra high finesse cavities. This is the domain of Quantum Electrodynamics (QED) where a strong coupling between light and atoms can be achieved. The Interaction strength between light and atoms is given by the vacuum Rabi frequency $g = d\sqrt{\omega/2\epsilon_0 V\hbar}$ introduced in the first chapter. A strong coupling is achieved by making the cavity size extremely small to reduce the mode volume V. The difficulty is to be able to achieve minimum losses per round trip so that the finesse, or the quality factor Q of the cavity is still kept high. Very high Q values, with small mode volumes, are achieved with whispering gallery modes of small transparent spheres [Armani et al., 2003] or in a super-conducting devices [Kuhr et al., 2007]. Although tremendous breakthroughs have been made over the past 20 years, building the required high finesse cavities is experimentally challenging. To overcome these technical issues, memory schemes relying on large atomic ensembles are

---

[1] The algorithm was found in 1977 by Ron Rivest, Adi Shamir, and Leonard Adleman. The letters RSA are the initials of their surnames.

[2] Although single photons and entangled states are required, the production of which uses large non-linearities, only linear elements are used for the actual local operations.

now investigated.

Pioneer work was done in Eugene Polzik's group in Copenhagen. A scheme using the off-resonant interaction of a light field with a large ensemble of three level atoms was first presented in [Kozhekin et al., 2000]. It was shown that a Gaussian state can be mapped efficiently onto a collective ground state coherence of three level atoms in a Raman configuration because the effective coupling strength is increased by a factor $\sqrt{N}$. To read out the spin state back into light, a teleportation scheme was proposed. Off-resonant Faraday rotation was also used as a mechanism for mapping quantum states of light onto atoms [Julsgaard et al., 2004]. The reading of the atomic state is done by performing a quantum non demolition measurement of the spin. Although the coupling between light and atoms is efficient, the reversible storage and read out required for quantum information science applications was not shown using this type of interaction.

Probably the most actively studied technique to achieve a reversible quantum memory for light in atomic ensemble utilizes Electromagnetically Induced Transparency (EIT). The idea was put forward and first experimentally realized by two groups [Liu et al., 2001, Fleischhauer and Lukin, 2000, Phillips et al., 2001]. In EIT, a strong control field can reversibly map and retrieve the information encoded on a weak probe field using long lived atomic states. This memory will be studied in detail in chapter 4 and 5. Shortly after the EIT quantum memory was proposed, it was realized that a proper temporal mode matching between the control field and the probe allows the information to be written and retrieved from an ensemble of three level atoms in an off-resonant Raman configuration [Nunn et al., 2007, Gorshkov et al., 2007a, Dantan and Pinard, 2004]. The reversible storage of a light field was also shown to be possible by controlling the spatial distribution of atomic shifts in optically thick ensembles of three level systems [Moiseev and Kröll, 2001, Sangouard et al., 2007], reminiscent of the early work of photon echoes in the 60's [Kurnit et al., 1964]. The technique was extended to a quantum memory for light using two level atoms [Hétet et al., 2008b] and will be presented in chapter 7. Those schemes have been the subject of high interest in the past few years. It is essential to point out here that, apart from some experimental considerations, all the quantum information protocols are equally efficient using discrete or continuous variables[3].

Quite often however, quantum memories do not perform ideally. It is then important to benchmark the experimental demonstrations. We now provide a theoretical analysis of noise and losses in quantum channels in section 2.2 and come to the actual benchmarks in the following section (2.3).

2.2 Channel transmission and noise

As this work is mainly concerned with the storage of Gaussian states, the preservation of displaced coherent states and entanglement will here be presented. In particular, the degradation of Gaussian quantum states in the presence of loss and excess noise is discussed.

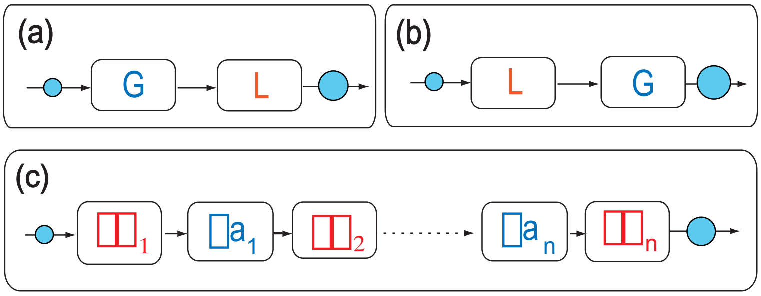

Figure 2.1: Sequence of amplification and loss on a quantum optical system. (a) gain followed by loss, (b) loss followed by gain,and (c) infinitesimal amplifying and attenuating slices of gains and losses.

2.2.1 Modelling transmission and noise

As excess noise is quite often associated with amplification, we first provide a general theory for non-ideal phase insensitive amplification. In [Caves, 1982], the signal to noise ratio of the measurement of a quantum optical field was shown to degrade in the presence of gain. Extra noise has to be inserted in the field equations to preserve the commutation relations. More precisely, it was shown that the output of an ideal linear amplifier with a gain factor $G > 1$, relates to the input state by

$$\hat{\mathcal{E}}_{\rm out} = \sqrt{G}\ \hat{\mathcal{E}}_{\rm in} + \sqrt{G-1}\ \hat{\mathcal{E}}_{\nu}^{\dagger}, \tag{2.1}$$

where $\hat{\mathcal{E}}_{\nu}^{\dagger}$ is a vacuum mode of the reservoir from which the energy was taken. As discussed in the first chapter (section 1.4.4), when the two modes $\hat{\mathcal{E}}_{\nu}^{\dagger}$ and $\hat{\mathcal{E}}_{\rm in}$ are not correlated, there is phase-insensitive amplification of $\hat{\mathcal{E}}_{\rm in}$. When $\hat{\mathcal{E}}_{\nu}^{\dagger} = \hat{\mathcal{E}}_{\rm in}$ however, we have phase-sensitive amplification of $\hat{\mathcal{E}}_{\rm in}$. As we saw in the earlier chapter, in phase-sensitive amplification, the noise can be below the standard quantum limit. This process is naturally not present in quantum memories and we do not consider it in this chapter. As this is more relevant to quantum channels, we will present here the theory of *non-ideal linear phase-insensitive* amplifiers.

From Eq.(2.1), the power spectrum at the output of an ideal phase insensitive amplifier is given by $S^{\pm}_{\rm out} = GS^{\pm}_{\rm in} + G - 1$, at zero Kelvin, where ± corresponds to the amplitude and phase quadratures. The output beam is then not shot-noise limited anymore due to the amplification process, and the evolution is not unitary.

In non-ideal amplifiers, Eq. (2.1) has to be modified to include losses. Before presenting the complete model, let us first consider the simpler cases of amplification followed by loss L, and loss followed by amplification respectively, as shown in Fig. 2.1(a)-(b). The total signal transmission η in both situations is GL but, in the first case, the noise is found to be $N_{g\rightarrow l} = 1 - 2L + GL$ and in the second case, $N_{l\rightarrow g} = 2G - 1 - GL$. It is then easy to show that $N_{l\rightarrow g} > N_{g\rightarrow l}$. Loss followed by gain is a noisier process than gain followed by loss, because the amplification process will also amplify the vacuum noise from the first lossy stage.

---

[3] A lot of work was, for example, done to extend the QKD protocols originally proposed for single photons to continuous variables in [Grosshans and Grangier, 2002a, Lance et al., 2005].

To consider more complex mechanisms closer to the non-ideal amplifier, we here develop a general theory for successive amplification and attenuation of a traveling wave [Jeffers et al., 1993]. By artificially concatenating m amplifying and attenuating infinitesimal slices with linear amplification $1+a\delta z$ and attenuation $1-\alpha\delta z$, where $\delta z = z/m$, we will calculate the noise properties of the field using Eq. (2.1) and the passive beam splitter relation. The sequence is depicted Fig. 2.1(c). The power spectrum of the measured field at a slice m can be found to be

$$\begin{aligned} S^{\pm}_{m} &= (1+\frac{(a-\alpha)z}{m})^{m}(S^{\pm}_{in}-1)+1 \\ &+ 2a\sum_{j=1}^{m}(1+\frac{(a-\alpha)z}{m})^{m-j}. \end{aligned} \tag{2.2}$$

By going to the limit $m \to \infty$, therefore converting the discrete slices into a continuous array, when $\alpha \neq a$, we get

$$S^{\pm}(z) = \eta(z)\ S^{\pm}_{in} + (1-\eta(z))(1+N_f), \tag{2.3}$$

where the noise factor and the total transmission are

$$N_f = \frac{2a}{\alpha - a} \quad \text{and} \quad \eta(z) = e^{(a-\alpha)z}, \tag{2.4}$$

respectively. We note that when $a = 0$, $N_f = 0$ so that in the absence of amplification, $S^{\pm}(z) = 1$. The output is then shot noise limited, as expected.

This general treatment allows us to assess the amount of excess noise present at the output of a system, when gain and attenuation are known quantities. Although this is experimentally usually not possible, in theory we can extract the gains and losses from the equations describing the whole system (as will be done for EIT in chapter 4). Formula 2.3 was also found in [Gardiner, 1985], where light propagating in a two level atom driven externally by a strong undepleted classical field was considered. When atoms are pumped in the excited state by the external field, the output light state is amplified. Because of spontaneous emission however, loss also occurs. A series of losses and gains affects the propagation of the light field to give the same result as Eq. 2.3.

2.2.2 Displaced coherent states

One of the aim of this thesis is to find regimes where the simultaneous storage of both quadratures of a probe beam, when amplitude and phase modulations are encoded on its sidebands, is efficient. The preparation of this state can be achieved experimentally by passing a light pulse through amplitude and phase modulators sequentially. Provided the modulation frequency is larger than the Fourier width $\Delta\omega$ of the pulse, classical information is encoded onto its sideband ω at the shot noise limit.

The envelope of the probe field, $\hat{\mathcal{E}}(z,t)$, obeys the commutation relation

$$[\hat{\mathcal{E}}(z,t), \hat{\mathcal{E}}^{\dagger}(z',t')] = \frac{L}{c}\delta(t - z/c - (t' - z'/c)), \tag{2.5}$$

where L is the quantization length and c the speed of light. We are interested in the evolution of the amplitude and phase quadrature operators at a given sideband frequency ω which will be denoted $\hat{X}^{+}_{\rm in}(\omega) = \hat{\mathcal{E}}_{\rm in}(\omega) + \hat{\mathcal{E}}^{\dagger}_{\rm in}(-\omega)$ and $\hat{X}^{-}_{\rm in}(\omega) = -i(\hat{\mathcal{E}}_{\rm in}(\omega) - \hat{\mathcal{E}}^{\dagger}_{\rm in}(-\omega))$

respectively. To distinguish between the classical signal and the quantum noise, we decompose $\hat{X}^{\pm}_{\rm in}(\omega)$ into

$$\hat{X}^{\pm}_{\rm in}(\omega) \;=\; 2\alpha^{\pm}_{\rm in}(\omega)+\delta\hat{X}^{\pm}_{\rm in}(\omega) \tag{2.6}$$

where $\alpha^{\pm}_{\rm in}(\omega)$ is the coherent amplitude encoded onto the probe via optical modulation, and $\delta\hat{X}^{\pm}_{\rm in}(\omega)$ its quantum fluctuations.

When normalized to the detection bandwidth, chosen to be much smaller than the applied modulation frequency, the measured power spectrum is

$$S^{\pm}(\omega)=\frac{c}{L}\langle|\hat{X}^{\pm}(\omega)|^2\rangle, \tag{2.7}$$

and the noise on the signal

$$V^{\pm}(\omega)=\frac{c}{L}\langle|\delta\hat{X}^{\pm}(\omega)|^2\rangle. \tag{2.8}$$

For the input probe state we then have $S^{\pm}_{\rm in}(\omega)=4\frac{c}{L}(\alpha^{\pm}_{\rm in}(\omega))^2+V^{\pm}_{\rm in}(\omega)$. The signal will be defined as $4\frac{c}{L}(\alpha^{\pm}_{\rm in}(\omega))^2$ and the noise as $V^{\pm}_{\rm in}(\omega)$, which is unity for a shot noise-limited laser beam.

If this state is inefficiently stored with some frequency and quadrature dependent loss $\eta^{\pm}(\omega)$ and if some excess noise with variance $V^{\pm}_{\rm noise}(\omega)$ is generated by the memory, we will have

$$S^{\pm}_{\rm out}=\eta^{\pm}(\omega)S^{\pm}_{\rm in}+1-\eta^{\pm}(\omega)+V^{\pm}_{\rm noise}(\omega). \tag{2.9}$$

The term $1-\eta^{\pm}(\omega)$ corresponds to uncorrelated vacuum noise, common to any system in the presence of linear loss and necessary to preserve the commutation relations of the output state. The excess noise $V^{\pm}_{\rm noise}(\omega)$ transforms an initial coherent state where $V^{\pm}_{\rm in}(\omega)=1$ into a mixed state where $V^{\pm}_{\rm out}(\omega)=1+V^{\pm}_{\rm noise}(\omega)>1$ due, for example, to the presence of gain in the medium Eq. (2.3).

Measuring $\eta^{\pm}(\omega)$ and $V^{\pm}_{\rm noise}(\omega)$ will be necessary to quantify the light storage and retrieval efficacy. Before specifying the values of $\eta^{\pm}(\omega)$ and $V^{\pm}_{\rm noise}(\omega)$ required to outperform classical devices, we present criteria for continuous variable entanglement. As we discussed, the storage of entangled state is of equal importance for quantum repeaters applications.

2.2.3 Criteria for continuous variable entanglement

To obtain entanglement in the continuous variable regime, two identical amplitude squeezed light sources, a and b, can be mixed on a beam-splitter with a $\pi/2$ phase difference between them [Ou et al., 1992, Bowen et al., 2003b], as shown in Fig. 2.2(i). A correlation measurement between the two outputs, c and d, can be performed using two homodyne detectors measuring the uncertainty of the quadrature operators $\hat{\rm X}^{\pm}_d$ and $\hat{\rm X}^{\pm}_c$. It can be shown that in the case of a and b being pure squeezed states, measuring any quadrature of c will allow us to infer the corresponding quadrature of d with uncertainty better than the quantum noise limit (QNL).

Formally, the variance of the conditional probability distribution of the signal $\hat{\rm X}^{\pm}_c$ given knowledge of the signal $\hat{\rm X}^{\pm}_d$ can be written as [Reid and Drummond, 1988]

$$\mathrm{V}^{\pm}(c|d) \;=\; \mathrm{V}^{\pm}_c\big(1-\frac{|\langle\hat{\rm X}^{\pm}_c\hat{\rm X}^{\pm}_d\rangle|^2}{\mathrm{V}^{\pm}_d\mathrm{V}^{\pm}_c}\big), \tag{2.10}$$

where $V^{\pm}_{c,d}$ is the variance of the amplitude/phase quadrature fluctuations of the beams c and d. When using amplitude squeezed beams as input states, the conditional variance between c and d will be below the QNL, given by $\mathrm{V}^{\pm}(c|d) = 1$, indicating a non-classical correlation between them.

The right-hand side of Fig. 2.2(i) displays the correlations between the amplitude and phase quadratures of c and d. The perimeter of the ellipses shows $\sigma^{\pm}_{\theta}$ given by

$$\sigma^{\pm}_{\theta} = \sqrt{\mathrm{V}^{\pm}_{\theta}(1 - (C^{\pm}_{\theta})^2)}, \tag{2.11}$$

where $\mathrm{V}^{\pm}_{\theta}$ is the variance of the data projected onto axes at an angle θ and $\mathrm{C}^{\pm}_{\theta} = |\langle \hat{\mathrm{X}}^{\pm}_{\theta}\hat{\mathrm{X}}^{\pm}_{\theta+\pi/2}\rangle|^2/\mathrm{V}^{\pm}_{\theta}\mathrm{V}^{\pm}_{\theta+\pi/2}$ is the correlation also measured along the rotated axes. For the situation shown in Fig. 2.2(i), we find that $\sigma^{\pm}_{\theta}$ is an ellipse with its axis oriented at

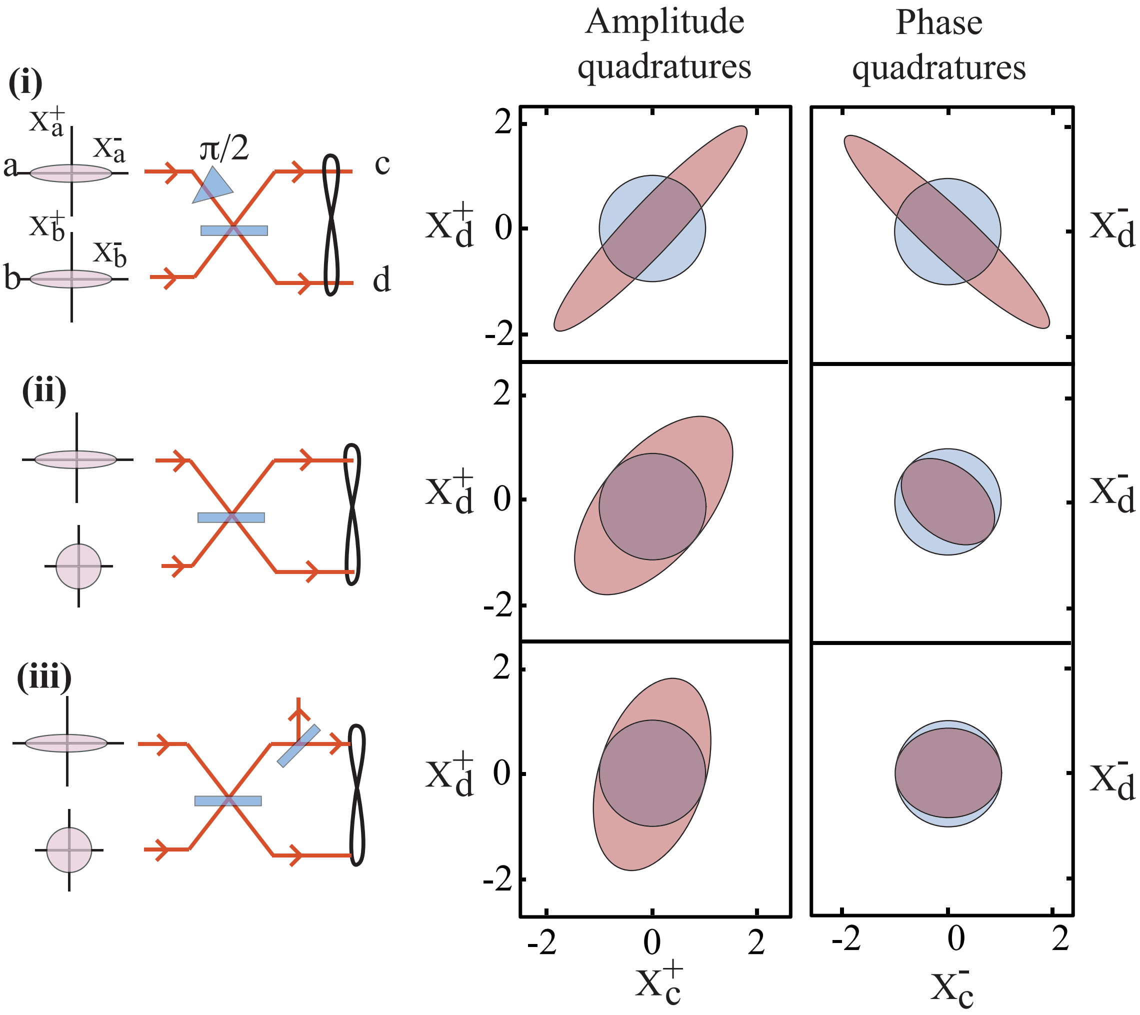

Figure 2.2: Different continuous variable entangled states. i) Two squeezed light sources a and b are mixed on a 50/50 beam-splitter. The resulting outputs c and d possess quantum correlations. On the right, the conditional deviation graphs for the output amplitude and phase quadratures. The blue circles represent the QNL conditional deviation and the red ellipses the entangled beam conditional deviation. ii) Beam b is replaced by a vacuum state. iii) Beam b is a vacuum state and beam c experiences some loss. Explanations in the text.

$+\pi/4$ for the amplitude quadratures and $-\pi/4$ for phase quadratures. In Fig. 2.2(i) these are shown in red.

The conditional variance $\mathrm{V}^{\pm}(c|d)$ can be found from $\sigma_{\theta}^{\pm}$ by measuring the square of the radius of the ellipse at the point where it crosses the horizontal axis, that is $\mathrm{V}^{\pm}(c|d) = (\sigma_{\theta=0}^{\pm})^2$. $\mathrm{V}^{\pm}(d|c)$ however will be found from the radius of ellipse at the points where it crosses the vertical axis, $\mathrm{V}^{\pm}(d|c) = (\sigma_{\theta=\pi/2}^{\pm})^2$. The QNL is obtained by replacing the squeezed beams by vacuum states. The QNL forms circles of unity radius as shown by the perimeters of the blue circles in Fig. 2.2(i). For the case in this figure it is clear that $\mathrm{V}^{\pm}(d|c) = \mathrm{V}^{\pm}(c|d) < 1$.

When $\theta = -\pi/4$ and $\theta = \pi/4$, for the amplitude and phase quadratures respectively, the correlations lie inside the unity circle and reaches a minimum. To see what these minima mean, one can calculate $\sigma_{\theta}^{\pm}$ as a function of the rotation angle (θ) and the input variances. We find [Buchler, 2001]

$$\begin{aligned}(\sigma_{\theta}^{\pm})^2 &= \frac{1}{2}(1-\sin(2\theta))\mathrm{V}_a^{\pm} + \frac{1}{2}(1+\sin(2\theta))\mathrm{V}_b^{\mp} \\ &- \frac{(\mathrm{V}_b^{\mp} - \mathrm{V}_a^{\pm})^2\cos^2(2\theta)}{2(1-\sin(2\theta))\mathrm{V}_b^{\mp} + 2(1+\sin(2\theta))\mathrm{V}_b^{\mp}}.\end{aligned} \tag{2.12}$$

We see that $\sigma_{-\pi/4}^{+} = \sqrt{\mathrm{V}_a^{+}}$ and $\sigma_{\pi/4}^{-} = \sqrt{\mathrm{V}_b^{+}}$, which are the two initially squeezed quadratures. We also have $\sigma_{\pi/4}^{+} = \sqrt{\mathrm{V}_b^{-}}$ and $\sigma_{-\pi/4}^{-} = \sqrt{\mathrm{V}_a^{-}}$, which are the two anti-squeezed quadratures[4].

The correlation ellipses provide, in summary, a unified graphical representation of the conditional variances between two signals c and d and the variances of the original inputs a and b. These quantities will be useful for the calculation of the entanglement figures of merit.

There are several criteria for measuring entanglement. We use the EPR criterion [Reid and Drummond, 1988] and the wavefunction inseparability criterion [Duan et al., 2000].

The EPR criterion

According to the EPR criterion, the product of the conditional variances $\mathrm{V}^{+}(c|d)\mathrm{V}^{-}(c|d) < 1$, for entangled beams. We can write the product of the conditional variances in terms of the input beams at the beam-splitter and find that

$$\mathrm{V}^{+}(c|d)\mathrm{V}^{-}(c|d) = \frac{4\mathrm{V}_a^{-}\mathrm{V}_b^{-}\mathrm{V}_a^{+}\mathrm{V}_b^{+}}{(\mathrm{V}_a^{-} + \mathrm{V}_b^{+})(\mathrm{V}_a^{+} + \mathrm{V}_b^{-})}. \tag{2.13}$$

It can be shown from this equation that entanglement can be obtained when the two input beams are pure squeezed states, i.e when $\mathrm{V}_{(a,b)}^{+}\mathrm{V}_{(a,b)}^{-} = 1$, and for example $\mathrm{V}_a^{+} < 1$ and $\mathrm{V}_b^{+} < 1$. Strong entanglement will be obtained in the regimes of large and pure squeezing. Entanglement can also be obtained when only one input beam is a pure squeezed state and the other input beam is vacuum (e.g. $\mathrm{V}_a^{+} < 1 < \mathrm{V}_a^{-}$ and $\mathrm{V}_b^{\pm} = 1$). This situation is depicted Fig. 2.2(ii). The state generated that way is called a biased entangled state [Bowen et al., 2003a] because of the asymmetry at the two output quadratures. The

---

[4] Experimentally, the orientation of the ellipses depends on the error signal used to lock the homodyne detectors. Changing the slope of the error signal on one of the homodyne detectors will reverse the orientation of the ellipse.

correlation plots indeed show that in this case one has $\mathrm{V}^+(c|d) = 1$ and $\mathrm{V}^-(c|d) < 1$ so the EPR inequality still holds.

Asymmetric losses

When the losses on the two entangled beams are equal, the conditional variances are the same whether the state is inferred from c to d or d to c. When the losses are different on each arm, like in the situation depicted in Fig. 2.2(iii), the conditional variance of d given c is larger than for c given d. These different ways to infer are referred to as direct reconciliation and reverse reconciliation respectively [Grosshans and Grangier, 2002b]. This gives rise to two numbers for EPR correlations. This is seen graphically in the corresponding correlation plots (Fig. 2.2(iii)) where the ellipses have both been rotated clockwise by an amount depending on the loss on the beam c. The difference between the $\mathrm{V}^{\pm}(c|d)$ and $\mathrm{V}^{\pm}(d|c)$ appears clearly.

Inseparability criterion

Let us now refer to another criteria for continuous variable entanglement. It was introduced by Duan et al. [Duan et al., 2000] and quantifies the degree of separability of the wave-function. A bipartite Gaussian entangled state can be shown to be described by its correlation matrix [Duan et al., 2000] which has the following elements

$$C^{ij}_{cd} = \frac{1}{2}\langle \hat{X}^i_c \hat{X}^j_d + \hat{X}^i_d \hat{X}^j_c \rangle - \langle \hat{X}^i_c \rangle \langle \hat{X}^j_d \rangle, \tag{2.14}$$

where $\{i,j\} \in \{+,-\}$. Before the inseparability criterion can be applied, the correlation matrix has to be in standard form II, which can be achieved by application of the appropriate local-linear-unitary-Bogoliubov-operations (local rotation and squeezing operations like Eq. (1.28)) [Duan et al., 2000]. The product form of the degree of inseparability [Bowen et al., 2003b] is then given by

$$\mathcal{I} = \frac{\sqrt{C^+_I C^-_I}}{k + 1/k}, \tag{2.15}$$

where

$$C^{\pm}_I = kC^{\pm\pm}_{xx} + (1/k)C^{\pm\pm}_{yy} - 2|C^{\pm\pm}_{xy}| \tag{2.16}$$

$$k = \left(\frac{C^{\pm\pm}_{yy} - 1}{C^{\pm\pm}_{xx} - 1} \right)^{\frac{1}{2}}. \tag{2.17}$$

$\mathcal{I} < 1$ is a necessary and sufficient condition of inseparability and therefore entanglement. In the case of equal losses on both arms it can be shown [Bowen, 2003] that the product form of the inseparability criterion is equivalent to

$$\mathcal{I} = \mathrm{V}(\mathrm{X}^+_c \pm \mathrm{X}^+_d)\mathrm{V}(\mathrm{X}^-_c \pm \mathrm{X}^-_d) < 1, \tag{2.18}$$

where $\mathrm{V}(\mathrm{X}_c \pm \mathrm{X}_d) = \min\langle(\mathrm{X}_c \pm \mathrm{X}_d)^2\rangle$. This last quantity can be evaluated quite easily, for example, from the conditional deviation ellipse Fig. 2.2(i). From the graph, we see that $\mathrm{V}(\mathrm{X}^+_c \pm \mathrm{X}^+_d) = (\sigma^+_{-\pi/4})^2 = \mathrm{V}^+_a$ which is the squeezed quadrature of beam a. On the other hand, $\mathrm{V}(\mathrm{X}^-_c \pm \mathrm{X}^-_d) = (\sigma^-_{\pi/4})^2 = \mathrm{V}^+_b$, which is the squeezed quadrature of beam b. In this situation $\mathcal{I} < 1$ so the state is not separable.

Asymmetric losses
When the losses are different on both arms, local unitary transformations have to be done to the correlation matrix to express it in standard form II. This process has a very simple graphical interpretation. In the case of unequal losses shown in Fig. 2.2(iii), the minima of the ellipses no longer appear on the diagonals at $\theta = \pm\pi/4$. The local transformations are just used to reorient the ellipses so that the minima will again appear on the diagonals. The local transformations do not change the value of these minima, so we can always find $\mathcal{I}$ directly from the minima of the conditional deviation ellipses without local transformations.

This criteria will be used in chapter 5. In the following, we use the EPR criterion to derive the quantum memory benchmarks.

2.3 Quantum information benchmarks

A quantum memory must *a priori* be able to store and recall the quantum information encoded on light at any time, and also preserve the input pulse shape of signals that have large time-bandwidth products. For a storage device to be labelled a quantum memory, it must be capable of storing quantum information more efficiently than a classical storage device. What is the efficiency that would be sufficient for the quantum memory to be distinguishable from classical storage devices ? What is the efficiency that would be sufficient to guarantee the security of QKD ? Why do we need to store signals that have large time-bandwidth products ? The object of this section is to answer these questions.

Several criteria have been developed in the past to distinguish classical and quantum distributions of states in other quantum information protocols, such as teleportation or quantum cryptography. The fidelity measure will be presented in the first part of this section. Signal-transfer coefficients T, and conditional variances $V_{\rm cv}$, have been used as a state-independent measure to analyze the effectiveness of teleportation experiments in the presence of non-unity gain [Ralph and Lam, 1998, Ralph et al., 1999, Bowen et al., 2003]. We propose implementing the *T-V diagram* to define benchmarks for the storage of continuous variable information and identify the parameters required to enable a transfer of information that outperforms any classical strategy in the next subsection. These criteria will enable the determination of whether a quantum strategy has been used in the storage and readout of a quantum state and whether the output of the storage process is the best clone of its input.

Fig. 2.3 shows the schematics of our quantum memory benchmark. It was shown in Ref. [Hammerer et al., 2004] that the optimal classical measure and prepare strategy for optical memory is the classical teleporter scheme as shown in Fig. 2.3 (b). We therefore benchmark the performance of quantum memories against this setup. In this classical scheme, the storage time can be arbitrarily long without additional degradation. However, two conjugate observables cannot be simultaneously measured and stored without paying a quantum of duty [Braunstein et al., 2000, Ralph and Lam, 1998]. Moreover, the encoding of information onto an independent beam using amplitude and phase modulators will also introduce another quantum of noise. In total, the entire process will incur an additional two units of noise in the output optical state.

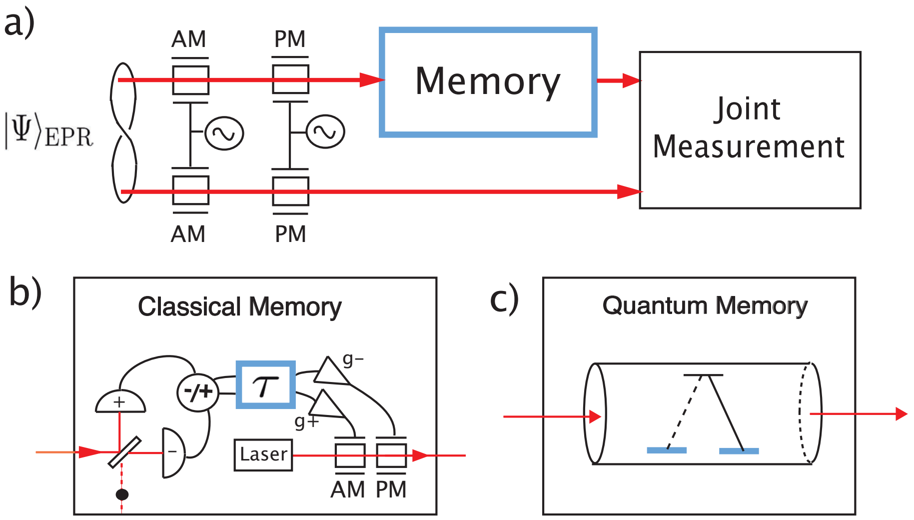

Figure 2.3: (a) General schematics for characterising an optical memory. A pair of EPR entangled beams are encoded with amplitude and phase quadrature information. One of these beams is injected into, stored and readout from the optical memory whilst the other is being propagated in free space. A joint measurement with appropriate delay is then used to measure the quantum correlations between the quadratures of the two beams. (b) A classical teleporter scheme used as an optical memory. The input state is measured jointly on both quadratures using two homodyne detection schemes. Analogous to classical teleportation the measured information is stored for a time τ before fed-forward onto an independent laser beam with a feedforward gain, g. The feedforward gain is analogous to a transmission of $\sqrt{\eta(\omega)}$ for quantum memories. (c) A quantum memory storing information in the ground state coherences of atoms.

2.3.1 Fidelity measure

Possibly the best known benchmark in quantum information protocols is the fidelity, which measures the wave function overlap between the output and input states. It is given by

$$\mathcal{F} = \langle \Psi_{\mathrm{in}} | \hat{\rho}_{\mathrm{out}} | \Psi_{\mathrm{in}} \rangle, \tag{2.19}$$

which, in the Wigner representation, can be written

$$\mathcal{F} = 2\pi \iint \mathrm{W}_{\mathrm{in}}(\mathrm{X}^+, \mathrm{X}^-) \mathrm{W}_{\mathrm{out}}(\mathrm{X}^+, \mathrm{X}^-) d\mathrm{X}^+ d\mathrm{X}^-. \tag{2.20}$$

As shown in the first chapter, for Gaussian states with coherent amplitude $\alpha^{\pm}$ and power spectrum $S^{\pm}$, the Wigner function is

$$\mathrm{W}(\mathrm{X}^+, \mathrm{X}^-) = \frac{2}{\pi S^+ S^-} \exp\Big[-\frac{(\mathrm{X}^+ - 2\alpha^+)^2}{2S^+} - \frac{(\mathrm{X}^- - 2\alpha^-)^2}{2S^-} \Big]. \tag{2.21}$$

The fidelity between the input and output states can be easily calculated [Bowen et al., 2003] using Eqs.(2.20,2.21) and gives

$$\mathcal{F} = \frac{2\, e^{-k^+ - k^-}}{\sqrt{(2 + V^+_{\mathrm{noise}})(2 + V^-_{\mathrm{noise}})}}, \tag{2.22}$$

where $k^{\pm} = \alpha_{\text{in}}^{\pm}\,(1-g^{\pm})^2/(2+V_{\text{noise}}^{\pm})$, $V_{\text{noise}}^{\pm}$ are the noise variances of the output field for the amplitude and phase quadratures and $g^{\pm}$ is the feedforward gain in the classical teleporter case, or classical transmission for a quantum memory. For an ideal classical memory (Fig. 2.3-b) with unity gain, $g^{\pm}=1$, a coherent input state gives $V_{\text{noise}}^{\pm}=2$. The two units of noise arise from the simultaneous measure of both quadratures and from the laser beam used to recreate the information. This gives a *classical limit* of $\mathcal{F} \geq 0.5$. It has been shown by Grosshans and Grangier [Grosshans and Grangier, 2001] that when the fidelity of a teleporter $\mathcal{F} \geq 2/3$, the output state is guaranteed to be the best cloned copy of the input state. This fidelity limit called the *no-cloning limit* for teleportation corresponds to the addition of only one quantum of noise in the entire process.

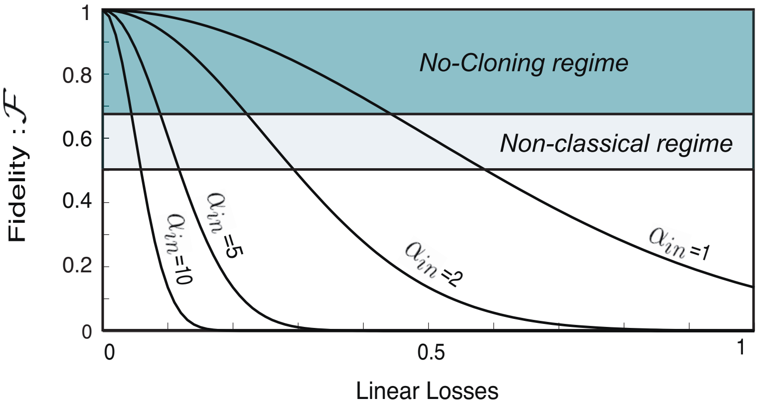

Figure 2.4: Fidelity as a function of memory loss for $\alpha_{\text{in}}(\omega) = 10, 5, 2, 1$. The non-classical and the no-cloning regimes are reached when $\mathcal{F} \geq 1/2$ and $\mathcal{F} \geq 2/3$, respectively.

The use of entanglement in the context of quantum teleportation, or quantum memories is necessary to break these limits. We now quantify quantum memories using this criterion, replacing the classical memory with the quantum memory in Fig. 2.3-a). There is a direct analogy between the feedforward gain g and the transmission $\sqrt{\eta(\omega)}$. Fig. 2.4 shows the behavior of $\mathcal{F}$, as defined in Eq. (2.22) using $g = \sqrt{\eta(\omega)}$, with varying memory loss for different coherent state amplitudes and setting V_{noise} to zero here. We note that the maximum amount of memory loss tolerable for beating both limits are dependent on the coherent amplitudes of the input states. This shows that fidelity is a state-dependent measure.

The formula for the fidelity can be extended to mixed input states using

$$\mathcal{F} = \left[\mathrm{Tr}\left(\sqrt{\sqrt{\hat{\rho}_{\text{in}}}\hat{\rho}_{\text{out}}\sqrt{\hat{\rho}_{\text{in}}}}\right)\right]^2. \tag{2.23}$$

Jeong *et al.* [Jeong et al., 2004] showed that this formula can again be used to benchmark quantum information protocols. Nevertheless, characterizing quantum memory using the state dependent fidelity as a measure will be complicated for exotic mixed states.

2.3.2 T-V diagram

An alternative measure to fidelity for the characterization of quantum information protocols was proposed by Grangier et al. [1998] for quantum non-demolition measurement

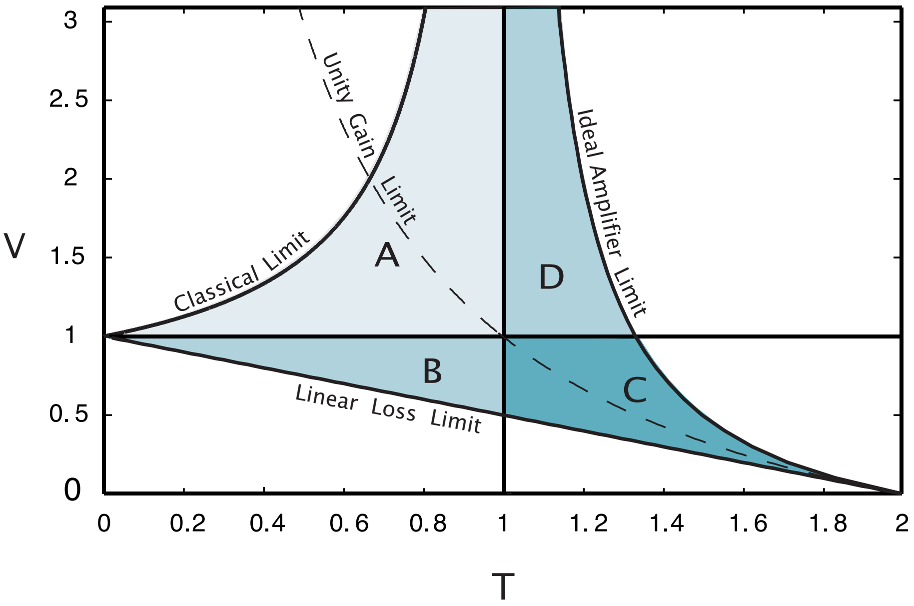

Figure 2.5: Diagram for total signal transfer coefficient T versus conditional variance product V. The classical limit line shows the optimal performance of a classical teleporter. The linear loss limit defines the performance of a memory that does not produce excess noise. The unity gain curve is obtained with increasing excess noise in a system with no loss. The ideal amplifier limit corresponds to the performance of a loss-less amplifier as a function of gain. Regions A, B, C and D correspond to the quantum regimes; Regions B and C represent the regime where EPR entanglement is preserved; Region D is the lossless amplification region ; Region C denotes the no-cloning limit.

and by Ralph and Lam [1998] for quantum teleportation. This alternative uses the signal transfer coefficients, $T^{\pm}$, and the input-output conditional variances, $V_{\text{cv}}^{\pm}$ to establish the efficacy of a process. The conditional variances[5] and signal transfer coefficients are defined as

$$V_{\text{cv}}^{\pm} = V_{\text{out}}^{\pm} - \frac{|\langle \hat{X}_{\text{in}}^{\pm}\hat{X}_{\text{out}}^{\pm}\rangle|^2}{V_{\text{in}}^{\pm}}, \tag{2.24}$$

$$T^{\pm} = \frac{\mathcal{R}_{\text{out}}^{\pm}}{\mathcal{R}_{\text{in}}^{\pm}} \tag{2.25}$$

where $\mathcal{R}_{\text{out/in}}^{\pm}$ is the signal to noise ratio of the output/input field defined by

$$\mathcal{R}_{\text{in/out}}^{\pm} = \frac{4(\alpha_{\text{in/out}}^{\pm})^2}{V_{\text{in/out}}^{\pm}}. \tag{2.26}$$

---

[5] We use the formula for direct reconciliation which gives the optimum bound in the case of asymmetric losses.

We now define two parameters that take into account the performances of the system on both conjugate observables

$$
\begin{aligned}
V &= \sqrt{V_{\mathrm{cv}}^{+} V_{\mathrm{cv}}^{-}}, &(2.27)\\
T &= T^{+} + T^{-}, &(2.28)
\end{aligned}
$$

Fig. 2.5 shows the plot of a T-V diagram. Similar to the fidelity, there are corresponding classical and no-cloning limits in the T-V-diagram for a teleporter or an optical memory. It can be shown that a classical teleporter cannot overcome the $T > 1$ or $V < 1$ limit. By tuning the feedfoward gain, g, a classical teleporter will perform at best at the "classical limit" curve as shown in Fig. 2.5. Ref [Ralph and Lam, 1998] shows that this classical limit can be surpassed using quantum resource (Region A). With limited quantum resource, it is possible to have an output state with $V < 1$ (Region B). When the input state is from a pair of entangled beams, this performance corresponds to the preservation of EPR entanglement at the output [Reid and Drummond, 1988]. With a stronger quantum resource, $T > 1$ and $V < 1$ can be satisfied simultaneously. Grosshans and Grangier [Grosshans and Grangier, 2001] showed that under these conditions the output state represents the best cloned copy of the input. The lower right quadrant of the T-V diagram (Region C) therefore corresponds to the no-cloning regime.

Linear loss regime

We now characterize the quantum memory in terms of the T-V diagram. When a system does not generate excess noise, the performance of the memory is described by the linear loss limit line. Assuming that the transmission through the medium is identical for both quadratures, it can be shown that $V = 1 - \eta(\omega)$ and $T = 2\eta(\omega)$. We note that the result suggests that a memory with linear loss will surpass the classical limit independent of $\eta(\omega)$. This is because, unlike the classical teleporter, the output state obtained from a linear loss memory is not being measured throughout the transmission. Thus there is no measurement quantum duty for all transmittivities. Moreover, because $V < 1$, an input entangled state through a linear loss device will always preserve some entanglement[6] at the output.

Amplification regime

However, when excess noise is introduced in the storage process, T will decrease and V increase more rapidly. This is the case if for example some amplification is involved. Indeed we have seen in the previous section that a noise penalty $G - 1$ will be introduced for a lossless memory with a gain G in order to preserve the commutation relations of the optical field at the output. The performance of such a lossless and amplifying memory is then described by the ideal amplifier line on the T-V diagram where we have $V = G - 1$ and $T = 2G/(2G - 1)$. The optimum situation will be when the gain of the amplifier is unity, so that $T = 2$ and $V = 0$. As the gain increases the memory no longer performs in the no-cloning regime and reaches region (D) where no quantum correlation exists between the input and output states anymore, even though the signal transfer is always larger than what a classical memory could achieve.

---

[6] As defined by the direct reconciliation formula used in the conditional variance product.

Excess-noise

There are, of course, other possible sources of noise that do not amplify the signal. For example, in memories using Raman transitions, any transfer from the coupling beam to the probe via non-linear processes [Matsko et al., 2002] or non-ideal polarizers will contribute to excess noise. We can introduce the excess noise phenomenologically with V_{noise}, which we can assume to be quadrature independent. The T-V performance is now given by $V = 1 - \eta(\omega) + V_{\text{noise}}$, and $T = 2\ \eta(\omega)/(1 + V_{\text{noise}})$. Unlike classical teleportation and in the absence of an amplification process, $\eta(\omega)$ can only be less than or equal to unity. If we assume perfect transmittivity with $\eta(\omega) = 1$, increasing excess noise produces the unity gain curve, or unity classical transmission curve in the T-V diagram. We note that although the classical input signal is perfectly transmitted, the excess noise leads to a degradation on both T and V.

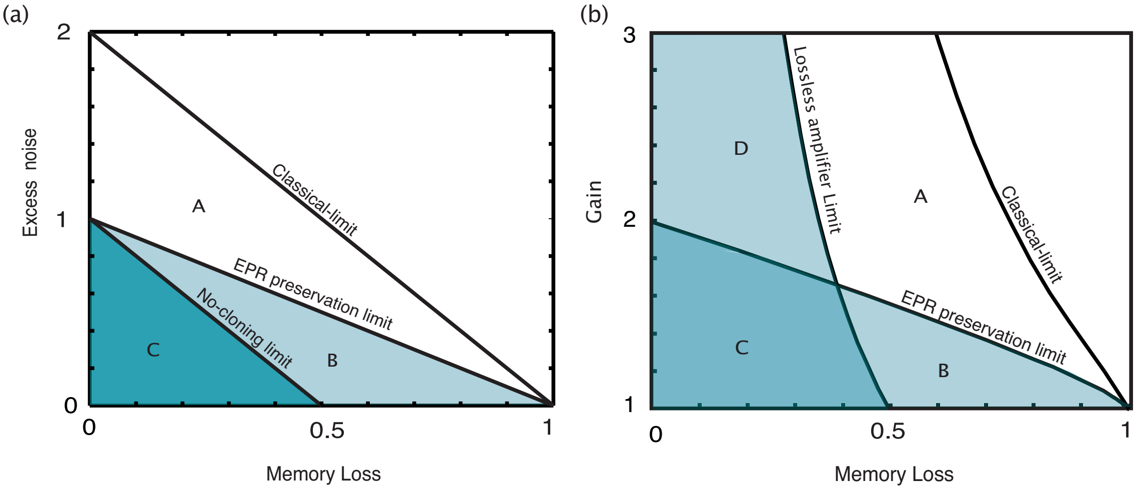

Figure 2.6: Classical, EPR and no-cloning regimes plotted as a function of linear losses and excess noise in (a). A is the non-classical regime; B is the EPR regime and C is the no-cloning regime. These limits are drawn in Fig. (b) on a loss-gain plot and have been derived from Equation (2.3). Contrary to the case of (a), with a large enough gain and sufficiently low losses in the memory, Region (D) can be reached.

2.3.3 Noise-loss diagram

We will now define the parameters required to reach the quantum regime. This is calculated separately in the situations when the noise arises from amplification and when its origin is not related to any gain in the medium. We plot these quantum regimes with excess noise versus linear loss in Fig. 2.6(a), and memory gain versus loss in Fig. 2.6(b). To define the graph shown Fig. 2.6(b), we calculated T and V using the theory for amplification and attenuation using Eq. (2.3). Then, we found the linear gain and linear losses for which the performance crosses our benchmarks. The gain/loss term in Fig. 2.6-(b) is the total amplification/attenuation introduced by the memory, defined as e^{al} and $e^{-\alpha l}$ respectively. These diagrams determine whether an experiment is sufficiently low noise and transmissive for quantum information storage. The no-cloning limit can only be surpassed when $\sqrt{\eta(\omega)} > 0.5$ and $V_{\text{noise}} < 1$ simultaneously in both cases.

2.3.4 Single and multi-mode light storage

The above benchmarks were proposed to quantify the efficacy of the storage of a single mode of the electromagnetic field, $\hat{\mathcal{E}}(t)$. One can also envisage to store several modes in the memory (and apply the same benchmarks for each mode).

Single-mode light storage

Single mode light storage is concerned with the writing and reading of a single mode from the atoms, To efficiently measure the single mode light state recalled from the memory, the detection has to be mode-matched to it. In continuous variable quantum optics, it means that the local oscillator *must be* in the same mode as the output light state as was described in [Dantan et al., 2006]. If it is not the case, the efficiency of the measurement of this mode drops. In the case of a lack of temporal mode matching for example, the measured power spectrum will be broader (or narrower) than the signal itself. It then gets measured at different frequencies which are "vacuum modes of the detection" [Delaubert, 2007, Treps et al., 2005] and therefore are not measured efficiently. In the case of a lack of transverse spatial mode matching, the signal gets measured in the vacuum modes of the local oscillator field transverse modes, which yields a poorer fringe visibility and a loss of signal.

Experimentally, as the quantum memory might distort the input state, the local oscillator cannot always have the same temporal profile as the input. The local oscillator profile then has to be re-optimized and matched to the output pulse shape.

Multi-mode light storage

One can also perform a multimode analysis of the memory, by measuring more than one mode at the output, the local oscillator being matched to each mode. In the case of the storage of many temporal modes, the measurement will be done successively for each pulse. The measurement however has to be done simultaneously for any other degrees of freedom (spatial transverse modes, polarisations...). Of course, all the modes have to be mutually orthogonal for such a measurement to be done without noise penalty.

We note that it is only the choice of basis that distinguishes multimode and single mode light storage. However, considering multi-mode light storage can a priori convey more information than single mode light storage. The simultaneous storage of several temporal modes was for example recently shown to yield improvements in the efficiency of quantum repeaters [Simon et al., 2007].

The noise, transmission, or correlations will be then measured by performing ensemble average measurements on each mode. That is, the input state is stored and released several times from the memory and the results averaged over the detection basis. When the mode matching is optimized, with no noise and no losses, The output state statistics will be identical to the input state statistics.

2.3.5 Time-bandwidth product

What would be the criteria that allows to distinguish single or multimode quantum memories ? We propose to use an overlap formula, defined by the classical conditional variance. This will allow us to assess the efficiency of quantum memories for the storage of several modes.

An important criteria for single-mode or multi-mode quantum memories is the time-bandwidth product. The time-bandwidth product quantifies the *maximum achievable* number of independent samples, or indistinguishable orthogonal modes, that can be stored and retrieved from the memory. Let us consider a coherent state for a duration T. We then introduce a cut-off in frequency space limiting the number of modes we can superimpose and measure. The envelope of the pulse inside T may have any temporal profile. Let us write the Fourier spread of this envelope $\Delta\omega$, defined by the full width at half maximum of the signal. The time-bandwidth product is defined by $T\Delta\omega$, counting the number of frequency modes with a well defined phase within $\Delta\omega$. If the memory is probed with a broadband modulation, the time-bandwidth product of the output pulse quantifies the distortion introduced by the memory.

Let us assume that the memory stores the signal for a time τ_s. We start acquiring the signal output at τ_s for a time T and measure its Fourier spread using a "classical" detection scheme. This will yield a certain value for $T\Delta\omega$. To increase the time-bandwidth product, we can either increase the length of the signal or modulate the temporal profile of the pulse faster. Because quantum memories are not always ideal, doing this might not always yield a larger time-bandwidth product. Most memories in fact have a limited bandwidth. Also, storing long signals means that the decoherence time of the memory has to be small so the number of modes that can be stored depends on the specification of the memory. We can quantify the time-bandwidth product of quantum memories via a "classical" conditional variance

$$V_c = \min_{g,\tau} \int_T dt |s_{\text{in}}(t) - g s_{\text{out}}(t-\tau)|^2, \tag{2.29}$$

where $s_{\text{in/out}}(t)$ are the envelopes $\langle\hat{\mathcal{E}}_{\text{in/out}}\rangle(t)$ of the input/output quantum states, g a variable gain (that is not allowed to vary with t), τ a variable delay and T the time window over which the measurement is done. We see that V_c measures the temporal mode matching between the input and output states. g is on the order of the inverse of the memory loss and τ is the storage time. When the output of the memory has the same temporal envelope as the input, one can tune the gain and delay to match the memory losses and storage time and get back the original signal temporal profile. This will give a small V_c, i.e a large time-bandwidth product. On the other hand, when the output pulse shape is distorted, after optimization of the gain and delay, the conditional variance will be large. This is a signature of a small time-bandwidth product.

Because it does not depend on the actual transmissivity of the quantum memory, the time-bandwidth product is not a benchmark for quantum channels. A memory could for example have a large time-bandwidth product therefore preserving the input shape optimally, and still operate far from the no-cloning regime. In classical communication however, a large time-bandwidth product together with poor overall transmission is not such a problem, as one can amplify the output signal to get back the original signal. The "eye diagram" [Holzlöhner et al., 2002] is often use in classical communication to quantify the ease with which one can discriminate between bits, effectively measuring the time-bandwidth product. This amplification stage is of course prohibited in quantum mechanics, so one can wonder what is there to gain with large time-bandwidths ?

For single mode light storage, large time-bandwidth products are crucial. As we discussed earlier, an efficient measurement of the memory output state relies on mode matching a local oscillator to the output state envelope. This measurement is trivial when the output pulse shape is identical to the input state envelope. However, when the memory distorts the input state, careful measurement of the output pulse shape has to be made prior to quantum measures to optimize the local oscillator accordingly and avoid extra losses in the measurement process. In most quantum information protocols, the memory output state will be mixed to other signals on beam-splitters. The mode-matching visibility on the beam-splitters has to be optimum not to introduce further losses, highlighting again the need for large time-bandwidth products.

In multimode light storage, the quantity of information stored does not scale with the time-bandwidth product as one still requires efficiency for all the modes. However, purification can be performed on all the stored modes to get back the quantum statistics. This feature makes memories with large time-bandwidth products (multimode quantum memories) rather attractive for quantum repeaters applications [Simon et al., 2007]. We will show that the gradient echo memory has some advantage over EIT in that respect.

In general, large time-bandwidth products allow one to clearly distinguish the signal that is retrieved from the memory to eventual parasitic signals that could accompany it. In the early EIT light storage experiments for example, due to the current lack of time-bandwidth products the output pulse was always reshaped, which brought some controversy as to what was really stored [Aleksandrov and Zapasskii, 2004, Lezama et al., 2006].

2.4 Conclusion

In this chapter, we proposed the use of quantum information criteria to benchmark the performance of quantum memories against optimal classical measure-and-prepare schemes. To find the required criteria, we present two quantum technologies that would require quantum memories. The state of the art in the field and a theory for noise and loss and criteria for entanglement preservation were then described. Based on these background information, we use fidelity, signal transfer and conditional variances as benchmarks for the transmission of Gaussian states. We have shown that the no-cloning regime can be reached when the noise does not exceed one unit of shot noise *and* the transmission is above 50%. Finally, we discuss how the measurement of the memory output state can be done. We also introduce a measure similar to the time-bandwidth product to quantify the preservation of the input pulse shape.

Chapter 3

Squeezed light for quantum memories in rubidium

As discussed in the preceding chapter, the control of quantum states of light is of great interest for quantum communication purposes. Many quantum information protocols rely on the possibility of coherently delaying and storing quantum information. This can, for example, be achieved using Electromagnetically Induced Transparency (EIT) or photon echo based quantum memories. Experimental and theoretical studies have shown that information carried by light can be delayed within a narrow bandwidth when light interacts on resonance with atoms in a lambda configuration [Vestergaard Hau et al., 1999, Akamatsu et al., 2004, Peng et al., 2005, Hsu et al., 2006a]. Light pulses were also stored efficiently within the absorption bandwidth of a broadened ensemble of two level atoms in photon echoes memories [Alexander et al., 2006, Hétet et al., 2008b].

One important step forward is the storage of quantum information through such systems. To achieve these goals, a non-classical light source, such as squeezed light, operating at low sideband frequencies and tuned to atomic transitions is required. Other applications of low frequency squeezing in atom optics include the generation of continuous variable entanglement between an atom laser beam and an optical field. This can be realized via outcoupling of atoms from a Bose-Einstein condensate using squeezed light in a Raman transition [Haine et al., 2006].

Many of these atom optics experiments are performed at the rubidium D1 line at 795 nm (the properties of rubidium will be presented chapter 5). The generation of squeezing at 795 nm has been the subject of many experimental efforts involving either atomic interactions in rubidium [McCormick et al., 2007a], or using non-linear effects in crystals [Appel et al., 2007, Tanimura et al., 2006].

We present here the generation of more than 5 dB of vacuum squeezed light at the rubidium D1 line using periodically poled $KTiOPO_4$ (PPKTP) in an optical parametric oscillator. We demonstrate squeezing at low sideband frequencies, making this source of non-classical light compatible with bandwidth limited atom optics experiments. We show a noise reduction of more than 4 dB stably locked down to 200 Hz. This is, for example, well within the bandwidth of Electromagnetically Induced Transparency (EIT) in rubidium hot vapour cells under the condition of large information delay.

Part of this work was published in [Hétet et al., 2007].

3.1 Introduction

Squeezing from atoms

One way to produce squeezed light at atomic transitions is to use the non-linearities from the atoms themselves. Squeezed states of light were first produced using four wave mixing from warm atomic vapours in an optical cavity by Slusher et al. [1985] and Hope et al. [1992]. Vacuum squeezing via self-rotation of the light polarisation in thermal vapour cells was demonstrated [Ries et al., 2003] but other groups failed to reproduce these results due to large atomic noise at the detection frequencies [Hsu et al., 2006b]. Squeezing from cold atoms in a cavity was also demonstrated [Lambrecht et al., 1996, Josse et al., 2004] with a quantum noise reduction of about 2 dB. Recent work demonstrated the relative intensity squeezing of 8.8 dB below the shot noise limit using four wave mixing in a warm rubidium vapor cell. In this scheme, the laser operates close to a rubidium transition and at low frequencies, so it is of great interest for quantum memory applications [McCormick et al., 2007b].

Other sources of squeezed light

Kerr non-linearities in optical fibres yielded more than 5dB of squeezed light [Heersink et al., 2005] close to the theoretical limit [Corney et al., 2006]. The problem is that, for quantum memories, the squeezed modes contains to many photons to be able to be stored efficiently, and as, so far, all quantum memories operate far from the saturation regime. Squeezing via second harmonic generation [White et al., 1996] also suffers from the same issue. Squeezed light at rubidium wavelength was also not demonstrated using these techniques.

The largest amount of squeezing was observed using optical parametric oscillation [Lam et al., 1999, Sørensen et al., 1998, Takeno et al., 2007], where the most recent result shows an impressive 10 dB of noise suppression [Vahlbruch et al., 2008] at 1064 nm. The difficulty for squeezing at 795 nm is to find non-linear crystals that present low losses for both the fundamental and the second harmonic. One advantage of below threshold OPO's is that the squeezed modes produced contain only a few photons, so they will not disturb the quantum memory operation.

We saw in the first chapter that, in continuous variable quantum optics, quantum states of light are created from a correlation between pairs of frequency modes, two *sidebands*. When the two sidebands are emitted in the same spatial mode this leads to the squeezing of the amplitude and phase quadratures of the electromagnetic field. To create the two mode correlations, strong non-linearities are required. In our experiment we start with a laser operating at 795 nm, double its frequency, and down-convert it using $\chi^{(}2)$ non-linearities to obtain squeezing, as shown Fig. 3.1.

3.2 Non-linear conversion

When a material is illuminated, the created polarisation, that is the sum of the optical dipole moments of each atom in the material, reradiates in the output light field mode. This causes losses and phase shifts on the input field. These absorption and dispersion properties, in standard materials far from atomic resonances, are often linear in the sense

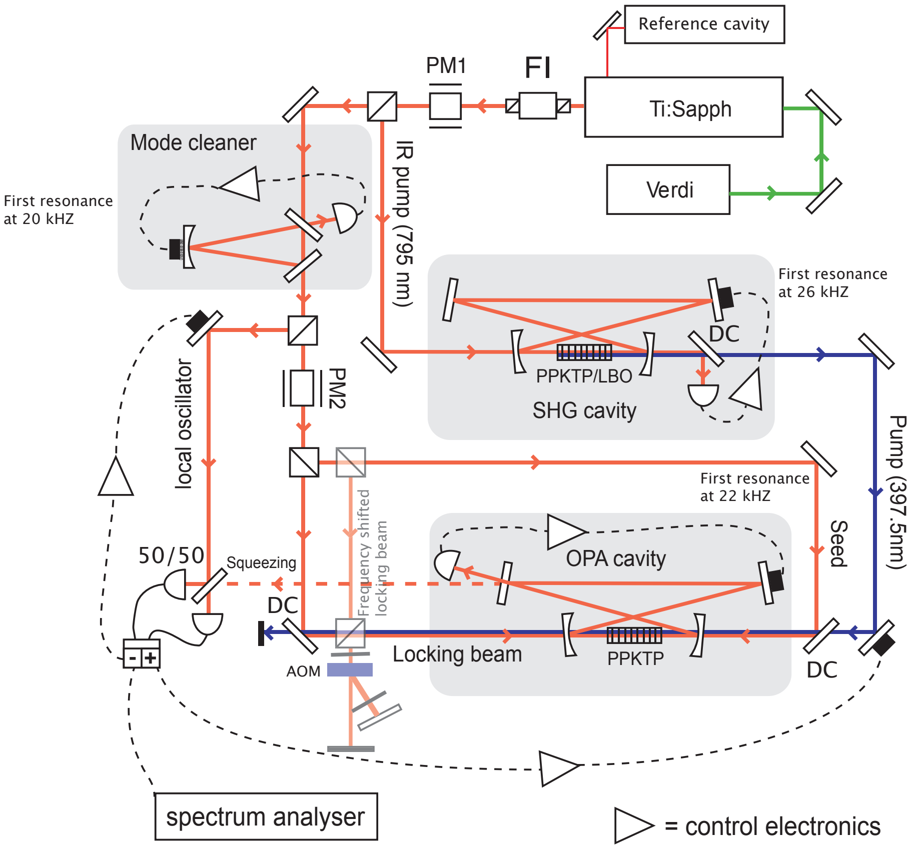

Figure 3.1: Schematic of the experimental setup. FI: Faraday isolator, PM: electro optic phase modulator, DC: Dichroic mirror, OPA: sub-threshold optical parametric amplifier. The control electronics typically consists of a mixer, a low pass filter, a Proportional Integral Differential (PID) controller, and high voltage amplifier. The resonance frequencies of the piezo-mount-mirror ensemble is also written for each cavity.

that they do not depend on the input light power. They are often called *normal* absorption and dispersion.

At high power densities this linear behavior might not hold anymore. For an instantaneous response of the atoms to the light field, we can expand the total atomic polarisation as a power series in the optical field. We have

$$P = \epsilon_0(\chi^{(1)}E + \chi^{(2)}E^2 + \chi^{(3)}E^3 + ...), \tag{3.1}$$

where the $\chi^{(i)}$'s are the i-th order susceptibilities of the material, the values of which are related to the symmetry properties of the crystal[1]. As the power of the field increases, the non-linear effects can become non-negligible and for example, if the input field oscillates at a frequency Ω, harmonics are created at 2Ω, 3Ω and so forth. We are interested here in the $\chi^{(2)}$ second order non-linearity, so we aim at optimizing the conversion from the wavelength 397.5 nm to 795 nm, and vice versa.

High conversion efficiencies are usually achieved at extremely large powers. To give

---

[1] For example, when the crystal has an inversion symmetry, it is easy to see that the even susceptibility terms must be zero.

an idea, good non-linear crystals can generate about 5mW of second harmonic light (at frequency 2Ω) for a fundamental input power of 500mW (at Ω) in single pass continuous wave mode. To obtain a better conversion efficiency one can improve the non-linear properties of the crystals or operate at larger input powers. The latter can be achieved using high power pulsed lasers or optical cavities. In this thesis we chose to use optical cavities for reasons that will become apparent shortly.

The interacting photons in the second order non-linear processes must of course preserve energy and momentum. That is, we require $2\Omega_{\mathrm{f}} = \Omega_{\mathrm{sh}}$ and $2k_{\mathrm{f}} = k_{\mathrm{sh}}$, where $k_{\mathrm{f,sh}}$ are the wave-vectors of the fundamental/second harmonics fields. This momentum preservation, or *phase matching* condition, is naturally not achieved in crystals because of normal dispersion. The refractive index varies linearly with frequency so the generated second harmonic field usually drifts out of phase with the fundamental as it propagates through the medium. After some distance, called the *coherence length*, the second harmonic field does not grow anymore, instead it destructively interferes with the fundamental, and decays.

3.2.1 Birefringence

One way to “phase match” a non-linear material is to use birefringence.

In birefringent crystals, the refractive index of one of the crystal axis, the extraordinary axis, is different than the refractive index of the orthogonal axis. This allows one to obtain phase matching between two orthogonal polarisations. We have a so called *Type I* phase matching, when the two fundamental photons have the same polarisation and the second-harmonic has the orthogonal polarisation[2]. Tuning the refractive index of the crystal is required to ensure maximum conversion efficiency. This is normally done by adjusting the temperature[3] of the crystal, or the angle of the crystal with respect to the input beam (this is called *critical phase matching*).

The temperature required to achieve phase matching can, however, be extremely high or really low, which can pose some technical constraints and also affect the crystal functioning. Some non-linear crystals therefore never phase match at the desired wavelength.

3.2.2 Quasi-phase matching

Another solution to ensure phase matching at the desired wavelength is to use *quasi-phase matching*. In quasi-phase matching, the crystal domain is periodically switched every coherence length[4]. This ensures a constant build up of the second harmonic field through the material and allows one to tailor the properties of non-linear media so that phase matching can be achieved for any desired optical frequency. Early experiments used periodically poled material in waveguide form, which offers a high non-linearity and an extended interaction length. However, losses in waveguides are higher than in bulk material due to technological issues. To date, 0.9 dB of squeezing at 795 nm have been reported using waveguides [Akamatsu et al., 2004].

---

[2] When the two fundamental photons have orthogonal polarisations, the phase matching is referred to as Type II. All the birefringence combinations can in fact be used depending on the crystal and the set-up, to give up to $2^3 = 8$ types of phase matching possibilities.

[3] The relation between the refractive index and the wavelength is often given empirically by the *Sellmeier relations*.

[4] We then have first order quasi-phase matching. When the domains are flipped every n-th coherence lengths we have n-th order quasi-phase matching.

When using $\chi^{(2)}$ non-linear media for the squeezed light generation, it can also be difficult to identify materials that have high non-linearities together with negligible passive losses. The second harmonic of the Rb D1 line, 397.5 nm light for example approaches the UV cut-off wavelength of many non-linear optical media.

3.2.3 Periodically poled KTP

Potassium titanyl phosphate, $KTiOPO_4$ (or KTP) presents a high non-linearity together with a good transmission at 397.5 nm which makes periodically poled KTP (PPKTP) a good candidate for experiments at the D1 rubidium line. The tensor coefficient normally used is the d_{33}, which is around 14 pm/V for KTP. The losses are around 0.1%/cm for ultra-violet and 0.01%/cm for infra-red.

Recent experiments showed the great potential of squeezed state generation in parametric downconversion using PPKTP. More than 7 dB of quadrature squeezing has been reported at 860 nm [Suzuki et al., 2006], while at 795 nm, squeezed vacuum has been observed [Tanimura et al., 2006]. This is the crystal we are using in this experiment. The crystals were bought from Raicol in Israel.

The required domain width (the coherence length in first order poling) can be calculated from the Sellmeier equations[5] by requiring it to be on the order of two times the wavelength mismatch ($2\pi/\Delta k$) in the material

$$l_c = 2\frac{2\pi}{\Delta k} = 2\frac{2\pi}{\left[\frac{n(\lambda_{sh})}{\lambda_{sh}} - \frac{n(\lambda_f)}{\lambda_f}\right]}. \tag{3.2}$$

Our PPKTP was poled to first order, so we find the domain width to be about 5 μm.

3.3 Second harmonic generation and down-conversion

In this section, we present the experimental design that lead us to demonstrating the production of 200mW of ultra-violet light in a second harmonic generator. When operating at half the threshold of an optical parametric amplifier, we then demonstrate a parametric gain of 10, with an escape efficiency of 83 %. This was achieved with the crystal pumped by about 50 mW of UV.

3.3.1 The laser

In all the experiments in the thesis we used a Ti:Sapphire laser, Coherent MBR (see Fig.(3.1)). It was tuned to 795 nm but the Ti-Sapphire crystal actually provides down-conversion from 650 to 1100 nanometers. We used it here to pump a second-harmonic generator (SHG), to seed an optical parametric amplifier (OPA), and to provide a local oscillator for the homodyne detection system in the squeezing measurement. The laser is pumped by a green source (a 10W Verdi, normally operated at 7 W) and delivers a maximum of 1.5 Watt in a "good" transverse mode shape[6]. The laser is made out of a bow-tie cavity. A birefringent filter placed inside the cavity allows one to tune its frequency. Fine tuning can be achieved using an etalon plate at the large cavity waist, and long term

---

[5] The refractive index for the UV/IR is about 1.94/1.84.

[6] Due to thermal effects in the Ti:sapph cavity, the transverse mode shape was found to depend on the Verdi power. The laser mode shape for different Verdi powers can be found in [Pilypas, 2006].

stability obtained by locking the laser to a linear reference cavity. The frequency stability was quoted to be around 100 kHz.

3.3.2 Generation of ultra-violet light.

We present here the results of the second harmonic generation from two different crystals, in the same bow-tie cavity.

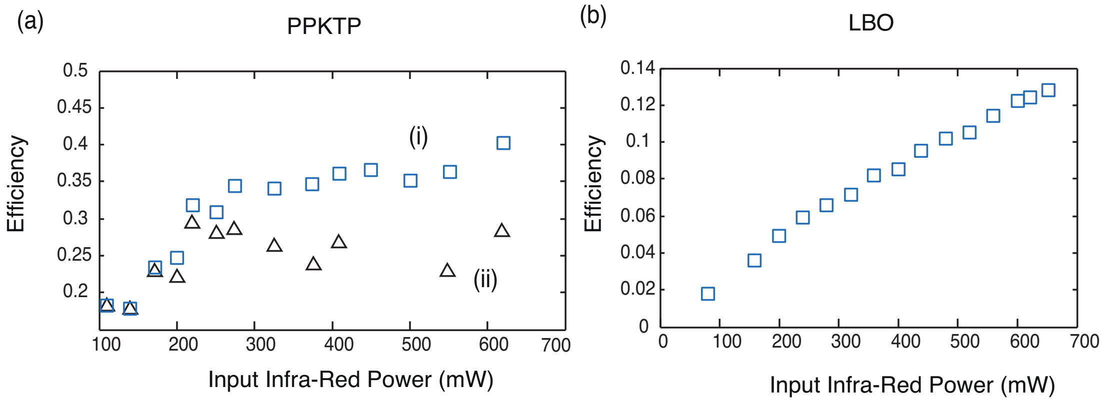

Figure 3.2: Second harmonic generation efficiencies as a function of pump powers from (a) the PPKTP and (b) LBO crystals. Trace (i) in (a) corresponds to the situation where the SHG output is measured while the cavity is scanned and (ii) when it is locked. The two ways of measuring gave identical results for LBO.

Cavity design

To generate large down-conversion (from 397.5 nm to 795 nm) in the OPO cavity a strong UV pump beam with good transverse mode quality is required. Using a Fabry-Perot cavity for doubling achieves both these purposes. A bow-tie cavity (shown Fig. 3.1) was chosen in this experiment. One advantage of such a ring configuration is that is allows more flexibility. For example, we will see in the next sections how it allows us to obtain stable vacuum squeezing from the OPO. The down-side is that such cavities are prone to astigmatism. The angle of the cavity is required to be small to ensure a pure transverse mode shape. In our design the cavity angle is about 8 degrees, giving an astigmatism of only around 0.5% (measured from the difference between the vertical and horizontal waists).

The cavity had a 600 mm round trip perimeter and two curved mirrors (100 mm radius of curvature) with the smaller waist being 40 μm. Apart from the input coupling mirror, the other mirrors are high reflectors ($>$ 99.5%) at 795 nm (with a tranmissivity of around 0.05% at normal incidence). The mirrors were also AR coated for 397.5 nm.

The cavity size has to be “locked” so that the cavity mode is resonant with the input light field. This is required because small temperature drifts or acoustic vibrations can easily change the cavity size by more than a wavelength. The locking of the cavity was done using a Pound Drever Hall (PDH) techniques [Drever et al., 1983]. A phase modulation at 10.4 MHz was applied on the pump using PM1. The error signal was measured on transmission, after rejecting the UV with a dichroic mirror, and fed-back to a piezoelectric crystal that actuates one of the cavity mirrors. The mechanical assembly (mirror-piezo-mount) has the first resonance frequency at 26 kHz. This gives a bandwidth that is large enough for our purpose, so the error signal was low pass filtered before this frequency[7]. It was then integrated, amplified and fed back to the piezoelectric crystal, ensuring the locking of the cavity on resonance.

Second harmonic generation with PPKTP

The first sets of results in this thesis were produced using PPKTP for second harmonic generation. The PPKTP crystal we bought has a length of 20 mm and a cross-section 1×2 mm^2. It is AR coated on both sides. The optimum waist according to the Boyd Kleinmann calculation [Boyd and Kleinman, 1968] is 20 microns. The waist size (40 μm) was deliberately chosen bigger than what is given by the Boyd Kleinmann calculations to minimize thermal effects. We will come back to this shortly. The infra-red input and the produced UV polarizations are both vertical.

With these parameters, a single pass efficiency of $\Gamma = \mathrm{P}_{2\omega}/\mathrm{P}_{\omega}^2 \sim 2.7\times10^{-2}$ W^{-1} for the PPKTP crystal was measured. Here, P_ω and $\mathrm{P}_{2\omega}$ refer to the pump power at the fundamental and the second harmonic field respectively[8]. The SHG cavity was pumped with infrared light via a 82 % reflectivity flat input coupling mirror. This is close to the calculated optimum input coupler that ensures impedance matching. With this cavity design, the total circulating power is about 5W, giving a power density of around 60kW/cm^3 at the waist. The whole system is enclosed in a Perspex box to minimize air currents that could disrupt the locking.

By varying the temperature of the crystal between 20 and 50°C we were able to produce UV light over a range of 1.5 nm around 795.3 nm. At a phase matching temperature of around 20°C, UV light at 397.5 nm was efficiently generated. The maximum second harmonic conversion efficiency reached in that regime was about 40%. The maximum power we measured there was about 230 mW, with an input power of 600 mW.

However, even with this rather low transmissivity input coupler, and large waist, thermal effects were still clearly observed and prevented a stable locking to be achieved at high pump powers. This is seen Fig. 3.2(a) where we plot the efficiency of the PPKTP doubler as a function of the fundamental input power. Trace (i) shows the efficiency of the doubler when the cavity is scanned (i.e by recording the maxima of the UV Airy peaks). The efficiency increases and reaches a plateau at around 40%. However, when the power is measured with the cavity locked, trace (ii), we get smaller conversion because large fluctuations of the crystal temperature prevented from obtaining a reliable UV production.

We also observed that our PPKTP crystal was prone to grey tracking when it is used for SHG at higher power density levels [Jacco et al., 1991, Fève et al., 1997]. We noticed a degradation in the efficiency of the frequency doubler as well as a distortion of the mode shape of the second harmonic output field after operating the SHG over a longer period of time. The effect of grey tracking was partly reversed by slowly heating the crystal up to around 120°C and baking it for a period of several days as suggested in Ref.

---

[7] The filter design can be found in [White, 1997, Lam, 1998, Buchler, 2001, Bowen, 2003]. It comprises a series of gain stages followed by an elliptic filter and a steep $1/f$ roll off. The filters ensures that phase shifts introduced close to the first mechanical resonance are efficiently supressed. The closed loop would otherwise be unstable at large gains.

[8] More details about the single pass efficiency, tunability and oven design can be found in [Pilypas, 2006].

[Boulanger et al., 1999]. To minimize grey tracking effects, we restricted the amount of UV light produced to around 50 mW. Operation in this regime also minimized photo thermal effects in the SHG cavity and allowed for a more stable locking. While grey tracking was observed in SHG with its relative high power density levels involved, we observed no deterioration of the non-linear crystal when it was used in the sub-threshold OPA we present next.

Second harmonic generation with LBO

Because of the above mentioned problems with the PPKTP crystal, we chose to change the crystal in the doubling cavity, but keeping the original cavity geometry. We moved to Lithium triborate (LBO). This crystal has a wide transparency range (from 160nm to 2600 nm) but possess lower non-linearity (around 1pm/V). Its dimensions are $5 \times 5 \times 4.8$ mm^3. It is also AR coated on both sides. The phase matching conditions was found by angle tuning, and the crystal temperature was actively controlled to provide the extra fine tuning of the cavity size after thermal contraction of the crystal.

The rather small crystal dimensions present a compromise between achieving large non-linearity (obtained with longer crystals) and keeping the maximum spatial overlap between the IR pump and UV in the crystal. In critical phase matching, the angle between the Poynting vector in the crystal, and the wave vector is not the same, which inevitably causes the two beams to lose their spatial overlap over long propagation distances. This *walk-off* of the two beams is then a major problem with LBO, which also reduces the spatial quality of the output beam.

The PPKTP used in the OPO allowed a rather low threshold to be obtained. As we will see, about 40 mW of UV pump are necessary to get a reasonable amount of squeezed light. We therefore chose to sacrifice efficiency for a better short, and also long term stability. To enable this power to be reached with the LBO crystal, the input coupler however had to be increased from 82% to 99.5%. The intra-cavity power was then much larger than in the PPKTP cavity but the crystal being much shorter and more transmissive, a better stability was still achieved. The efficiency as a function of input infrared power is shown Fig. 3.2(b). The plateau seen in the doubler using PPKTP case was not reached, meaning that we are still far from reaching impedance matching. However, the results are identical when the cavity is locked and when the UV is measured by scanning the cavity size, showing the good stability of the SHG. This improvement was especially important to obtain low frequency squeezing.

3.3.3 Mode cleaning cavity

An aluminum triangular “mode cleaning cavity”, see Fig. (3.1), was used to generate a pure TEM$_{00}$ beam to facilitate the mode matching of the beams into the OPA cavity and ensure a high interference contrast for the homodyne detection.

The cavity had a total optical path length of 39 cm, giving an FSR of 0.8 GHz. It comprised two closely spaced plane mirrors (99.5% transmissive) and one curved high reflectivity mirror (99.95%, radius of curvature 1m). The cavity acted as a spatial filter and not to as a frequency filter, which as we will see, would be quite a challenge. The finesse of the cavity was then modest (the linewidth was measured to be around 2.2 MHz, giving a finesse of 360). The back mirror was used to control the cavity length. The ensemble {O-ring-back mirror holder-piezo} had a mechanical resonance frequency of 20 kHz.

As the angle made by the beam at the curved mirror is quite small, it ensured minimum astigmatism. This allowed us to obtain a good interference contrast with the beam from the OPO and a good mode matching of the seed and counter-propagating beams inside the OPO cavity. The cavity was stabilized using PDH locking with the same phase modulation (PM1) used for the doubler. When locked, the cavity transmission was measured to be about 92%, limited mainly by the presence of high order transverse modes at the laser output.

3.3.4 Optical parametric oscillation.

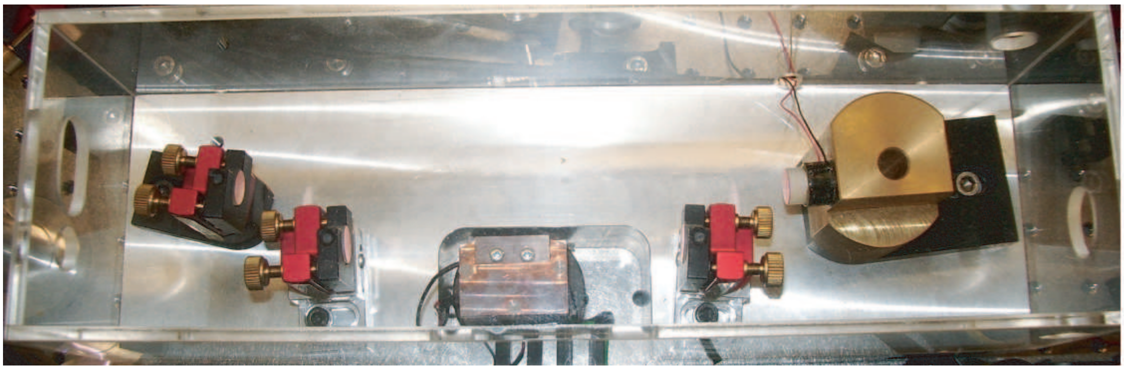

Figure 3.3: Photo the optical parametric oscillator. The crystal is pumped from the right from one of the curved mirrors. The infrared exited from the top left mirror. The ensemble was enclosed in a perspex box to minimize air currents.

To obtain squeezed light, we used an optical parametric oscillator (OPO). A picture of the OPO cavity is shown Fig.3.3. The OPO consisted of a PPKTP crystal inside a bow-tie cavity similar in geometry to the SHG. The waist size at the center of the crystal was around 35 μm for the IR fundamental. We injected an IR seed through the right to measure amplification and deamplification. The pump beam was input via the curved mirrors on the right, high reflector for Infrared ($>$ 99.95% at 4 degrees of incidence) and transmissive for UV ($<$ 5% at 4 degrees of incidence). The system is also enclosed in a Perspex box.

As the OPA cavity was highly impedance mismatched, deriving an error signal from the reflected seed was difficult and yielded non optimum locking. The OPA cavity length was therefore locked on resonance using an auxiliary beam propagating in the opposite direction (coupled via the left curved mirror in the picture) to the pump beam. The beam path is shown Fig. 3.1. The modulator PM2 provided phase modulation sidebands at 5.6 MHz allowing the generation of a PDH error signal for the OPA cavity. Furthermore, locking the cavity via the counter propagating beam allowed for the stable generation of vacuum squeezing as the cavity length can be locked independently from the seed. A resonance frequency of 22 kHz of the piezo-mount in the OPO was measured here. Depending on how the cavity was aligned, residual coupling of locking beam to the seed could be observed on the homodyne detection and the photodetector used to lock the cavity. They were due to reflections of the locking beams from the surface of the crystal, which after being amplified in the OPO, were easily observed. Slight changes were made later on to eliminate those spurious effects and enable low frequency squeezing. They will be presented in the next section.

After optimizing the mode matching of the pump into the cavity, we obtained efficient parametric amplification and reached a threshold at 25 mW, with an output coupler of 95%. The total losses inside the OPA are then estimated to be around 0.5%. For the actual squeezed state generation, we changed the reflectivity of the output coupling mirror to 92%. This enhanced the squeezing escape efficiency, which we calculated to be 93%. The corresponding theoretical threshold is now 68 mW. We pumped our OPA with 40 mW allowing a parametric gain of around 10 to be observed.

3.4 Squeezing at rubidium wavelengths.

Thanks to the high non-linearity of the PPKTP and the small losses in the crystal, the threshold is quite low. We then expect to obtain squeezed light with a reasonably low pump power. We present here the generation of squeezing at rubidium wavelengths and show quantum noise suppression of a vacuum field using optical parametric oscillation (OPO). By operating our system with a seed beam of low power (i.e. by running the OPO as an amplifier, OPA), we then locked the system to deamplification and show amplitude quadrature squeezing down to 150 kHz. Let us first present the photodiodes used and the laser noise spectrum.

3.4.1 Quantum noise detection

We describe here the photodiode functioning. To obtain a good quantum efficiency at 795 nm we used silicon photodiodes. The photodiodes were the model S3883 from Hamamatsu. Their quantum efficiency was measured to be close to 95% with a sensitive ammeter measuring the current directly across it. The number of electrons produced divided by the number of photons gives the quantum efficiency. The calibration was then done using a standard power-meter. This did not provide an absolute number for the efficiency, but allowed us to decide which diodes were the best from the batch that was bought.

The detector comprises a low noise trans-impedance stage followed by amplification. The design can be found in [White, 1997, Lam, 1998, Buchler, 2001, Bowen, 2003]. A noise clearance above the detection dark noise of 10 dB was achieved with 4 mW of light from DC to about 15 MHz.

3.4.2 Laser noise

Before turning to the squeezing results, it is important to know the noise characteristics of the Ti:sapph laser. We perform a self-homodyne measurement of the laser noise and obtain the results shown Fig. 3.4. The achieved cancellation of the laser noise was about 35 dB from 100 kHz to 5 MHz, when operating with a local oscillator power of 1 mW. The measurements reveal that the laser is shot noise limited above 1.5 MHz. At low frequencies a broadband noise component attributed to the Verdi pump laser was observed. The peaks were due to the internal locking servos. The larger peak occurring at 87 kHz, came from the signal used to lock the cavity Etalon. In theory, a non-shot noise limited laser is however not an issue when producing and detecting vacuum squeezed light.We will see how it can sometimes become a problem in practice.

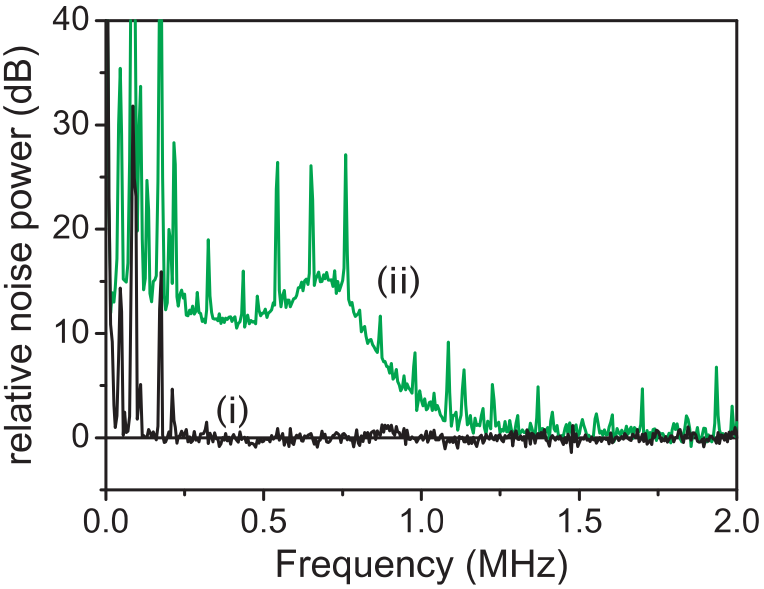

Figure 3.4: Self-homodyne spectrum of the laser in the range between 100 kHz and 5 MHz at a laser power of 1mW. Trace (i) is the shot noise (difference signal between the photocurrent from the two photodetectors) and trace (ii) the laser noise (sum signal).

3.4.3 Vacuum squeezing

We demonstrate here the production of vacuum squeezing. In the first step we blocked the seed, thus running the OPA as an OPO to generate a squeezed vacuum state. The squeezing was measured with a homodyne detection scheme. The mode matching between the local oscillator and the OPA output was about 97% for the present measurement[9]. The overall efficiency, also taking into account the escape efficiency of the squeezing from the cavity, is approximately 83%.

Figure 3.5 shows the homodyne detection signal measured in zero span mode at 400 kHz with a spectrum analyser, when the phase of the local oscillator was scanned. The resolution bandwidth was 30 kHz and the video bandwidth 100 Hz. This curve shows a noise reduction of 5.2 dB ± 0.4 dB below the quantum noise limit when correcting for electronic noise[10] (which is 10 dB below the quantum noise level defined by our local oscillator beam), the anti-squeezing level is 12 dB ± 0.4 dB.

3.4.4 Locked squeezing

Next, we seeded the OPO to run it as a parametric amplifier. To generate squeezing at a particular quadrature, the phases of the pump beam and of the local oscillator with respect to the seed beam need to be controlled. We chose to lock the pump phase to deamplify the seed and thus generate an amplitude squeezed beam. The locking signal was derived from the phase modulation of the seed beam at 5.6 MHz. This modulation

---

[9] Optimum mode matching was achieved by careful polarization selection with Glan Thomson polarisers, three axis mounts and lenses from Newport.

[10] The electronic noise of the photodetectors have to be subtracted to both noise levels when the measurement is performed in a logarithmic scale.

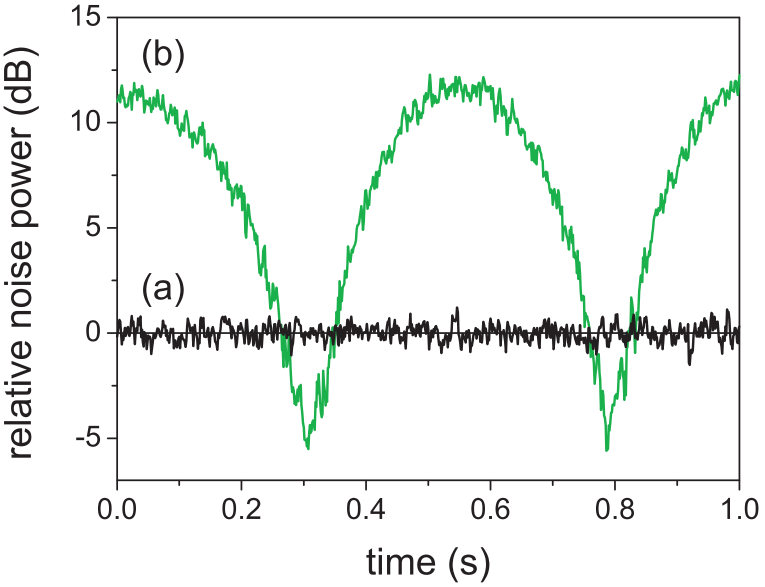

Figure 3.5: Quantum noise levels for squeezed vacuum generation. (a) Quantum noise level and (b) squeezing trace when scanning the local oscillator phase. Noise levels are displayed as the relative power compared to the shot noise level.

signal was transmitted through the cavity via the seed beam and measured on the two homodyne detectors. The sum signal of the detectors was then demodulated and low pass filtered thus providing an error signal to lock the pump phase with respect to the seed beam. As we wanted to measure the amplitude quadrature of the squeezed beam, the homodyne detector needed to be locked to the bright/dark fringe. The same phase modulation at 5.6 MHz which was used for locking to deamplification, was also used to lock the homodyne detection, as shown Fig. 3.1. The locking signal was obtained via the difference of the photocurrents of the two detectors. Figure 3.6.(a) shows the dependence of the squeezing spectrum measured at sideband frequencies within the cavity bandwidth. The quantum noise suppression gets more efficient at low frequencies as expected. At sideband frequencies below 1 MHz, "technical noise" is coupled into the system.

The ultimate sources of noise limiting the low frequency performance of the squeezer are the noise on the seed and noise on the pump (coupled onto the squeezed beam when the OPA is seeded). At such low frequencies, most lasers show technical noise (see Fig. 3.4). Different techniques have been proposed and implemented to overcome these issues. One approach relies on interferometric cancellation of common mode noise, either by interference of two squeezed beams from two OPAs which were seeded by the same laser on a symmetric beam splitter, [Bowen et al., 2002] or by placing a squeezer inside a Mach-Zehnder configuration [Schnabel et al., 2004]. Alternatively the seed power level can be reduced. This minimises the technical noise at low frequencies on the seed beam, but also reduces the coupling of noise from the pump onto the squeezed field [McKenzie et al., 2004]. In the limit of zero power in the seed, no noise is coupled to the squeezed field, however, to lock the local oscillator to a particular quadrature, a different locking technique such as quantum noise locking must be used. We present the results from quantum noise locking in the next section.

To lock the squeezer to deamplification, we first reduced the power level of the seed

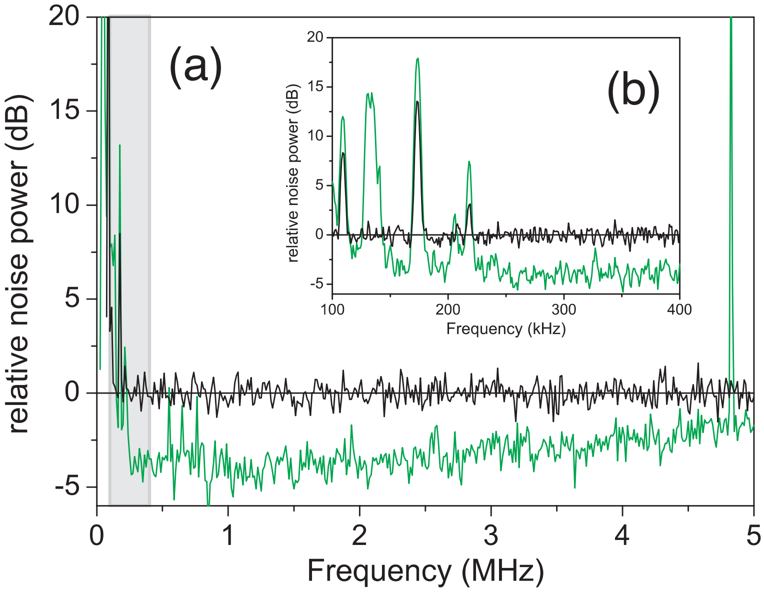

Figure 3.6: Squeezing spectra observed from the OPA, normalised to the quantum noise limit. a) broad frequency range, b) squeezing in the low frequency range 100 kHz-400 kHz (shaded area in a). The resolution bandwidth was 3 kHz for these measurements, the video bandwidth was 30 Hz (300 Hz) for the narrow (broad) frequency range.

beam to minimise the noise coupling onto the squeezed beam while still being able to generate large enough error signals. As the locking stability of the system, on the other hand, relies on the total power in the seed, a compromise between seed power and coupling of low frequency noise into the squeezed beam and locking stability needed to be found. In the inset (b) of Fig. 3.6, the low frequency part of the squeezing spectrum is plotted. More than 3 dB of amplitude squeezing were measured at sideband frequencies down to 150 kHz. The results presented here were obtained with a seed power of 2 μW whilst we were still able to lock the set-up for a few minutes at a time.

Our main motivation for the generation of squeezing at atomic wavelengths was to study the performance of EIT in rubidium to delay and store quantum information. The amount of delay possible in such atomic systems at a given sideband frequency is governed by the dispersion properties, which in turn are linked via the Kramers Kronig relation to the transmission bandwidth. For a quantum delay line to be efficient, passive losses must be avoided. Thus, useful sideband frequencies where the information is encoded are limited to the sub-megaHertz regime. With our squeezing source at hand, it will be possible to demonstrate the storage of quantum information at a sideband frequency of 150 kHz with moderate losses. However, recent sudies showed that additional sources of decoherence might limit the performance of such systems further, i. e. restrict the transmission and also add extra noise [Hsu et al., 2006a]. Our next aim is to produce large stably locked squeezing at an even lower frequency range to probe the capabilities of quantum memories or light.

3.5 Low frequency squeezing

To go to even lower sideband frequencies we performed a few modifications to the above set-up. First it is clear that we could not use a seed to stably lock the detection. We then moved to a technique that allowed us to lock the detection using vacuum squeezing. We then observed further excess noise at lower sideband frequencies. The locking beam was single out as the source of this excess noise so we moved to using a frequency shifted counter-propagating TEM_{02} mode to lock the cavity. A Standford research preamplifier was used to perform efficient common mode subtraction of the laser noise down to DC. As the preamp response varied from DC to 1 MHz, quantum noise measurement were restricted to this range of frequencies.

3.5.1 FM to AM conversion

One source of low frequency noise we had to tackle was conversion from frequency noise to amplitude noise generated by the mode cleaner cavity. Large frequency noise was in fact emitted directly by the laser when locked to the reference cavity. After going through the mode cleaning cavity, the frequency noise was inevitably transferred to low frequency (DC to 500 kHz) amplitude noise, even after thorough improvement on the locking of the mode cleaner was performed. To enable shot noise limited detection at low frequencies we then chose not to lock the laser to the reference cavity but to the saturated absorption signal (as will be explained chapter 5).

3.5.2 Noise locking

The homodyne detection setups were controlled using quantum noise-locking [McKenzie et al., 2005, Schori et al., 2002, Laurat et al., 2006]. This system used the quadrature asymmetry of squeezed states. The noise power over some range of sideband frequencies was measured and used to derive an error signal that locked the homodyne detectors to the desired quadrature. The advantage of this technique was that it did not rely on any coherent amplitude in the squeezed beam. Injection of coherent amplitude into the OPO has been identified as one of the most significant reasons for poor squeezing at low frequencies [McKenzie et al., 2004].

In our experiment, noise in a frequency band between 0.1 and 1 MHz was used to lock the phase of the local oscillators. The error signal was generated by applying a dither at 110 kHz on the piezo controlling the phase of the local oscillator. The band pass filtered signal was sent to an envelope detector. This signal was then demodulated and low pass filtered to give the error signal. The circuit design was adapted from [McKenzie, 2007].

One issue with the Noise locking technique, when applied in the context of EIT-quantum memories, is that at high optical depths and low control beam powers, a large part of this frequency range could be absorbed by the medium. With noise-locking in place however, squeezed light could be measured down to 60 kHz as shown in Fig. 3.7 (upper noise trace).

3.5.3 Orthogonal mode for the cavity locking

As can be seen Fig. 3.7, below 60 kHz, another source of noise was observed. In order to actively stabilise the OPO cavity for vacuum squeezing, we used a TEM_{00} beam that travelled in the reverse direction around the OPO cavity. It transpired that this beam was

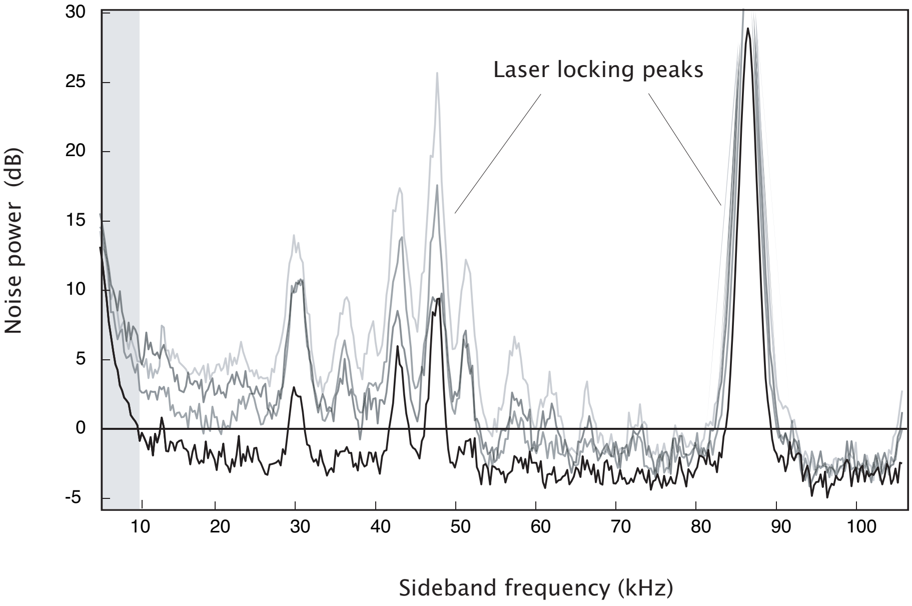

Figure 3.7: Influence of the locking beam : Squeezing spectra from the OPO, normalised to the quantum noise limit in the frequency range 5 kHz-100 kHz as a function of the locking beam power. The locking beam power values are [1,10, 20, 100] μW from the bottom to the top trace.

partially reflected by the surfaces of the OPO crystal leading to some residual coherent amplitude in the squeezed output. Fig. 3.7 shows the evolution of the low frequency noise as a function of the locking beam power. At low locking beam powers we could partially recover squeezing at low sideband frequencies.

To allow a stable locking of the cavity at any power, a backwards propagating TEM_{02} transverse mode was used to lock the OPO cavity. The cavity was slightly misaligned to generate a TEM_{02} mode. Because of the different Guoy phase shifts of the TEM_{02} and TEM_{00}, they did not resonate at the same frequency in the cavity. To maintain resonance for a TEM_{02} mode, the counter propagating beam was frequency shifted using an acousto-optic modulator in double pass configuration as shown Fig. 3.1. The frequency shift given by the AOM needed to compensate for the Guoy phase shift was found to be 128 MHz[11].

The light power used to lock can be made much higher now, without disturbing the low frequency performance of the OPO. The combination of noise-locking and a frequency shifted OPO locking beam allowed us to produce stably locked low frequency squeezing.

The spectrum analyzer we used, does not allow measurements below 10 kHz, as can be seen by the shaded area Fig. 3.7. In order to measure at lower sideband frequencies we perform a time domain analysis of the squeezed light.

---

[11] Using an orthogonal polarization to lock the cavity was also tried. It was however found not practicable because of the birefringence of KTP. The AOM frequency had to be changed whenever the crystal temperature changed, for example because of thermal effects induced by the pump.

3.6 Digital analysis of squeezed states

To perform low frequency detection and to measure the quantum correlations between optical signals in chapter 5, we then measured our signals in the time domain. This technique also allowed more flexibility and more efficient processing of the signals.

3.6.1 Time domain analysis

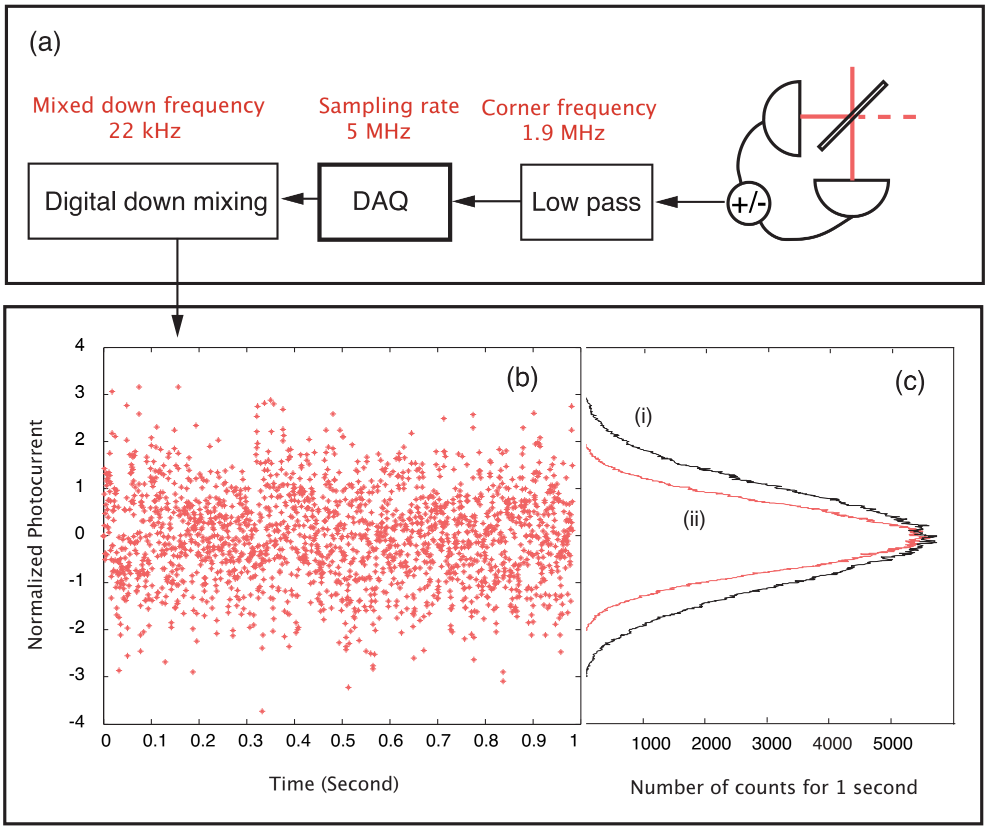

Figure 3.8: (a) Steps followed for the digital acquisition. The subtracted signal was low pass filtered at 1.9 MHz, acquired digitally at 5 MHz and mixed down at 22 kHz. (b) Time series of the homodyne signal at a sideband frequency of 22kHz. (b) Corresponding histogram. Trace(i) is the squeezing distribution and trace(ii) the shot noise.

The acquisition of the signals was done using an 8 bits National instrument-digital card, (which gives a dynamic range of 50 dB in signal intensity). This dynamic range was at the limit of our signal strengths, (cf. Fig. 3.7) so a proper choice of amplification before entering the card was crucial to allow a good noise clearance (without excessive clipping of the laser peaks) to be reached.

A sampling rate ranging between 0 to 100 Megasamples/second could be chosen, giving a maximum frequency resolution of 50 MHz. There was here no limit to how low can the detection frequencies be, as long as the acquisition times were long enough for the required resolution. One word of caution here : As an antialiasing filter was not available in this system, after the sampling rate was chosen, one had to filter the high frequency components efficiently. The high frequency components would otherwise give unwanted signals, modulo the sampling rate frequency. The steps followed before entering the DAQ card are depicted Fig. 3.8-(a).

To perform an analysis of the signals, we often first Fourier transformed the data[12]. The other way to measure the signal noise power was to down-mix the time series data digitally. We select a sideband frequency, mix-down at this frequency and then low pass filter to eliminate the higher order frequency component, as depicted Fig. 3.8-(a)[13]. The resulting signal was a time series representing the noise in a frame at the chosen center frequency (here 22 kHz).

We show Fig. 3.8-(b) a time series of a squeezed laser beam at a center frequency of 22 kHz, and a sampling rate of 5 MHz. The subtracted signal from the homodyne detection was acquired for 1 second. We plot a histogram of the photocurrent for the squeezed light Fig. 3.8-(c), trace (ii). The same procedure was followed with the squeezed light blocked. We then obtain the shot noise Fig. 3.8-(c), trace (i). We see that the noise distribution of both the shot noise and the squeezed light is Gaussian. From this result, we could calculate the width of both Gaussian distributions and obtain the noise power and squeezing value. We obtained here a squeezing of 4 dB, in agreement with the spectrum analyzer results.

3.6.2 Sub-kHz squeezing

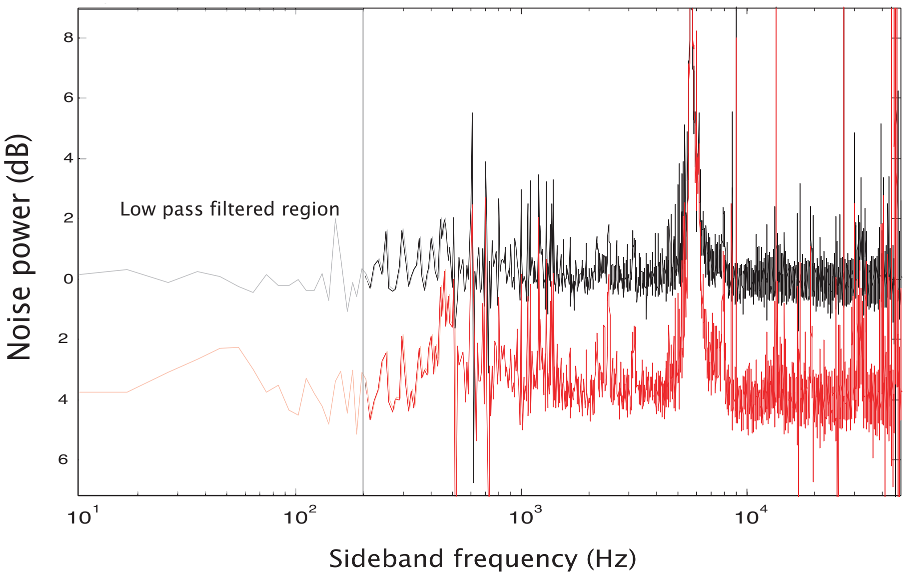

Figure 3.9: Squeezing spectra observed from the OPO, normalised to the quantum noise limit in the range 10 Hz- 5kHz. The sampling rate was 100 kHz (initially low pass filtered at 50 kHz), the integration time was 2 seconds.

---

[12] We checked that the result was identical to the spectrum analyzer measurement.

[13] The data were post processed in Matlab by multiplication with a sine function at the center frequency and low pass filtering in the time domain by convolution with a truncated sinc function. Care was taken to perform the operations far enough from the residual locking peaks from the laser. To enhance the measurement bandwidth one could however filter them out digitally with an appropriate (causal) filtering function.

Low frequency squeezing was achieved by several groups in the world driven by the interest in gravitational wave detection. Thanks largely to the expertise in this field, we were able to show the squeezing of quantum fluctuations in the Hertz regime. Fig. 3.9 shows the squeezing result normalized to shot noise between 10 Hz and 5 kHz on a logarithmic scale. The peaks are mainly due to the detector dark noise and other RF noise from the oscilloscopes and room lights. Due to unstable changes in power at low frequencies and a stationary roll up in the shot noise spectrum going above the dynamic range[14], we low pass filtered frequencies below 200 Hz. This low frequency excess noise was also observed in [Vahlbruch et al., 2006, McKenzie, 2007] and was attributed to dust particles randomly scattering light and crossing the local oscillator. Suppression of noise below the quantum noise was observed at 200 Hz (when the shot noise is a flat response of frequency), and even further down to the Hz in the low pass filtered region.

3.7 Conclusion

In conclusion, we have demonstrated 5.2 ± 0.4 dB of vacuum squeezing at the rubidium D1 line using optical parametric oscillation. Using PPKTP, we were able to stably lock the OPA to generate amplitude squeezing in the frequency range compatible with bandwidth limited atom optics experiments.

Then after some important modifications to the set-up, we demonstrated around 4 dB of quantum noise suppression down to 200 Hz. The low frequency performance was limited by drifts due to dust, as observed in [Vahlbruch et al., 2006, McKenzie, 2007]. The squeezing generated gave us the possibility to efficiently examine the quantum performance of EIT-based delay lines, as will be shown chapter 5, and can potentially be used as a source of non-classical light to generate non-classical atom laser beams and characterise other quantum memories.

---

[14] The same measurement was also performed using a dynamic network analyzer and show the same transients.

Part II

Electromagnetically induced transparency

Chapter 4

Quantum study of EIT based quantum memories

This chapter presents a quantum study of Electromagnetically Induced Transparency (EIT) as a delay channel and storage device for continuous variable quantum states.

Electromagnetically Induced Transparency takes place when two beams interact with atoms in a so called Λ configuration. The two optical dipoles created by the beams *interfere* in the excited state and trap the populations in the ground states. Under optimum operation, this interference leads to full transmission of the two beams. This effect has a wide range of applications, from large non-linearities at low light powers [Braje et al., 2003], to ultraslow light propagation [Vestergaard Hau et al., 1999], and stopped light [Fleischhauer and Lukin, 2000]. In this chapter we will focus on the quantum properties of slow and stopped light.

A semi-classical description of the Λ system introduces the main theoretical ideas behind "coherent population trapping" in the first section. When one of the beams is dim, therefore acting as a perturbative *probe* to the system, it can be slow down by several orders of magnitude smaller than the speed of light. We calculate the group velocity of the probe and present limits to the slow light propagation.

The probe is then treated as a multimode quantum state in section 4.2. Various sources of noise generated by the medium are then calculated using both a phase space method and a simple analytical model to quantify the efficiency of EIT as a quantum delay line.

Finally, we use both a phase space treatment and Heisenberg-Langevin equations solved analytically in the weak probe approximation to describe the efficiency of light storage using EIT. We explain the behaviour of the atomic noise and give an expression for the time-bandwidth product of this system in the presence of decoherence. We then implement the *T-V diagram* to identify the parameters required to enable a transfer of information that outperforms any classical strategy.

Part of the work described here was published in [Hétet et al., 2008].

4.1 Semi-classical analysis of the three-level atom

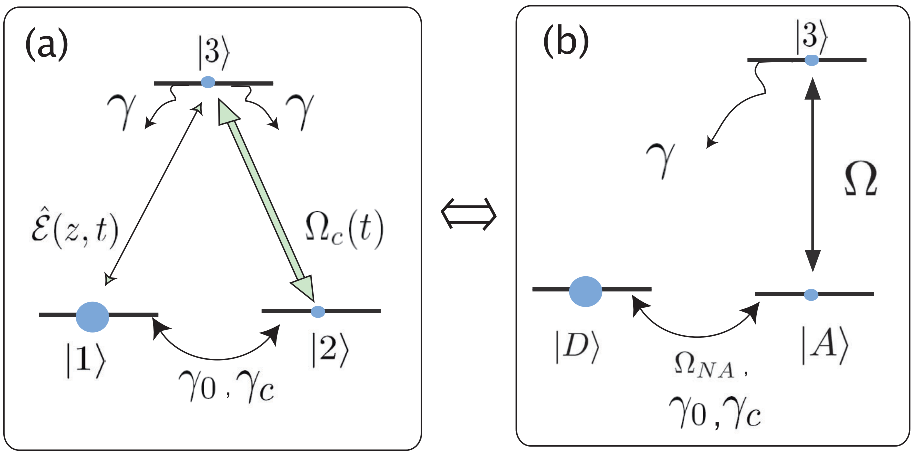

Figure 4.1: (a) EIT level structure. $\hat{\mathcal{E}}(z,t)$ is the envelope operator of the probe field, and $\Omega_c(t)$ is the coupling beam Rabi frequency. Almost all the atoms are pumped into state $|1\rangle$ initially. γ is the spontaneous emission rate from the upper state and γ_0, γ_c are mean decoherence rates between the two ground states for pure dephasing and population exchange respectively. (b) shows the dark state basis. The dark state $|D\rangle$ is coupled to the bright absorbing state $|A\rangle$ via fast variations of the control and probe beams or ground state decoherence.

The atomic structure considered for EIT is the three-level atomic Λ system shown in Fig. 4.1(a). In the absence of ground state decoherence the master equation of this system is

$$\frac{\partial}{\partial t}\hat{\rho} = \frac{1}{i\hbar}[\hat{\mathcal{H}}_{\text{int}}, \hat{\rho}] + \mathcal{L}_{31}[\hat{\rho}] + \mathcal{L}_{32}[\hat{\rho}], \tag{4.1}$$

where $\hat{\rho}$ is the reduced density matrix of the optical field and atomic variables and $\hat{\mathcal{H}}_{\text{int}}$ is the interaction Hamiltonian.

We use here the formalism describing the interaction of light with ensembles of atoms presented in the first chapter. In the rotating wave approximation, the interaction Hamiltonian is

$$\hat{\mathcal{H}}_{\text{int}} = \int \frac{N\hbar}{L}[g\hat{\mathcal{E}}(z,t)\hat{\sigma}_{31}(z,t) + \Omega_c(t)\hat{\sigma}_{32}(z,t) + h.c.]dz, \tag{4.2}$$

where g is the coupling strength on the probe transition. The $\mathcal{L}_{3i}$ are Liouvillians modelling spontaneous emission from the upper state $|3\rangle$, and are defined by

$$\mathcal{L}_{3i}[\hat{\rho}] = \gamma \sum_{z_k \in \delta z} (\hat{\sigma}^k_{i3}\hat{\rho}\hat{\sigma}^k_{3i} - \frac{1}{2}\hat{\sigma}^k_{i3}\hat{\sigma}^k_{3i}\hat{\rho} - \frac{1}{2}\hat{\rho}\hat{\sigma}^k_{i3}\hat{\sigma}^k_{3i}). \tag{4.3}$$

The summation is done over all the single atom operators within a slice δz, which commute when they belong to a different slice δz of the atom. For simplicity we assumed the decay rates from the upper state to the states $|2\rangle$ and $|1\rangle$ to be the same.

In this section, we describe the semi-classical evolution of the atom, treating the two beams as classical fields. We will consider Liouvillians modelling different ground state decoherence processes in the subsection 4.1.3. In the other sections, we treat the probe beam as a general quantized field and calculate the atomic noise added to it.

4.1.1 Dark state basis

One of the features of the three-level system is the presence of a so called dark state $|D\rangle$, which, once prepared, does not interact with the fields anymore. In this subsection, we show that the dark state carries the information about the relative phase and amplitude between the probe and the control, and allows both of them to be fully transmitted through the medium when they do not vary too fast in time.

Let us find semi-classical solutions for the three-level system in the Schrödinger picture. Using the Hamiltonian $\hat{\mathcal{H}}_{\text{int}}$ and doing a spectral decomposition in the basis $\{|i\rangle\}$, the Schrödinger equation yields

$$\frac{\partial}{\partial t}\begin{bmatrix} c_1 \\ c_2 \\ c_3 \end{bmatrix} = \begin{bmatrix} 0 & 0 & -i\Omega_p \\ 0 & 0 & -i\Omega_c \\ -i\Omega_p^* & -i\Omega_c^* & -\gamma \end{bmatrix}\begin{bmatrix} c_1 \\ c_2 \\ c_3 \end{bmatrix}, \tag{4.4}$$

where we assume $\Omega_p = g\langle\hat{\mathcal{E}}\rangle$, to be a classical field, and inserted the decay term γ from the exited state. In this basis, the evolution of all the coefficients is linked to the others. After diagonalising the Hamiltonian, we find the eigenstate basis

$$\begin{bmatrix} c_D \\ c_A \\ c_3 \end{bmatrix} = \frac{1}{\Omega}\begin{bmatrix} \Omega_c & -\Omega_p & 0 \\ \Omega_p^* & \Omega_c^* & 0 \\ 0 & 0 & 1 \end{bmatrix}\begin{bmatrix} c_1 \\ c_2 \\ c_3 \end{bmatrix}, \tag{4.5}$$

where $\Omega = \sqrt{|\Omega_p|^2 + |\Omega_c|^2}$ and c_D/c_A are the coefficient of the so-called Dark/Absorbing states. The dark state $|D\rangle = \frac{1}{\Omega}(\Omega_c|1\rangle - \Omega_p|2\rangle)$, carries information about the amplitude and relative phases of the two beams. To understand the physics given in this new basis, we derive an equation of motion for the $\{c_D, c_A, c_3\}$ coefficients using Eq.(4.5) and Eq.(4.4) and obtain

$$\frac{\partial}{\partial t}\begin{bmatrix} c_D \\ c_A \\ c_3 \end{bmatrix} = \begin{bmatrix} 0 & -\frac{\Omega_{NA}}{2} & 0 \\ -\frac{\Omega_{NA}}{2} & 0 & -i\frac{\Omega}{2} \\ 0 & -i\frac{\Omega}{2} & -\gamma \end{bmatrix}\begin{bmatrix} c_D \\ c_A \\ c_3 \end{bmatrix}, \tag{4.6}$$

where $\Omega_{NA} = 2(\dot{\Omega}_p\Omega_c - \Omega_p\dot{\Omega}_c)/\Omega^2$. The term Ω_{NA} is a non-adiabatic parameter. It quantifies the effect of the variations of the control and probe beams in time on the dark state [Fleischhauer and Manka, 1996, Harris, 1994]. Only when $\Omega_{NA} \neq 0$, does the dark state evolve. The other states are however always evolving even when $\Omega_{NA} = 0$ and are coupled via the effective driving field Ω. This description of the three-level system can be represented by the coupling shown in Fig. 4.1(b).

It can be shown using Eq. (4.6) that provided the rate Ω^2/γ at which $|A\rangle$ and $|3\rangle$ are damped is much larger than the adiabatic parameter Ω_{NA}, i.e when the time scale over which the two beams change is large, the dark state is decoupled from the other states and remains unperturbed. The dark state then follows the slow variations of the probe and control. However, when the evolution of the fields is too fast, the dark state is no longer maintained and will be coupled to the absorbing "bright" state $|A\rangle$, as depicted Fig. 4.1-(b).

When Ω_c is constant and Ω_p time dependent, the adiabatic following will be valid only for control beam powers larger than the probe *or* for small time variations of the probe compared to γ/Ω_c^2 (as seen from Ω_{NA}'s expression). The system stays in the dark state and the probe unabsorbed when its fluctuations remain within a frequency transmission band as wide as allowed by the adiabatic following. We have electromagnetically induced transparency for the small frequency components of the probe field and the probe fluctuations faster then γ/Ω^2 will be absorbed. We come back to the transparency window description and calculate its shape using the Heisenberg picture in the next subsection.

When the control beam is also kept time dependent, its time variations have to be small not to introduce any more coupling to the absorbing state. These considerations are critical for light storage in EIT, where both the control beam and the probe are both time dependent.

4.1.2 Transparency window and slow light

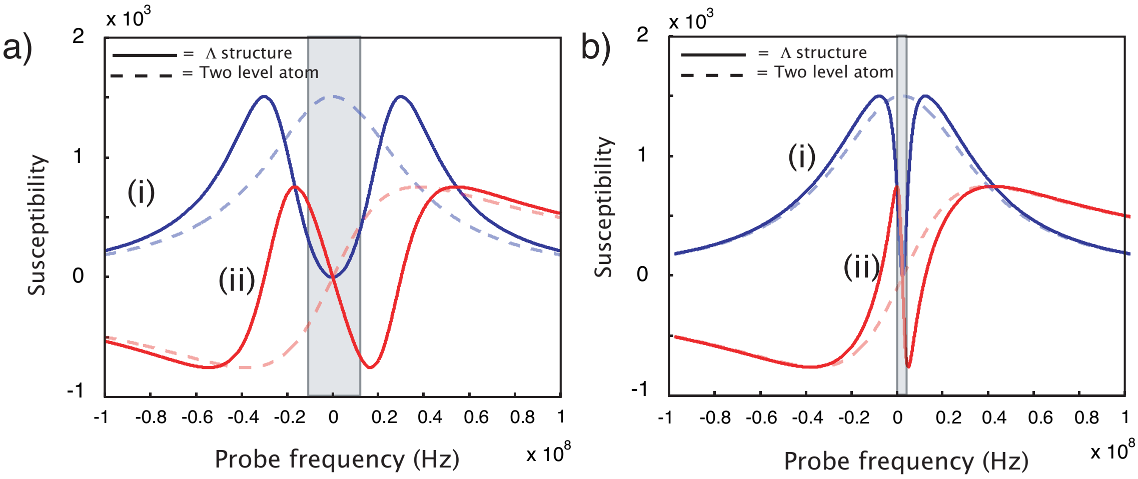

Figure 4.2: Real (curve (i)) and imaginary (curve (ii)) parts of the EIT susceptibility, (a) for a control beam Rabi frequency of 30.10^6 MHz and (b) for a control beam Rabi frequency of 10.10^6 MHz. For both graphs, we also plotted the two level atom absorption and dispersion (dashed lines).

We adopt here a description of the three-level system in a weak probe approximation and show that, in this regime, the dispersion at the center of the EIT window can be extremely steep, allowing ultraslow propagation of the probe in the medium. We also present another way to describe the EIT properties in the Heisenberg picture by letting the operators describing the atoms and the light field evolve, and keep the time and space dependence of the probe field.

Ignoring decoherence affecting the ground states, and using the same procedure as for

Eq. (1.42) in chapter 1, we get a set of Bloch equations

$$\begin{aligned}
\dot{\sigma}_{11} &= \gamma\sigma_{33} - ig\mathcal{E}\sigma_{31} + ig^*\mathcal{E}^\dagger\sigma_{13} \\
\dot{\sigma}_{22} &= \gamma\sigma_{33} - i\Omega_c\sigma_{32} + i\Omega_c^*\sigma_{23} \\
\dot{\sigma}_{13} &= -\gamma\sigma_{13} + ig\mathcal{E}(\sigma_{11} - \sigma_{33}) + i\Omega_c\sigma_{12} \\
\dot{\sigma}_{32} &= -\gamma\sigma_{32} + i\Omega_c^*(\sigma_{33} - \sigma_{22}) - ig^*\mathcal{E}^\dagger\sigma_{12} \\
\dot{\sigma}_{12} &= -ig\mathcal{E}\sigma_{32} + i\Omega_c^*\sigma_{13} \\
\frac{\partial}{\partial z}\mathcal{E} &= \frac{igN}{c}\sigma_{13}, \qquad (4.7)
\end{aligned}$$

where we substituted $\mathrm{Tr}_{\mathrm{at}}(\hat{\rho}\hat{\sigma}_{ij}(t)) = \langle\hat{\sigma}_{ij}\rangle(t)$ by σ_{ij}. We also rewrote the Maxwell equation in a moving frame at the speed of light.

We now derive an expression for the susceptibility of the medium by doing a weak probe approximation. In this weak excitation limit, we will be able to obtain a linear relation between the atomic polarization and the probe in the Fourier domain.

The weak probe approximation assumes the probe field Rabi frequency to be much weaker than the control beam Rabi frequency. In steady state, the atoms are then all prepared in state $|1\rangle$ via optical pumping induced by Ω_c and the control beam will be undepleted throughout the process. Its dependence on z can therefore be safely ignored. We now have $\sigma_{11} \simeq 1, \sigma_{22} \simeq \sigma_{33} \simeq 0$, and can obtain a set of closed, self consistent linear equations

$$\begin{aligned}
\dot{\sigma}_{13}(z,t) &= -\gamma\sigma_{13}(z,t) + ig\mathcal{E}(z,t) + i\Omega_c\sigma_{12}(z,t) \\
\dot{\sigma}_{12}(z,t) &= i\Omega_c^*\sigma_{13}(z,t) \\
\frac{\partial}{\partial z}\mathcal{E}(z,t) &= \frac{igN}{c}\sigma_{13}(z,t), \qquad (4.8)
\end{aligned}$$

where we here explicitly included the time and space dependence of the dipoles and probe field. We now calculate the evolution of the probe as it propagates through the medium following the same procedure as in [Peng et al., 2005, Fleischhauer and Lukin, 2000] by solving the equations in the Fourier domain. We define

$$\tilde{O}(z,\omega) = \frac{1}{\sqrt{2\pi}}\int_0^\infty dt O(z,t)e^{i\omega t}, \qquad (4.9)$$

temporal Fourier transform of the variable $O(z,t)$. After Fourier transforming the equations and integrating the simplified set of equations over space, we obtain

$$\tilde{\mathcal{E}}(L,\omega) = e^{-\Lambda(\omega)L}\tilde{\mathcal{E}}(0,\omega), \qquad (4.10)$$

where L is the length of the sample and

$$\Lambda(\omega) = \frac{g^2N}{c}\frac{-i\omega}{-i\omega(\gamma - i\omega) + \Omega_c^2}, \qquad (4.11)$$

is the susceptibility of the EIT medium. The real part of the susceptibility quantifies the absorption of the probe field and the imaginary part, the dispersion of the EIT medium. We can shown that when $\omega \ll \frac{|\Omega_c|^2}{\gamma}$ the transmission is close to 100%, in agreement with the interpretation given in the Schrödinger approach, where the loss at high frequencies was related to non-adiabatic following of the dark state. The Fourier components of the probe outside the EIT transparency window are absorbed because, in the dark state basis, the dark state couples to the other absorbing state via the Ω_{NA}, when the probe varies too quickly.

The real and imaginary parts of the susceptibility are plotted in Figure 4.2 for two different control beam powers as a function of ω. Together with the EIT results, we plotted the two-level atom susceptibility for comparison. In Fig. 4.2(a), curve (i) represents the absorption cross section of the EIT medium for large control beam power. The absorption is negligible at small frequencies (within the shaded area) and increases at higher frequencies. The absorption ultimately goes down again at frequencies outside the atomic linewidth, like in the two-level atoms case. Associated with this absorption profile is the dispersion curve (ii), giving the amount of phase shift for each frequency of the probe inside the medium. At frequencies close to zero, the EIT dispersion slope has the opposite sign as the two level atom dispersion and is linear, resulting in a reduction of the group velocity of the light field.

At lower control beam powers, Fig. 4.2(b) shows that the width of the transmission window is smaller, allowing slower light propagation to be reached. The group velocity of the probe is defined as $v_g = \partial\omega/\partial k$, which equals $-\omega/\Im(\Lambda(\omega))$ in the linearly dispersive regime. For low frequencies we then find

$$v_g = \frac{\Omega_c^2 L}{\gamma d}, \tag{4.12}$$

where $d = \frac{g^2 NL}{\gamma c}$ is the optical depth of the medium as seen by the probe field. The group velocity of the probe can then be tuned by the control field and reach extremely small values. This has allowed experimentalists to demonstrate ultraslow propagation of light in various systems. The most impressive experiment perhaps being the group velocity of 17 m.s^{-1} achieved in a cold atomic sample in Lin Hau's group [Vestergaard Hau et al., 1999]. One can also explain these experiments as a coherent exchange of photons between the two beams. When the probe enters the sample its energy is given to the control and its information written in the ground states. After a time given by the inverse of the scattering rate $\Gamma = \Omega_c^2/\gamma$, the energy is borrowed again from the control field, and the probe is coherently reemitted out of the sample whilst reading out the ground state coherence. This explains how the pulse can be delayed by more than its width without losing energy, as we will show section 4.2.1.

We note that EIT was described here from a purely semi-classical treatment. The quantum explanation using the dressed state picture and level splittings is often used to interpret the induced transparency. Such a description is not required to explain EIT. Again, the transparency window opens due to an *interference* between the two dipoles and its width is given by the rate at which the dark state can follow the variations of the probe field.

4.1.3 Ground state decoherence effects

In most experiments, the transmission and delay of the light propagating through a medium prepared in EIT conditions is affected by various mechanisms. We can distinguish two classes of effects. Those affecting the ground state coherence "directly" and those involving the interaction with other atomic levels. Both will affect the ground state coherence and result in reduced or sometimes enhanced transmission. Their influence will be crucial and need to be well understood for a good functioning of the quantum memory.

A list of the effects is presented in the experimental part of this thesis.

Most decoherence mechanisms can be cast into two quantities : γ_0 and γ_c modelling the mean dephasing and population reshuffling rates respectively. As will be discussed in the experimental chapter, they encompass the physics involved in the slow light propagation of the probe in most systems. Two corresponding Liouvillian terms $\mathcal{L}^{deph}_{[1,2]}$ and $\mathcal{L}^{coll}_{[1,2]}$, can be added to the master equation (4.1) to account for their influence on the system evolution in the thermal bath.

$\mathcal{L}^{deph}_{[1,2]}$ accounts for off-diagonal dephasing arising from elastic collisions or atoms moving in and out of the interaction region defined by the probe beam quantized mode. Its expression is obtained from the phase damping Liouvillian presented in the first chapter. It can be written

$$\begin{aligned}\mathcal{L}^{deph}_{[1,2]}[\hat\rho] &= \gamma_0 \sum_{z_k\in\delta z} (\hat\sigma^k_{11}\hat\rho\hat\sigma^k_{11} - \frac{1}{2}\hat\sigma^k_{11}\hat\sigma^k_{11}\hat\rho - \frac{1}{2}\hat\rho\hat\sigma^k_{11}\hat\sigma^k_{11})\\ &+\gamma_0 \sum_{z_k\in\delta z} (\hat\sigma^k_{22}\hat\rho\hat\sigma^k_{22} - \frac{1}{2}\hat\sigma^k_{22}\hat\sigma^k_{22}\hat\rho - \frac{1}{2}\hat\rho\hat\sigma^k_{22}\hat\sigma^k_{22}). \qquad (4.13)\end{aligned}$$

As discussed chapter 1, this term does not affect the atomic populations. If the pumping preparation is not optimum or if inelastic collisions are non-negligible, a population exchange term $\mathcal{L}^{coll}_{[1,2]}$ must be included. It is defined as

$$\begin{aligned}\mathcal{L}^{coll}_{[1,2]}[\hat\rho] &= \gamma_c \sum_{z_k\in\delta z} (\hat\sigma^k_{12}\hat\rho\hat\sigma^k_{21} - \frac{1}{2}\hat\sigma^k_{12}\hat\sigma^k_{21}\hat\rho - \frac{1}{2}\hat\rho\hat\sigma^k_{12}\hat\sigma^k_{21})\\ &+\gamma_c \sum_{z_k\in\delta z} (\hat\sigma^k_{21}\hat\rho\hat\sigma^k_{12} - \frac{1}{2}\hat\sigma^k_{21}\hat\sigma^k_{12}\hat\rho - \frac{1}{2}\hat\rho\hat\sigma^k_{21}\hat\sigma^k_{12}). \qquad (4.14)\end{aligned}$$

$\mathcal{L}^{coll}_{[1,2]}[\hat\rho]$ also affects the off-diagonal terms of the density matrix in the same way as $\mathcal{L}^{deph}_{[1,2]}[\hat\rho]$, but as the sources of these two decoherence processes are different we monitor them separately. It should be noted that this last term does not account for a pure loss of atoms out of the system, due to possible atomic motion out of the interaction region or atoms moving into other hyperfine states. We also assume the mean dephasing rates describing quantum jumps from $|1\rangle$ to $|2\rangle$ to be the same as the mean rates describing quantum jumps from $|2\rangle$ to $|1\rangle$ for simplicity. The ratio between γ_0 and γ_c depends on the atomic system used. In a cool enough atomic sample where the mean free path of the atoms is on the order of the probe beam size, γ_0 would for example be dominant.

From the master equation traced over the atomic variables, we now have

$$\begin{aligned}\dot\sigma_{11} &= \gamma\sigma_{33} + \gamma_c(\sigma_{22}-\sigma_{11}) - ig\hat{\mathcal{E}}\sigma_{31} + ig^*\hat{\mathcal{E}}^\dagger\sigma_{13}\\ \dot\sigma_{22} &= \gamma\sigma_{33} + \gamma_c(\sigma_{11}-\sigma_{22}) - i\Omega_c\sigma_{32} + i\Omega_c^*\sigma_{23} +\\ \dot\sigma_{13} &= -(\gamma+\gamma_0/2+\gamma_c/2)\sigma_{13} + ig\hat{\mathcal{E}}(\sigma_{11}-\sigma_{33}) + i\Omega_c\sigma_{12}\\ \dot\sigma_{32} &= -(\gamma+\gamma_0/2+\gamma_c/2)\sigma_{32} + i\Omega_c^*(\sigma_{33}-\sigma_{22}) - i\ g^*\hat{\mathcal{E}}^\dagger\sigma_{12}\\ \dot\sigma_{12} &= -(\gamma_0+\gamma_c)\sigma_{12} - ig\hat{\mathcal{E}}\sigma_{32} + i\Omega_c^*\sigma_{13}. \qquad (4.15)\end{aligned}$$

To simplify the system of equations (4.15), it will be solved to first order in $\hat{\mathcal{E}}$, γ_c/γ and γ_0/γ. To ensure an efficient pumping into the dark state, therefore an optimum electromagnetically induced transparency, we will also assume $|\Omega_c|^2 \gg (\gamma\gamma_0, \gamma\gamma_c)$.

We first perform a steady state analysis of the problem in this approximate regime.

From the last three Bloch equations, we get a relation between the coherences and the populations terms. Using this result, the first two Bloch equations and the population preservation relation, an expression for the populations can be obtained. Assuming the coupling beam Rabi frequency to be real, the atomic steady states are found to be

$$\begin{aligned}\langle\hat{\sigma}_{11}\rangle &= 1-2\frac{\gamma_c}{\gamma}\ ,\ \langle\hat{\sigma}_{22}\rangle=\frac{\gamma_c}{\gamma}\ ,\ \langle\hat{\sigma}_{33}\rangle=\frac{\gamma_c}{\gamma}\\ \langle\hat{\sigma}_{12}\rangle &= -\frac{g\langle\hat{\mathcal{E}}\rangle}{\Omega_c}\ ,\ \langle\hat{\sigma}_{13}\rangle=\frac{ig\gamma_0}{\Omega_c^2}\langle\hat{\mathcal{E}}\rangle\ ,\ \langle\hat{\sigma}_{23}\rangle=\frac{i\gamma_c}{\Omega_c}.\end{aligned} \tag{4.16}$$

We note that the atoms are no longer fully pumped in the state $|1\rangle$ due to population exchange γ_c ($\langle\hat{\sigma}_{11}\rangle < 1$), and therefore a non-zero dipole $\langle\hat{\sigma}_{23}\rangle$ appears on the coupling beam transition. In this chapter, however, we have assumed that the coupling beam is not depleted. In order for these solutions to be consistent, we then need to find the regimes where the coupling beam is negligibly absorbed. We do so by solving the following Maxwell equation describing the coupling beam propagation

$$\frac{\partial\Omega_c(z)}{\partial z}=\frac{ig^2N}{c}\langle\hat{\sigma}_{23}\rangle, \tag{4.17}$$

the solution for which is

$$\Omega_c^2(z)=\Omega_c^2(0)+2d\gamma\gamma_c z/L, \tag{4.18}$$

where $d=\frac{g^2NL}{\gamma c}$ is the optical depth of the medium seen by the probe field without control field and decoherence. Although the coupling beam intensity is absorbed linearly through the medium, a negligible depletion is guaranteed under the condition

$$\frac{\Omega_c^2}{\gamma\gamma_c}\gg 2d, \tag{4.19}$$

which we will require in all the calculations where this decoherence term is used.

We also note that because of the pure dephasing γ_0, a dipole $\langle\hat{\sigma}_{13}\rangle$ is created on the probe transition. Solving Maxwell equation, we then find that a portion of the mean probe field is absorbed by the medium by an amount $e^{-\alpha_0 L}$, where $\alpha_0=\frac{gN}{c}\frac{\gamma_0}{\Omega_c^2}$.

This analysis is important for the study of EIT as a delay and storage device. The losses and, as we will see next, the associated noise will affect dramatically their efficacies.

4.2 Quantum noise in the EIT delay line

As demonstrated in the previous chapter the measurement of the transmission and noise completely characterise the memory and allows one to tell whether or not it is performing better than any classical measurement device. In this section we will calculate the transmission $\eta^{\pm}(\omega)$ and noise $V^{\pm}_{\text{noise}}(\omega)$ for EIT as a delay line for quantum states, using phase space simulations in the positive-P representation and an analytical model in the Heisenberg picture.

Previous theoretical work has characterized the efficiency of EIT as a delay line for continuous variable quantum states [Dantan and Pinard, 2004, Peng et al., 2005, Hétet et al., 2006]. Considering a three-level atom such as the one depicted in Fig. 4.1(a), under conditions where there is a pure dephasing rate between the ground states, the information flow can be slowed down within a narrow frequency window, and no additional noise is introduced beyond that which is necessary to preserve the canonical commutation relation of the field [Peng et al., 2005, Hétet et al., 2006]. We go further here and include population shuffling term γ_c and the associated noise together with phase damping decoherence (modeled by γ_0). The control field will still be treated as a classical field, a reasonable assumption in the weak probe regime which will be justified in the next section.

4.2.1 Phase space simulations

We first solve the problem numerically using phase space simulations. To model this system, we used stochastic phase space methods in the positive-P representation [Drummond and Gardiner, 1980]. This representation is computationally intensive but has the advantage of being exact in most regimes as opposed to the truncated Wigner representation, [Gilchrist et al., 1997]. We choose the following normal ordering of the operators

$$(\hat{\mathcal{E}}^\dagger, \hat{\sigma}_{13}^\dagger, \hat{\sigma}_{23}^\dagger, \hat{\sigma}_{12}^\dagger, \hat{\sigma}_{11}, \hat{\sigma}_{33}, \hat{\sigma}_{22}, \hat{\sigma}_{12}, \hat{\sigma}_{23}, \hat{\sigma}_{13}, \hat{\mathcal{E}}), \tag{4.20}$$

mapped to the c-numbers

$$(\beta, \sigma_{11}, \sigma_{10}, \sigma_9, \sigma_8, \sigma_7, \sigma_6, \sigma_5, \sigma_4, \sigma_3, \alpha). \tag{4.21}$$

We then define

$$\hat{\Xi}(\underline{\lambda}, z) = e^{\lambda_\beta \hat{\mathcal{E}}^\dagger(z)} \Big(\prod_i e^{\lambda_i \hat{O}_i(z)} \Big) e^{\lambda_\alpha \hat{\mathcal{E}}(z)}. \tag{4.22}$$

The sum is performed with i decreasing from 11 to 3. $\hat{O}_i(z)$ refers to the ith atomic operator in our normally ordered definition and $\underline{\lambda} = (\lambda_3 ... \lambda_i ... \lambda_{11})$ is a real vector. The normally ordered characteristic function is then

$$\chi(\underline{\lambda}, z) = \mathrm{Tr}(\hat{\rho}\ \hat{\Xi}(\underline{\lambda}, z)). \tag{4.23}$$

The equations of motion for $\chi(\underline{\lambda}, z)$ are calculated using the master equation (4.1), including the ground state Liouvillians, and the commutation properties of the atomic and field operators. As an example, we give the equations of motion for the interaction of the atoms with the control beam

$$\begin{aligned} \frac{\partial \chi}{\partial t}\Big|_{ac} &= iN_z\Omega_c(1 - e^{i\left(\frac{\lambda_8-\lambda_7}{N_z}\right)})(\frac{\partial}{\partial \lambda_{10}} + \frac{\partial}{\partial \lambda_4})\chi - \Omega_c e^{i\left(\frac{\lambda_8-\lambda_7}{N_z}\right)}(\lambda_5 \frac{\partial}{\partial \lambda_3} + \lambda_9 \frac{\partial}{\partial \lambda_{11}})\chi \\ &+ \Omega_c(\frac{\partial}{\partial \lambda_7} - \frac{\partial}{\partial \lambda_8})(\lambda_4 + \lambda_{10})\chi + \Omega_c(\lambda_3 \frac{\partial}{\partial \lambda_5} + \lambda_{11} \frac{\partial}{\partial \lambda_9})\chi \\ &\quad -i\frac{\Omega_c \lambda_4}{N_z}(\lambda_3 \frac{\partial}{\partial \lambda_3} + \lambda_4 \frac{\partial}{\partial \lambda_4} - \lambda_5 \frac{\partial}{\partial \lambda_5})\chi \\ &\quad -i\frac{\Omega_c \lambda_{10}}{N_z}(\lambda_9 \frac{\partial}{\partial \lambda_9} - \lambda_{10} \frac{\partial}{\partial \lambda_{10}} - \lambda_{11} \frac{\partial}{\partial \lambda_{11}})\chi. \end{aligned} \tag{4.24}$$

After Fourier transforming this equation we get an equation of motion for P

$$\begin{aligned}\left.\frac{\partial P}{\partial t}\right|_{ac} = {} & -N_z\Omega_c(1-e^{-\frac{1}{N_z}\left(\frac{\partial}{\partial\alpha_8}-\frac{\partial}{\partial\alpha_7}\right)})(\alpha_{10}+\alpha_4)P \\ & -\Omega_c e^{-\frac{1}{N_z}\left(\frac{\partial}{\partial\alpha_8}-\frac{\partial}{\partial\alpha_7}\right)}(\frac{\partial}{\partial\alpha_5}\alpha_3+\frac{\partial}{\partial\alpha_9}\alpha_{11})P \\ & -\Omega_c(\alpha_7-\alpha_8)(\frac{\partial}{\partial\alpha_4}+\frac{\partial}{\partial\alpha_{10}})P-\Omega_c(\frac{\partial}{\partial\alpha_3}\alpha_5+\frac{\partial}{\partial\alpha_{11}}\alpha_9)P \\ & -\frac{\Omega_c}{N_z}\frac{\partial}{\partial\alpha_4}(\frac{\partial}{\partial\alpha_3}\alpha_3+\frac{\partial}{\partial\alpha_4}\alpha_4-\frac{\partial}{\partial\alpha_5}\alpha_5)P \\ & +\frac{\Omega_c}{N_z}\frac{\partial}{\partial\alpha_{10}}(\frac{\partial}{\partial\alpha_9}\alpha_9-\frac{\partial}{\partial\alpha_{10}}\alpha_{10}-\frac{\partial}{\partial\alpha_{11}}\alpha_{11})P. \end{aligned} \tag{4.25}$$

Because of the exponential terms appearing on the first two lines, the equation is of infinite order in $\frac{1}{N_z}(\frac{\partial}{\partial\alpha_8}-\frac{\partial}{\partial\alpha_7})P$. It is then not a Fokker-Planck equation. To obtain a Fokker Planck equation, one needs to assume a large number of atoms in each slice δz compared to $(\frac{\partial}{\partial\alpha_8}-\frac{\partial}{\partial\alpha_7})P$. We then perform a series expansion of the exponential terms to second order in $1/N_z$. This approximation in fact linearises the problem as it assumes that the atomic population difference (in this case between states $|2\rangle$ and $|3\rangle$) does not vary much.

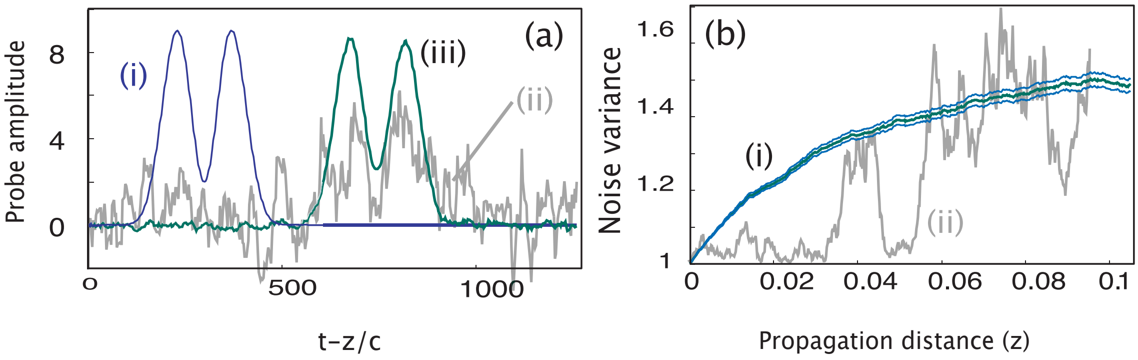

Figure 4.3: Results from the numerical simulations. (a) Expectation values of the amplitude quadrature at the input (i) and output (iii) of the EIT medium after 1000 trajectories in phase space. Trace (ii) is one trajectory showing the field at the output. (b)-(i) Variance of the amplitude quadrature at a frequency inside the EIT window, as a function of propagation depth. (ii), a single trajectory.

The same procedure is repeated for the remaining terms in the master equation (the probe-atom interaction, and all the Liouvillians) and a drift and a diffusion matrix D can be obtained. To get a set of stochastic differential equations we then solve for B in the equation $D = B^T B$ and finally obtain a set of nine complex-valued Itô stochastic partial differential equations (SPDE) describing the atomic dynamics. We found “a” solution for B that introduces 18 uncorrelated noise terms. The SPDE are given in Appendix C. The Stratonovitch corrections used in the numerical simulations are also listed in the appendix, but they are negligibly small compared to all the other variables and are not included in the simulations. The Maxwell equations for the probe c-numbers, in a moving frame at the speed of light, are

$$\frac{\partial}{\partial z}\alpha(z,t) = \frac{igN}{c}\sigma_3(z,t) \tag{4.26}$$

$$\frac{\partial}{\partial z}\beta(z,t) = \frac{igN}{c}\sigma_{11}(z,t), \tag{4.27}$$

where the c-numbers α and β represent the operators $\hat{\mathcal{E}}$ and $\hat{\mathcal{E}}^\dagger$, and σ_3, σ_{11} correspond to the atomic operators $\hat{\sigma}_{13}$, $\hat{\sigma}_{13}^\dagger$.

The evolution of α and β in space and time is computed when amplitude and phase modulations at a frequency 0.005γ are encoded onto a $50/\gamma$ long coherent input state; the envelope of the field then shows two cycles in both quadratures. We chose parameters realistic to atom optics experiments with ^{87}Rb atoms. The atomic density was chosen to be $10^{12}\,\mathrm{cm}^3$ with a total length of 12 cm, the control beam Rabi frequency to be 3γ and decoherence rates $\gamma_c = 0.005\gamma$ and $\gamma_0 = 0.001\gamma$. At these optical depths and control field power, faster modulation frequencies are absorbed significantly by the medium so we restrict ourselves to low sideband frequencies. We numerically evaluate the expectation values of the two quadrature operators $\langle \hat{X}^+(z,t)\rangle = \overline{\alpha(z,t)+\beta(z,t)}$ and $\langle \hat{X}^-(z,t)\rangle = -i\ (\overline{\alpha(z,t)-\beta(z,t)})$ and their noise spectra $S^\pm(\omega) = \frac{c}{L}\overline{X^\pm(z,\omega)X^\pm(z,-\omega)}$, where the averaging is done over a large number of trajectories in phase space. The noise floor $V^\pm(z,\omega)$ was obtained by turning off the signal on the probe. [1]

Numerical results

Fig. 4.3 shows the results of the numerical simulations. As shown in Fig. 4.3(a) a coherent state (i) is input the medium[2]. The noisy trace (ii) is the result of one trajectory in phase space at the output of the sample. After 1000 trajectories, the expectation value $\langle \hat{X}^\pm(z_{\mathrm{out}},t)\rangle$ is finally obtained with a negligible statistical error, as can be seen from the statistical standard deviation in trace (iii). We see that the input light state is delayed by more than its width and that its shape is well preserved, showing that EIT slowed the probe field down in the linearly dispersive regime.

To quantify the noise performance, we compute the noise variance as a function of propagation distance at a modulation sideband within the EIT window. The result is shown Fig. 4.3(b). The noisy trace (ii) is one trajectory in phase space and after 1000 trajectories we obtain trace (i). An exponential increase of the noise power is observed (the dashed lines are one standard deviation). This shows that, in this regime, EIT adds substantial noise to the output light field. This result is independent of the quadrature considered.

To understand these results, we now explore different parameter regimes. Fig. 4.4(a) and (c) show the evolution of the noise $V(z) = 1 + V_{\mathrm{noise}}(z)$ and the signal to noise ratio as a function of the depth of propagation in three different regimes[3]. We consider the following decoherence combinations, $(\gamma_0, \gamma_c) = (0, 0.005\gamma)$, corresponding to curves

---

[1] We solved these stochastic equations using the open source numerical package XMDS For these simulations, we used a cross propagation step, with a lattice size of 1000 for the time dimension and 500 points for the z dimension, and use an algorithm in the Semi-Implicit Interaction Picture (SIIP). These simulations were run using MPI (Multiple Parallel Interface) on 3 computers and a total of 10 CPUs. The computation time was then less than 1 hour for a total a 1000 trajectories in phase space.

[2] The input coherent state is a Dirac function in the positive P representation.

[3] The signal to noise ratio was defined by $\mathcal{R}^\pm(z) = 4(\alpha^\pm(z))^2/V^\pm(z)$ in chapter 2.

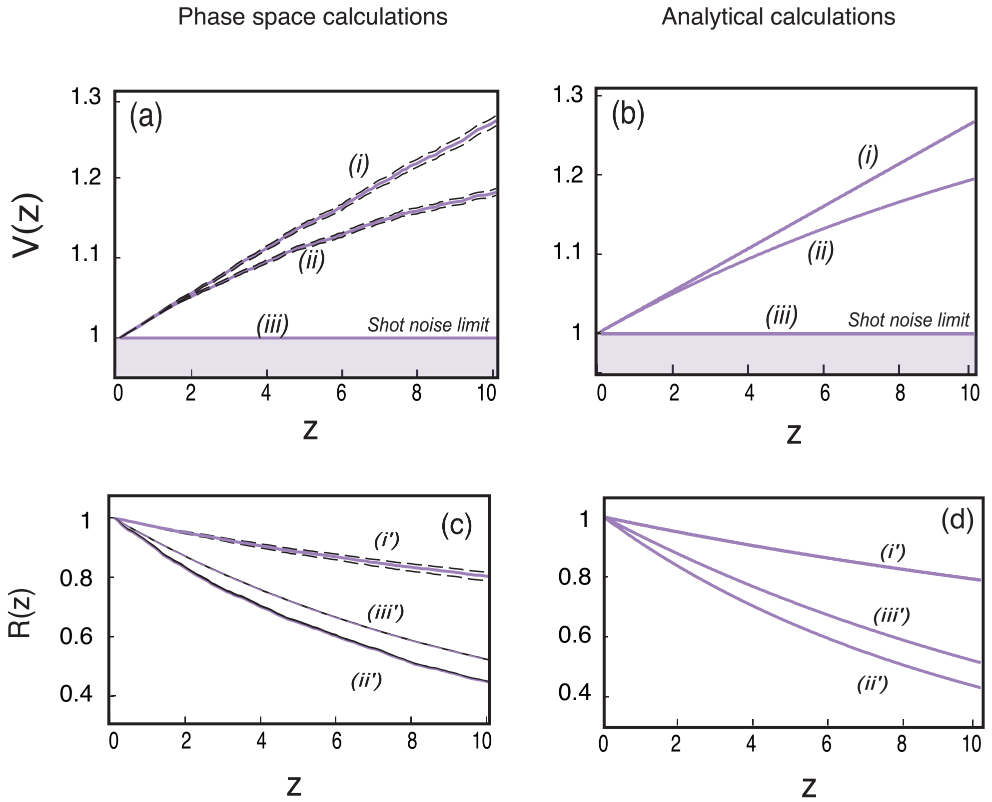

Figure 4.4: Signal to noise ratios and noise results for, (a) and (c) the numerical solutions, (b) and (d) the analytical solutions. (i) and (i') correspond to $\gamma_c = 0.005\gamma$ and $\gamma_0 = 0$; (ii) and (ii') to $\gamma_c = 0.005\gamma$ and $\gamma_0 = 0.005\gamma$ and (iii) and (iii') to $\gamma_0 = 0.005\gamma$ and $\gamma_c = 0$.

(i) and (i'); $(\gamma_0, \gamma_c) = (0.005\gamma, 0.005\gamma)$, curves (ii)-(ii') and $(\gamma_0, \gamma_c) = (0.005\gamma, 0)$, curves (iii)-(iii').

From these graphs, we found that γ_0 degrades the SNR but does not introduce excess noise to the output light field being delayed by the EIT medium (iii). Population shuffling, however, introduces large excess noise on the output field (as shown by traces (i) and (ii)). The interpretation of these results will now be done from analytical solutions derived in the Heisenberg picture.

4.2.2 Analytical treatment

In this section, we provide an explanation of the results found in the above phase space simulations. We first discuss the effects of decoherences on the losses and atomic noise introduced during the slow light propagation. We will show that excess noise can be understood as a preservation of the canonical commutation relations of the probe mode in the presence of phase-insensitive gain in the medium. We will quantify this by solving the Heisenberg-Langevin equations in the same approximate regime as in section 4.1.3, and compare it with the general theory of non-ideal phase insensitive amplifiers presented chapter 2.

Equations

From the interaction Hamiltonian Eq. (4.2), and following the same procedure as in chapter 1, we can obtain a set of Heisenberg-Langevin equations

$$\begin{aligned}
\dot{\hat{\sigma}}_{11} &= \gamma\hat{\sigma}_{33} + \gamma_c(\hat{\sigma}_{22} - \hat{\sigma}_{11}) - ig\hat{\mathcal{E}}\hat{\sigma}_{31} + ig^*\hat{\mathcal{E}}^\dagger\hat{\sigma}_{13} + \hat{F}_{11} \\
\dot{\hat{\sigma}}_{22} &= \gamma\hat{\sigma}_{33} + \gamma_c(\hat{\sigma}_{11} - \hat{\sigma}_{22}) - i\Omega_c\hat{\sigma}_{32} + i\Omega_c^*\hat{\sigma}_{23} + \hat{F}_{22} \\
\dot{\hat{\sigma}}_{13} &= -(\gamma + \gamma_0/2 + \gamma_c/2)\hat{\sigma}_{13} + ig\hat{\mathcal{E}}(\hat{\sigma}_{11} - \hat{\sigma}_{33}) + i\Omega_c\hat{\sigma}_{12} + \hat{F}_{13} \\
\dot{\hat{\sigma}}_{32} &= -(\gamma + \gamma_0/2 + \gamma_c/2)\hat{\sigma}_{32} + i\Omega_c^*(\hat{\sigma}_{33} - \hat{\sigma}_{22}) - i\ g^*\hat{\mathcal{E}}^\dagger\hat{\sigma}_{12} + \hat{F}_{32} \\
\dot{\hat{\sigma}}_{12} &= -(\gamma_0 + \gamma_c)\hat{\sigma}_{12} - ig\hat{\mathcal{E}}\hat{\sigma}_{32} + i\Omega_c^*\hat{\sigma}_{13} + \hat{F}_{12} \\
\frac{\partial}{\partial z}\hat{\mathcal{E}} &= \frac{igN}{c}\hat{\sigma}_{13}.
\end{aligned} \tag{4.28}$$

We have included the decays of the atomic dipole operators, and their associated Langevin noise operators $\hat{F}_{ij}$ describing the coupling of the atoms to vacuum modes of large reservoirs.

The non-zero Langevin correlations corresponding to the system of equations (4.28) are calculated using the Einstein generalized equations derived in the first chapter and the non-zero contributions are

$$\begin{aligned}
\langle\tilde{F}_{13}(z_1,\omega_1)\tilde{F}_{13}^\dagger(z_2,\omega_2)\rangle &= K((\gamma + \gamma_c + \gamma_0)\langle\hat{\sigma}_{33}\rangle + 2\gamma\langle\hat{\sigma}_{11}\rangle - \gamma_c\langle\hat{\sigma}_{11} - \hat{\sigma}_{22}\rangle) \\
\langle\tilde{F}_{13}^\dagger(z_1,\omega_1)\tilde{F}_{13}(z_2,\omega_2)\rangle &= K(2\gamma\langle\hat{\sigma}_{33}\rangle - 2(\gamma + \gamma_0 + \gamma_c)\langle\hat{\sigma}_{33}\rangle) \\
\langle\tilde{F}_{13}^\dagger(z_1,\omega_1)\tilde{F}_{12}(z_2,\omega_2)\rangle &= K(\gamma_c + \gamma_0)\langle\hat{\sigma}_{32}\rangle \\
\langle\tilde{F}_{12}^\dagger(z_1,\omega_1)\tilde{F}_{13}(z_2,\omega_2)\rangle &= K(\gamma_c + \gamma_0)\langle\hat{\sigma}_{23}\rangle \\
\langle\tilde{F}_{12}(z_1,\omega_1)\tilde{F}_{12}^\dagger(z_2,\omega_2)\rangle &= K((\gamma + \gamma_c + \gamma_0)\langle\hat{\sigma}_{33}\rangle + \gamma_c\langle\hat{\sigma}_{22} + \hat{\sigma}_{11}\rangle + 2\gamma_0\langle\sigma_{11}\rangle) \\
\langle\tilde{F}_{12}^\dagger(z_1,\omega_1)\tilde{F}_{12}(z_2,\omega_2)\rangle &= K(\gamma\langle\hat{\sigma}_{33}\rangle + \gamma_c\langle\hat{\sigma}_{22} + \hat{\sigma}_{11}\rangle + 2\gamma_0\langle\sigma_{22}\rangle),
\end{aligned} \tag{4.29}$$

where $K = \delta(z_1 - z_2)\delta(\omega_1 + \omega_2)/n\mathcal{A}$, n is the atomic density and $\mathcal{A}$ the cross sectional area of the beam in the medium. Using the steady state solutions listed in Eq. (4.16) (and so working in the same approximate regime) we can eliminate the second order terms in the probe field and negligible Langevin noise contributions.

Solutions

We will now calculate the evolution of the probe quantum field as it propagates through the medium. To simplify the equations, the fast-decaying atomic variables will be adiabatically eliminated ($1/T \ll \gamma$, where T is a characteristic timescale), making these equations valid over timescales larger than the spontaneous emission decay time[4], which is the regime of interest for EIT. The Maxwell equation for the field can be solved in the Fourier domain

---

[4] It was noticed in [Gorshkov et al., 2007a,b,c,d] that this adiabatic approximation is actually less severe even when ground state decoherence is taken into account. By solving the Maxwell equation for the probe field and substituting it back into the equation of motion for $\hat{\sigma}_{13}$ we find that $1/T \ll \gamma(1 + d)$ is in fact a sufficient condition.

to give

$$\begin{aligned}\hat{\mathcal{E}}(z,\omega) &= \hat{\mathcal{E}}(0,\omega)e^{-\Lambda(\omega)z} \\ -\frac{gN}{c} & \int_0^z \mathrm{d}s\; e^{-\Lambda(\omega)(z-s)}\frac{\omega - i\gamma_d}{\mu(\omega)}\hat{F}_{12}(s,\omega) \\ +\frac{gN}{c} & \int_0^z \mathrm{d}s\; e^{-\Lambda(\omega)(z-s)}\frac{i\Omega_c}{\mu(\omega)}\hat{F}_{13}(s,\omega), \end{aligned} \tag{4.30}$$

where $\mu(\omega) = \Omega_c^2 - i\omega(\gamma + \gamma_d/2)$; $\gamma_d = \gamma_0 + \gamma_c$ is the total decoherence rate and the susceptibility of the medium is given by

$$\Lambda(\omega) = \frac{g^2 N}{c}\frac{(\gamma_d - i\omega)\langle\hat{\sigma}_{11} - \hat{\sigma}_{33}\rangle - i\langle\hat{\sigma}_{32}\rangle\Omega_c}{\mu(\omega)}. \tag{4.31}$$

The first part of Equation (4.30) describes the absorption and phase shift of the probe propagating with a group velocity given by $v_g = -\omega/\Im(\Lambda(\omega))$ inside the EIT medium. The last two terms in Equation (4.30) correspond to atomic noise added to the field due to decoherence.

We now calculate the power spectrum of the output state as a function of the input state using Equation (4.30) and the Langevin correlations (4.29). First, we note that

$$2\Re(\Lambda(\omega)) = \frac{\Omega_c^2\langle[\hat{F}_{12},\hat{F}_{12}^\dagger]\rangle + \omega^2\langle[\hat{F}_{13},\hat{F}_{13}^\dagger]\rangle}{|\mu(\omega)|^2}, \tag{4.32}$$

which links the linear absorption $\Re(\Lambda(\omega))$ with the atomic noise, a direct consequence of the fluctuation dissipation theorem. This allows us to obtain

$$S^{\pm}(z,\omega) = \eta(z,\omega)\; S^{\pm}_{in}(\omega) + (1 - \eta(z,\omega))(1 + N_f), \tag{4.33}$$

where $\eta(z,\omega) = e^{-2\Re(\Lambda(\omega))z}$, and

$$\begin{aligned} N_f &= 2\frac{\Omega_c^2\langle\hat{F}_{12}^\dagger\hat{F}_{12}\rangle + \omega^2\langle\hat{F}_{13}^\dagger\hat{F}_{13}\rangle}{\Omega_c^2\langle[\hat{F}_{12},\hat{F}_{12}^\dagger]\rangle + \omega^2\langle[\hat{F}_{13},\hat{F}_{13}^\dagger]\rangle} \\ &= \frac{4\gamma_c\Omega_c^2}{2\gamma_0\Omega_c^2 + \omega^2(2\gamma + \gamma_0 - 3\gamma_c)}. \end{aligned} \tag{4.34}$$

We note that the noise power spectrum is phase independent, indicating that the response of the medium is the same for both quadratures of the field. As expected, the normally ordered Langevin correlations are responsible for excess noise on the output field. Using the notation defined chapter 2, we have $V^{\pm}_{\text{noise}}(z,\omega) = (1 - \eta(z,\omega))N_f$. When the normally ordered Langevin correlations are all zero, $N_f = 0$ so $V^{\pm}(z,\omega) = 1$. From the Langevin correlations (4.29), we see that $\langle\hat{F}_{13}^\dagger\hat{F}_{13}\rangle = 0$ to first order in γ_c/γ. This means that spontaneous emission does not contribute to the excess noise found in the phase space simulations. However, $\langle\hat{F}_{12}^\dagger\hat{F}_{12}\rangle = 4\gamma_c$ so the noise arises from the population shuffling terms.

Interpretation

In order to understand why population exchange between the ground states is responsible for noise, we will simplify the equations further and concentrate on sideband frequencies close to the carrier. We will then show that there is more than a similarity between Eq. (4.33) and Eq. (2.3) from chapter 2.

We first solve for the steady states with the shuffling terms $\gamma_c(\hat{\sigma}_{11}-\hat{\sigma}_{22})$ and $\gamma_c(\hat{\sigma}_{22}-\hat{\sigma}_{11})$ as the *only* source of ground state decoherence by removing the dephasing terms γ_c and γ_0 appearing in the equation of motion of $\hat{\sigma}_{12}$. We find a new solution for the atomic polarisation

$$\langle\hat{\sigma}_{13}\rangle = -\frac{i\gamma_c}{\Omega_c^2}\langle\hat{\mathcal{E}}\rangle, \tag{4.35}$$

and insert it into the Maxwell equation to obtain

$$\langle\hat{\mathcal{E}}(z)\rangle = \langle\hat{\mathcal{E}}_{\text{in}}\rangle e^{az} \quad \text{where} \quad a = \frac{gN}{c}\frac{\gamma_c}{\Omega_c^2}. \tag{4.36}$$

This expression corresponds to a population exchange driven *amplification* of the probe field inside the medium, the energy for which will be provided by the coupling beam, up to a limit set by Equation (4.19).

The shuffling term alone is, however, not physically realistic. As can be seen from the stochastic equations listed in the appendix and the Equations (4.28), the Liouvillian $\mathcal{L}^{coll}_{[1,2]}$ also includes an off diagonal ground state dephasing with mean rate γ_c giving an extra linear loss $\alpha_c = \frac{gN}{c}\frac{\gamma_c}{\Omega_c^2}$ similar to α_0. When solving for the steady state in this case, we find the net transmission close to zero frequency to be unity. The losses in fact exactly compensate for the gain, and the EIT medium no longer performs amplification. Even though the transmission that includes $\mathcal{L}^{coll}_{[1,2]}$ gives no net amplification, this underlying gain term results in excess noise on the output.

Using Eq. (4.34) close to $\omega = 0$ and for $\gamma_0 \neq 0$ we find the noise to be

$$V_{\text{noise}} = 2\frac{\gamma_c}{\gamma_0}(1-e^{(a-\alpha_0-\alpha_c)z}), \tag{4.37}$$

and for $\gamma_0 = 0$, $V_{\text{noise}} = 2az$. The presence of excess noise on the output field can be recognised from the theory of phase-insensitive quantum amplifiers presented chapter 2. In fact, Eq. (4.37) could have been found directly from Eq. (2.3) by replacing α by $\alpha_0+\alpha_c$ and (a,α) by their value in the EIT system, which validates this interpretation[5].

Comparison with the numerical treatment

Fig. 4.4(b) represents the evolution of the noise from this analytical model. This theory and the phase space model are in agreement. For curve (iii) there is no population exchange between the ground state and therefore the noise never exceeds the shot noise level. For curve (i), the noise increases linearly as predicted when $\gamma_0 = 0$, whereas for curve (ii), the noise increases exponentially according to Eq. (4.33).

Fig. 4.4(c) and Fig. 4.4(d) compare the signal to noise ratios results from the numerical and analytical approaches and a good agreement is found between them. Even though the excess noise power is larger for (i) than for (ii) and (iii), the signal transmission is 100 % with γ_c only, therefore the output signal to noise ratio is larger for (i') than for (ii') and (iii').

---

[5] We note that a similar expression was also found in the theory of two beam coupling presented in [Gaeta et al., 1992].

To conclude, we have shown both from a phase space method in the Schödinger picture and from an analytical treatment in the Heisenberg picture that continuous variable quantum states of light can be slowed down without excess noise using EIT if population exchange between the ground state is absent. In section 4.3.4, we will quantify the parameters required to surpass the no-cloning regime for light storage.

4.2.3 Noise coupling from control beam

Before coming to the modelling of light storage, we come back tho our original assumption that the control beam can be treated as a classical field. In all the above treatments, we have not considered the control field as an operator. It was assumed that it is sufficiently strong so that it is undepleted and that its noise contribution to the output probe mode can be negligible, which seems reasonable. It is interesting to investigate to what extent does this approximation still hold and study the regime where it breaks down. This study was in fact motivated by the measurements done in [Hsu, 2008] where it was shown that a non-shot noise limited control beam can couple noise to the output probe state. Intuitively, one can expect that temporal modulations of the control beam creates a time dependent transmission of the probe. The EIT width would oscillate, thereby increasing and decreasing periodically the transmission of the probe at sideband frequencies inside the EIT window. We will see how this naive picture compares with theory in this section. Also, studying the dynamics of the control field is important to understand light storage mechanisms.

Obtaining stochastic equations describing the problem when the two fields are quantized is not much more difficult than with a classical control field. New equations have been derived and simulated[6] when the probe is much weaker than the control, and have given the same results. This validates the approximation that the control beam can be treated a c-number in the weak probe regime. The situation is of course more interesting when the probe power is on the order of the control beam power. We have shown that when the probe was quantized one has to make sure the population variations are negligible. This was necessary to get a Fokker-Planck equation. The phase space simulations then break down when the probe or pump powers vary significantly through the medium, which is the case if we consider both beams to be large.

Progress towards non-linear solutions when the two beams have a comparable strength are being made [Martinelli et al., 2004, Sautenkov et al., 2005, Dantan et al., 2003, Barberis-Blostein and Zagury, 2004, Harris, 1993, Fleischhauer, 1994]. Even though linearized Heisenberg-Langevin equations are usually solved, a wealth of interesting phenomenon were still shown to arise in these regimes, which also motivated the present discussion. We will here study the transfer of classical noise from the control to the probe field and vice versa without including the quantum noise from the atoms. Contrary to in the earlier sections, we here have to keep all the population terms and the spatial dependence of the control field. We solve the problem analytically, using linearized equations and without decoherence affecting the ground states. We then give an interpretation of the predicted effects.

---

[6] No major corrections to the equation in the appendix arise, so we chose not to show the equations.

Linearized equations

The problem will be solved by linearizing the equation of motions, considering only small fluctuations around the mean values for all the operators. For instance, we may write $\hat{\Omega}_c = \langle\Omega_c\rangle + \delta\hat{\Omega}_c$ and perform a mean field approximation which allows one to Fourier transform the equations of motions. As an example, after neglecting second order terms, the Heisenberg equation (4.28) for the optical coherence $\hat{\sigma}_{13}$ yields

$$i\omega\delta\hat{\sigma}_{13} = -\gamma\delta\hat{\sigma}_{13} + ig\delta\hat{\mathcal{E}}(\langle\hat{\sigma}_{11}\rangle - \langle\hat{\sigma}_{33}\rangle) + ig\langle\hat{\mathcal{E}}\rangle(\delta\hat{\sigma}_{11} - \delta\hat{\sigma}_{33})) + i\delta\Omega_c\langle\hat{\sigma}_{12}\rangle + i\langle\Omega_c\rangle\delta\hat{\sigma}_{12}. \quad (4.38)$$

We also have for the steady states $0 = -\gamma\langle\hat{\sigma}_{13}\rangle + \langle\hat{\mathcal{E}}\rangle(\langle\hat{\sigma}_{11}\rangle - \langle\hat{\sigma}_{33}\rangle) + i\langle\Omega_c\rangle\langle\hat{\sigma}_{12}\rangle$. We follow the same procedure for all the Pauli operators and get a matrix relation between the fluctuating atomic operators and the optical fields.

Solving for the atomic steady states first, we find

$$\langle\hat{\sigma}_{11}\rangle = \frac{\Omega_c^2}{\Omega_p^2 + \Omega_c^2}, \langle\hat{\sigma}_{22}\rangle = \frac{\Omega_p^2}{\Omega_p^2 + \Omega_c^2}, \langle\hat{\sigma}_{12}\rangle = \frac{-\Omega_p\Omega_c^*}{\Omega_p^2 + \Omega_c^2}, \langle\hat{\sigma}_{23}\rangle = \langle\hat{\sigma}_{13}\rangle = 0. \quad (4.39)$$

We note that population is exchanged between the two ground states due to optical pumping from both beams. Two steady state optical coherences are also zero so the two fields are never absorbed by the medium and $\Omega_{p,c}(z) = \Omega_{p,c}$. The reason is because the ground state coherence never decays here. A perfect interference between the two excitation pathways occurs which allows lossless propagation of the two fields and a coherent population exchange bewteen the ground states.

We also obtain an expression for the optical polarisations $\delta\hat{\sigma}_{13}$, and $\delta\hat{\sigma}_{23}$ as a function of the probe and control beam powers

$$\begin{bmatrix} \delta\hat{\sigma}_{13}(z) \\ \delta\hat{\sigma}_{23}(z) \end{bmatrix} = F(\omega) \begin{bmatrix} \langle\sigma_{11}\rangle & \langle\sigma_{12}\rangle \\ \langle\sigma_{21}\rangle & \langle\sigma_{22}\rangle \end{bmatrix} \begin{bmatrix} \delta\Omega_p(z) \\ \delta\Omega_c(z) \end{bmatrix}, \quad (4.40)$$

where

$$F(\omega) = \frac{-i\omega}{(\Omega_p^2 + \Omega_c^2 - \omega(\omega + i\gamma))}. \quad (4.41)$$

The Maxwell equations for the fluctuating part of the control and probe field are then easily found. Integrating over z, we have

$$\begin{bmatrix} \delta\Omega_p(z) \\ \delta\Omega_c(z) \end{bmatrix} = \begin{bmatrix} \sigma_{11}e^{k_s(\omega)z} + \sigma_{22}e^{k_f(\omega)z} & \sigma_{12}(e^{k_s(\omega)z} - e^{k_f(\omega)z}) \\ -\sigma_{12}(e^{k_s(\omega)z} - e^{k_f(\omega)z}) & \sigma_{22}e^{k_s(\omega)z} + \sigma_{11}e^{k_f(\omega)z} \end{bmatrix} \begin{bmatrix} \delta\Omega_p(0) \\ \delta\Omega_c(0) \end{bmatrix}, \quad (4.42)$$

where $k_s(\omega) = (g^2N/c)F(\omega)$ and $k_f = 0$, representing the EIT and free space susceptibilities (in a moving frame at the speed of light) respectively.

First of all, we note that no phase sensitivity is present in this system of equations, therefore the response is identical for both quadratures of the fields. We note that in the weak probe limit ($\langle\sigma_{11}\rangle = 1$, $\langle\sigma_{22}\rangle = 0$) we recover the earlier results where the probe propagates without loss at a small group velocity given by $-\omega/\Im(k_s(\omega)) = \frac{\Omega_c^2 L}{\gamma d}$ and the control propagates at the speed of light. No noise transfer between the two beam happens in this regime. Another interesting limit is when the two beams have the same power. In this situation, the ground state coherence is maximal ($\langle\sigma_{12}\rangle = -1/2$) and the transfer from one beam to the other extremely efficient as can be seen Eq. (4.42). Both the probe and the control beams are in a superposition between a slow and a fast wave. As noted in [Barberis-Blostein and Bienert, 2007], the variance of the beam fluctuations in the medium, follows an oscillatory behavior. We found the same result here and interpret these oscillations as the result of a beating between the slow and fast waves in each transition.

Interpretation

There are several possible interpretations for such a transfer of fluctuations. To understand what is happening, it is instructive to introduce the degree of coherence. The degree of coherence g between two arbitrary waves a and b is defined as

$$g = \frac{\langle ab^* \rangle}{\sqrt{\langle |a|^2 \rangle \langle |b|^2 \rangle}}. \tag{4.43}$$

This quantity is 1 when the two waves are coherent, that is when their phase relation is fixed. This can easily be transposed to two oscillating atomic dipoles such as $\hat{\sigma}_{13}$ and $\hat{\sigma}_{23}$ created by the probe and control fields in the three-level system. We find that

$$g = \frac{\langle \hat{\sigma}_{13} \hat{\sigma}_{23}^\dagger \rangle}{\sqrt{\langle \hat{\sigma}_{13}^\dagger \hat{\sigma}_{13} \rangle \langle \hat{\sigma}_{23}^\dagger \hat{\sigma}_{23} \rangle}} = \frac{\langle \hat{\sigma}_{12} \rangle}{\sqrt{\langle \hat{\sigma}_{11} \rangle \langle \hat{\sigma}_{22} \rangle}} = 1. \tag{4.44}$$

Where we used the commutation relations between the Pauli operators and the steady state results from Eq. (4.39). The EIT medium always adjusts to create a perfect coherence between the two atomic dipoles independent of the two beam powers, (and in the absence of ground state decoherence). The interference between the two excitation pathways in the Λ system leads to a ground state coherence that automatically compensates for any phase difference between the beams in the medium. When the probe is weak (the product $\langle \hat{\sigma}_{11} \rangle \langle \hat{\sigma}_{22} \rangle$ is small), the degree of coherence g remains maximal when the ground state coherence is small. There is then no transfer of fluctuations between the pump and the probe. When the two beams have equal powers, then $\sqrt{\langle \hat{\sigma}_{11} \rangle \langle \hat{\sigma}_{22} \rangle} = 1/2$, a large ground state coherence is then created to maintain a large g. This enables a strong transfer of fluctuation between the two beams resulting in an ideal correlation between them. This was recognized in [Harris, 1993] where EIT was shown to allow pulse matching between two light fields.

Conclusion

Important for quantum information purposes, we found that only when the probe power is non-negligible can the control beam noise couple efficiently to the probe beam. With a dim probe beam, or vacuum squeezed light, a non-shot noise limited control beam is not a problem (to first order in the linearized approach).

Coming back to our original asumption, where we supposed that when the transparency window varies due to the control beam fluctuations at a frequency ω_m, a large transfer should happen to the probe and signals should appear at $\omega \pm \omega_m$ for all ω's within the transparency window. This picture would in fact be described by second order terms in the mean field approximation, where the modulation at ω_m of the amplitude of the control field at a sideband ω creates two other sidebands at $\omega \pm \omega_m$ on the probe and is therefore a rather small effect. We studied here the first order effect describing the transfer of fluctuations at the same frequency ω_m.

The above linearized treatment allows one to get a simple expression relating the fluctuations of the pump with the fluctuations of the probe and vice versa. In the presence of decoherence however, the steady state fields are absorbed and an analytical solution cannot be found. This is one feature that differs from the measurement performed in [Hsu, 2008]. Another difference is the absence of oscillations in the experiment, that the theory predicts. Last the quadrature asymmetry is not predicted by the present theory and clearly observed in the experiment. Including various decoherence mechanisms in numerical simulations and performing the experiment in a buffer gas cell might yield agreement between the two results.

4.3 Quantum theory of light storage and retrieval

We identified sources of noise in slow light propagation using EIT. To what extent will this noise influence light storage ? We will give the answer to this question in this section and find the regimes where the EIT quantum memory performs better than any classical strategy.

We will consider here the simultaneous storage of both quadratures of the probe when amplitude and phase modulations are encoded within the EIT bandwidth in the case where the coupling beam is switched off and on abruptly. Provided the modulation frequency is larger than the Fourier width $\Delta\omega$ of the pulse, classical information is encoded onto its sideband ω at the shot noise limit.

We present numerically and analytically, a calculation of the degradation of the signal and added noise during the storage process in the presence of decoherence mechanisms. Specifically, we consider dephasing affecting the ground state coherence and also allowing an exchange of population between the two ground states. In the first subsection, we describe the initial proposed description of light storage in terms of *polaritonic* excitations and analyze its merit and limitations. Then, we identify the parameters where EIT performs better than the classical and no-cloning limits using stochastic simulations. Finally, we propose an analytical theory for light storage. Our theory is valid when the probe is compressed inside the medium before the switching of the control beam. It allows one to compute the time-bandwidth product and the efficiency of the memory in the presence of decoherence affecting the ground states and also population reshuffling.

The storage process can be understood as follows. The coupling beam prepares the atoms initially in the Zeeman state $|1\rangle$ through optical pumping and is kept on. The weak probe propagates in the medium and coherences are created between the two ground states of the atoms. These coherences acquire the sideband information of the probe pulse during its spatial compression inside the medium. After the compression, most of the probe field energy has been transferred to the coupling beam and left the cell at the speed of light. At this point in time, the atoms possess the information of the probe within the transparency window. When the coupling beam is turned off, the remaining energy in the probe field leaves the medium without affecting the information stored. The information will be saved provided the readout is performed before the decoherence processes have affected the atomic state. When the coupling beam is switched back on, the probe beam is regenerated with the supply of photons from the coupling beam and leaves the medium while reading the spin state of the atoms. The main constraints for these processes, are that the signal has to be encoded at frequencies within the transparency window and that the compressed pulse has to fit the size of the atomic sample. When these criteria are satisfied, the efficiency of this process is close to unity [Fleischhauer and Lukin, 2000]. The switching of the coupling beam can be done adiabatically or abruptly if the pulse is totally compressed within the medium [Matsko et al., 2001b, Zibrov and Novikova, 2005, Liu et al., 2001] but recent theoretical work shows that the way the coupling beam is shaped in time enhances the efficiency when the optical depth is limited [Gorshkov et al., 2007a,b,c,d].

4.3.1 Polariton approach

The Polariton theory was proposed by Fleischauer and Lukin [Fleischhauer and Lukin, 2000] and follows the discovery of the EIT normal modes by Steve Harris [Harris, 1994]. It was found that even when the control beam is kept time-dependent there exists a basis where a coherent superposition between light and matter obeys bosonic commutation properties, a *polariton.* This picture gives a elegant insight on the light storage mechanism. We will present it in this subsection.

In the theory presented here, we will ignore Langevin noise terms. This is justified when only ground state dephasing is considered, as we saw that it solely gives vacuum noise in the weak probe regime. When population shuffling is introduced, we have shown how the noise scaled with the different parameters of the system when the control beam is constant. The only thing we have to be careful about here, is whether the time variation of the control beam changes populations significantly so that the noise evolves. For simplicity we assume the decoherence rate that effects the populations to be negligible. We will present calculations including γ_c in the next sections.

The time dependence of the control beam $\Omega_c(t)$ has to be kept all along the calculations. In the weak probe approximation, we can rewrite equations (4.28) and get

$$\begin{aligned} (\frac{\partial}{\partial t}+\gamma)\frac{1}{\Omega_c^*(t)}(\frac{\partial}{\partial t}+\gamma_0)\hat{\sigma}_{12}+g\hat{\mathcal{E}} &= -\Omega_c(t)\hat{\sigma}_{12} \\ (\frac{\partial}{\partial t}+c\frac{\partial}{\partial z})\hat{\mathcal{E}} &= \frac{g^*N}{\Omega_c^*}(\frac{\partial}{\partial t}+\gamma_0)\hat{\sigma}_{12}. \end{aligned} \tag{4.45}$$

In order to solve this system of equations one can introduce *dark* and *bright* polariton operators as follows

$$\begin{aligned} \hat{\Psi}(t) &= \cos\theta\hat{\mathcal{E}}-\sin\theta\sqrt{N}\hat{\sigma}_{12} \\ \hat{\Phi}(t) &= \sin\theta\hat{\mathcal{E}}+\cos\theta\sqrt{N}\hat{\sigma}_{12}, \end{aligned} \tag{4.46}$$

where θ is a mixing angle defined by

$$\tan\theta=\frac{g\sqrt{N}}{\Omega_c(t)}. \tag{4.47}$$

When Ω_c is large, $\theta=0$ and we see from Eq.(4.46) that the polariton is mainly photonic. When Ω_c is zero, $\theta=\pi/2$ and the polariton is mainly atomic[7]. The transfer from light to atom can in fact be done efficiently and reversibly provided the reduction of the control field is done smoothly, as we will show. Substituting the expressions Eq.(4.46) in Eq.

---

[7] This result can also be found from a Schödinger approach using a Dicke basis. The interaction was shown to have a family of dressed eigenstates with zero adiabatic eigenvalue, the so called dark-states [Fleischhauer and Lukin, 2000] that we presented in the semi-classical treatment of this chapter.

(4.45) we reach

$$\Big(\frac{\partial}{\partial t} + c\,\cos^2\theta\frac{\partial}{\partial z} + \gamma_0\,\sin^2\theta\Big)\hat{\Psi}(t) \;=\; \big(\gamma_0\cos\theta\sin\theta - \dot{\theta}\big)\hat{\Phi} - c\,\cos\theta\sin\theta\frac{\partial\hat{\Phi}}{\partial z}, \quad (4.48)$$

and

$$\dot{\hat{\Phi}} \;=\; \frac{\sin\theta}{g^2N}\big(\frac{\partial}{\partial t} + \gamma\big)\tan\theta\big(\frac{\partial}{\partial t} + \gamma_0\big)(-\hat{\Phi}\cos\theta + \hat{\Psi}\sin\theta). \quad (4.49)$$

Let us assume that γ_0 is now negligible. Let us also assume a slow variation of the control beam amplitude. To the lowest order in g^2N/T we then perform the adiabatic elimination discussed section 4.1.1, which simplifies the equations considerably. We obtain

$$\Big(\frac{\partial}{\partial t} + c\,\cos^2\theta\frac{\partial}{\partial z}\Big)\hat{\Psi}(t) \;=\; 0 \quad (4.50)$$

$$\hat{\Phi}(t) \;=\; 0. \quad (4.51)$$

The bright state polariton $\hat{\Phi}$ is then not populated and the dark state polariton $\hat{\Psi}(t)$ evolves at a velocity $c\cos^2\theta$ without losses. By turning the control beam strength down, the information on the probe can be mapped onto the ground state coherence and retrieved at any time by turning the control beam back on. In this process, the polariton slows down, becomes atomic, and picks up speed again while being more and more photonic.

Non-adiabatic corrections can also be calculated. They give an extra spectral narrowing of the probe, which results in a pulse matching of the probe and control[8]. The non-adiabatic corrections also yield a non ideal transfer of information from the probe to the atoms when the optical depth is too small.

In the presence of γ_0, things are not so simple and care have to be taken with the adiabatic approximation. When keeping γ_0 and performing the adiabatic elimination of the control field variations, we obtain

$$\Big(\frac{\partial}{\partial t} + c\,\cos^2\theta\frac{\partial}{\partial z} + \gamma_0\,\sin^2\theta\Big)\hat{\Psi}(t) \;=\; \gamma_0\cos\theta\sin\theta\hat{\Phi} - c\,\cos\theta\sin\theta\frac{\partial\hat{\Phi}}{\partial z} \quad (4.52)$$

and

$$\big(\frac{\partial}{\partial t} + \frac{g^2N}{\gamma_0\sin^3\theta}\big)\hat{\Phi} \;=\; -\tan\theta\frac{\partial}{\partial t}\hat{\Psi}(t). \quad (4.53)$$

The spatiotemporal evolution of the dark and bright states is not so simple to solve analytically anymore.

We therefore chose to solve the full set of stochastic differential equations without any approximations, including γ_0 and γ_c, finite optical depths and a rapid switching of the control field. This is presented in the next section. It was in fact found in [Matsko et al., 2001b] that the adiabatic switching of the control field is not required when the pulse is already inside the medium. This discovery also allows analytic solutions to be found in this regime and provides another insight on the storage mechanism. An analytical solution in the presence of decoherence, and finite optical depth will be presented in section 4.3.3, in this fast switching regime. This derivation of the light storage theory allows us to derive boundaries close to the actual experimental situations. We will for example find

---

[8] This is the same result as the one found in the section 4.2.3 in the Fourier domain.

the time-bandwidth product of EIT, that is the largest number of orthogonal frequency modes that can be stored efficiently, in the presence of decoherence.

4.3.2 Stochastic Simulations

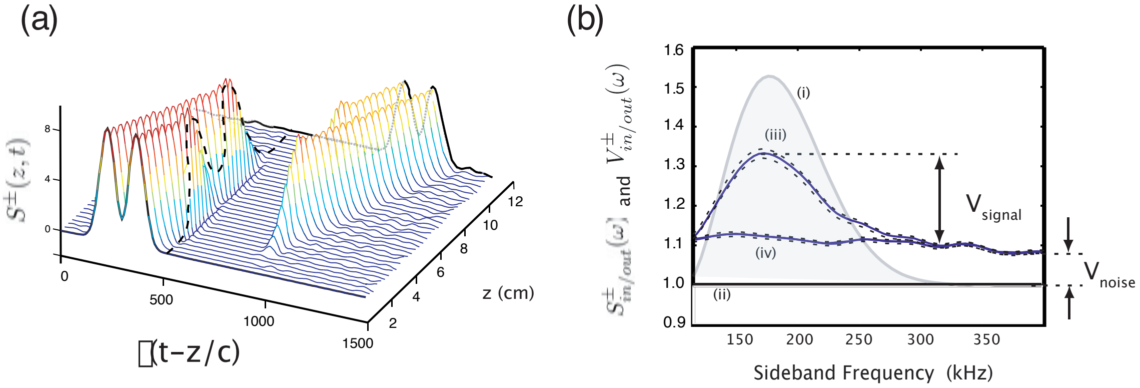

Figure 4.5: Phase space numerical simulations of quantum information storage using EIT. Amplitude and phase modulations are applied to the pulse. The decoherence rates are $\gamma_0 = 250$ Hz, $\gamma_c = 100$ Hz. a) 3D graph showing the storage of the probe amplitude quadrature on a time-space grid. b) Variances of the input/output fields for the amplitude and phase quadratures, with 1 corresponding to the quantum noise limit. (i)-(iii) is the power spectrum of the input/output state and (ii)-(iv) are the noise floor of the input/output state. The dashed lines corresponds to statistical standard deviations. These simulations are the average of 2000 trajectories.

We here present the result of stochastic numerical simulations when the control beam is switched off when the probe is completely inside the medium. We include a finite optical depth and also the (γ_0, γ_c) decoherence mechanisms.

Fig. 4.5 shows the results of this simulation where two quadratures of the multimode field have been stored including the atomic noise. For these particular simulations, we chose a dephasing rate $\gamma_0 = 250$ Hz and an inelastic scattering rate $\gamma_c = 100$ Hz. The stochastic simulations were averaged over 2000 trajectories here.

Fig. 4.5 (a) shows the time and space storage and read-out of the amplitude quadrature of the modulated pulse through the EIT system. The results are identical for the phase quadrature and are not shown. We can see that the EIT-memory preserves the shape of the signal with minimal distortion. To better quantify this we plot the power spectrum of the input and output fields in Fig. 4.5 (b). The asymmetry in the transmission reveals a frequency-dependent absorption of the pulse as it propagates through the system, characteristic of the EIT Lorentzian transmission window. For these simulations, 60 % of the classical signal is absorbed and extra noise is added to the field. Using the previously defined notation, the transmission $\eta^{\pm}(\omega) = 0.40$ and the excess noise $V^{\pm}_{\text{noise}}(\omega) = 0.12$. When turning off the population shuffling γ_c, the excess noise is negligible. We conclude that no excess noise is introduced by turning off the control field.

The results show that switching off the control beam can map the probe information onto the atoms and be retrieved at a later time, even when decoherences are taken into account. The result suggests that the storage process is linear and efficient in this regime. To get a deeper insight on the mapping and retrieval of the probe quantum state, we now propose a description of the complete light storage mechanism from an analytical point of view.

4.3.3 Sequential theory

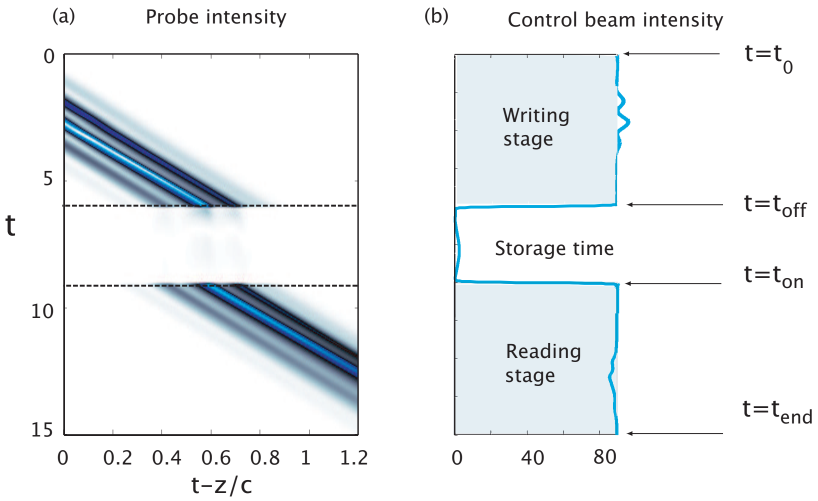

Figure 4.6: Storage and retrieval of a modulated probe beam using EIT with the control beam switched off abruptly. (a) Probe field intensity on a space time grid. (b) time dependence of the control field at the output of the sample. The small oscillations during the writing and reading stages in (b) correspond to the probe energy being coherently borrowed and given to the control field.

In this section, we present an analytical model of the light storage protocol. Our treatment describes the transfer of information from the modulation sidebands of the probe beam to the atomic coherences in the sample and vice versa, taking into account the decoherence effects γ_0 and γ_c, and the finite optical depth. We describe the mapping and readout of the information encoded on the probe, derive boundaries for optimum storage, and quantify the maximum information that can be stored in this system. We will again consider fast switching and symmetric conditions for the writing and retrieval. Information delay can then be seen as light storage where the coupling beam has been switched off and back on immediately afterwards[9]. It is clear that during the writing and reading stages, the noise can be obtained from the previous delay study. We can therefore ignore the Langevin operators at these stages and add the noise corresponding to population shuffling at the very end. However some care will have to be taken to describe what happens after the switching of the control beam, since, as opposed to information delay, some photons will leak through the medium.

The storage process is treated in three steps. To picture the sequence, Fig. 4.6 shows numerical simulations of the control field and probe variations during the storage process. We also included the space dependence of the control field to let the exchange of energy between the two fields appear. First, we describe the mapping of a pulse of duration T

---

[9] This is true provided the sudden switching of the control beam does not degrade the efficiency or introduce extra-noise

on the atomic coherences in momentum space, the *writing stage*. The second step, the *storage time* discusses the influence of the decoherences when the coupling beam is off. To show that no noise is introduced by the switching of the coupling beam, the Langevin operators will be retained for this time interval. The last step, the *reading stage*, is the mapping of the information stored in momentum space back to a probe field.

We model the relaxation between the ground states with the decoherence terms γ_0 and γ_c introduced previously, in the same regime (adiabatic elimination of the probe polarisation dynamics, and efficient pumping into the dark state). Similarly to [Matsko et al., 2001b], to first order in $\hat{\mathcal{E}}$, two coupled linear equations can be derived and are given by

$$\begin{aligned}(\frac{\partial}{\partial z} + d'/L)\ \hat{\mathcal{E}}(z,t) &= \chi\ \hat{\sigma}_{12}(z,t) &(4.54)\\ (\frac{\partial}{\partial t} + \Gamma_p)\ \hat{\sigma}_{12}(z,t) &= \nu\ \hat{\mathcal{E}}(z,t), &(4.55)\end{aligned}$$

where we introduced the quantities

$$\Gamma_p \;=\; \gamma_d + \frac{\Omega_c^2}{(\gamma+\gamma_d/2)}\ ;\ d' = d\frac{\gamma\langle\hat{\sigma}_{11}-\hat{\sigma}_{33}\rangle}{\gamma+\gamma_d/2}. \tag{4.56}$$

Γ_p describes the pumping rate of photons from the coupling beam (defining the EIT bandwidth) and d' the optical depth seen by the probe without coupling beam and in the presence of population shuffling. To simplify the notation we also defined

$$\chi \;=\; -\frac{gN}{c}\frac{\Omega_c}{\gamma+\gamma_d/2}\ ;\ \nu = -ig\langle\hat{\sigma}_{32}\rangle - \frac{g\Omega_c\langle\hat{\sigma}_{11}-\hat{\sigma}_{33}\rangle}{\gamma+\gamma_d/2}. \tag{4.57}$$

As equations 4.54 and 4.55 are linear, we can treat the atomic and field variables as c-numbers.

(a) Writing stage : from t_0 to t_{off}

We introduce the *collective ground state coherence* as the Fourier transform in space of the locally averaged ground state coherence operator $\sigma_{12}(z,t)$,

$$\sigma_{12}(k,t) = \frac{1}{L}\int_0^L \sigma_{12}(z,t)e^{ikz}dz. \tag{4.58}$$

During the writing stage, the state of the probe at each point in space can be found using Eqs. (4.54) and (4.55) in the frequency domain. The result is then found identical to the deterministic part of Equation (4.30), as expected. We then obtain the mapping of the field in ω space to the coherences in momentum space when integrating Eq. (4.55). We consider the memory to work in the linearly dispersive regime, i.e. the differential phase shift seen by all the spectral components of the field is the same. This allows us to change variables from ω_0 to k_0v_g when integrating Eq. (4.55) and get

$$\sigma_{12}(k,t) \;=\; \int dk_0\mathcal{E}_{in}((k_0-k)v_g)\mathcal{D}_W(k_0,t) \tag{4.59}$$

where $\mathcal{D}_W$ is a transfer function quantifying the losses due to the finite EIT bandwidth, and the finite length of the cell. It is given by

$$\mathcal{D}_W(k_0,t) \quad = \quad \frac{\nu v_g}{\Delta\omega}\Big(\frac{e^{(ik_0-\zeta((k-k_0)v_g))L}-1}{ik_0L-\zeta((k-k_0)v_g)L}\Big)\Big(\frac{e^{(\Gamma_p-i(k-k_0)v_g)t}-1}{\Gamma_p-i(k-k_0)v_g}\Big), \tag{4.60}$$

where $\zeta(\omega)=\Re(\Lambda(\omega))$. The integration of Eq. (4.59) is performed between $k-\Delta\omega/(2v_g)$ and $k+\Delta\omega/(2v_g)$ where $\Delta\omega=1/T$. Eq. 4.59 describes the transfer of information from the probe to the atoms.

We now require the frequency where the information is encoded to be smaller than the pumping rate Γ_p. This condition ensures a high efficiency of the writing process as we will see. In this regime Eq. (4.59) reduces to

$$\sigma_{12}(k,t) \quad = \quad \frac{\nu v_g}{\Delta\omega\Gamma_p}(1-e^{-\Gamma_p t})\int dk_0\mathcal{E}_{in}((k_0-k)v_g)\mathrm{sinc}(\frac{\mathrm{k_0L}}{2}). \tag{4.61}$$

This equation describes a down-sampling of the information from the probe field to the atoms due to a finite optical depth. The information is loaded at a rate Γ_p onto the collective ground state coherences. This process is much faster than the time it takes for the pulse to enter the sample (which is on the order of T). When Fourier transforming back to the spatial coordinate at a time $t_{\rm off}\simeq T$, we get an expression in the form of a convolution

$$\sigma_{12}^{t_{\rm off}}(z) \quad = \quad \frac{\nu}{\Gamma_p}\mathrm{sinc}(\Delta kz)*\big[H(L)\mathcal{E}_{\rm in}(-z/v_g)\big], \tag{4.62}$$

where $H(L)$ is a top hat function defining the atomic sample boundaries. For the probe pulse to fit the atomic sample we then require the duration of the pulse to satisfy the relation $T\ll L/v_g$. In this case and Eq. (4.62) can be written

$$\sigma_{12}^{t_{\rm off}}(z)=\frac{\nu}{\Gamma_p}\mathcal{E}_{\rm in}(-z/v_g). \tag{4.63}$$

The statistics of the probe field is then distributed in space onto the atomic ground states as it propagates through the medium, and most of its energy transferred to the coupling beam.

(b) Storage time : from $t_{\rm off}$ to $t_{\rm on}$

The coupling beam will be switched off at $t=t_{\rm off}$ and switched back on at a time $t=t_{\rm on}$. The evolution of the atomic coherence and of the remaining probe field inside the medium will here be solved during this interval.

Because Equation (4.19) does not hold in this regime, we now have to consider the spatial dependence of the control beam. Even though it is not input to the system, it might be generated due to ground state coherence and then affect it. From the general ground state coherence equation of motion in Eq. (4.28), and the Maxwell equations of the two fields we get

$$(\frac{\partial}{\partial t}+\gamma_d)\hat{\sigma}_{12}(z,t)=\frac{c}{gN}\frac{\partial}{\partial z}(\hat{\mathcal{E}}(z,t)\Omega_c(z,t))+\hat{F}_{12}(z,t). \tag{4.64}$$

As the control beam will be at most on the order of $g\hat{\mathcal{E}}$ after the switching (energy conservation), the first term on the right-hand side is on the order of $g^2\hat{\mathcal{E}}^2/\gamma d$. The effect of those extra photons leaking outside the medium on the ground state coherence is therefore negligible and the writing efficiency of the classical information will not be affected by the switching. This also means that the populations will not change after the switching. This small leakage of photons can be seen in Fig. 4.6.

The Langevin correlations $\langle\hat{F}_{12}(z,t)\hat{F}_{12}^{\dagger}(z,t)\rangle$ and $\langle\hat{F}_{12}^{\dagger}(z,t)\hat{F}_{12}(z,t)\rangle$ only depend on the populations so their value will not differ significantly from the writing and reading stage. Again, the excess noise can be calculated from the previous delay study. After neglecting those two terms we obtain

$$\sigma_{12}^{t_{\rm on}}(z) \quad = \quad e^{-\gamma_d(t_{\rm on}-t_{\rm off})}\sigma_{12}^{t_{\rm off}}(z), \tag{4.65}$$

which describes a simple exponential decay of the coherences over time due to a non-zero dephasing rate γ_d.

(c) Reading stage : from $t_{\rm on}$ to t_{end}

To describe the reading stage, we evaluate the coherences in the presence of a field on the probe transition in momentum space. We first solve for $\sigma_{12}(k,t)$ independently of the probe field by combining Eq. (4.54) and Eq. (4.55). We obtain

$$\sigma_{12}(k,t) = e^{-\beta(k)t}\sigma_{12}^{t_{on}}(k) \tag{4.66}$$

where

$$\beta(k) = \Gamma_p - \frac{\nu\chi}{d/L - ik}. \tag{4.67}$$

We will follow the same procedure as in the writing stage. The Maxwell equation (4.54) is solved in ω space to give

$$\mathcal{E}(z,\omega) \quad = \quad \int dk_0\ \sigma_{12}^{t_{\rm on}}(\frac{\omega-\omega_0}{v_g})\mathcal{D}_R(z,\omega_0), \tag{4.68}$$

where $\mathcal{D}_R$ is a transfer function now affecting the transfer from the atomic coherences to the field and is given by

$$\mathcal{D}_R(z,\omega_0) \quad = \quad \frac{\chi}{\Delta k v_g}\Big(\frac{e^{(i\omega_0-\zeta'(\frac{\omega-\omega_0}{v_g}))t}-1}{(i\omega_0 T-\zeta'(\frac{\omega-\omega_0}{v_g}))T}\Big)\Big(\frac{e^{(d'/L-i\frac{\omega-\omega_0}{v_g})z}-1}{d'-i\frac{\omega-\omega_0}{v_g}L}\Big), \tag{4.69}$$

where $\zeta'(.) = \Re(\beta(.))$. The integration of Eq. (4.68) is performed between $\omega - v_g\Delta k/2$ and $\omega + v_g\Delta k/2$. Under the same conditions as for the writing stage (large enough pumping rate Γ_p), we obtain

$$\mathcal{E}(z,\omega) \quad = \quad \frac{\chi L}{v_g\Delta k d'}(1-e^{-d'z/L})\int dk_0\sigma_{12}^{t_{\rm on}}(\frac{\omega-\omega_0}{v_g})\,\mathrm{sinc}(\frac{\omega_0 T}{2}). \tag{4.70}$$

We can again transform this expression in time and space to obtain a relation between the field and the atoms at the output of the sample given by

$$\mathcal{E}_{\rm out}(t) \quad = \quad \frac{\chi L}{d'}\mathrm{sinc}(\Delta\omega t) * \big[H(T)\sigma_{12}^{t_{on}}(-v_g t)\big]. \tag{4.71}$$

The down-sampling also occurs when the information is transferred from the ground state coherences to the probe due to the finite optical depth. This expression can be simplified further in the case where the retrieved probe fits entirely within the atomic sample, i.e. when the duration of the pulse T satisfies the relation $T \ll L/v_g$. There is then no loss of information and Eq. (4.71) can be written

$$\mathcal{E}_{\rm out}(t) \;\; = \;\; \frac{\chi L}{d'}\sigma_{12}^{t_{on}}(-v_g t). \qquad (4.72)$$

The statistics stored in the ground state coherences, are then transfered back to the probe field.

Summary

By continuity arguments, one can combine Eq. (4.72), Eq. (4.63) and Eq. (4.65) to show that

$$\mathcal{E}_{\rm out} \;\; = \;\; \frac{\nu\chi L}{\Gamma_p d'}e^{-\gamma_d(t_{\rm on}-t_{\rm off})}\mathcal{E}_{\rm in}. \qquad (4.73)$$

This expression relates the input and output probe states in the presence of pure dephasing and population exchange between the ground states in the limit of large density and large pumping rate Γ_p. One can show that without ground state decoherence (when $\gamma_d = 0$), the output is then the perfect replica of the input state.

EIT time-bandwidth product

The result given by Eq. (4.73) was obtained after making two main assumptions, $L \gg v_g T$ and $\Delta\omega \gg \Gamma_p$, which can be expressed by the inequality relation

$$v_g/L \ll \Delta\omega \ll \Gamma_p. \qquad (4.74)$$

The information has to be encoded at frequencies ω that satisfy this relation for perfect storage efficiency. The lower bound has to be satisfied for the pulse to fit the atomic sample. With a long input pulse, i.e. a small spectral extent $\Delta\omega$, a high density or a weak coupling beam is required, whereas for a short input pulse v_g/L can be made larger. On the other hand, the upper bound defines the minimum EIT bandwidth tolerable to minimize the losses. A short input pulse will require a large coupling beam power, whereas a weaker coupling beam power (narrower EIT bandwidth) can be used with a longer pulse. The time-bandwidth product of the system ($\Gamma_p L/v_g$) is d', i.e the number of independent samples from the probe that can be faithfully stored depends only on the density. At infinite density one can then store an infinitely broad probe spectrum. We see that not only does γ_c introduce excess noise on the output probe mode as discussed in the previous sections, but it also reduces the time-bandwidth product at a given d. We note that, with a-priori knowledge about the input pulse shape, optimization can be performed on the control field shape to enhance the time-bandwidth product. We come back to this in section 4.4.2.

4.3.4 EIT benchmarks

We presented ways to solve the EIT equations for light storage and found, qualitatively, the regimes where it is efficient. We will define here the conditions for EIT to be in the quantum memory regime.

We have identified two main sources of inefficiencies affecting the EIT based quantum memories. Using phase space methods, γ_c was shown to introduce excess noise but no losses. A pure off-diagonal dephasing γ_0 on the other hand was shown to yield losses without excess noise. We explained the physics behind those processes using an analytical treatment of light storage and show that the switching the control field off does not affect the output light state quantum statistics. We go a little further here and find the regimes where EIT can surpass classical memories and allow a performance within the no-cloning regime. We solve the problem using the numerical simulations for an accurate determination of the efficiency. We use stochastic simulations to map the T-V and noise-loss diagrams presented chapter 2 when changing the dephasing rates (γ_c, γ_0). Fig. 4.7-(a) shows the result of simulations where we chose three γ_c values, and varied γ_0 for each of them. We obtain the three dashed lines in the T-V diagram.

Let us concentrate on the line (i) of the T-V diagram. For this line, $\gamma_0 = 0$. When γ_c is also zero, we note that (T,V) is not (2,0), because of the finite optical thickness of the EIT medium. With the above parameters the bounds in Eq.(4.74) is satisfied by only one order of magnitude which makes the storage process nonideal even in the absence of dephasing. The no-cloning limit is, however, still overcome in that case. When γ_c increases from 0 to 0.005γ, the EIT performance degrades. The conditional variance increases, the signal transfer decreases significantly and the EIT memory follows the unity gain curve to finally leave the no cloning regime. The corresponding evolution is plotted on the noise-loss graph Fig. 4.7(b) trace (i). The losses are almost constant with varying γ_c, whereas the noise increases so that the memory no longer performs in the no-cloning regime at $\gamma_c \approx 0.004$.

The other lines correspond to regimes where $\gamma_0 \neq 0$. Line (ii) was found using $\gamma_0 = 0.0005\gamma$ and line (iii) when $\gamma_0 = 0.001\gamma$. We see that the evolution of the memory performance with γ_0 and γ_c is radically different. For both decoherence terms, when the decoherence rates increase, T monotonically decreases and at some decoherence rate value the quantum regime is no longer reached, but an increase in γ_c results in a faster increase of the conditional variance, as expected. It is also important to note that for any values of (γ_c, γ_0) the loss-less amplification regime (region D, cf. previous chapter) is never reached, this is because the gain term from population exchange is always associated with loss so the EIT memory never gets within the lossless amplifier regime.

4.4 Conclusion and perspectives

We have developed a quantum multi-mode treatment describing the delay and storage of quantum information encoded on the sideband quadrature amplitudes of a light pulse using both stochastic simulations and an analytical treatment. The two models both included the atomic noise and decoherence rates of realistic experiments. In our model we have, however, assumed an ideal three-level atomic structure with incident light fields that have constant transverse spatial intensities, and a mono-kinetic atomic ensemble for which light is exactly tuned on resonance. We have also neglected the effect of the back coupling from spontaneous emission into the light field, such as “radiation trapping” [Matsko et al., 2001a]. With these assumptions, the optimum sideband frequency for which the storage

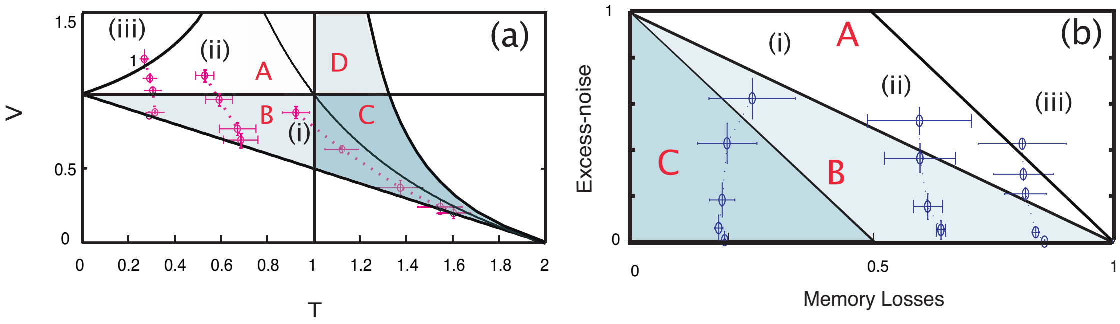

Figure 4.7: T-V diagrams showing the performance of the EIT memory. (a) Evolution of the EIT efficiency for three different γ_c values, the dotted lines representing the loci for a constant γ_0 and varying γ_c. (b) Performance of the EIT memory on a loss-noise plot in the same regimes. The error bars are statistical deviations. A,B,C and D are the non-classical, EPR, no-cloning and loss-less amplification regimes respectively (cf. chapter 2).

process can be efficiently performed depends mainly on the optical density and the coupling beam power chosen to set-up the EIT. We described the effects of the control beam noise on the probe propagation and found that to first order in the weak probe, the control beam does not introduce excess noise on the probe path.

We used the quantum information criteria to benchmark the performance of EIT quantum memories against an optimal classical measure-and-prepare scheme. We show that for typical decoherence rates in current experiments quantum information on the sideband quadrature amplitudes can be stored for milliseconds in the no-cloning regime, in the presence of small amounts of linear loss and excess noise.

We now finish this chapter by two ideas that might be worth pursuing.

4.4.1 Storage of two mode squeezed states in two memories

We have presented here the storage of an amplitude and phase modulated pulse. Our results can easily be extended to the storage of other Gaussian states such as squeezed light or entangled states. The knowledge of η and V_{noise} is enough to tell if the memory can store better than the no-cloning regime. One common issue with the storage of these states is that the information has to be encoded at sideband frequencies within the EIT window. As we showed in chapter 3, this raises lots of technical issues, mainly due to the environmental noise a low frequencies. An attractive solution that comes to mind when one wants to delay or store correlated sidebands is to focus on each individual sidebands, and delay or store them separately in two atomic ensembles. Storing separate sidebands in two separate EIT allow the two atomic ensembles to be entangled [Huntington et al., 2005, Cviklinski et al., 2007].

We can think about various ways to achieve this. The sidebands can be separated initially using a Fabry-Perot cavity and subsequently stored in two separate memories. The EIT memories have to be resonant with each of the sidebands, which can be achieved experimentally by detuning the control beam frequency or applying a biased DC magnetic field. This initial sideband separation stage is however not required when the squeezing exists at sideband frequencies above the absorption band of the medium. Typically, it corresponds to the linewidth γ of the transition. In that case, one can make one of the sidebands resonant with a first EIT medium, and store it whilst the other is transmitted and stored in a second EIT medium. This simplifies the experimental difficulties with high finesse Fabry-Perot cavities. In a warm vapor cell however, the absorption band corresponds to the Doppler width, which can be as high as 500 MHz. The situation is more favorable in cold atoms where the absorption band can be smaller (in Rubidium for example it would be around 6π MHz) but still rather large for the squeezed light sources using parametric oscillation. One possibility could be to use Kerr non-linearities in fibres where the squeezing extends to high frequencies, but no squeezed light resonant with atomic transitions has been demonstrated yet using this technique. One can also use two frequency shifted control beams resonant with both sidebands, in the same medium in a kind of *Double EIT* configuration, but this does not allow the entanglement of two atomic ensembles from a single squeezed light source.

4.4.2 Matching of control and probe temporal modes

Another related issue is the optimization of the storage efficiency for a given optical depth. How can we make sure that the light information was stored in the most efficient way ?

A theoretical iterative procedure was recently proposed to optimize the coupling beam shape and power in [Gorshkov et al., 2007a,b,c,d]. We also performed some simulations by adiabatically shaping the control field and noticeable improvements were found on the bandwidth and noise of the memory. In this chapter, we chose our (time independent) coupling beam Rabi frequency by maximizing the output signal without decoherence, i.e. we found a trade off between off line center absorption and the compression of the pulse required to fit the sample. In this case the efficiency η was found to be 80 %, only limited by the lack of optical depth. At higher densities optimized coupling beam strength (but fast switching), we found a transmission close to unity.

One of the most important points that recurrently appeared throughout this chapter is the time dependence of both the probe and the coupling beam. In [Gorshkov et al., 2007a], conditions for efficient light storage were derived from numerical optimization algorithms. A paper from [Nunn et al., 2007], also dealt with this optimization problem in the Raman regime. They showed that the *temporal mode matching*, between the probe and the control was required to efficiently store the probe information onto the ground states of atoms in a Raman configuration. In a more recent paper, the optimum shape of the control beam was claimed to be optimum in EIT [Gorshkov et al., 2007d] using a “gradient ascent optimization” procedure. The resulting optimum shape of the control beam was found similar to the probe but advanced in time and larger. It would be of fundamental interest to get a general picture describing the physics behind these temporal shapes and to obtain a simple understanding between the optimum control and input probe shapes as a function of atomic parameters.

Chapter 5

Storage of quantum states using EIT in a warm vapour cell

In this chapter we investigate experimentally the properties of Electromagnetically Induced Transparency (EIT) as a memory for continuous variable quantum states in rubidium vapours.

In the first section, we present the spectroscopic properties of rubidium 87 atoms. The saturated absorption measurements in three different vapour cells are reported and analyzed. We then demonstrate narrow dark resonances associated with coherent population trapping in the ground states and report EIT transmission of up to 90 % in a buffer gas system.

In the second section, we demonstrate the delay of squeezed light and entanglement using EIT in a rubidium vapour cell. By performing quadrature amplitude measurements of the probe field, we found no appreciable excess noise from the EIT process. We show that the presence of buffer gas in the medium permitted a quantum noise limited performance of the delay line. From an input squeezing of 3.1 dB at low sideband frequencies, we observed the survival of 2 dB of squeezing at the EIT output. By splitting the squeezed light on a beam-splitter, we generated biased entanglement between two beams. We transmitted one of the entangled beams through the EIT cell and correlated the quantum statistics of this beam with its entangled counterpart. We observed a 2 μs delay of the biased entanglement and obtained a preserved degree of wavefunction inseparability of 0.71, below the unity value for separable states.

In the last section, we demonstrate the storage and retrieval of a weak probe onto and from the ground state coherence of rubidium atoms. We examine the limits to the efficiency of light storage using EIT in warm vapour cells and determine the ground state decoherence rate in the buffer gas system by comparing the results with a numerical model. Part of the work described here was published in [Hétet et al., 2008a].

5.1 Rubidium spectroscopy in a warm vapour cell

In this section, we present the chemical and spectroscopic properties of rubidium. We then present Doppler and saturated absorption spectra for different rubidium vapour cells and interpret the results.

5.1.1 Rubidium 87 hyperfine structure.

Rubidium is naturally present in two isotopes, ^{87}Rb and ^{85}Rb with concentrations of 28% and 72%, and nuclear spins of 3/2 and 5/2 respectively. Rubidium belongs to the Alkali family, with only one electron out of the 37 in the outermost shell. The vapour pressure dependence of rubidium with temperature can be taken from a vapour-pressure model that can be found in [Nesmeyanov, 2007]. The melting point is found to be about 40 C.

Rubidium 87 possess two *fine* optical transitions. The D_2 line at 780 nm (addressing the $5^2S_{1/2} \rightarrow 5^2P_{3/2}$ states), and the D_1 line at 795 nm (addressing the $5^2S_{1/2} \rightarrow 5^2P_{1/2}$ states)[1]. These two transitions result from the coupling between the outer electron orbital angular momentum **L** and its spin angular momentum **S**, giving a total electron angular momentum **J**=**L**+**S**. Rubidium also has a *hyperfine* structure due to the coupling between **J** and the nuclear angular momentum **I**. The magnitude of the total atomic angular momentum **F**=**J**+**I** can take the values

$$|J - I| \leq F \leq J + I. \tag{5.1}$$

For the rubidium D_1 line, $J = 1/2$ and $I = 3/2$. We then have $F = 1$ and $F = 2$ as two possible hyperfine transitions for both the excited and ground states, as shown Fig. 5.1-(a). The energy splittings between the ground and excited states were measured in [Arimondo et al., 1977] to be about 6.834 GHz, and 816 MHz respectively. For the excited state of the D_2 line[2], $J = 3/2$ and $I = 3/2$. We then have $F = 0, 1, 2$ or 3, and $F = 2$.

5.1.2 Zeeman sublevels

The hyperfine levels each contain 2F+1 magnetic sub-levels (so called Zeeman sub-levels, labelled m_F, where $-F \leq m_F \leq F$) which are at the same energy in the absence of magnetic field. The strength of the optical transitions between ground and excited states Zeeman sub-levels is governed by selection rules allowing or not the exchange of quanta of momentum between light and atoms. The spontaneous emission rate (and associated coupling strength[3]) is around 20 MHz for rubidium, but vary from one transition to another. The Clebsch-Gordan coefficients are elements of the dipole matrix giving the coupling strength for each transition[4].

Without resonant light field, the atomic population is in a thermal equilibrium with an identical probability of finding the atom in the different ground states sub-levels. This population distribution can however be made “asymmetric” via *optical pumping* [Happer, 1972]. Let us assume we apply a circularly polarized beam σ^+ to an atom whose quantization axis is aligned with the light propagation direction. If the laser field is resonant with a transition where $F_g \geq F_e$, it optically pumps atoms to the ground state of the Zeeman sub-level with the largest magnetic spin, $m_F = F$. After a few spontaneous emission events, and assuming no re-thermalisation, the medium does not interact with the field anymore.

Applying a laser field polarised σ^+ resonant with a transition where $F_e > F_g$ is rather different. After a transient, the laser field interacts indefinitely, or “Rabi flops”, with the optical transition $m_F = F_g \rightarrow m_F = F_e$[5]. For this reason, the transition is called a

---

[1] $n^{2S+1}X_J$ means that the electron belongs to the orbital X =S, P, D, F... giving an orbital angular momentum L=0, 1, 2, 3 ..., has an electronic spin S, a total orbital angular momentum J and its principal quantum number is n.

[2] As we do not use the D_2 line in this thesis, we do not show its level structure.

[3] The link between the two was shown in the first chapter.

[4] They can be found for example at http://steck.us/alkalidata/.

[5] This is of course true as long as there are atoms to interact with. To ensure a constant Rabi flopping on this transition, optical pumping from the hyperfine level where the atoms moved to is often used.

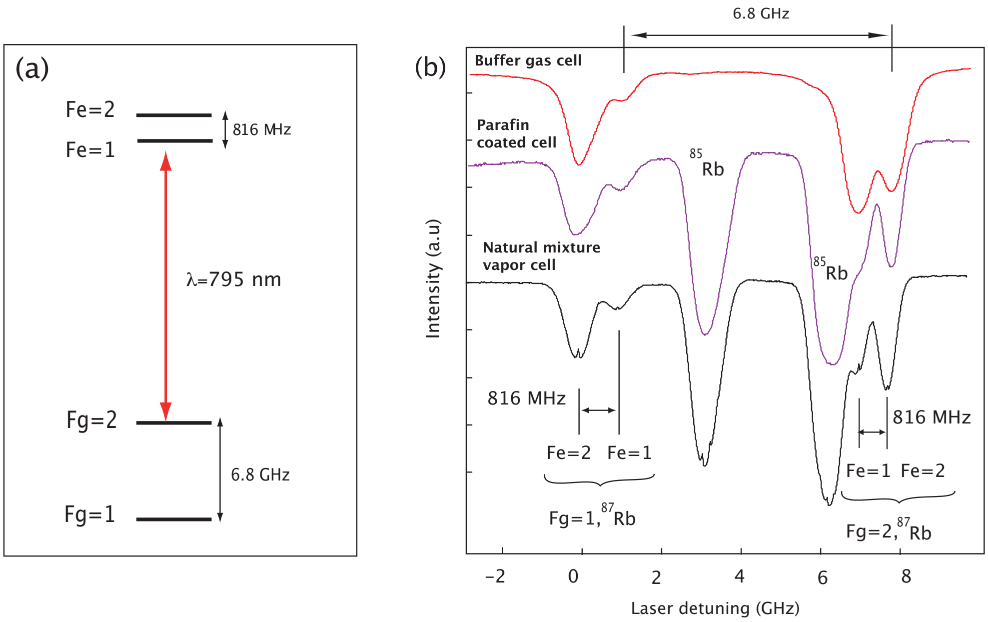

Figure 5.1: (a) Rubidium D_1 line hyperfine levels. (b) Saturated absorption spectra at the rubidium D1 line for three different cells. A rubidium 87 cell containing 5 Torr of Helium buffer gas, a paraffin coated cell and a natural mixture of rubidium. The traces have been translated for clarity, but all the traces initially had the same off-resonance DC level.

"cyclic" transition.

It is relatively easy to transfer momentum to the atoms via photon scattering using cyclic transitions, so the D_2 transition is relevant to laser cooling. The D_1 line, and especially the transition $F_g = 2$ to $F_e = 1, 2$, is of more interest for dark state preparation in the atomic ground states.

5.1.3 Effects of atomic motion

The main issue with atom optics experiments in warm vapour cells is that the atoms move, which has two main consequences. The first and obvious one is that the atom do not stay in the beam. The second is that the absorption frequencies of the atoms shift depending on their longitudinal velocity due to the Doppler effect.

Time-of-flight

To give an order of magnitude for atomic motion, we can, to a good approximation, equate the atom kinetic energy to the Boltzman thermal energy[6] and obtain

$$v_{\mathrm{rms}} = \sqrt{\frac{3k_B T}{2m}} \simeq 100 \text{ m.s}^{-1}. \tag{5.2}$$

With a beam size of 0.5 cm, this gives a "time-of-flight" of an atom inside the beam of around 50 μs. This time-of-flight induces an overall relaxation rate that limits the efficacy of memories in warm vapour cells. This is not a problem if the atom escapes from the beam area and comes back in the same spin state after hitting the cell walls. The probability of

---

[6] Equipartition theorem.

these events is unfortunately quite rare, for obvious geometric reasons. Even if the atom comes back in the beam, its spin state is likely to have changed due to inelastic collisions with the cell walls. Several solutions can be envisaged to tackle this issue.

1. Laser cooling : The internal atomic energy for a single atom is usually extremely small, but when the atom is driven by a strong light field on a cyclic transition, momentum exchange between the atom and the light field can become really large. When the light field saturates the transition, the total momentum exchange can exceed the external atomic energy $k_B T$, and the speed of the atom can change by a significant amount. By appropriate arrangement of those "trapping beams" [Phillips, 1998, Cohen-Tannoudji, 1998, Chu, 1998] the atoms can cool down to only a few μK, and stay within the beams for long times.

2. Paraffin coated cell : When the cell walls are paraffin coated, the atoms can hit them without losing their internal states. Using such a system allows one to use big beams that cover the whole cell. This practically makes the time of flight really long. It was the option chosen in experiments reported in, for example [Julsgaard et al., 2004, Cviklinski et al., 2007].

3. Buffer gas: The use of a buffer gas also increases the time-of-flight of the atoms inside the beam. The buffer gas are usually big and inert atoms, so that even after several elastic collisions with the buffer gas, the atoms do not lose their spin states [Arimondo, 1996, Fry et al., 1993]. This is the option chosen in this chapter and in chapter 8.

Doppler broadening

The other manifestation of atomic motion is Doppler broadening. When the atoms move, in the lab frame, their apparent resonance frequency shifts. For example, for atoms moving towards the light beam, the apparent resonance frequency decreases, so the transition is effectively red shifted. At room temperature, the full width at half maximum of the Doppler broadening, $\delta\nu$, can calculated to be about

$$\delta\nu = k v_{\mathrm{L}} \simeq 500 \text{ MHz}, \tag{5.3}$$

where k is the wavector ($k = 2\pi/\lambda$, with λ the wavelength corresponding to the rubidium transition) and v_{L} the projection of the atomic velocity vector onto the optical axis, which is about the v_{rms} calculated above. As the homogeneous linewidth γ in rubidium is around 20 MHz, it can then not be resolved by a simple scanning of the laser frequency around the transition[7].

Doppler is actually not a big problem for EIT experiments when the control and probe beams are co-propagating, as they both interact with the same velocity class[8]. However,

---

[7] One could, however, think about applying a hole burning technique to eliminate Doppler broadening. We describe the hole burning technique used in solid state systems in chapter 6. The time it takes for an atom to change its speed is, however, on the order of the time it would take to scan the frequency of the laser across the whole Doppler profile, repump with a another "narrow" linewidth laser and do the experiment. This technique would also only allow one to empty atoms that are moving longitudinally in direction of the beam.

[8] Doppler is more an issue with the Λ-GEM scheme, as will be discussed chapter 8.

to be able to tell what the frequency of the laser is initially, and to eventually lock it close to a hyperfine transition, it is a problem. To resolve the homogeneous linewidth γ in our experiments, and to lock the laser on resonance, we used saturated absorption spectroscopy.

5.1.4 Saturated absorption

The schematic of the saturated absorption set-up is shown Fig. 5.2, part (ii). The Ti:sapphire[9] laser frequency is scanned across the Doppler profile and input to a rubidium vapour cell (without magnetic shielding) in two opposite directions.

Let us concentrate on a laser frequency $\nu + \Delta$, where by convention, $\Delta = 0$ exactly on resonance with atoms for which $v_L = 0$. ν is the optical frequency of the laser. The atoms moving at a longitudinal speed $v_L = \Delta/k$ with respect to the first incoming beam are pumped in the excited state. The other, off-resonant, atoms are not excited. The same beam is now sent through the cell again, but in the opposite direction. If the atomic velocity is such that $|kv_L| > \gamma$, the retro-reflected beam is this time absorbed by the atoms moving at $-kv$. These atoms did not interact with the first beam, and are therefore still in the ground state. For laser frequencies where $|\Delta| > \gamma$, we then observe a broad Doppler absorption spectrum.

When $|\Delta| < \gamma$ however, the retro-reflected beam interact with atoms that have been excited by the first laser beam and have a small longitudinal speed v_L. It then stimulates the emission of a photon in the same direction as the counter propagating beam, thereby enhancing the transmission obtained without population inversion, and creating a transmission peak in the Doppler absorption profile, whose width is on the order of the homogeneous linewidth γ.

This reasoning holds as long as the time it takes for the atoms to change their speed is less than the time it takes for them to be excited, and as long as the Zeeman structure plays no role [Arimondo, 1996]. We will come back to these limiting cases shortly.

Results

The results are shown Fig. 5.1. The first trace at the bottom was taken using a mixture of ^{85}Rb and ^{87}Rb without buffer gas. We observed Doppler absorption profiles (on the order of 500 MHz) for all the transitions, and also observed peaks due to saturated absorption of atoms for which $v_L = 0$, in the middle of the Doppler profiles.

The transmission peaks were subsequently used to derive error signals to lock the laser as shown Fig. 5.2-(ii). The error signal was derived using a PDH locking technique, by using the inherent large phase modulation on the laser at 87 kHz. The two traces above it are saturated absorption spectra taken with cells that contains buffer gas and paraffin coated cells. We found no transmission peaks for any cell temperature here.

Possible explanation including Zeeman structure

To understand the behavior of the saturated absorption signals, let us first imagine a simpler scenario where a magnetic shielding is present. The earth's magnetic field, which can be as large at 500 mG in some directions, is then eliminated. We also neglect re-

---

[9] The laser is described in chapter 3.

thermalisation in the mean time, assuming that the atoms stay in the beam and do not collide with the cell wall. We therefore assume that any spin state is long lived.

With these simplifying assumptions, for a transition where $F_g \geq F_e$, atoms that are not moving longitudinally cannot be inverted by the two counter propagating beams. These atoms should be trapped in a dark state and the light totally transmitted (that is, we have EIT). For transitions where $F_g < F_e$, Electromagnetically induced absorption (EIA) [Taichenachev et al., 2000, Lezama et al., 1999] plays a role and enhances the absorption of the light due to a transfer of ground state coherence to the excited state. Due to atoms that are moving longitudinally, light will be absorbed because of the two-photon detuning caused by Doppler shifts[10]. The narrow peaks expected for atoms where $|kv_L| < \gamma$ will then be difficult to observe.

Saturated absorption is usually not measured with a magnetic shielding though, and for laser frequencies satisfying $|\Delta| < \gamma$, zero two-photon detuning might not be achieved for atoms where $|kv_L| < \gamma$. Instead, it can be satisfied for atoms that are moving longitudinally at a speed where the Doppler shift matches the surrounding magnetic field. Because the earth magnetic field is not homogeneous, the sub-natural EIT or EIA features are rarely observed. What would be observed instead, is a Doppler profile without any narrow features.

Saturated absorption “would” then only be observed when the Zeeman structure does not play a role, which is the case for systems with efficient population reshuffling or large ground state dephasing rates.

Pure rubidium cell In a pure rubidium vapour cell, inelastic and elastic collisions are frequent and the atoms do not stay in the beam for long. Zeeman coherences cannot survive on time scales where the laser frequency is scanned. The two-level atom explanation for saturated absorption given earlier holds here because the magnetic moment is not a preserved quantity anymore, allowing saturated absorption peaks to be observed.

Cell with 5 torr of Helium buffer gas No saturated absorption signal was observed. The atoms stay in the beam for a long time, allowing, for example, much efficient EIT to be observed.

In vapour cells with higher buffer gas concentrations, collisions with the buffer gas are even more frequent so that the atomic velocity can change faster. Given the relatively low buffer gas concentration, we believe that the effect of velocity changing collisions are negligible here[Arimondo, 1996].

Paraffin coated cell As paraffin coated cells allow the atoms not to lose their coherence upon hitting the cell walls, the Zeeman structure plays a role here in the dynamics as well.

To conclude, effects relying on Zeeman coherences such as EIT, EIA or optical pumping have to be included for a full understanding of saturated absorption spectra. The strong correlation we found between the presence of transmission peaks and the lifetime of the ground state population/coherence suggests strongly that this would be the case. We

---

[10] This effect was in fact used to cool atoms on dark transitions using Velocity Selective Coherent Population Trapping, VSCPT, in [Aspect et al., 1988].

did not intend to provide a definite answer to the problem, but rather to point out the complexity of the physics involved in saturated absorption using Alkali atoms.

We now move to a specific Zeeman coherence effect, Electromagnetically induced Transparency.

5.2 EIT in warm vapour cells

EIT measurements on the $F_g = 2 \rightarrow F_e = 1$, D_1 line are now presented using a steady state (henceforth referred to as DC) and dynamic (AC) measurements.

To observe EIT we used the set-up depicted Fig. 5.2-(iii). As discussed earlier, in warm vapour cells the control and probe must be co-propagating, otherwise, atoms where $|kv_L| \geq \gamma$ will introduce a two-photon detuning causing the light to be absorbed. In most of our experiments, we used the D_1 line of ^{87}Rb (795 nm). The atomic levels used were the $|5^2S_{1/2}, F_g = 2\rangle$ for the ground state and the $|5^2P_{1/2}, F_e = 1\rangle$ for the excited state. After optical pumping, the coupling beam accessed the $|5^2S_{1/2}, F_g = 2, m_F = -2\rangle$ Zeeman sublevels, and the probe beam the $|5^2S_{1/2}, F_g = 2, m_F = -2\rangle$ sublevel.

Both beams were derived from the Ti:Sapphire laser. The degeneracy of the Zeeman sublevels was broken using an externally applied longitudinal magnetic field of 8.5 Gauss. To maintain the two-photon resonance condition required for EIT, the control beam was frequency shifted by 6 MHz[11] with respect to the probe light using two cascaded AOMs in a double-pass configuration (using AO$_1$ and AO$_2$). This non-degenerate configuration greatly simplifies the alignment procedure used to optimize the EIT. When the beams are frequency degenerate, residual polarization cross-coupling between the probe and the control beams leads to parasitic low frequency fluctuations of the beam powers. The introduced Zeeman shift between the ground states shifts these fluctuations to a frequency of 6 MHz, which is well outside of the measurement bandwidth.

In this section, the EIT medium consists of a 8 cm long vapour cell containing isotopically enhanced ^{87}Rb, heated to 70°C and filled with 5 Torr of Helium buffer gas. The cell was AR coated on the outside windows, which gives 92% transmission in the absence of any active atoms. This represents the best possible transmission our EIT system can achieve. In order to reduce stray magnetic fields, μ-metal shielding was used around the cell. The diameters of the control (C) and probe (P) beams were around 2 cm and 0.3 cm inside the vapour cell, respectively.

A 20 mW/cm^2 repump beam (R) from an external cavity diode laser was used to bring atoms from the F=1 ground state hyperfine level to the F=2 ground state. The diode laser (from Toptica) delivers a maximum output of 100 mW. It is situated on another adjacent optical table. 10 mW were used for saturated absorption and the rest was mode matched to a single mode optical fiber (cylindrical lenses were used to compensate astigmatism). The fiber output can be seen Fig. 5.2-(iii) on the left. The light was then coupled with an angle to the medium with a beam size of about 2 cm inside the cell. This repumping procedure enhances the optical depth seen by the weak probe field without significant impact on the ground state coherence.

To characterize our system we first measured the EIT window.

---

[11] The Zeeman splitting dependence with magnetic field is 0.7 MHz/Gauss for this transition.

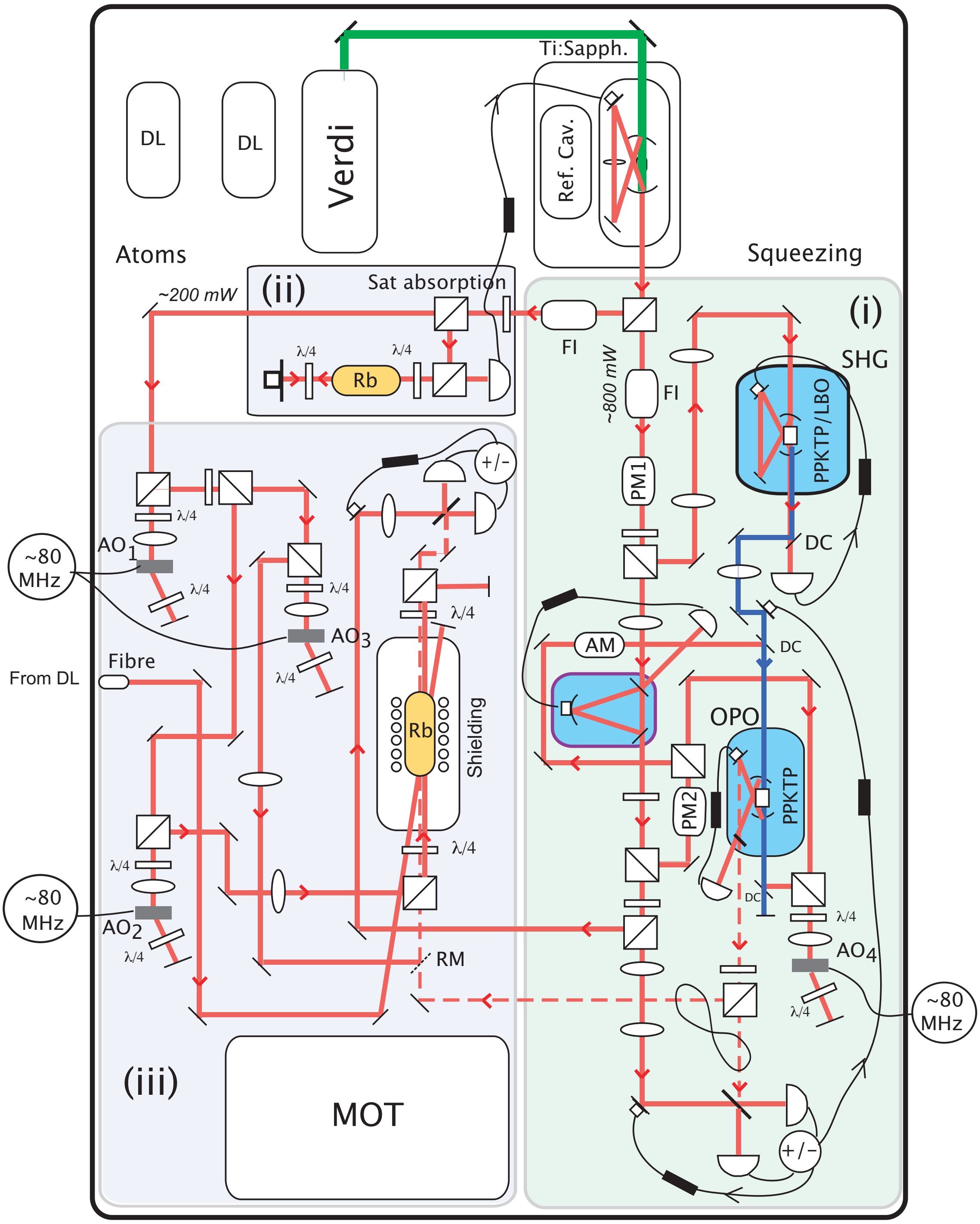

Figure 5.2: Schematic of the experiment. DC=dicroic mirror, DL=diode laser, FI=Faraday isolator, AO=acousto optic modulator, the black rectangles refer to the control electronics described in the chapter on squeezing generation. PM and AM=phase and amplitude modulations and RM=removable mirror. The unlabeled white rectangles are half wave plates.

5.2.1 Transmission as a function of two-photon detuning

We performed a DC measurement of the EIT window by scanning the frequency of the control field with an acousto-optic modulator. We were then able to monitor the probe transmission as a function of two-photon detuning.

Fig. 5.3-(a) shows the result of such a measurement for different control beam powers (the powers used are mentioned in the figure caption). The results show that, as the control beam Rabi frequency decreases, the EIT window gets narrower and narrower. Thanks to the presence of buffer gas in the cell the EIT feature is relatively narrow (the FWHM was about 50 kHz for a control beam power of 5 mW/cm^2) without a significant loss of transmission. Such narrow and transmissive lines were not be achieved with pure rubidium vapour cells.

Even in the presence of buffer gas however, the finite time-of-flight of the atoms inside the beam introduced an effective ground state dephasing. The EIT transmission was therefore not ideal for control beam powers approaching $\sqrt{\gamma\gamma_0}$, (assuming that the loss of transmission can be modeled by the pure dephasing rate γ_0, introduced chapter 4). The pumping into the dark state can only be efficient above this value, which explains the increased transmission and broadening for large control beam powers.

An unexpected effect was also observed. The EIT maximum shifted as a function of control beam power. We attribute this shift to an AC-Stark effect induced by the hyperfine level, $F_e = 2$, situated at $\Delta_0 = 816$ MHZ above the $F_e = 1$ hyperfine level. The contribution of the extra level on the frequency shift can be evaluated to be $\Omega_c^2/2\Delta_0 \simeq 200$ kHz[12], which is about what we observed here.

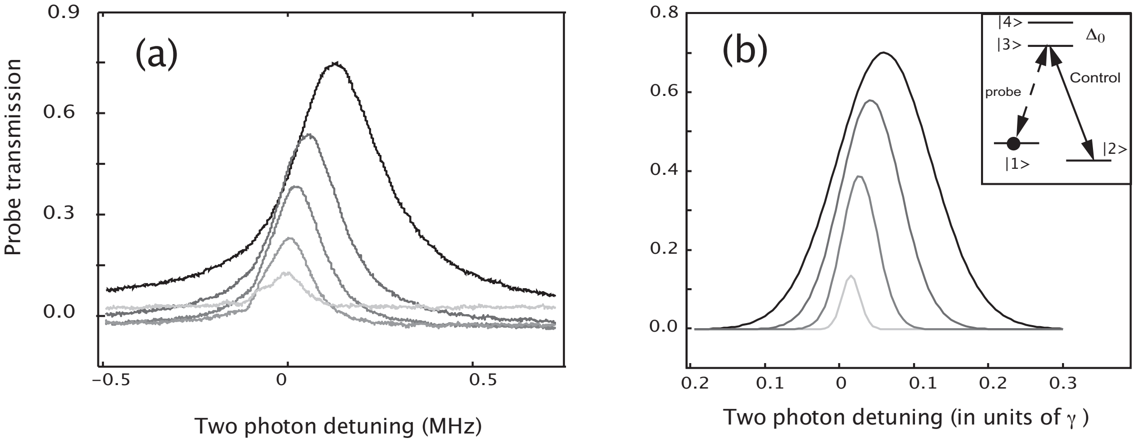

Figure 5.3: (a) Probe transmission as a function of two-photon detuning for different control beam powers. From the upper to the lower curve, we used control beam powers of [20,10,5,1,0.4] mW/cm^2. (b) Modelling taking into account an extra atomic level detuned by $\Delta_0 \approx 40\gamma$. For these simulations we used a ground state dephasing rate of 0.005γ and control beam Rabi frequencies of $[0.8,0.6,0.4,0.3]\gamma$.

To convinced ourselves, we also performed numerical simulations using the Quantum Optics Toolbox for Matlab[13]. The level structure we used is shown in the inset of Fig. 5.3-(b). We solved for the atomic dipole steady states $\langle\sigma_{13}(\delta)\rangle$ and $\langle\sigma_{14}(\delta)\rangle$ as a function of two-photon detuning δ between the two beams, using the Hamiltonian of the double-Λ system. We then use the steady state results as source terms for the Maxwell equation by writing

$$\mathcal{E}_{\text{out}} = \mathcal{E}_{\text{in}} + iN(g_{13}\langle\sigma_{13}(\delta)\rangle + g_{14}\langle\sigma_{14}(\delta)\rangle)L, \tag{5.4}$$

---

[12] The formula will be demonstrated in the off-resonant three-level atom, beginning of chapter 8.

[13] This package allows one to numerically solve the Von Neuman equation from the Jaynes-Cummings Hamiltonian, and can be found at http://www.qo.phy.auckland.ac.nz/qotoolbox.html.

where L is the length of the sample, N the optical density and g_{13} and g_{14} the coupling strengths for the transitions $|1\rangle - |3\rangle$ and $|1\rangle - |4\rangle$ respectively. The results are shown Fig. 5.3-(b) and the parameters given in the figure caption. The shift of the EIT feature as a function of Rabi frequency was also observed in this semi-classical model.

As we did not include Doppler broadening in these calculations and neglected the z-dependence of the probe inside the medium, we did not expect a full quantitative agreement. Nevertheless, good qualitative agreement was found between the experiment and the theory, which supports our interpretation.

To enable a large delay of information, the control beam must be below the transition saturation (about 3 mW/cm^2), in which case the frequency shift is then rather small, so the effect should not be detrimental to the good functioning of the memory.

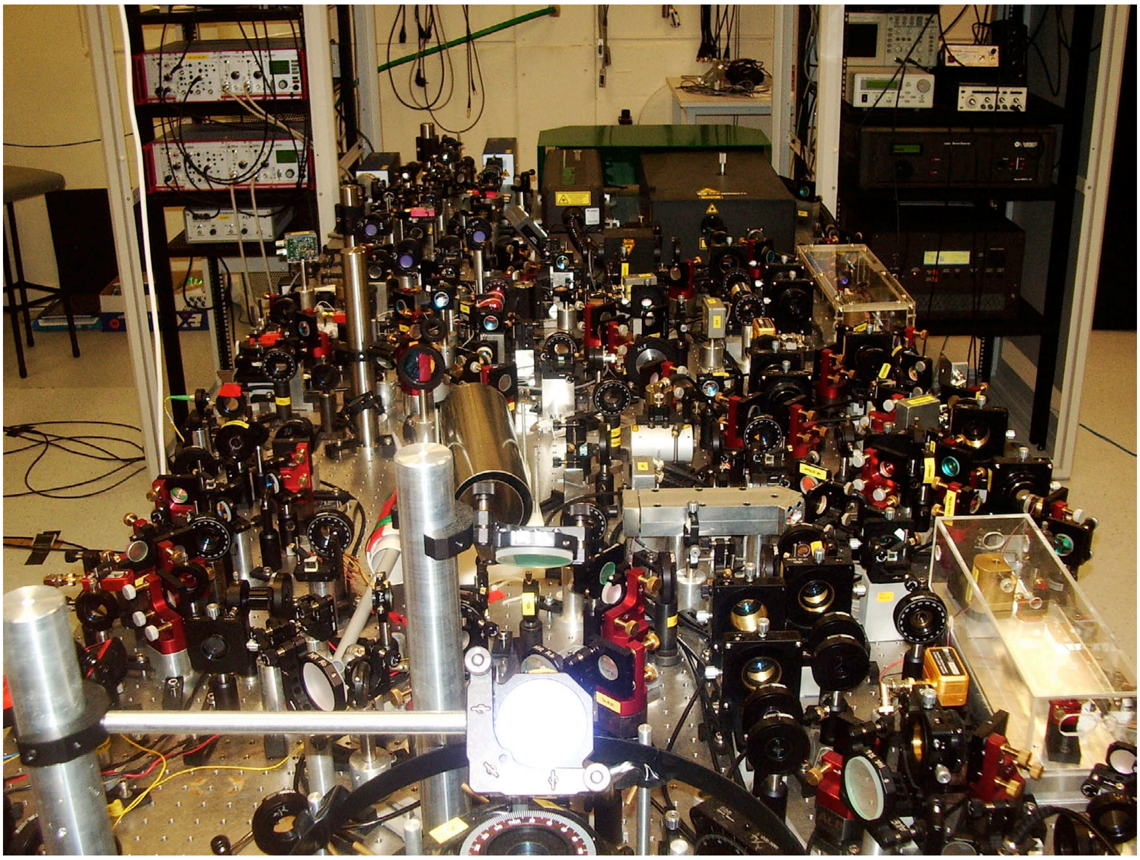

Figure 5.4: Picture of the set-up. The Ti:sapphire laser is located at the back, the two perspex boxes on the right are the SHG and OPO (from top to bottom). The μ-metal shielding surrounding the cell is the cylinder in the middle.

5.2.2 AC measurement

To measure the EIT transmission window, one can also probe the dynamics of the three level system. This can be done by applying a broadband amplitude modulation on the probe and measuring how the dark state follows its fluctuations or by sending a pulse in the medium and measure the pulse reshaping.

Our measurements of the EIT bandwidth and transmission here focus on a sideband frequency of 50 kHz. Defining the bandwidth of the EIT window to be the width-at-half-maximum, or 3 dB point, we show the transmission of 50 kHz sidebands as a function of the

EIT bandwidth in Fig. 5.6(a). The bandwidth was determined by applying a broadband 20 dB modulation using AM shown Fig. 5.2-part (i) and measuring the transmission after the cell on a spectrum analyser. Due to the presence of the other atomic level and residual single-photon and two-photon detunings, the EIT window might not always be perfectly symmetric. Our measurement technique averages over any such asymmetry. The results show that a best transmission of 90% for the 50 kHz sidebands with an EIT bandwidth of 500 kHz.

We now turned to the measurement of transmission and delay of squeezed light.

5.3 Delay of squeezing and entanglement

Shortly after the initial demonstration of ultraslow pulse propagation [Vestergaard Hau et al., 1999] and storage of classical light using EIT [Liu et al., 2001, Phillips et al., 2001], the same techniques were extended to single photons [Eisaman et al., 2005, Chanelière et al., 2005, Laurat et al., 2006] and squeezed light [Appel et al., 2007, Honda et al., 2008]. Whilst being impressive demonstrations of the potential of EIT as a quantum memory for light, these proof of principle experiments still suffer from residual decoherence effects that limit the delay time and the efficiency. In Ref [Arikawa et al., 2007], near complete transmission of 1.6 dB of squeezing was observed, although no delay was measured. In Ref [Akamatsu et al., 2006], it was shown that starting with 1.1 dB of squeezing, about

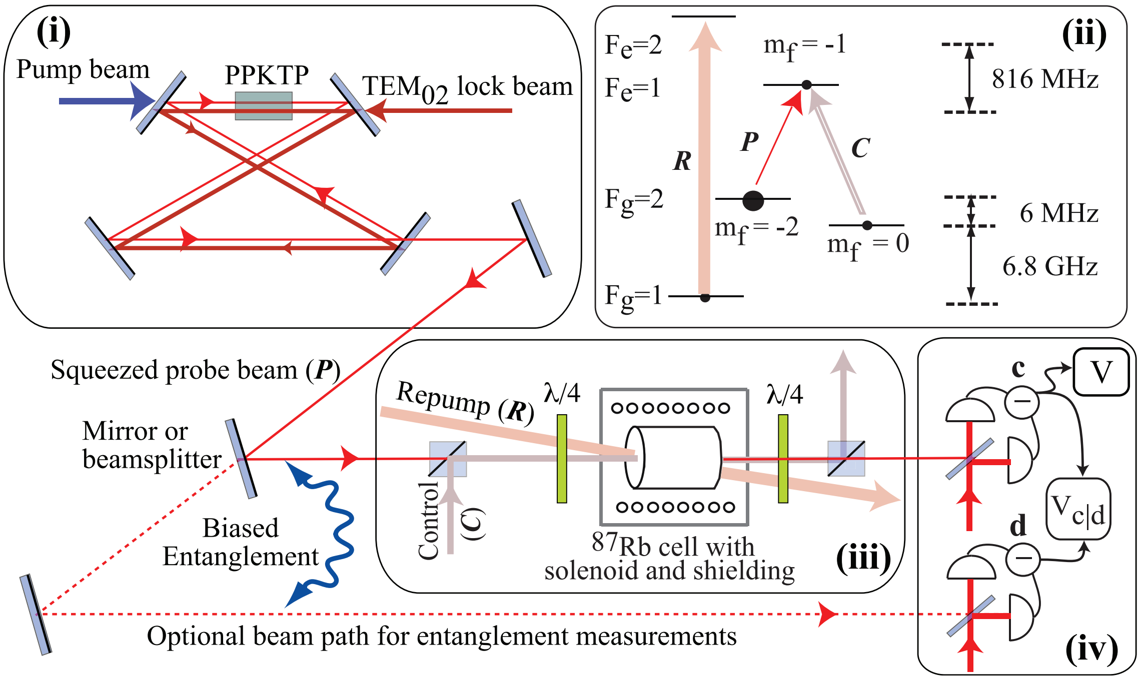

Figure 5.5: Schematic of the experiment. (i) Bow-tie PPKTP optical parametric amplifier. See chapter 3 for details. The squeezed beam (P) is either injected directly into the EIT setup or divided using a beam-splitter to produce a pair of biased entangled beams. (ii) The EIT level scheme. A strong control field (C) pumps most of the atoms in the $m_F = -2$ state and provides the transparency for the squeezed vacuum. A repumping beam (R) brings atoms from the $F_g = 1$ hyperfine sub-level to the $F_g = 2$ level from level $F_e = 2$. (iii) The gas cell used for EIT. (iv) Joint measurements are performed using two homodyne detectors to analyse the quadrature amplitude correlations.

0.2 dB survived propagation through an EIT medium delaying light by 3.1 μs. Appel *et al.* [Appel et al., 2007] and Honda *et al.* [Honda et al., 2008] reported the storage of squeezed light using EIT in a vapour cell and a magneto-optical trap (MOT), respectively. With a storage time of 1 μs in gas cell, 0.21 dB of squeezing was retrieved from an input of 1.86 dB [Appel et al., 2007]. With 1.2 dB of input squeezing, 0.07 dB was recalled from a MOT after being stored for 3 μs [Honda et al., 2008].

In this section, we present results obtained from two experiments performed to investigate the transmission of quantum correlations through an EIT medium. In the first experiment, we investigate the direct transmission of a squeezed light beam through the EIT medium. With an input squeezing of 3.1 dB, we demonstrate the transmission of 2.0 dB of squeezing through an EIT feature created in the ^{87}Rb cell filled with buffer gas. In our second experiment, we demonstrated the delay and preservation of continuous variable entanglement by transmission through the EIT medium. Our scheme for delaying entanglement is shown in Fig 5.5. By splitting a single squeezed light beam, biased entanglement is generated between the two output beams of the beam-splitter [Bowen et al., 2003a]. We sent one of the beams through the EIT vapour cell and performed joint measurements of the quadrature amplitudes of both beams. By analysing the quantum statistics of the joint measurements, we could directly calculate the amount of delay and entanglement between the two beams. Delay of entanglement between remote atomic ensembles was achieved in the continuous variable regime using the off-resonant Faraday rotation [Julsgaard et al., 2004]. Although the off-resonant Faraday rotation scheme can successfully store quantum optical states, the retrieval of information has to be indirectly achieved through a quantum non-demolition measurement. Entanglement delay with EIT, on the other hand, can potentially facilitate direct reversible retrieval of quantum states.

The section is structured as follows: We first present measurements of noise generated by an EIT system. Then, squeezed vacuum propagation through an EIT feature is demonstrated. Lastly, we show the generation of continuous variable entanglement and coherently delay one half of it.

5.3.1 Noise measurement and interpretation

Before sending a squeezed vacuum through the EIT system, we measured the noise introduced into the probe mode by the atoms prepared without a coherent probe beam and compare it with the theory developed in the preceding chapter. In other words, we examined the properties of an EIT system when the control field is on, but the input probe state is just a vacuum. The atomic noise measurement was made using a homodyne detector mode-matched to the probe vacuum mode. Fig 5.6(b), trace (i) shows the shot noise level and Fig 5.6(b)-trace (ii) shows the noise measurement made with an EIT window of 300 kHz and a vacuum state probe. This result shows that the atoms do not add noise to the probe mode and we can reasonably expect the same behaviour for a squeezed vacuum mode which contains a few photons.

When performing the same experiment on a rubidium vapour cell without buffer gas, large excess noise was observed, as can be seen Fig. 5.6(b)-trace (iii). This noise was also measured in Ref. [Hsu et al., 2006a]. We attribute the excess-noise to non-optimum pumping into the $m_F = -2$ Zeeman sublevel and/or inelastic collisions with the cell walls. Both these mechanisms result in non-negligible atomic populations of Zeeman sublevels that are not interacting with the probe.

Two effects are expected with residual populations in the levels $m_F = -1$ and $m_F = 0$,

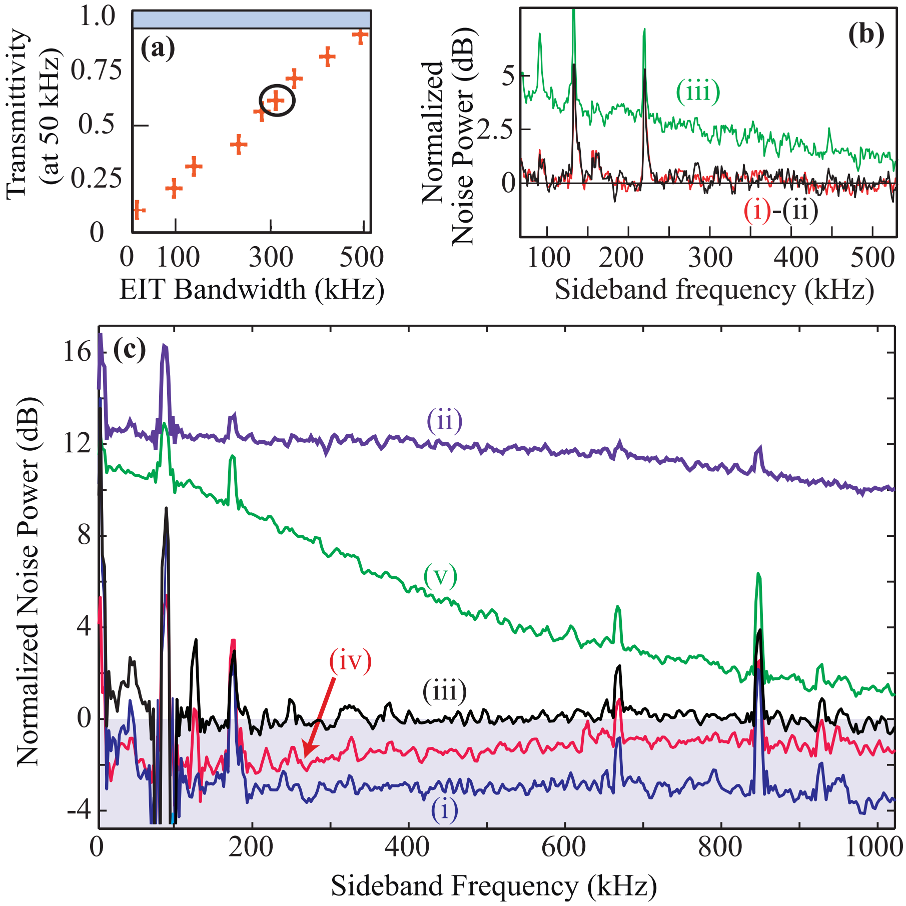

Figure 5.6: (a) EIT bandwidth as a function of the transmission measured at 50 kHz, obtained by varying the control beam power. The circle is the regime where graph (c) was obtained. The cell transmission limit is shown by the grey area. (b) Noise measurements of an EIT medium in enhanced ^{87}Rb vapour cells, (i) Shot noise, (ii) with buffer gas and (iii) without buffer gas. (c) Transmission spectra of the squeezed light through an enhanced ^{87}Rb vapour cell with buffer gas. (i) Squeezing and (ii) anti-squeezing measured off-resonance; (iii) shot noise; and (iv) squeezing and (v) anti-squeezing measured on resonance under EIT conditions.

resonant with the control field. It was shown in the preceding chapter that this situation will give rise to gain in the probe mode. This gain will in turn give excess noise following the EIT transmission window as observed in [Hsu et al., 2006a] with a bright probe beam. Another possibility is that the fluorescence generated due to the pumping induced from the control field is being detected on the probe mode. The fluorescence emitted into the probe mode will be filtered by the transmission spectrum of the EIT feature leading again to excess noise within the EIT window.

These spurious effects are greatly reduced with the use of buffer gas or cold atoms that ensure a longer period spent within the control beam and reduce or eliminate atomic collisions with the cell wall. The ground state coherence can survive many collisions with the buffer gas which results in longer interaction time and narrower EIT features [Figueroa et al., 2006]. The situation also seems favorable in paraffin coated cells where no excess noise was observed [Cviklinski et al., 2007].

5.3.2 Squeezed light propagation through an EIT window.

With our low sideband frequency squeezing and without atomic noise generated from the EIT system, we can probe the efficiency of EIT as quantum delay line. Fig. 5.6(c) traces (v) and (iv) shows the typical transmission spectrum of squeezing and anti-squeezing through the EIT system. Around 2 dB of vacuum squeezed light was observed in the low frequency range. The roll up of the noise corresponds to the EIT Lorenztian transmission window. The antisqueezing displays the same feature and rolls down from 12 dB to almost 0 at higher sideband frequencies. The DC loss in this regime does not exceed 50% and still allows us to use noise-locking (see chapter 3) to stably control quadrature detection on the output homodyne.

This experimental set-up alone however does not allow a direct measurement of the delay experienced in the EIT medium. To do this measurement, we will split the squeezed beam into two parts and compare the quantum correlations between the part that is directly detected and the other part that goes through the EIT, as shown in Fig. 5.5. This also allows us to demonstrate the delay of continuous variable entanglement, as suggested, for example in Ref. [Peng et al., 2005]. The complete set-up is drawn Fig. 5.2.

5.3.3 Delay of entanglement

We now proceed and calculate the degree of entanglement produced by splitting our squeezed light source in two, and demonstrate that entanglement remains after transmission of one beam through the EIT medium. This is the experiment shown Fig. 5.5, including now the optional beam path and second homodyne detector. This system is similar to the case of chapter 2, where the passive loss on one of the arms is now the EIT medium. As we will see, biased entanglement is sufficient to find the delay and show preservation of wavefunction inseparability.

An initial characterization of our entanglement source was done off-resonance, i.e. without any active atoms in the gas cell. Around 1.5 dB of squeezed light was sent though the vapour cell and the remaining 1.5 dB in free space. The visibilities on the cell and free space homodyne detectors were 97 % and 99 % respectively.

The subtracted signals on both homodyne detectors were acquired for $0.5s$, mixed down digitally from 50 kHz to DC and low pass filtered at 10 kHz. This process gives a picture of the time domain data in a bandwidth around 50 kHz, as presented chapter 3. When measuring amplitude quadratures on both homodyne detectors, we obtain the scatter plot shown in Fig. 5.7(i). For phase quadrature measurements we get Fig. 5.7(ii). From this data, we calculate the conditional deviation ellipses. These ellipses are shown by the thick solid lines. The thinner circles show the QNL. We note that the ellipses are not rotated from the diagonal axis, which demonstrates that each beam experiences near equal loss.

From the conditional deviation curves we can read off the EPR and wavefunction inseparability criteria. We find EPR values of $\mathrm{V}^{+}(c|d)\mathrm{V}^{-}(c|d) = 0.8 \times 1.6 = 1.28 \pm 0.01$ and $\mathrm{V}^{+}(d|c)\mathrm{V}^{-}(d|c) = 0.8 \times 1.62 = 1.30 \pm 0.01$. The inference from d to c gives a slightly larger EPR value due to small extra losses from the cell windows and the difference in the homodyne visibility. These values are above 1, so according to the EPR criterion there is no entanglement. This is primarily due to the impurity of our squeezed state. Internal loss inside the OPO cavity always leads to squeezed states with non-minimum uncertainty and, as discussed, the EPR criterion is sensitive to the purity of the initial squeezing.

Using the wavefunction inseparability criterion we find $\mathcal{I} = 0.65 \pm 0.01$ which is clearly

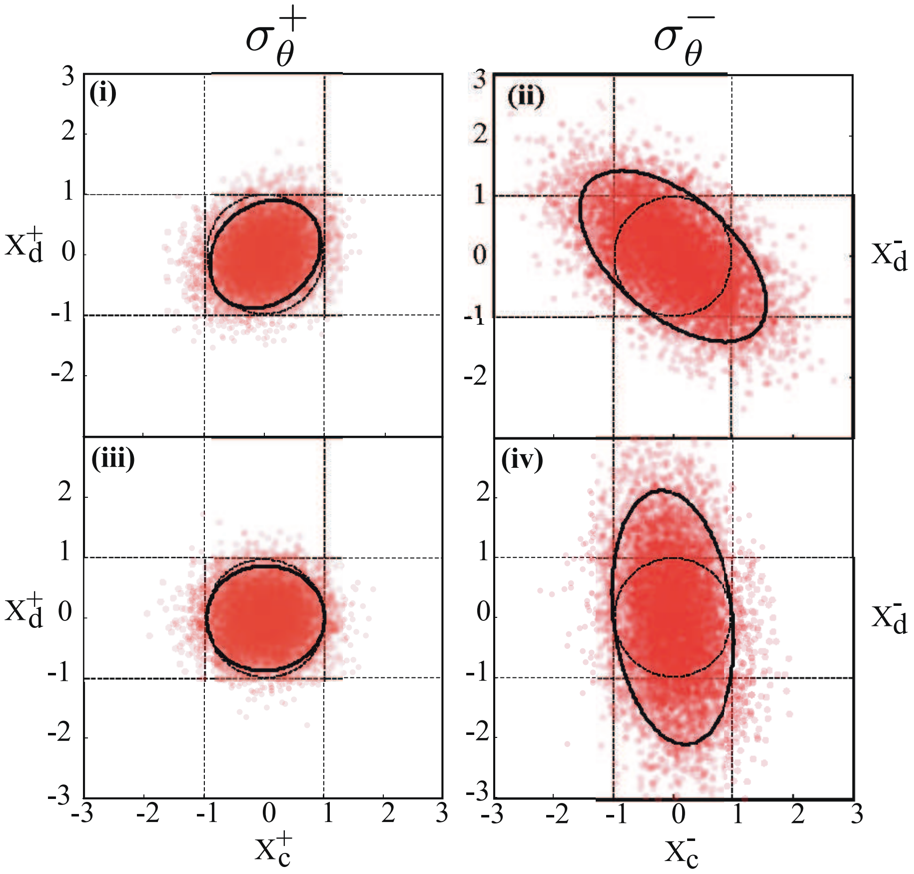

Figure 5.7: Correlation measurements. (i) and (ii): Scatter plots of the amplitude and phase quadratures respectively as measured for the beams c and d. The lasers were not resonant and there is no EIT. (iii) and (iv): Data as above but with EIT switched on. The solid black curves show the conditional deviation $\sigma_\theta^\pm$ calculated from the data. The dashed circles show the QNL conditional deviation obtained by blocking the two entangled paths. The coordinates of the red data points have been scaled down by a factor of two for clarity.

well below unity. So, while we can not show EPR, we easily show wavefunction inseparability.

Having established a performance benchmark using the off-resonant atoms we tuned the laser frequencies to obtain an EIT feature in our gas cell. Measurements of the amplitude and phase quadratures were made as for the off-resonant case and the data is shown in Fig. 5.7(iii) and (iv).

We note that the ellipse is now rotated compared to the off resonance case, indicating the presence of loss in the EIT medium. To better quantify this, we again use our entanglement criteria. As expected, we find distinct EPR measures depending on how the inference is done for the conditional variance measure. We find $\mathrm{V}^+(c|d)\mathrm{V}^-(c|d) = 1 \times 1.25 = 1.25 \pm 0.01$ and $\mathrm{V}^+(d|c)\mathrm{V}^-(d|c) = 0.8 \times 4 = 3.20 \pm 0.01$. We note that the presence of loss in the EIT medium does not change the conditional variance significantly when inferring from the beam propagating in free space.

From the criterion for inseparability we find $\mathcal{I} = 0.71$, after converting the covariance matrix to the required standard form or using $\min_\pm \sigma_\theta$. This value is higher than the off-resonance case but still below 1, demonstrating that our EIT system preserves inseparability.

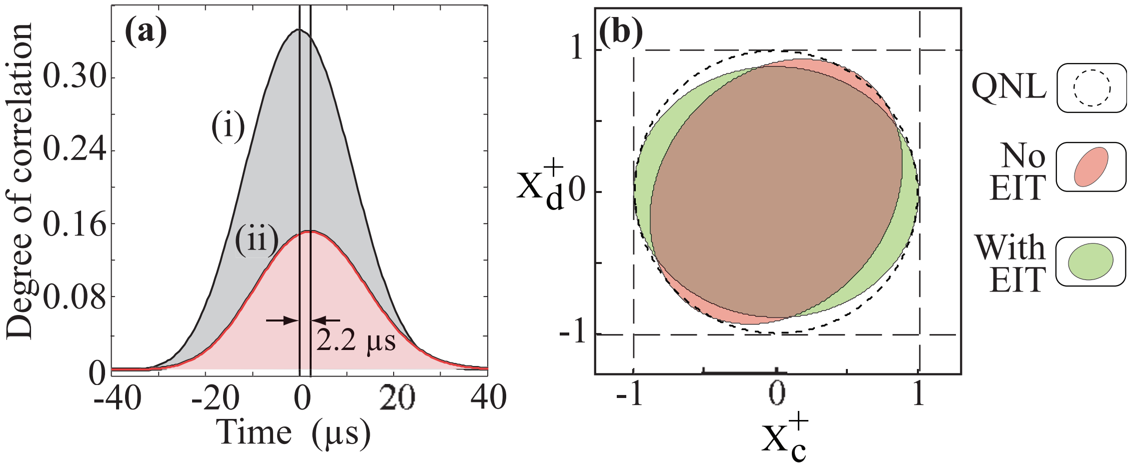

Figure 5.8: a) Degree of correlation between the two entangled arms as a function of delay, τ. b) Output photocurrent versus input photocurrent conditional deviations. The dashed circle represents the shot noise limit. The non-rotated and rotated plain line ellipses are the off-resonance and EIT case.

We now compute the degree of squeezing correlation $g(\tau) = \langle \mathrm{X}_c^+(t)\mathrm{X}_d^+(t-\tau)\rangle$ as a function of the delay, τ, between c and d. By looking for a peak correlation as a function of τ we can find the delay introduced by the EIT transmission. Fig. 5.8(a) represents the degree of correlation between c and d with the atoms off (i) and on resonance (ii). This shows that EIT delayed the transmission of beam c by 2.2 μs. Some amount of correlation is clearly lost in transmission through the EIT as the peak of curve (ii) is substantially lower than case with no EIT. Fig. 5.8(b) compares the amplitude quadrature conditional deviations with and without EIT. The reduced correlation is also clear in this figure.

Larger delays could not be observed due to the lack of noise-locking stability in the high optical depth or small control beam regime. Decreasing the control beam or increasing the optical depth cuts-off the frequency band necessary to obtain reliable noise-locking. At such low frequencies however, getting long term stability is particularly crucial since the intregration times required for measurement are also larger. An alternative to noise-locking would be some form of coherent vacuum locking, as demonstrated by Vahlbruch *et al.* [Vahlbruch et al., 2008]. In this scheme a frequency shifted beam is injected into the OPO. This beam also senses the OPO gain and can therefore be used for quadrature locking downstream. The only complication here is that this frequency shifted beam must also pass through the gas cell without disturbing the EIT properties or being absorbed.

5.4 Classical light storage using EIT

We showed that quantum states of light can be slowed down by several orders of magnitude smaller than the speed of light using EIT. One of the other attractive feature of EIT is its potential to store quantum states of light by manipulating the control field in time. We present here experimental results of storage and retrieval of a classical pulse from a gas of rubidium atoms in the same experimental conditions as for light delay. Our experimental results are found to be similar to the first demonstrations of light storage in [Phillips et al., 2001].

5.4.1 Experimental demonstration of light storage

To demonstrate the storage of a classical pulse, we used the left part of the set-up Fig. 5.2(iii) and flipped the removable mirror to use a different probe beam. Because both the probe and control beams here have to be controlled in time, the probe field is now frequency shifted by an AOM. The AOM is operated in double pass configuration and gives a total frequency shift of 160 MHz in the first diffracted order.

For this experiment, we kept the longitudinal DC magnetic field at 8.5 G. To maintain two-photon resonance, we shifted the control beam frequency by 154 MHz, using only one of the AOMs (AO_2 on the setup). The laser did not operate exactly on the transition $F_g = 2 \rightarrow F_e = 1$ anymore, so to enable long term stability of the laser, it was locked to the reference cavity[14].

The pulsing of the two light beams was done using a program written in Labview, that provided the synchronous control of 8 analog outputs. One of the outputs was used to gate a function generator that inputs programmable waveforms to a driver of the probe AOM (AO_3), thereby modulating temporally the power being diffracted. The maximum switching speed given by the AOM was measured to be around 100 ns. A second analog output was used as a TTL signal for a switch controlling the VCO driving AO_2. The other outputs were used to control magnetic fields in the Λ-GEM experiment chapter 8.

To store light in the atoms, we prepared the EIT feature, tuned the control beam frequency to ensure two-photon resonance and sent a weak probe pulse through the cell. We then turned off the control field, and switched it on again at a later time. Fig. 5.9-(a) and (b) shows the result of the light storage experiment for storage times of 1 μs and 10 μs respectively.

Trace (i) shows the input light field temporal profile. As expected the input light was then delayed after going through the EIT medium, resulting in a shifted maximum of the Gaussian pulse. The delayed light is shown trace (ii). As the group delay did not exceed the input pulse duration, only part of the light fitted the sample at any time. The best efficiency was found when the control beam was turned off at t=2μs, after more than half of the light had left the sample. Trace (iii) is the delayed light being detected before the turning off the control beam[15] (the control beam profile is shown by the dashed line above Fig. 5.9-(a)). At this point, the atomic coherence possessed information about the stored probe temporal profile, distributed spatially across the atoms. To retrieve the stored information, we turned the control beam back on.

When the control field was turned on, part of the stored probe field was reemitted out of the sample as shown trace (iv). The efficiency of the process (measured by calculating the output versus the input area) was only 5%, mainly limited by the fact that the pulse does not fit the atomic ensemble and by dephasing mechanisms. Longer storage times were achieved by switching the control field later, but with a significant reduction of efficiency due to the atomic decoherence. This can be seen Fig. 5.9(b) where the two traces show the transmitted and recalled pulses.

---

[14] The frequency noise introduced by the cavity locking (discussed chapter 3) does not affect the result presented here

[15] For the whole compressed pulse to fit the sample, a smaller group velocity of the probe inside the medium is required. As noted in the first chapter of this part, this can only be done optimally at large optical depths (or by shaping the control field in time[Gorshkov et al., 2007a]), which only enhances decoherences in our system. We come back to this time-bandwidth problem in chapter 7.

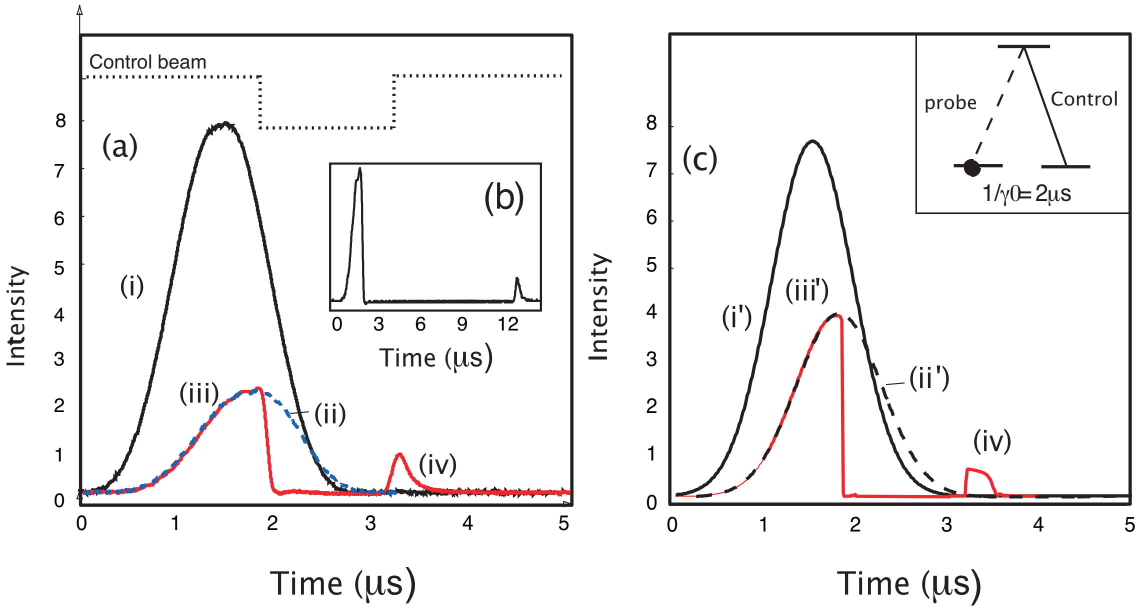

Figure 5.9: Light storage using EIT. (a)-(b) Experimental results, and (c) numerical modelling. (a) Trace (i) is the probe pulse measured by removing the cell from the probe path. Trace (ii) shows the delayed pulse after the cell, when the control field was constant in time. The control beam is turned off abruptly at $t = 2\mu s$ (the dotted line shows the control beam temporal profile). Part of the light had already left the sample, as can be seen from trace (iii). The information stored in the ground state coherence is then scattered off the sample by turning the control field back on. Trace (iv) is the recalled light pulse. (b) Same experiment for a storage time of $10\mu s$. (c) Numerical simulations using a ground state decoherence time of 2 μs.

5.4.2 Simulations

For a better understanding of the storage mechanism in our experiment, we performed semi-classical simulations of light storage including ground state dephasing. The optical depth, control beam power and decoherence were left as free parameters. Fig. 5.9-(c) shows the result of the simulations. A qualitative agreement between the experiment and the theory was found with $1/\gamma_0 = 2\ \mu s$.

We found it impossible, however, to obtain a quantitative result. The transmitted light (trace (iii')) could be made to match the height of the experimental trace (iii) (by changing the coherence time to $1/\gamma_0 = 5\ \mu s$) but the recalled output was then much weaker than the experimental curve. The ratio between the recalled and transmitted light varies dramatically with γ_0 in our theory. Experimentally, the ratio always seemed to stayed constant in any regime (for different optical depths or control beam powers). In our system, an extra source of loss seemed to affect the transmitted light (trace (iii)) without affecting the ground state coherence (responsible for the recall efficiency).

Dependence of losses with optical density

The efficiency of EIT is limited mainly by the lack of time bandwidth product, which can only be achieved at high optical densities. To improve on the efficiency of EIT, a study of the dependence of decoherences with optical depth is critical and will provide a figure of merit for comparing different atomic systems. Work in this direction was undertaken, for example by [Figueroa et al., 2006, Oberst et al., 2007]. Such characterization can be done in a number of ways, for example by measuring the light storage efficiency, the broadening of the EIT feature as a function of coupling beam power, measuring the atomic noise and/or using photon echoes.

5.4.3 Probing phase coherence

The experiment presented above was performed using a DC longitudinal magnetic field (to efficiently filter out the control field, as explained section 5.2) . We also did the experiment with the set of coils used for the Λ-GEM experiment presented in the second part of this thesis. The DC magnetic field could then be made linearly varying. This, in fact, provided a way to probe the phase coherence of the atoms, by monitoring the storage efficiency as a function of applied magnetic field strength and storage time.

We noticed that the magnetic field slope had to be optimized for different storage times to rephase the ground state coherence when all the fields are off. This is a good indication of the coherent nature of the process generating the output light, resulting from a constructive interference between the amplitudes of the individual dipole wavelets. When the atoms interact with a different magnetic field, they will acquire different phases during the storage time. In this case, the retrieval efficiency will depend (periodically) on the storage time, as was also studied in [Mair et al., 2002, Cviklinski et al., 2007].

5.5 Conclusion and perspectives

A narrow and large contrast EIT feature was generated in a warm ^{87}Rb vapour in the presence of buffer gas. Using a buffer gas allowed us to obtain quantum noise limited delay, removing the excess noise observed previously [Hsu et al., 2006a].

Using this system we demonstrated the efficient transmission of squeezing through an EIT feature. Out of an initial 3.2 dB of squeezing, 2 dB was observed at the EIT output. By splitting the squeezing in two, we generated a source of biased entanglement that could be used to measure the delay due to EIT transmission and also demonstrate preservation of wavefunction inseperability. With this method, we found our EIT system to delay light by about 2.2 μs. The wavefunction inseparability after EIT delayed of one half of the entangled state was measured to be 0.71.

We then investigated light storage and retrieval using a classical pulsed signal and stored information about the probe pulse for more than 10 μs in our buffer gas system. These results are steps towards the reversible storage of continuous variable quantum information, a necessary milestone for many quantum information protocols.

Part III

Gradient echo quantum memory

Chapter 6

Photon echo quantum memories using a reversible inhomogeneous broadening

In this chapter, we present the principles of quantum memories for light based on photon echo techniques. Specifically, we present the technique of Controllable Reversible Inhomogeneous Broadening (CRIB), a variant of the photon echoes memories [Hahn, 1950, Mossberg, 1982, Sjaarda Cornish et al., 2000], proposed for the storage of quantum states in [Moiseev and Kröll, 2001, Nilsson and Kröll, 2005]. Contrary to Hahn-echoes [Hahn, 1950], the CRIB technique can be used to store and retrieve quantum states from ensembles of three-level atoms with 100% efficiency. This chapter focusses mainly on the description of the interaction of many two-level atoms, that may or may not have the same absorption frequencies, with a classical light pulse. The tools given in this chapter are essential to understand the Gradient Echo Memory scheme presented chapter 7 and 8.

The chapter is organized as follows : In the first section, the interaction of light with an ensemble of inhomogeneously broadened two-level atoms is presented. Then, we focus on the atoms, and describe their evolution on the Bloch sphere. This allows us to introduce free induction decay, an important concept and a first step towards observing photon echoes. We then explain how photon echoes are generated and present the idea of Controlled Reversible Inhomogeneous Broadening as a mechanism to fully reconstruct a quantum state stored in inhomogeneously broadened ensembles of *three-level* atoms. Up to section 6.2, the equations describing the storage process will be made linear by a weak probe assumption so the treatment can easily be carried over to the quantum regime.

6.1 Interaction of light with inhomogeneously broadened two-level atoms

There has been a lot of interest for solid state materials [Ham et al., 1999, Alexander et al., 2006, Kurnit et al., 1964] and atomic gases [Mossberg et al., 1979, Patel and Slusher, 1968, Scully et al., 1968, Carlson et al., 1983, Sjaarda Cornish et al., 2000] as systems for information storage using photon echoes. For example, it was shown possible to take advantage of the broad absorption spectrum offered naturally by imperfect crystal structures, to store many bits of information [Mossberg, 1982].

To present the physics behind those protocols, we describe the interaction of light with inhomogeneously broadened two-level atoms. We first present the sources of broadening in solid state systems and gases, and introduce the mechanism of hole burning. We conclude this section by a theoretical description of the effects of broadening on the propagation of short and weak pulses of light. These theoretical considerations are important steps towards understanding the storage of quantum states using photon echo approaches.

6.1.1 Natural sources of broadening

Due to imperfect crystal structures in a solid, or due to atomic motion in a gas, the linewidth of the absorption profile broadens. This is because the absorption frequencies of the atoms differ from one another. The homogeneous linewidth (defined by $1/T_1$ in the first chapter) is then not measurable without extra specific techniques. The observation of the natural linewidth is even more difficult at high atomic densities where these effects are the largest.

The overall decay time caused by these inhomogeneous effects is quantified by T_2^*. Its origin is radically different to the damping terms $T_{1,2}$ that arise from the coupling of the atoms to vacuum modes of the sample. As the T_2^* is not related to an irreversible loss, if $T_{1,2} \ll T_2^*$, after light excitation, the total atomic polarization (sum of all the dipoles) will decrease because of the loss of macroscopic coherence. Microscopically, each atomic dipole coherence however keeps the same magnitude.

We first provide a summary of the inhomogeneous broadening present in the usual quantum memory systems, namely rare earth doped solid states and atomic gases. Then, we show how a weak light pulse propagates in such media.

Lanthanide

One of the systems of choice for quantum information storage, are rare earth solid states. Rare earths are also called lanthanides, where the $4f$ atomic orbitals are partially filled. The higher energy orbitals ($5s$, $5d$) in fact, screen the $4f$ orbital which creates an efficient shield against perturbations from the surroundings. The lifetime of each atom is then extremely long. The rare earths are often introduced as dopants in yttrium ortho-silicate (Y_2SiO_5) substrates and substitute for yttrium in vacancies. Because yttrium has about the same size as the lanthanides, the strain introduced by the host on the new dopants is minimal.

At room temperatures, homogeneous linewidths are broad because of spontaneous phonon processes. Typical values lie between 10 to 100 GHz. This can be tackled by working at helium liquid temperatures where phonons are efficiently suppressed. Long excited state lifetimes of about 0.1 seconds have for example been measured at 4 Kelvin [Sun et al., 2002]. Due to dipole-dipole interactions, the homogeneous linewidth is however slightly greater than the natural spontaneous emission rate.

Another issue in solid state systems is that, due to residual crystal strains, each ion in the crystal has a different frequency. The result is an inhomogeneous broadening on the order of 10's of GHz. This can be alleviated by using *hole-burning*, a method that allows interaction with a chosen class of narrow linewidth ions. Let us briefly describe how it works here.

Hole burning inside a inhomogeneous profile.

To explain hole-burning, we consider the level structure of praseodynium shown Fig. 6.1-(a). In Fig. 6.1-(b) we show the absorption profile of a probe field A. The general

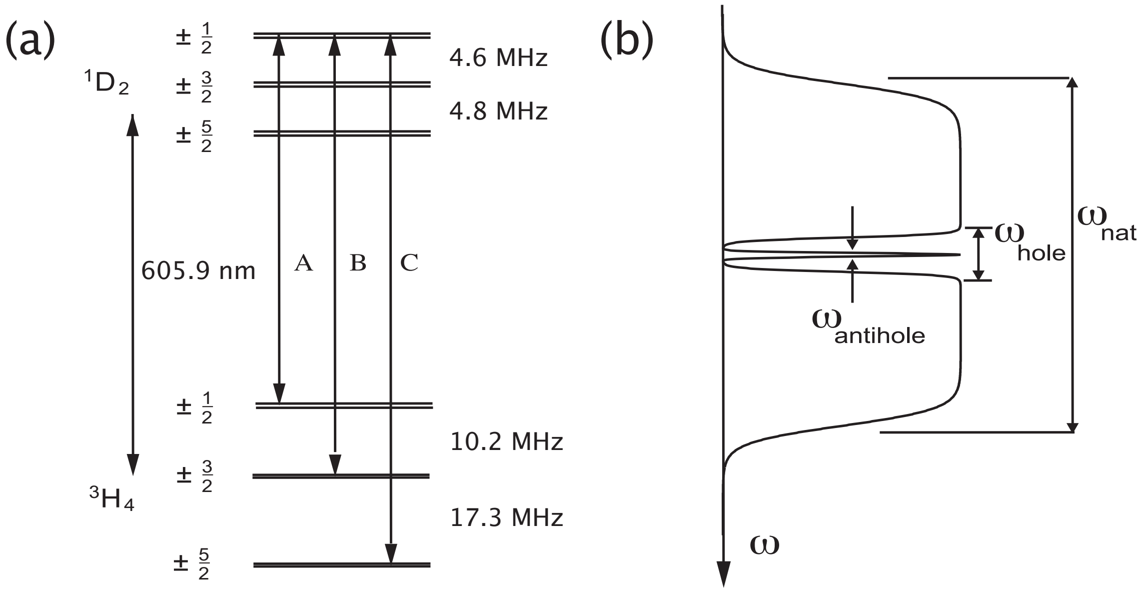

Figure 6.1: Energy level diagram and spectral scheme for the praseodymium dopants in yttrium orthosilicate Pr^{3+}:Y_2SiO_5. The light at frequency A is the light to be stored by the memory. Explanations in the text.

idea is to deplete the ground state population of a class of atoms via optical pumping and to repopulate only one class by pumping back from other levels.

The natural inhomogeneous linewidth of the sample, ω_{nat}, is a few GHz wide. An applied light is swept around frequency A to create a spectral hole a few MHz wide, ω_{hole}. A narrow linewidth laser is then applied at frequencies B and C to pump back atoms into the original ground state, thereby preparing a narrow antihole around A with linewidth ω_{anti} at the chosen center frequency. Antihole widths varying around $\omega_{\text{antihole}} \approx 30$ kHz were reported using this technique in praseodynium [Fraval et al., 2004] and erbium [Pryde et al., 2000]. The technique allows one to address extremely narrow linewidth two-level atoms at a certain frequency.

More details about hole burning and lanthanide spectroscopy can be found in [Longdell, 2003].

Atomic vapours

We already described inhomogeneous broadening in vapour cells in some details in chapter 5. We here give a brief summary. In warm vapour cells, the Doppler broadening can reach 500 MHz due to atomic motion (at around 50 C) whilst the homogeneous linewidth is around 6π MHz in Rubidium 87 (corresponding to an excited lifetime of 27 ns).

Contrary to solid state systems, where the broadening has to be eliminated for many memory applications, Doppler broadening is not a major limitation when operating with co-propagating beams. The issue here, is to operate faster than the time of flight of the atoms in the beam. Solid state systems offer a great advantage over gas cells in that respect. Storage times of seconds were for example reported in [Longdell et al., 2005] using EIT in a erbium doped yttrium ortho-silicate (Y_2SiO_5). To obtain longer coherence times in gases, one option is to work with cold atoms.

6.1.2 Other broadening mechanisms

In the above mentioned systems, there are other potential issues that one has to suppress to implement an efficient memory. We list here two other sources of broadening from possible experimental imperfections.

Control beam spatial profile

In nearly all current experimental operations, quantum memories rely on auxiliary beams. They are used to couple to ground states for longer storage times or prepare the medium initially. Those beams have to interact *in the same way* with all the atoms. If this is not the case, extra sources of broadening will be introduced, usually not included in theoretical treatments.

Memory protocols often rely on initial pumping to a single atomic sub-level. The efficiency of this preparation stage might not reach 100% due to atomic collisions or dipole-dipole interactions. The control beams used will then be absorbed and the optical intensity seen by the atoms will drop with distance. Such longitudinal inhomogeneities imply that the effective optical depth depends on propagation distance, and the way the storage mechanisms work might then change significantly. The same applies if the hole burning mechanism is not efficient enough.

Another perhaps most obvious problem, is the fact that the light beam transverse mode is not flat. This means that the atoms in the center of the beam will contribute differently compared to the atoms on the side. Such a transverse inhomogeneity can be solved by working with apertured beams, or by making the control beams bigger than the interaction area of the quantum state to be stored. Diffraction effects might still be an issue here, and limit the efficiency.

Inhomogeneous magnetic field

Whether information is encoded onto a ground state coherence or superposition between ground and excited states, the energy difference has to be very well controlled. The Earth's magnetic field strength is on the order of 500 mG. In rubidium atoms the Zeeman response to a magnetic field is around 1 MHz/G. As the stray magnetic field is not homogeneous in space, and is of course not in the same direction as the quantized mode of the sample, level shifts on the order of MHz's will be generated. The magnetic field therefore has to be controlled appropriately. As we saw in chapter 5, μ-metal shielding is an expensive, but easy way to control the residual magnetic field induced broadening in gas cells. In magneto-optical-traps, μ-metal shielding cannot easily be engineered to suit the space requirements and extra magnetic coils are usually placed around the cell containing the vapour to cancel the earth magnetic field.

In solid state systems, the magnetic field is usually not an issue since the magnetic susceptibility is small. Controlling larger magnetic fields can in fact become an advantage and can improve the hyperfine coherence times [Longdell et al., 2006].

The distribution of frequency shifts introduced by the above mechanisms can, for example, be modelled as a Lorentzian centered at 0 with a FWHM of $1/T_2^*$

$$g(\Delta) = \frac{1}{1/T_2^* - i\Delta}. \tag{6.1}$$

Although in Doppler broadened systems, a Gaussian distribution is closer to reality, the physics does not depend critically on the shape of the distribution. The influence of the different distributions in the efficiency of light storage was for example studied in [Sangouard et al., 2007, Gorshkov et al., 2007d].

We will now study the propagation of a pulse short compared to the natural linewidth of the two-level atom excited state, with and without inhomogeneous broadening.

6.1.3 Absorption of weak and short light pulses

The treatment of the absorption of weak and short pulses by ensembles of two-level atoms will be studied in two regimes : when the inhomogeneous broadening is larger and smaller than the pulse spectral width respectively. In both regimes, the pulse duration t_0 is assumed shorter than the excited state lifetime, so we ignore decay from the excited state here. We provide a summary of the solution given in [Crisp, 1970].

We assume that we have a cylindrical sample, such as the one depicted chapter 1 Fig. 1.2, where the inhomogeneous broadening is uniform in space but when we have many atoms with different frequencies within each slice δz. The averaged atomic dipole operators at a frequency detuning Δ are defined here as

$$\hat{\sigma}_{ij}(z,t,\Delta) = \frac{1}{N(\Delta,z)} \sum_{z_k \in \delta z} \hat{\sigma}^k_{ij}(z,t,\Delta), \tag{6.2}$$

where $N(\Delta, z)$ is the number of atoms at a frequency detuning Δ within a slice δz of the sample. We now assume that the light field is weak so that the operators can be treated as c-numbers. We have, in the weak probe regime and in the interaction picture, (from Eq. 1.43 in the first chapter)

$$\frac{\partial}{\partial t}\sigma_{12}(z,t,\Delta) \quad = \quad -i\Delta\sigma_{12}(z,t,\Delta) + ig\mathcal{E}(z,t). \tag{6.3}$$

One can write the Maxwell equation (in a moving frame at the speed of light) as

$$\frac{\partial}{\partial z}\mathcal{E}(z,t) \quad = \quad igN \int d\Delta g(\Delta)\sigma_{12}(z,t,\Delta), \tag{6.4}$$

where the quantity $g(\Delta)$ is defined by Eq. (6.1). This equation describes the influence of the atoms, within a slice δz, on the light evolution.

Solutions

We now derive a general expression for the pulse at any point in space as a function of the input pulse. After solving Eq. (6.3) in the time domain, and Fourier transforming in frequency space, we obtain

$$\sigma_{12}(z,\omega,\Delta) \quad = \quad ig\mathcal{E}(z,\omega)\big[\delta(\Delta-\omega) + \frac{1}{i(\Delta-\omega)}\big], \tag{6.5}$$

where δ is the Dirac distribution. Substituting this expression in the Maxwell equation (6.4), we obtain

$$\Big(\frac{\partial}{\partial z} + \Lambda(\omega)\Big)\mathcal{E}(z,\omega) \;=\; 0, \tag{6.6}$$

where

$$\Lambda(\omega) \;=\; -g\mathcal{N}\int d\Delta g(\Delta)\Big[\frac{1}{i(\omega-\Delta)} + \delta(\omega-\Delta)\Big]. \tag{6.7}$$

$\Lambda(\omega)$ is the susceptibility of the medium, quantifying the losses and phase shifts imposed by the atoms on the laser field. Fourier transforming back in the time domain, we find that the field evolves with distance like

$$\mathcal{E}(z,t) \;=\; \int d\omega \int dt'\; \mathcal{E}(0,t')e^{i\omega(t-t')}e^{-\Lambda(\omega)z}. \tag{6.8}$$

An analytical expression can not be found easily in the general case, but it is straigthforward when the input pulse Fourier width $1/t_0$ is smaller than the inhomogeneous broadening width $1/T_2^*$. We first solve the equation in this regime and then in the intermediate regime where the pulse width t_0 is shorter than, or on the order of, the inhomogeneous decay time T_2^*.

Exponential absorption

In the case where the input pulse Fourier width is smaller than the inhomogeneous broadening width $1/T_2^*$, we find a simple relation between the susceptibility and the inhomogeneous broadening

$$\Lambda(\omega) \;=\; -g\mathcal{N}T_2^*. \tag{6.9}$$

When inserting this expression into Eq.(6.8) we find

$$\mathcal{E}(z,t) \;=\; \mathcal{E}(0,t)e^{-g\mathcal{N}T_2^* z}, \tag{6.10}$$

which shows that the field amplitude decays exponentially with distance, as described by Beer's law. We also note that no phase shift is present. This behavior is shown Fig. 6.2-(a) where the propagation of a Gaussian pulse, with a duration $t_0 \gg T_2^*$, is shown for different points in the sample[1].

Anomalous absorption

When the pulse spectral width is larger than the inhomogeneous broadening, the frequency dependence of the susceptibility makes it hard to obtain an analytical solutions for Eq. (6.8). We solve the problem numerically using XMDS[2].

To model inhomogeneous broadening, the atomic detunings are distributed periodically using a sine wave that oscillates at a spatial frequency k much larger than the rate at which

---

[1] Of course, this scaling law only holds when the broadening does not depend on propagation distance. We will for example show in the next chapter that, when the broadening varies linearly with distance, a totally different result can be found.

[2] The description of the method was given chapter 1.

the phase of the field changes[3]. As we used a sine wave, the distribution of frequency shifts is not a bell-type distribution but the physics is qualitatively the same, and we found similar results to the work of Crisp [1970]. We consider that in a slice δz on the order of one period $2\pi/k$ we have many atoms within a band of frequencies $\Delta\omega = 1/T_2^*$.

We plot the evolution of the light field for different propagation distances when the pulse width t_0 satisfies $t_0 = T_2^*/10$ in Fig. 6.2-(b). In this case, the field phase changes as a function of time and space and the pulse propagation is not as simple anymore, as the different Fourier components of the light are phase shifted by off resonant atoms and not absorbed as efficiently. This results in a significant distortion of the input pulse.

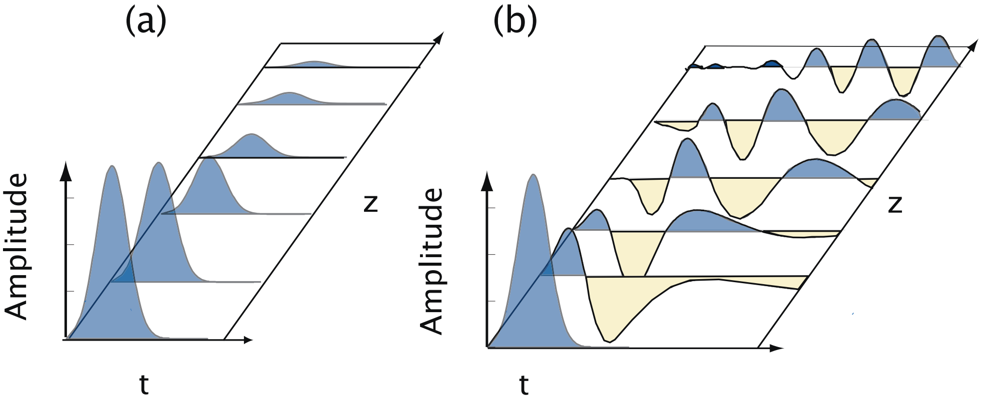

Figure 6.2: Absorption of a weak pulse of full width at half maximum t_0 through an inhomogeneously broadened medium, when (a) $T_2^* = t_0/10$ and (b) when $T_2^* = 10\ t_0$. The two graphs represent the real part of the light field as a function of time for different points in the sample.

The results found Fig. 6.2-(a) are not surprising. All the Fourier components are absorbed by the same amount at each slice δz so each Fourier component obeys Beer's law. We then expect from a linear system, that the total pulse area also drops exponentially with distance.

To explain the results found Fig. 6.2-(b), it is instructive to calculate the dispersion relation associated with the two-level atoms, in the limit where there is no broadening. Fourier transforming Eq. (6.3) and (6.4) in the spatial and temporal frequency domains, we find the simple relation $\omega = -g\mathcal{N}/k$. The group velocity $v_g(\omega_0) = \partial\omega/\partial k|\omega_0$ is then defined around any frequency ω_0, and equals $\omega_0^2/(g\mathcal{N})$. It is then small for large optical density and small frequencies. This explains the propagation dynamics of the short pulse. As the pulse enters the medium, the large frequency components are transmitted at the speed of light, whereas the small frequencies slowed down and escape the medium much later.

6.2 Representation of two-level atoms on the Bloch sphere.

The study of the propagation of short pulses of light in two-level atoms is an important step towards the storage and recall of quantum states. Another necessary approach is the atomic evolution during the light propagation. This is what we provide in this section.

---

[3] We checked for self-consistency by running simulations for much larger oscillations frequencies k, making sure the same results were obtained.

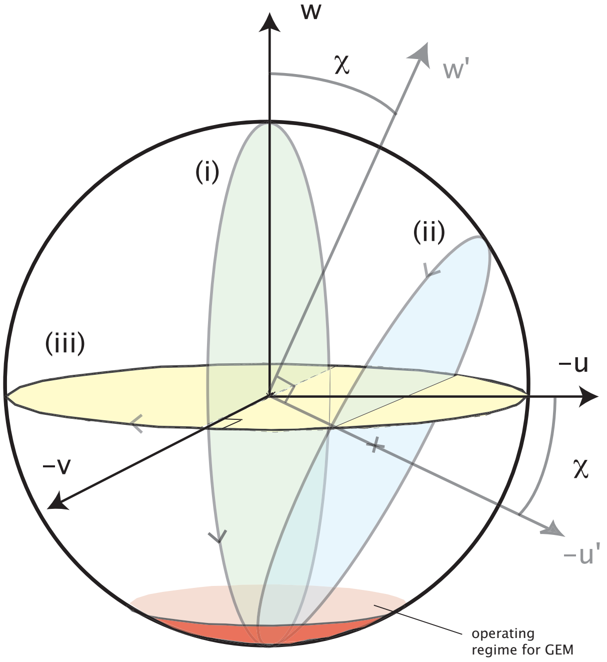

Figure 6.3: The Bloch sphere. Evolution of a single atomic dipole on the Bloch sphere for three different situations. Trace (i) shows the evolution of the atom on resonance with the light excitation, as a function of time. Trace (ii) shows the evolution of the atom for an off resonance excitation and trace (iii) shows its evolution after excitation by a $\pi/2$ pulse. The red shaded volume corresponds to the operating regime for the Gradient Echo Memory.

We will here assume that the input light pulse is turned on and off quickly and stays constant with space. That is, we neglect its dependence with propagation distance thereby describing a thin slab of material. In most of this section, we also ignore the time variation of the probe field[4]. These two assumptions greatly simplify the equations, but ignore interesting light-atom superpositions, that will be presented in the next chapters. We will use large area input pulses for clarity here, but the physics of the rephasing is qualitatively the same as for small area pulses.

We first present the evolution of a single dipole exited by a light field, introducing the *Bloch sphere*, then move to the evolution of a collection of dipoles within the thin slab, introducing the important concept of *free induction decay.*

6.2.1 The Bloch sphere

A common representation of the two-level atom is the Bloch sphere. To write equations of motion in the Bloch sphere frame, we perform two transformations on Eq. (1.42) of chapter 1. Let us introduce the population inversion $S_3 = \sigma_{11} - \sigma_{22}$, and the two quadratures of the atomic dipole, $S_1 = \sigma_{12} + \sigma_{21}$ and $S_2 = -i(\sigma_{12} - \sigma_{21})$. In this coordinate system

---

[4] The associated frequency spread would in fact result in the propagation dynamics presented in the earlier section.

Eq. (1.42) can be written

$$\frac{\partial}{\partial t}\begin{bmatrix} S_1 \\ S_2 \\ S_3 \end{bmatrix} = g \begin{bmatrix} 0 & -\Delta & -P(t) \\ \Delta & 0 & X(t) \\ P(t) & -X(t) & 0 \end{bmatrix} \begin{bmatrix} S_1 \\ S_2 \\ S_3 \end{bmatrix}, \tag{6.11}$$

where we introduced the light classical quadrature operators $P(t) = -i(\mathcal{E}(t) - \mathcal{E}^*(t)) = \mathcal{E}_0(t)\sin\phi$ and $X(t) = \mathcal{E}(t) + \mathcal{E}^*(t) = \mathcal{E}_0(t)\cos\phi$. This equation can be written in an even simpler form by performing a rotation of angle ϕ, $(u, v, w) = (\cos\phi S_1 + \sin\phi S_2, -\sin\phi S_1 + \cos\phi S_2, S_3)$. We then get

$$\frac{\partial \overrightarrow{\rho}}{\partial t} = \overrightarrow{\Omega} \times \overrightarrow{\rho}, \tag{6.12}$$

where $\overrightarrow{\Omega} = (-g\mathcal{E}_0(t), 0, \Delta)$ and $\overrightarrow{\rho} = (u, v, w)$. (u, v, w) is the orthogonal basis used to represent the atomic evolution on the Bloch Sphere. Equation (6.12) describes a precession of $\overrightarrow{\rho}$ around the vector $\overrightarrow{\Omega}$ at the generalized Rabi frequency $\Omega = \sqrt{\Delta^2 + (g\mathcal{E}_0(t))^2}$, *Rabi flopping*, and has a natural graphical representation on the Bloch sphere shown Fig. 6.3). The specific parameter regimes defined on the sphere will be presented next.

When spontaneous emission is ignored, the Bloch sphere has a radius of 1. We will again not discuss the effects of spontaneous emission here. Full solutions of the problem can be found in [Torrey, 1949].

On-resonance situation

Let us consider the on-resonance situation, where $\Delta = 0$. We can here solve equation (6.12) and still keep the time dependence of $\mathcal{E}_0(t)$. In this case the solutions for $\overrightarrow{\rho}$ are found to be

$$\overrightarrow{\rho} = \begin{bmatrix} 0 \\ \sin\mathcal{A}(t) \\ \cos\mathcal{A}(t) \end{bmatrix}, \tag{6.13}$$

where we assumed the atom to be initially in the ground state, and introduced the dimensionless parameter $\mathcal{A}(t) = \int_0^t g\mathcal{E}_0(t')dt'$, the *area* of the light pulse.

When the duration and strength of the light field interacting with the atoms are such that $\mathcal{A} = \pi$, the atomic dipole is fully inverted (the population difference $w = -1$) and the optical coherence is zero. This corresponds to the Bloch vector pointing to the north pole of the Bloch sphere. When the duration and strength of the light field are such that $\mathcal{A} = \pi/2$, the dipole is in a superposition between states $|1\rangle$ and $|2\rangle$, and there is an equal probability of finding the atom in the excited or ground state, so $w = 0$. Fig. 6.3, trace (i) shows the evolution of the dipole on the Bloch sphere, on resonance. As discussed, the dipole executes a rotation around the vector $\overrightarrow{\Omega} = (-g\mathcal{E}_0(t), 0, 0)$.

Off-resonance situation

When the light field interacts off resonance with the atom, the vector $\overrightarrow{\Omega}$ is tilted by an angle $\chi = \arctan(\Delta/g\mathcal{E}_0(t))$, the evolution of the state vector on the Bloch sphere is represented by trace (ii). In this case one can perform a change of basis and get the same rotation but at the (now larger) generalized Rabi frequency Ω. We note that full population inversion is not possible off resonance, even for large Rabi frequencies.

A solution to equation (6.12) can also be found off-resonance, but in the case of a steady state field. It is worth writing down the solution

$$\overrightarrow{\rho} \;=\; \frac{1}{\Omega^2}\begin{bmatrix} -\Delta g\mathcal{E}_0(1-\cos\Omega t) \\ g\mathcal{E}_0\Omega\sin\Omega t \\ (g\mathcal{E}_0)^2\cos\Omega t+\Delta^2 \end{bmatrix}, \tag{6.14}$$

assuming again that the dipole starts off in the ground state.

Dipole evolution after excitation

Another important case is the evolution of the dipole after the light has been turned off.

Let us imagine that the atom is excited off-resonance by a $\pi/2$ pulse, where $g\mathcal{E}_0 \gg \Delta$[5]. After a fast switching of the field at a time $t = 0$, the torque vector $\overrightarrow{\Omega}$ rotates instantaneously[6] to an angle $\chi \approx \pi/2$. In the interaction picture, the further evolution of the dipole will be described by a rotation at a frequency Δ on the equatorial plane. This rotation is naturally described by the matrix

$$\begin{bmatrix} u(t) \\ v(t) \\ w(t) \end{bmatrix} = \begin{bmatrix} \cos\Delta t & -\sin\Delta t & 0 \\ \sin\Delta t & \cos\Delta t & 0 \\ 0 & 0 & 1 \end{bmatrix}\begin{bmatrix} u(0) \\ v(0) \\ w(0) \end{bmatrix}, \tag{6.15}$$

where the initial state is given by Eq. (6.14) when $g\mathcal{E}_0 \gg \Delta$ and $\Omega t = \pi/2$. We find the simple expression

$$\overrightarrow{\rho} \;=\; \begin{bmatrix} -\cos\Delta t \\ -\sin\Delta t \\ 0 \end{bmatrix}, \tag{6.16}$$

which describes the rotation of the dipole at a rate Δ on the equatorial plane of the Bloch sphere. Trace (iii) shows such a precession around the w axis.

6.2.2 Free induction decay

We now turn to the evolution of a collection of dipoles.

Let us consider a thin sample comprising many two-level atoms, all having different detunings with respect to the light field, with a distribution of detuning $g'(\Delta)$. In the frame we are using, the radiating part of the dipole is u. The amount of light that is radiated from a collection of atoms is then the coherent sum (or interference) of all the wavelets generated by each atoms that "were" in phase with the light. Let us write the macroscopic polarisation density P like

$$P(t) = \int d\Delta g'(\Delta)u(t,\Delta). \tag{6.17}$$

---

[5] This approximation does not change significantly the conclusion in this section and provides a clear picture of the physics.

[6] If the switching of the input field were done at a rate much smaller than the detuning, the torque vector $\overrightarrow{\Omega}$ would adiabatically follow the change in Rabi frequency. Again, here we do not consider the time dependence of $\mathcal{E}_0$.

We now calculate P after having excited the atoms by a $\pi/2$ pulse. After the light pulse is off, all the atoms are displaced from the south pole with angles that depend on their detunings with respect to the light field frequency, as we discussed earlier on. The dipoles precess around their respective torques, as described by Eq. (6.16). Let us assume that the medium comprises a collection of atoms that, this time, have a Gaussian distribution of frequencies. We then have

$$g'(\Delta) = \frac{T_2^*}{\pi} e^{-\frac{-(T_2^*\Delta)^2}{\pi}}. \tag{6.18}$$

The total atomic polarisation can then be calculated to be

$$P(t) = e^{-t/T_2^*}. \tag{6.19}$$

The total polarisation decays due to a destructive interference between all the dipoles' amplitudes at a rate $1/T_2^*$. The polarisation will then radiate light only for a time given by T_2^*, the inverse of the spread in frequency of the dipoles. This is termed *free induction decay* (FID). After a time $t > T_2^*$, $P(t)$ reaches zero but again, provided no spontaneous emission occurs, the atoms will still evolve on the Bloch sphere at their own frequencies so in principle, if one could keep track of the phase evolution of all the dipoles, one could reconstruct the initial light state.

The description presented here is a simplified version of reality. We ignored the spread of the input pulse frequencies and assumed it is essentially a monochromatic wave. We also assumed that the medium is optically thin. Including the finite duration of the pulse, some other frequency components of the light can be off resonant with the atoms which, in an optically thick medium, leads to interesting, but more complicated effects, as we will see in the next chapters.

6.3 Reversible absorption, photon echoes

The inhomogeneous broadening manifests itself as a drop of macroscopic coherence with a time scale T_2^*. As discussed above this loss is not irreversible. If after light exitation, one were able to "time reverse" the FID, the macroscopic coherence can be recovered in principle from the microscopic coherences and the light can be reemitted. This is the principle of photon echoes.

6.3.1 Hahn photon echoes

Photon echoes were first observed in a solid state using the inhomogeneous broadening introduced by crystal strains [Kurnit et al., 1964] and are the optical analog of spin echoes that have mainly been developed for nuclear magnetic resonance (NMR) Like in NMR, the rephasing was performed by applying a sequence of pulses as shown Fig. 6.4. A $\pi/2$ pulse is input to an ensemble of inhomogeneouly broadened two-level atoms (i). If its duration is about the inverse of the width of the broadening, the whole pulse frequencies are absorbed and decay exponentially with distance (as was shown Fig. 6.2-(a) for a small area pulse.). The atoms are excited in the equatorial plane and start to precess around the central axis, as depicted in (ii). The sign of the dipole rotation depends on the sign of their detunings with respect to the input light field frequency. The total macroscopic coherence then decays. If after a time shorter than the *homogeneous* damping of the atoms, a π

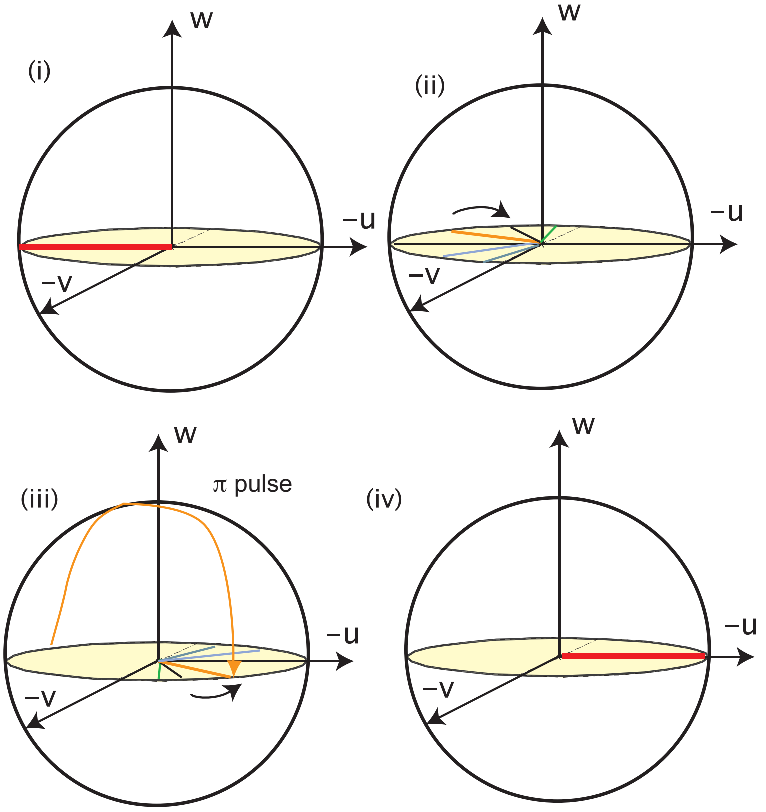

Figure 6.4: Sequence describing the production of a “standard” photon echo.

pulse is applied to the sample, the rotation of the dipoles is then reversed, as shown in (iii). After a time given by the time difference between the π pulse and the input $\pi/2$ pulse, the dipoles come together at the same point on the Bloch sphere (iv). This means that the macroscopic coherence is retrieved and the ensemble is capable of radiating light. An echo is then produced.

The technique is not efficient for quantum state storage using long optically thick samples. The reason is that atoms at the beginning of the sample will emit a light field that will be reabsorbed by (or interfere destructively with) the light that is emitted by other atoms at the same absorption frequency. The efficiency is then limited, and tends to zero at large optical depths. We will come back to this quantitatively in the next chapters.

A close variant of the technique was used to efficiently store many bits of information [Sjaarda Cornish et al., 2000]. By inverting the medium initially, efficiencies above 100% were actually reached using a close version of the Hahn-echo scheme. The technique will however not allow to store quantum states, as excess noise associated with amplification will mask the quantum statistics (as described chapter 2).

6.3.2 Storage of quantum states using Doppler broadened vapours

To fully reconstruct the input quantum state, one needs to satisfy phase matching. The lack of phase matching is precisely the reason why the output light interferes destructively with the other atoms during the rephasing, leading to a reduced echo amplitude. A method was proposed in [Moiseev and Kröll, 2001] to retrieve the global phase by using a π pulse in the reversed direction in a Doppler broadened ensemble of three-level atoms. The time

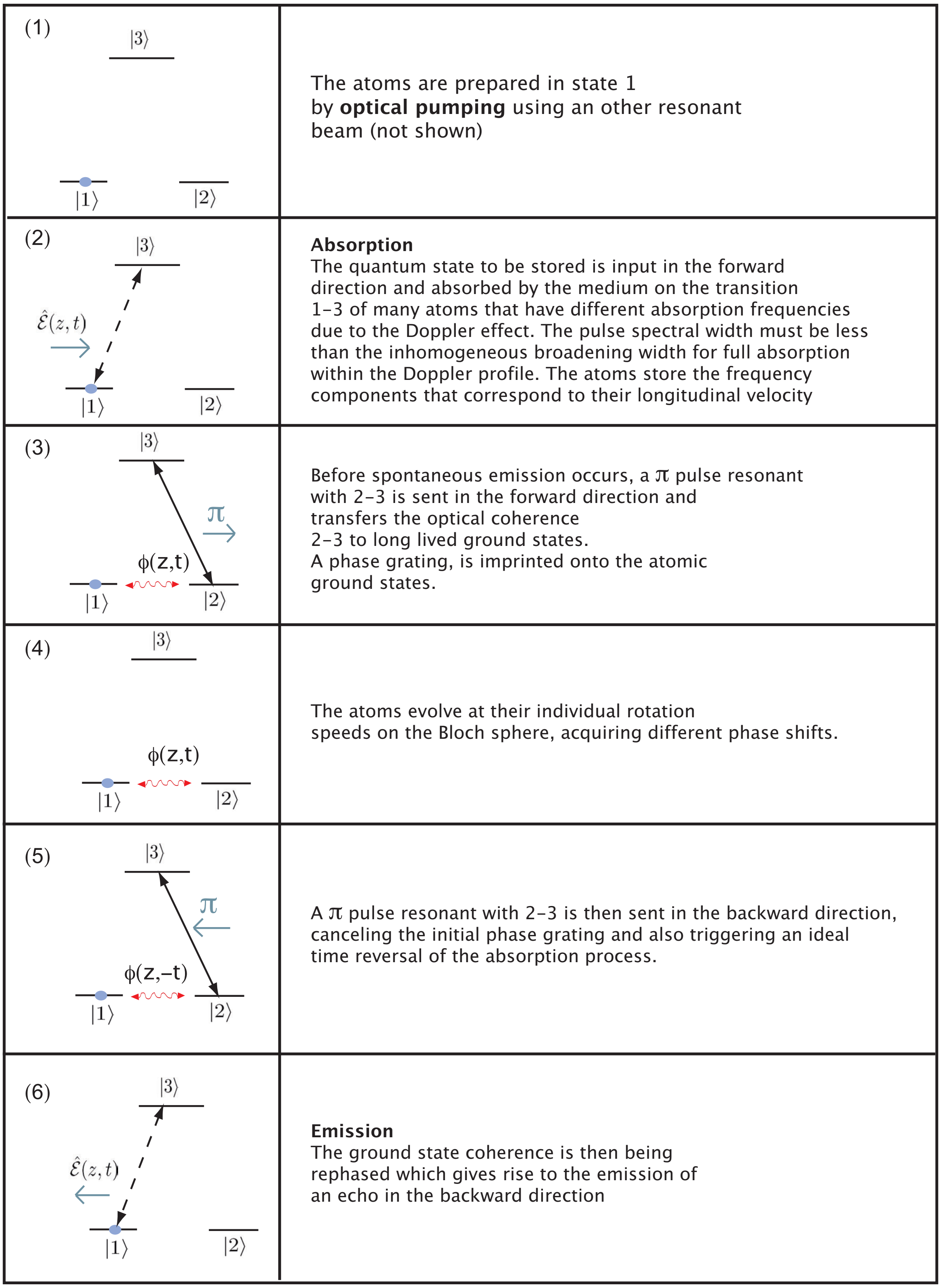

The atoms are prepared in state 1 by **optical pumping** using an other resonant beam (not shown)

Absorption
The quantum state to be stored is input in the forward direction and absorbed by the medium on the transition 1–3 of many atoms that have different absorption frequencies due to the Doppler effect. The pulse spectral width must be less than the inhomogeneous broadening width for full absorption within the Doppler profile. The atoms store the frequency components that correspond to their longitudinal velocity

Before spontaneous emission occurs, a π pulse resonant with 2–3 is sent in the forward direction and transfers the optical coherence 2–3 to long lived ground states. A phase grating, is imprinted onto the atomic ground states.

The atoms evolve at their individual rotation speeds on the Bloch sphere, acquiring different phase shifts.

A π pulse resonant with 2–3 is then sent in the backward direction, canceling the initial phase grating and also triggering an ideal time reversal of the absorption process.

Emission
The ground state coherence is then being rephased which gives rise to the emission of an echo in the backward direction

Figure 6.5: Principle of a quantum memory for light based on controlled reversible inhomogeneous broadening (CRIB).

sequence is shown Fig. 6.5.

The quantum state can fully be reconstructed at large optical depths using this technique [Moiseev and Kröll, 2001]. Such a sequence is however rather complicated as the timing precision of the π pulses is hard to achieve. Also, as it was proposed in an atomic gas, the storage is limited to about 10 μs [Nilsson and Kröll, 2005]. No experimental demonstrations of this scheme were reported in warm vapours.

6.3.3 Quantum memory using controlled reversible inhomogeneous broadening

Motivated by the potential of quantum memories for quantum information processing, new ideas quickly followed the initial proposal to store quantum states of light in different systems.

The rephasing was shown to be efficient in other ensembles of atoms provided the inhomogeneous broadening is controlled and reversible. To achieve such a rephasing in solids, the idea was to introduce an extra shift that can be controlled [Nilsson and Kröll, 2005, Kraus et al., 2006] and to *eliminate* any "uncontrolled" inhomogeneous broadening. To eliminate the uncontrolled inhomogeneous broadening in solid state systems, and thus prepare an initially narrow linewidth absorption line, hole burning may be used.

When a narrow homogeneous line is prepared, Nilsson and Kröll [2005] and [Kraus et al., 2006] suggested to broaden the line using Stark or Zeeman splitting[7]. No particular spatial profile for the broadening was suggested. The idea of the protocol is then close to the proposal from Moiseev et al., but allows the implementation from an initially homogeneously broadened system. π pulses driving an auxiliary level in the forward and backward directions are still required to achieve the phase matching requirement and obtain 100% efficiency in the backward direction.

Without auxiliary levels and π pulses, that is, by only flipping the inhomogeneous broadening after the light absorption, the efficiency was shown to be limited to 54% at some optimal optical depth in [Sangouard et al., 2007]. Such a simplified scheme is however particularly attractive as it only uses two-level atoms, allows the echo to come out in the forward direction and the only light seen by the ensemble is the light field of interest.

This two-level scheme was successfully implemented in [Alexander et al., 2006] using a linearly varying electric shift. Due to the lack of optical depth, the efficiency was only about -60dB. The full scheme using three level atoms and π pulses was then demonstrated later in [Alexander et al., 2007], where also multiple pulses were stored. At this stage again, the shape of the broadening was not shown to matter dramatically.

Once the absorption feature is prepared, the three-level scheme actually works without broadening, provided the bandwidth of the input pulse is within the absorption feature width. This adaptation of the CRIB proposal was realized by Gorshkov et al. [2007d]. The question arised then, what is the use of the initial broadening ? It was shown by Gorshkov et al. [2007d] that for single mode light storage (see chapter 2 for a definition) the improvement in the efficiency using an extra broadening is in fact limited.

6.4 Conclusion

We have described the interaction of short light pulses with inhomogeneously broadened atomic ensembles. We first presented the sources of broadening in various material systems. Then we derived and solved the equations describing the propagation of a short and

---

[7] Light shifts introduced by from a strong, focussed, off resonant beam were also suggested by Kraus et al. [2006].

small area light pulse with an inhomogeneously broadened system by varying the width of the broadening with respect to the light pulse Fourier width. In the second section we presented the evolution of the atoms on the Bloch sphere and introduced the concept of the free induction decay.

This background information allowed us to present photon echoes as a tool for quantum memory applications. We discussed the limits of the plain Hahn photon echo for quantum optical information storage. Then, we presented an approach that allows one to store and recall with 100% efficiency, a quantum state from a Doppler broadened vapour. The idea was adapted to other systems using a controlled reversible inhomogeneous broadening (CRIB) and we discussed the recent experimental results using CRIB in solid state systems. We then concluded by mentioning a recent work that aimed at finding the optimum parameters for a good efficiency of the storage devices [Gorshkov et al., 2007d]. The advantage of CRIB over an identical scheme without controlled broadening was shown by the authors of [Gorshkov et al., 2007d] to be limited.

Chapter 7

Gradient echo quantum memory for light

In this chapter, we describe a technique that allows efficient storage and retrieval of quantum states from ensembles of two level atoms, the Gradient Echo Memory (GEM). The technique is similar to the controled reversible homogeneous bradening technique (CRIB) presented in the preceding chapter. In contrast with CRIB however, the protocol is greatly simplified. By controlling a *monotonic* Stark-shift, an input pulse can be mapped onto two level atoms and retrieved in the forward direction by simply flipping the Stark-shift slope. The efficiency is 100% in the limit of large optical depth.

In the first section, we present the general properties of the quantum memory. We show the result of numerical simulations and present experimental demonstrations performed in a solid state system[1]. Experimental efficiencies of 15% were reached, in good agreement with the numerical simulations.

We enter in a bit more details in a second section, by studying the dynamics of the scheme. After calculating analytically the susceptibility of the medium, we identify freely evolving polariton modes. The GEM protocol in fact successively creates normal modes in the Stark-shifted medium. This is analogous to the polaritonic description of EIT. From this finding, we then draw a distinction between other memory schemes and GEM by noticing that GEM is a frequency encoding scheme in constrast with most memories, like EIT, where the information is stored spatially as the temporal profile of the input state. The consequence of this property is that GEM has a large time-bandwidth product.

In the last section, we finally present interesting properties of the GEM scheme. We show that the forward CRIB protocol can be though of as a sequence of GEM memories, allowing a clear insight to be gained into the CRIB performance. Next, we again highlight the frequency encoding nature of GEM by showing that we can optimize the storage of two continous variables modes by a proper engeering of the Stark-shift. This, for example, opens the possibility of simply and efficiently generating atom-light entanglement from a single squeezed light source. We then show that if the medium is initally inverted, the light can be stored and the echo comes out as an amplified version of the input state. We finish by showing that turning the Stark-shift slope to zero after the mapping stage creates a stationary light wave in the medium. The localised electromagnetic energy can be retrieved at will by tuning the Stark-shift slope to the opposite of its initial state.

---

[1] The experiment presented here was done in the Solid State Spectroscopy group at the Research School of Physical Sciences and Engineering by Jevon Longdell, Anabel Alexander and Matt Sellars.

7.1 Simulations and experimental demonstration

In this section, we present numerical simulations and experimental results of the Gradient Echo memory. We show that GEM can efficienctly store quantum states without excess noise.

7.1.1 Protocol

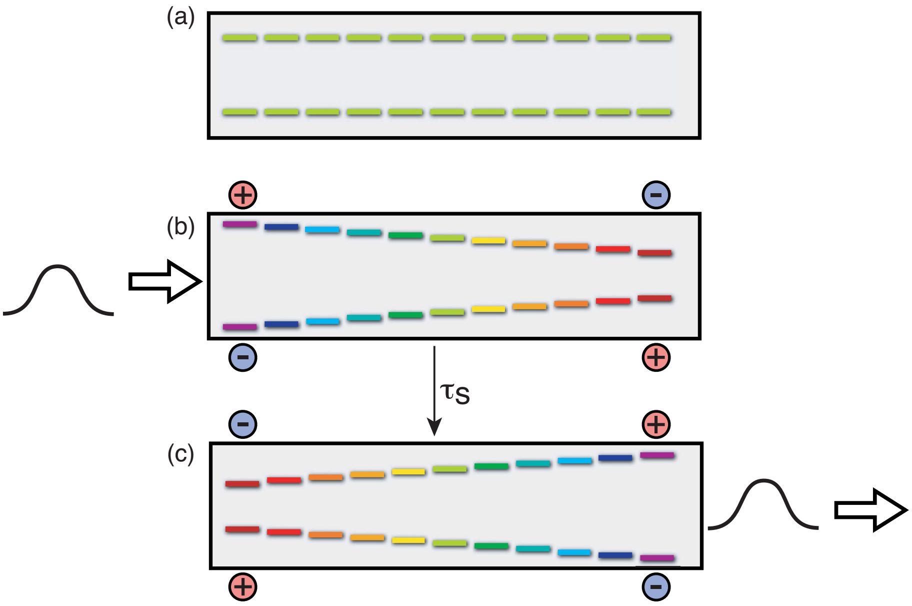

Figure 7.1: Schematic of the GEM protocol. (a) an ensemble of identical two level atoms is prepared. (b) A linear Stark shift is applied, thereby allowing the medium to absorb the input pulse. (c) After switching the polarity of the electric field, the input pulse comes out as an echo.

Figure 7.1 illustrates the GEM scheme. An ensemble of identical two-level atoms with homogeneous linewidth γ is subjected to an electric field that varies linearly with z causing a linearly varying Stark shift. A pulse of light is then sent into the storage medium. Provided the Stark shift width is larger than the pulse frequency spread, and the optical density of the sample is sufficiently high, each frequency component of the pulse is absorbed by two-level atoms at the right energy. Similarly to in nuclear magnetic resonance (NMR) where a magnetic field gradient is applied, the spectral components of the signal are thereby mapped linearly along the length of the sample. After excitation, the dipole ensemble dephases leading to a decay of the light field. It is, however, possible to recover the ensemble macroscopic coherence. After some time $\tau_s/2$ the electric field gradient is switched, leading to temporal and spatial reversal of the system dynamics. At a time τ_s, the dipoles have all rephased and the input light pulse emerges in the forward direction. The only light seen by the atomic ensemble during the entire process is then the light field of interest and the echo propagates in the forward direction without being reabsorbed provided the Stark-shift is linear along the sample length. We will show that the output echo is an ideal time reversed copy of the input field in the limit of large optical depth.

The principle benefit of such a two-level scheme lies in its simplicity. Firstly, the absence of phase matching π pulses greatly simplifies the implementation. The precision of the electro-optic switching is not as critical as the π pulse parameters. The scheme is also more robust than those using optical control, where cross-coupling and transverse-modal effects may reduce the process efficiency. Secondly, as the memory requires only two atomic levels, this scheme is applicable to many more atomic systems. In particular erbium dopants which allow operation at the tele-communication wavelength of 1.5 μm, have been shown to have very good two-level characteristics [Böttger et al., 2006], whilst a lambda system has yet to be demonstrated.

We now show that the memory allows the storage of quantum states with 100% efficiency at large optical depths.

7.1.2 Numerical simulations

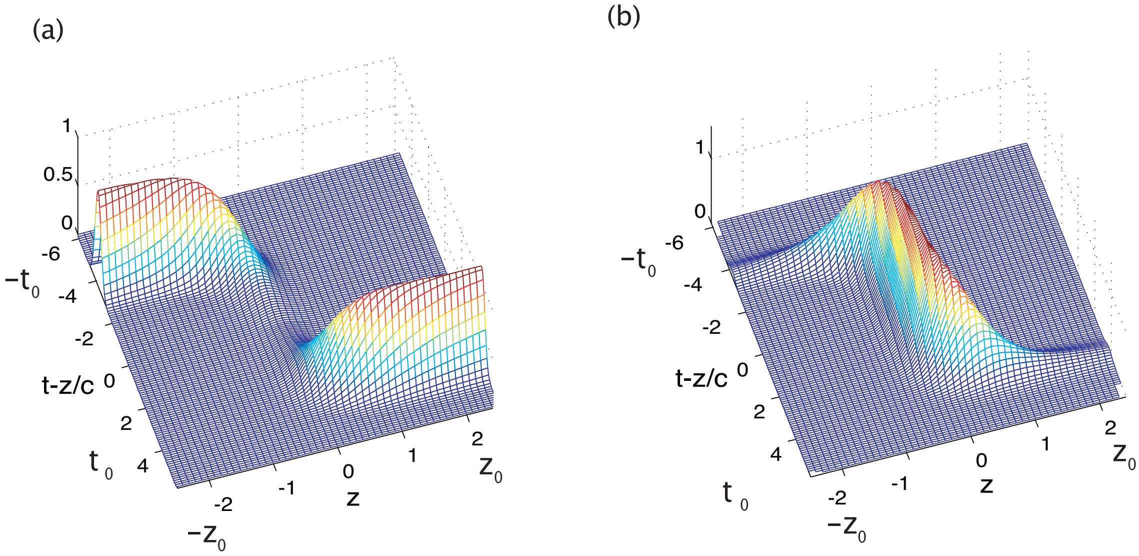

Figure 7.2: With no decoherence $\gamma = 0$, and the optical depth chosen to be $gN/\eta = 10/3$, (a) and (b) show the space-time grid plots of the light field intensity and the atomic polarization, respectively. The input pulse duration is $t_{\text{pulse}} = t_0/4$ and the quadrupole induced broadening is $2/t_{\text{pulse}}$.

To demonstrate the efficiency of the memory, we consider the interaction between a collection of two-level atoms and a quantum optical field with slowly varying envelope $\hat{\mathcal{E}}(z,t)$. As shown in Fig. 7.2 (a), a pulse with duration t_{pulse} enters the medium at $z = -z_0$, $t = -t_0$ and the detuning of the atoms is flipped at $t = 0$. We follow the same procedure as in [Fleischhauer and Lukin, 2000] and use locally averaged atomic operators. The Heisenberg-Langevin equations describing the interaction in a moving frame at the speed of light are in the interaction picture

$$\begin{aligned} \dot{\hat{\alpha}} &= - \quad (\gamma/2 \pm i\eta z)\hat{\alpha} + ig\hat{\mathcal{E}}(\hat{\sigma}_g - \hat{\sigma}_e) + \hat{F}_\alpha && (7.1)\\ \dot{\hat{\sigma}}_g &= \quad \gamma\hat{\sigma}_e + ig(\hat{\mathcal{E}}^\dagger\hat{\alpha} - \hat{\mathcal{E}}\hat{\alpha}^\dagger) + \hat{F}_g && (7.2)\\ \partial_z\hat{\mathcal{E}} &= \quad i\mathcal{N}\hat{\alpha} && (7.3) \end{aligned}$$

where $\hat{\alpha}$ is the atomic polarisation operator; $\hat{\sigma}_{e/g}$ the population of the excited/ground state; g the atomic transition coupling strength; $i\eta z$ is the linearly varying detuning from resonance. $\mathcal{N}$ is the effective linear density defined as $\mathcal{N} = gN/c$.

We also introduced γ as a decay rate from the excited state and the corresponding Langevin operators. Under a small pulse approximation, ensuring that a negligible amount of atoms reaches the excited state ($\hat{\sigma}_e \ll \hat{\sigma}_g$), the non-zero noise correlations are found to be [Cohen-Tannoudji et al., 1993]

$$\langle \tilde{F}_\alpha(z_1,t_1)\tilde{F}_\alpha^\dagger(z_2,t_2)\rangle = 2\gamma\frac{\delta(z_1-z_2)\delta(t_1-t_2)}{n\mathcal{A}}, \tag{7.4}$$

where $\mathcal{A}$ is the cross section area of the beam and n the atomic density. As was discussed chapter 1, because the spontaneous excitation of atoms to the excited states requires large energy, the noise arises from the normally ordered Langevin correlations and is therefore vacuum noise [Cohen-Tannoudji et al., 1993]. Furthermore, the Heisenberg-Langevin equations are linear after the weak probe approximation so the atomic and optical field variables can be treated as c-numbers [Fleischhauer and Lukin, 2000]. These two results ensure that transmissivity is the only quantity needed to fully characterize the memory.

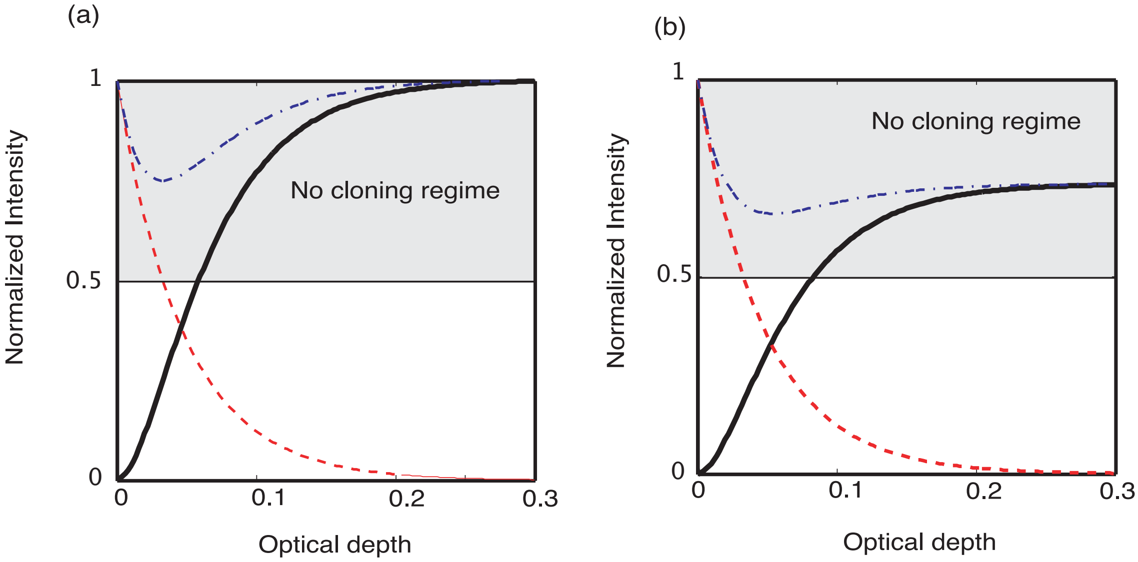

Figure 7.3: Memory efficiency as a function of optical depth when the Stark-shift is linear with position. Solid lines represent the efficiency of the memory; dashed lines, the fraction of transmitted light; and dot-dashed lines, the total energy exiting the medium. Shaded regions are the no-cloning regimes. Trace (a) and (b) show the result of simulations with and without decoherence respectively.

The effective optical depth of the sample is $g\mathcal{N}/\eta$. This ratio quantifies the portion of the input light that is not stored in the sample. $2\eta z_0$ on the other hand gives the spectral coverage of the absorption process. We will here let $g\mathcal{N}/\eta = 10/3$ and $2\eta z_0 = 2/t_{\text{pulse}}$ to ensure an optimum writing efficiency. The sign of the Stark-shift will be reversed after the absorption of the pulse. Fig. 7.2 (a) and (b) show the results of numerical simulations with a zero decay rate $\gamma = 0$. Fig. 7.2 (a) reveals that with these parameters, a large echo comes out of the sample after flipping the electric field. As the light pulse enters the medium, its frequency components gets mapped linearly across the sample. As a consequence, the temporal profile gets broader. Some atomic polarisation is then created. When the sign of the Stark-shift is reversed, the light leaves the medium in the forward direction out of the sample and the polarisation decreases. Because of the monotonicity of the Stark-shift with

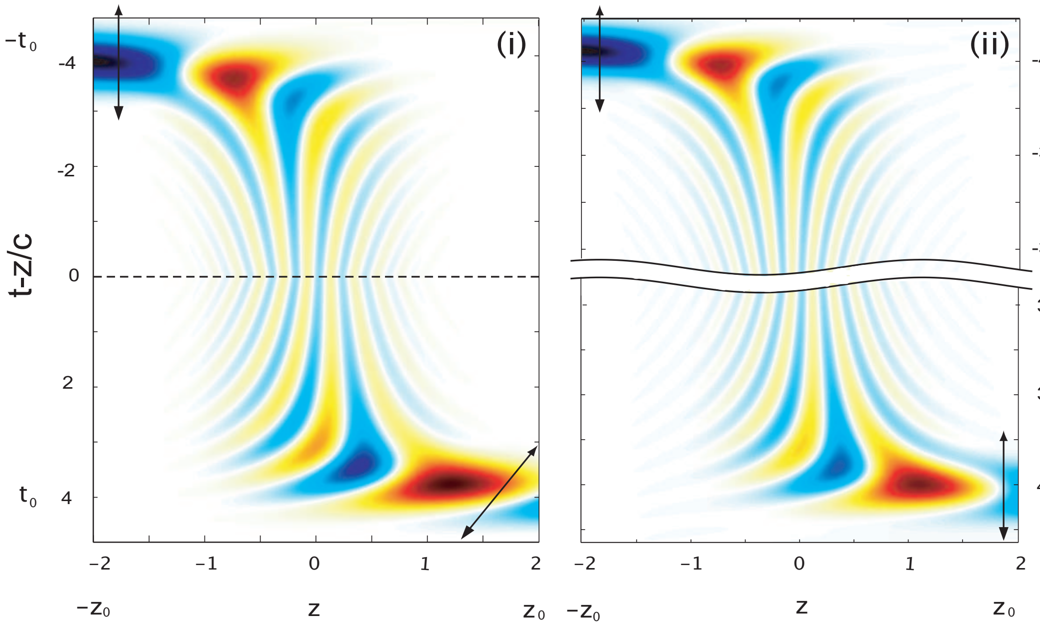

Figure 7.4: Real part of the optical field in a moving frame at c. At $t = -t_0$, the light field enters the sample and is gradually absorbed by the medium. At $t = 0$, the quadrupole field is flipped and the time reverse process commences producing a forward propagating pulse. For the parameters given in Fig. 7.2, with a storage time of $8t_{\text{pulse}}$, (i) shows a small phase shift across the retrieved pulse. With a storage time $80t_{\text{pulse}}$, (ii) shows a near ideal pulse retrieval. The arrows denote the wavefront of the light fields.

space, all the spectral components of the pulse escape the sample without being resonant with the atoms. A detailed description of this light-matter superposition in this scheme will be presented in the next section.

Figures 7.3 (a) and (b) show plots of the electro-optic memory efficiencies as a function of optical depth without and with excited state decay respectively. It can be seen in Fig. 7.3 (a) that the efficiency of our memory asymptotes to 100% with optical depth, whereas it was shown in [Sangouard et al., 2007] that the efficiency of such a two level atom electro-optic memory is limited when the broadening is non-monotonic. We will come back to this case in section 7.3.1. Fig. 7.3 (b) shows the result of simulations using a non-zero decay from the excited state. For these simulations we chose $\gamma = 0.04/t_0$. The no-cloning regime is still reached with this decoherence value but a higher optical depth is required.

Our modelling also demonstrates that a small spatial non-linearity of the Stark-shift, ηz, and finite switching speed of the applied electric field have very little influence on the efficiency. As the efficiency of our electro-optic memory can be well above 50% with no excess noise, the echo is guaranteed to be the best possible copy of the input state [Grosshans and Grangier, 2002a], demonstrating that our scheme is a quantum memory for light. More details about benchmarks for quantum memories can be found chapter 2.

Fig. 7.4 shows a contour map of the real part of the electric field. Because of the large phase shift seen by the field when it enters the medium, the last atoms in the sample absorb the field a long time after the first atoms. The storage time is then required to be large enough for the atoms to reradiate the whole input pulse. Fig. 7.4 (i) presents simulations where the storage time is four times the pulse duration. In that situation, a time varying phase shift is present across the output pulse, so that it is frequency shifted with respect to the input. Fig. 7.4 (ii) shows simulations where the Stark-shift is flipped after nearly all the atoms have absorbed the field. The frequency shift is then eliminated and only a constant phase shift is present.

Frequency shift compensation : One way of compensating for the frequency shift would be to cascade two electro-optic memories using opposite switching procedures. Another method would be to use an electro-optic phase shifter driven with the appropriate voltage waveform. Maybe a simpler way would be to introduce an electric field offset that matches the frequency shift at the output for the reading stage.

We will come back to a more detailed study of the dynamics of the memory in the next section.

7.1.3 Implementation in a solid state system

The initial demonstrations of photon echoes via CRIB used a linear Stark-shift [Alexander et al., 2006], as in the current proposal. At the time it was thought that a more difficult experiment involving an auxiliary atomic level and counter propagating π pulses would be required to achieve a quantum memory for light as discussed chapter 6. The above analysis shows that this is not the case.

Compared with the initial Stark-echo demonstrations of [Alexander et al., 2006], the efficiency has been improved by more than 5 orders of magnitudes, in complete agreement with the theory. A large part of this improvement is due to a change of the dopant ions used to praseodymium allowing larger optical depths to be reached.

The experiment was performed at the research school of physical sciences in the group of Matt Sellars. The experiment was carried out on a spectral antihole which was prepared as described in the preceding chapter, Fig. 6.1. Light from a highly stabilised dye laser was frequency shifted and gated with acousto-optic modulators. The pulse was then steered towards the sample of $Pr^{3+} : Y_2SiO_5(0.05\%)$. The sample was approximately a 4 mm cube and was held at temperatures in the range 2-4 K. Four electrodes were placed around the sample in a quadrupole arrangement and provided an electric field that varied linearly along the optical path. The electrodes were 1.7 mm diameter rods separated by 8 mm. Voltages of approximately ± 5 V were used to broaden the antihole and were able to be switched in 1 microsecond. Heterodyne detection was used to detect the transmitted pulses. The beam diameter in the sample was approximately 200 μm and the corresponding pulse areas $\pi/20$.

Fig. 7.5, traces (a) and (b), show the experimental traces of the electro-optic echo memory with and without the preparation of the two-level anti-hole. In the results, 49% of the incident light was transmitted straight through the sample (with less than 2% absorption without the antihole) and 15% of the total input light was recalled as an echo. The recall efficiency, defined as the ratio between the reemitted and absorbed light is 26 %, showing the potential improvements of our system with larger optical depths. A minimal output pulse distortion was observed, which demonstrates the rather large time-bandwidth product in our experiment. We will come back to this feature in the next section.

Using our numerical model, we vary the spectral width of the unbroadened anti-hole and the optical depth of the sample to match the experimental results. Close agreement between the experimental results and the simulations is obtained only with these two free parameters. Our numerical model suggests an anti-hole width of 30 kHz, in agreement with the experimental expectation if the hyperfine transition broadening were the main

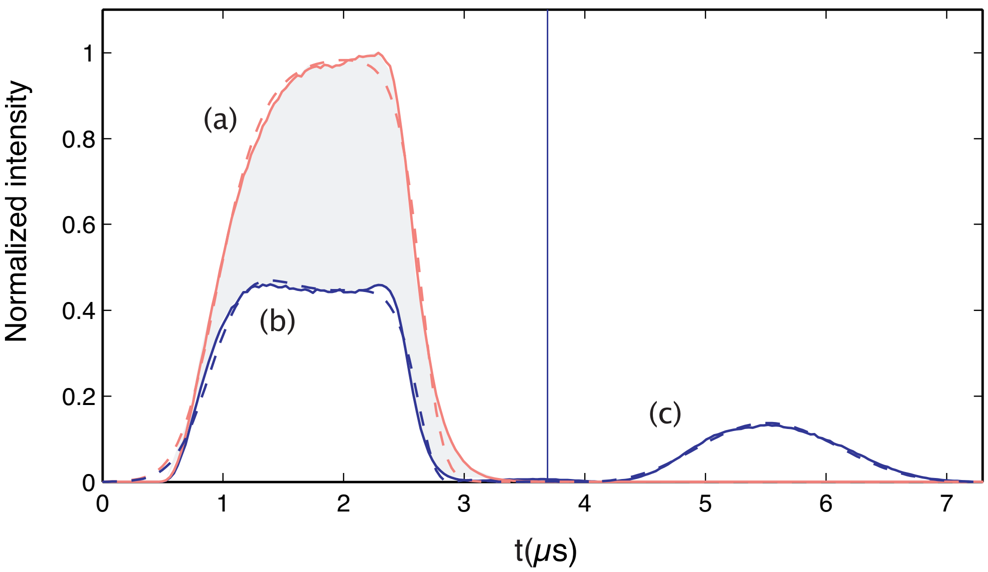

Figure 7.5: Experimental results (solid lines) and numerical simulations (dash lines) of the electro-optic echo setup. Trace (a) shows the input pulse detected after transmission through the sample when no antihole is prepared. Trace (b) shows the transmitted pulse and (c) the stored-and-recalled pulse components. The vertical line at 3.7 μs denotes the time at which the polarity of the Stark-shifting electric field is flipped.

limitation to the antihole width.

For a given pulse length, the optimization of the experiment is dependent on a compromise between increasing the ratio between applied and intrinsic broadenings and maximizing the optical depth of the sample. In our experiment, $2\eta z_0/\gamma$ is around 12 whilst the optical depth $g\mathcal{N}/\eta = 0.06$. For each crystallographic site where praseodymium is located, there is another related to it by inversion. In order to implement a completely efficient memory, only one of the site pair can be used. In principle, this could be achieved by Stark-shifting with a homogeneous electric field and optical pumping. In our experiment, however, both orientations were used. The theoretical modelling on Fig. 7.5 takes into account these two orientations by having two Bloch equations and two source terms for the optical field. Simulations suggest that using Fourier limited pulses, selecting only one orientation of the praseodymium ions and increasing the optical depth by a factor of three would enable the scheme to reach more than 50% efficiency.

In contrast to existing quantum memories based on controlled inhomogeneous broadening, our scheme requires only two atomic levels and is therefore applicable to a wide range of systems. Moreover, the scheme does not require auxiliary optical pulses for the imprint and recall process. Modest improvements on the experimental parameters will allow efficiencies higher than 50% to be achieved.

7.2 Dynamics of the memory

We have shown that the gradient echo memory is perfectly efficient in the limit of large optical depth and presented the properties of the memory. We calculated numerically the evolution of the phase of the probe and described what happened at short switching times.

In the present section, we give more detail and study the internal evolution of the light-atoms superposition. We find that, just like EIT, the gradient echo memory is capable of creating polaritons by controlling of the Stark shift slope with time. Before coming to this polariton description, we first calculate the susceptibility of the medium.

7.2.1 Susceptibility

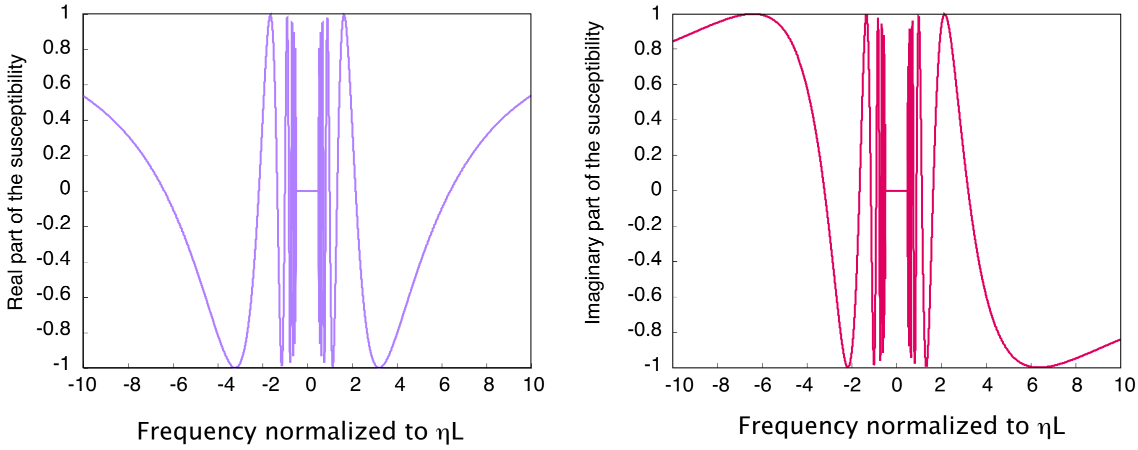

Figure 7.6: Real and imaginary parts of the GEM susceptibility. Parameters : $\eta = 0.5$, $g\mathcal{N}/\eta = 10$, and $\gamma = 0.001$.

We here present analytical solutions of the memory during the writing stage and calculate the absorption and phase shifts imposed by the atoms to the light including a finite excited state lifetime. Because of the complex phase shifts involved, the full analytical theory is not as straightforward as the EIT memory shown chapter 4. The main advantage is that there is no need to perform approximations on the time dependence of the Stark shift, compared with the adiabatic elimination required for EIT. We will come to this in the next subsection.

We start with the Maxwell-Bloch equations in the weak probe regime and calculate the susceptibility during the writing stage (assuming a positive stark-shift slope)

$$\frac{\partial}{\partial t}\alpha = (-\gamma + i\eta z)\alpha + ig\mathcal{E} \tag{7.5}$$

$$\frac{\partial}{\partial z}\mathcal{E} = i\mathcal{N}\alpha. \tag{7.6}$$

When integrating the Bloch equation (7.6) over time we get

$$\alpha(z,t) = ig\int_{-\infty}^{+\infty} H(t-\tau)e^{(\gamma - i\eta z)(t-\tau)}\mathcal{E}(z,\tau)d\tau, \tag{7.7}$$

where we assume that there is no polarisation in the medium initially and where $H(.)$ is the Heavy-side function. We then Fourier transform this expression in the frequency domain and get

$$\alpha(z,\omega) = ig\mathcal{E}(z,\omega)[\frac{1}{-\gamma + i(\eta z - \omega)}], \tag{7.8}$$

which gives a linear relation between the atomic polarisation and the light field frequency modes. We can substitute this expression back in the Maxwell equation and obtain

$$\frac{\partial}{\partial z}\mathcal{E}(z,\omega) \;=\; -g\mathcal{N}\mathcal{E}(z,\omega)\big[\frac{1}{\gamma - i(\eta z+\omega)}\big]. \tag{7.9}$$

After integration from $-z_0$ to z, we get

$$\mathcal{E}(z,\omega) \;=\; \mathcal{E}(-z_0,\omega)\chi(z,\omega), \tag{7.10}$$

where

$$\chi(z,\omega) = \Big[\frac{\gamma - i(\eta z+\omega)}{\gamma - i(-\eta z_0+\omega)}\Big]^{-i\beta}, \tag{7.11}$$

is the susceptibility of the medium, giving the amount of phase shift and absorption seen by the light when propagating through the sample. $\beta = g\mathcal{N}/\eta$ is the optical depth of the medium. The difference with usual linear absorbers is that the susceptibility depends on the propagation distance here.

We plot the real and imaginary parts of the susceptibility as a function of ω in Fig.7.6 at the end of the sample. We see that the real and imaginary parts present a gap with width ηL where light will be fully absorbed (in the limit of large β). Around this absorption window, oscillations appear with a frequency decreasing with probe frequency ω.

The equations present a discontinuity at $\gamma = 0$ and need to be corrected in this case. To find the expression for the susceptibility when $\gamma = 0$, one can go back to the original equations Eq.7.5. When $\gamma = 0$, after integration of the Bloch equation and Fourier transform in the frequency domain gives in this case

$$\alpha(z,\omega) \;=\; ig\mathcal{E}(z,\omega)\big[\delta(\omega+\eta z) - \frac{1}{i(\eta z+\omega)}\big], \tag{7.12}$$

and then

$$\mathcal{E}(z,\omega) \;=\; \mathcal{E}(-z_0,\omega)e^{-\pi\beta(H(\eta z_0-\omega)-H(\eta z-\omega))}\Big|\frac{\eta z+\omega}{-\eta z_0+\omega}\Big|^{-i\beta}. \tag{7.13}$$

This expression reveals that, even when each atom has an infinitely narrow linewidth, the large phase shifts allows to trap the light within the atoms. We will use it in section 7.3.1 to calculate the efficiency of GEM analytically.

7.2.2 Polariton picture

We now investigate the properties of the collective atomic and probe evolution after the initial mapping stage described above.

The properties of GEM are now described by identifying a normal mode that evolves in k-space. This analysis also highlights the flexibility of GEM with regards to the external control of the storage process. The GEM modes are lossless and can be dynamically controlled by the switching of the external Stark field.

We here assume the storage time to be much less than the excited state lifetime so that the decay rate γ can be ignored. The natural coordinate system in which to describe the collective evolution of the system is (k,t). We make a plane wave decomposition of the optical and atomic fields inside the medium by introducing collective operators in time and *k-space*

$$\begin{bmatrix} \mathcal{E}(k,t) \\ \alpha(k,t) \end{bmatrix} = \frac{1}{\sqrt{2\pi}} \int \begin{bmatrix} \mathcal{E}(z,t) \\ \alpha(z,t) \end{bmatrix} e^{ikz} dz. \tag{7.14}$$

In this k-space/time coordinate space, we can identify the normal modes

$$\Psi(k,t) = k\mathcal{E}(k,t) + \mathcal{N}\alpha(k,t), \tag{7.15}$$

which, from Eqs. 7.5 at times t greater then the input pulse duration, have the following equation of motion

$$\left(\frac{\partial}{\partial t} - \eta(t)\frac{\partial}{\partial k} - \frac{ig\mathcal{N}}{k}\right)\Psi(k,t) = 0. \tag{7.16}$$

This equation shows that the evolution of Ψ inside the medium is lossless and can be controlled in direction and magnitude by the imposed Stark shift $\eta(t)$.

Bosonic fields

Considering the quantum operators, we find the commutator $[\hat{\Psi}, \hat{\Psi}^\dagger] = k^2 + \mathcal{N}^2$, in the weak probe regime. The commutator is then not preserved if $\Psi(k,t)$ changes k. We are, however, free to engineer a time interval where $\eta(t) = 0$. In this case, $\hat{\Psi}$ "propagates" with constant k so that $\hat{\Psi}_k(t) = \hat{\Psi}/\sqrt{k^2 + \mathcal{N}^2}$ will be bosonic at all times.

This combined atom-light superposition $\hat{\Psi}_k$, is the result of the creation of periodic spatial variations of the polarisation, collective modes. After the initial mapping (described by section 7.2.1), when the Stark-shift slope is left on, collective spin waves $\alpha(k+\eta\delta t, t)$ are created as a result of the linearly varying phase shift[2].

This collective spin wave will radiate and in turn give rise to a new light field mode $\mathcal{E}(k+\eta\delta t, t)$, whose strength is given by the Maxwell-Equation to be $gN\alpha(k+\eta\delta t, t)/(k+\eta\delta t)$. If the Stark shift slope is turned off, the combined atom-light excitation in the created mode $k' = k + \eta\delta t$, $(\Psi_{k'}(t))$ then does not move to high k's anymore. We can identify $\hat{\Psi}_{k'}(t)$ as a polariton. From the Maxwell equation we see that the orthogonal normal modes $\Phi(k,t) = k\mathcal{E}(k,t) - \mathcal{N}\alpha(k,t)$ are never excited. The picture can be seen as the linear "mixing" of two correlated excitations $\mathcal{E}(k)$ and $\alpha(k)$. The correlation is obvious as the atomic oscillation generates the light field in a phase preserving fashion.

When the Stark shift slope is left on, the polariton in the mode k' is annihilated to give rise to a polariton in the mode $k' + \eta\delta t$. However the strength of the light components decreases with time as the polaritons modes correspond to higher k's. This is because the atoms lose their macroscopic coherences, and cannot radiate efficiently in the light field modes. This is equivalent to the free induction decay (FID) presented chapter 6.

If the sign of the Stark shift is reversed at a time t, the normal mode reaches a lower spatial frequency and the time reversal of the dynamic creation of normal modes operates. The dynamics of this process is now presented.

---

[2] A linearly varying phase shift is equivalent to a translation in Fourier space.

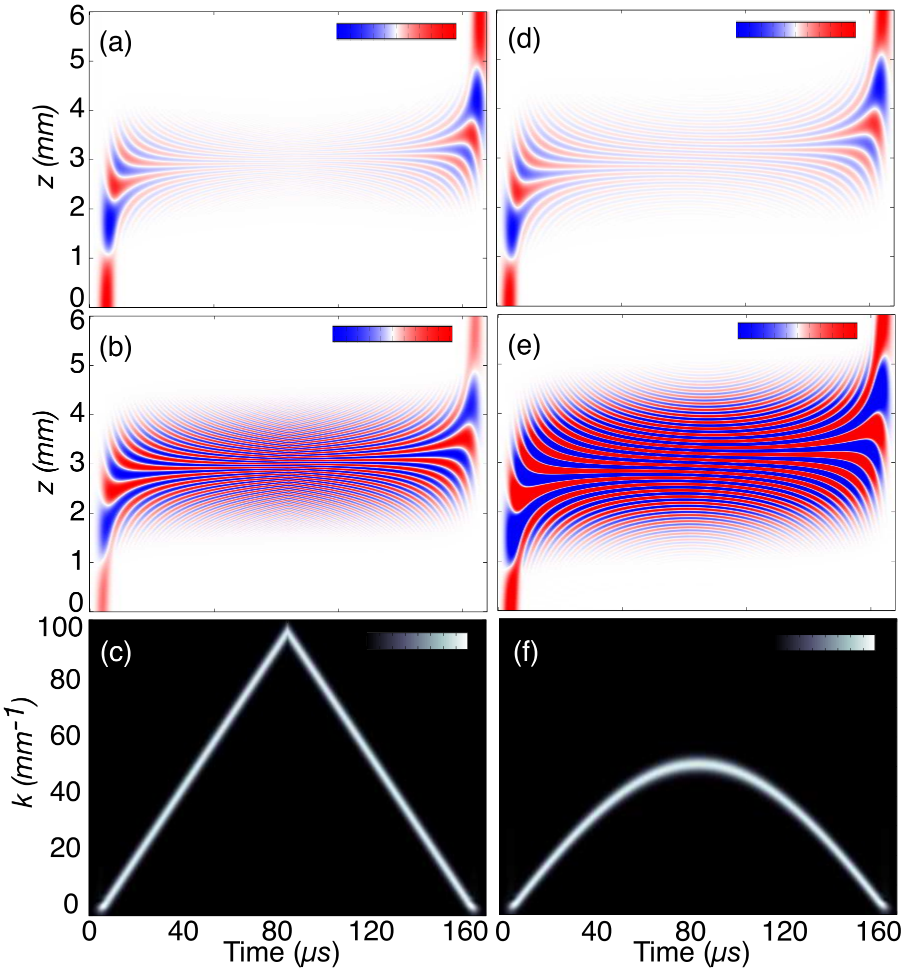

Figure 7.7: Instantaneous (left column) and slow (right column) switching in GEM. Panels (a) and (d) show the real part of $\mathcal{E}$, (b) and (e) show the real part of α, while (c) and (f) show $|\Psi|$. Red and blue shades indicate the positive and negative sign of the fields, respectively. The slow switch uses a tanh function with time constant $58\,\mu s$. In all cases, the dipole ensemble spans $z = 0$ to 6 mm, a Gaussian pulse enters the medium with its peak at $t = 5\,\mu s$, the Stark shift is switched at $80\,\mu s$, and the optical depth $g\mathcal{N}/\eta = 3.3$.

Polaritons' Dynamics

Some example numerical simulations are shown in Fig. 7.7. On the left we have the case of an abrupt switch of $\eta(t)$. As time increases towards the switching point, (a) and (b) show the coherent transfer of energy from the optical field to the atomic polarisation. We also observe the spatial structure of the fields becoming increasingly fine. After switching, the optical field picks up speed and intensity, eventually exiting the medium. Without switching, the atomic wave would keep on showing even finer oscillations and nothing would come out of the sample. The evolution of the normal modes is shown in (c). A constant velocity and intensity in k-space is observed up to the switching point, when the sign of the velocity is reversed.

In the case of slower switching, we obtain the behaviour shown in (d)-(f). The optical field and atomic polarisation show slower phase oscillations. Accordingly, the modes Ψ with large spatial frequencies are not excited. In both the fast and slow switching cases, the normal mode propagation is seen to be lossless and shape preserving, so that the efficiency of the light storage is ideal.

Using the amplitude modulated pulse shown in Fig. 7.8 (b), we will now directly compare the GEM and EIT modes. Figure 7.8 (c) shows the EIT normal mode. A spatial cross-section at 45 μs shows that the temporal profile of the input pulse has been mapped into a spatial profile of the normal mode. Figure 7.8 (d) shows the absolute value of $\mathcal{E}$ in a GEM system. When the Stark shift is flipped the echo emerges in the forward direction and, as demonstrated by the cross-sections, the output pulse is a time-reflected image of the input. Figure 7.8 (e) shows the absolute value of the atomic polarisation in the GEM medium and a spatial cross-section at 45 μs. Our simple explanation of GEM is that each frequency component of the pulse is stored at a different point on the z axis of the sample. The accuracy of this picture is apparent since the z cross-section is the Fourier spectrum of the input pulse. Panel (f) again demonstrates this Fourier relationship by showing the k-space GEM normal modes. Any cross-section in the k-axis shows the temporal profile of the pulse, as seen in the inset.

This shows that the atoms carry spatially information as a Fourier transform of the input.

7.2.3 Large time-bandwidth products

There has been much work on light storage using techniques such as Electromagnetically Induced Transparency (EIT) [Liu et al., 2001, Longdell et al., 2005, Chanelière et al., 2005, Appel et al., 2008, Honda et al., 2008], absorptive Raman transfer Kozhekin et al. [2000], Deng et al. [2002], photonic devices [Xu et al., 2007] and stimulated Brillouin scattering [Zhu et al., 2007]. All these methods rely on *time-encoding* whereby the temporal profile of the optical signal is directly mapped into a spatial profile within the storage medium. For finite optical depth or length, these techniques have a limited *time-bandwidth product*: it is only possible to store a wide frequency bandwidth *or* a long time interval [Hétet et al., 2008, Sun et al., 2005, Matsko et al., 2005, Gorshkov et al., 2007a]. The time-bandwidth product was defined in the chapter 2 of this thesis, and calculated for EIT in chapter 4.

For the multi-mode EIT technique there is a trade-off between the temporal length and spectral width of a signal that can be stored, resulting in a time-bandwidth product related to the optical depth [Hétet et al., 2008, Novikova et al., 2007, Deng et al., 2002, Gorshkov et al., 2007a]. In order to store the whole length of a signal, it must be spatially compressed into the EIT medium, which requires a sufficiently small group velocity. The control beam can then be switched off, leaving the signal encoded in the atomic coherence. In order to store a longer time interval, the group velocity in the writing stage has to be further reduced. A smaller group velocity, however, means a reduced transmission bandwidth so that high frequency modulations can no longer be stored in the EIT medium. Careful manipulation of the control field, for a known probe pulse profile, can optimise the efficiency and bandwidth of the writing stage [Novikova et al., 2007, Gorshkov et al., 2007a]. Even so, EIT is a resonant narrow-band phenomenon and, for a given optical depth, and without knowledge of the input shape, one has to compromise between clipping the length of the pulse, or narrowing the frequency bandwidth. This is true without ground state decoherence, which if considered, reduces the total efficiency. In atomic storage systems, larger time-bandwidth products can in principle be obtained by increasing the optical density, although this usually enhances decoherence processes [Matsko et al., 2005, Novikova et al., 2007]. Alternatively, the storage bandwidth could be improved by running parallel devices over a range of frequencies [Deng et al., 2002].

Unlike time-encoding quantum memories, GEM does not suffer from a time-bandwidth limit for any optical depth. This is a result of GEM operating in the frequency domain, leading us to classify it as a *frequency-encoded* memory. In a sense, GEM is a one step realisation of the suggestion made in [Deng et al., 2002]. Many resonant systems are spread over a frequency interval to achieve a uniform time and frequency response. There is also a similarity between the frequency encoding technique in GEM and the enhancement of spatial resolution provided by the magnetic field gradient in NRM imaging. The bandwidth of the memory is simply given by the range of the controlled Stark shift. When the broadening covers the whole pulse spectrum, the memory operates optimally regardless of the pulse shape. Provided the pulse is sufficiently weak so that the medium is not saturated, there is no limit to the length of pulse that can be stored meaning that GEM has no time-bandwidth limit. Throughout our analysis we have ignored the exited state decay, which will eventually limit the length of signal that can be stored. In rare-earth systems, however, the decoherence times can be a few milliseconds [Alexander et al., 2006].

This is not to say that GEM provides ideal storage for any signal. Like any quantum

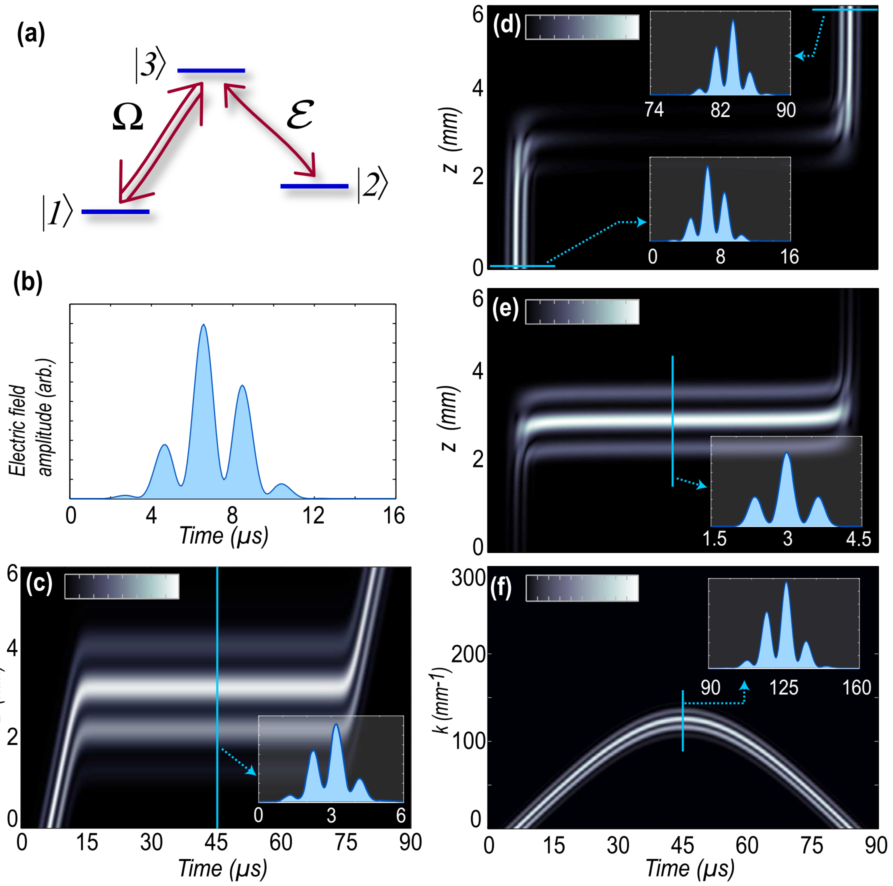

Figure 7.8: (a) The Λ level scheme used for EIT. (b) The modulated pulse used in the simulations that follow. (c) The EIT normal mode. Model parameters were N=5000, g=1 and $\Omega(0) = 50$, normalized to the spontaneous emission rate. The control field was switched using tanh functions with a 2 μs time constant at 14 and 75 μs. In the case of GEM storage, (d) shows $|\mathcal{E}|$, (e) shows $|\alpha|$ and (f) shows $|\Psi|$. The switching was done at 45 μs using a tanh function of time constant 20 μs. Optical depth $g\mathcal{N}/\eta = 3.3$. The efficiency in both schemes is close to 100%.

memory that uses an ensemble of atoms, the efficiency is ultimately limited by optical depth. For a given number of atoms, the storage bandwidth of the medium is made larger by increasing the size of the initial Stark shift η. When $g\mathcal{N}/\eta < 1$, however, the dipoles in the medium will be spread too thinly in frequency space, leading to reduced storage efficiency. Although not all the photons will be stored, the loss is spread evenly over the signal spectrum so the pulse shape is preserved.

In conclusion, this section reveals several important and attractive features of the GEM scheme. We have identified a lossless normal mode that propagates in k-space, leading us to categorise GEM as a frequency-encoding memory. GEM is also shown to be insensitive to the switching dynamics of the Stark shift used to control the photon echo. This contrasts with EIT where the shaping of the control field is crucial.

7.3 Other properties

We presented above the general properties of the gradient echo memory. Other interesting features were also found in this scheme. It is, for example, possible to generalize the forward CRIB protocol, presented in [Sangouard et al., 2007] and mentioned chapter 6, by concatenating several Gradient echo memories. The evolution of the efficiency of the scheme versus optical depth can then be derived easily for the forward CRIB system directly from the GEM results, without having to solve the full Bloch equations for CRIB. This discovery also allowed us to demonstrate that one can retrieve excitations left in the sample by switching the electric field several times, thereby generating multiple echoes. This applies to both the forward CRIB, and the (optical depth limited) GEM memories. We then present a way to optimize the storage of two modes in two GEM memories. For continuous variable memories, the technique has the potential to entangle two macroscopic ensembles using a single squeezed light source.

We finish the section by coming back to the polariton picture, to show that GEM can, just like EIT, traps “stationary” light fields in the medium.

7.3.1 Generalisation to the two-level atom CRIB protocols.

We here present a picture describing the behavior of the forward Controlled-Reversible-Inhomogeneous-Broadening scheme. The scheme was mentioned in the preceding chapter and is similar to the GEM proposal, but with a Stark-shift that varies randomly across the sample.

As discussed in the first chapter of this part, the efficiency of such a forward CRIB method is limited. We demonstrate here how one can think about this mechanism from the GEM functioning and calculate its efficiency. To illustrate this simply, we model the GEM and forward CRIB memories using a beam splitter approach. The model is shown Fig. 7.9.

GEM efficiency versus optical depth

GEM can be modelled by the combination of two beam splitters as shown Fig. 7.9-(a). An input state is transmitted by an amount ϵ through the Stark-shifted medium and a portion $1-\epsilon$ is mapped in the atomic medium, or “reflected off” the beam splitter. The other port of the beam splitter can be thought of as atomic ground state modes (in the vacuum state). After flipping the Stark-shift slope another beam splitter "reflects off" the light field and generates an echo. The other empty port of the beam splitter can be thought of as a vacuum input field. We here calculate the splitting ratios of the beam splitters. Assuming an optimum spectral coverage and a negligible spontaneous emission rate, an expression for the efficiency of the memory as a function of optical depth will then easily be found.

The amount of transmitted light going straight through the sample was calculated analytically in section 7.2.1, by solving the equations before the switching in the frequency domain. Substituting $z = +z_0$ in the equation 7.13 one finds that the transmitted pulse is equal to the the incident pulse multiplied by an attenuation factor $\exp(-\beta\pi)$. In the limit of large β the light is completely absorbed in the material.

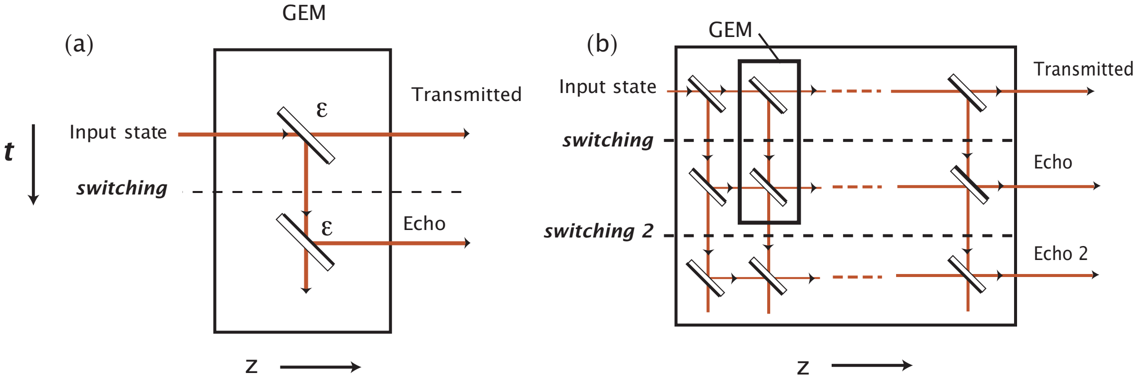

Figure 7.9: (a) Schematic describing GEM using beam splitters. The splitting ratio ϵ depends on the optical depth. (b) Description of CRIB using multiple GEM systems. When the optical depth is large, multiple echoes can be retrieved by switching the electric field several times.

To find out how much light is recalled as an echo after switching the best coordinate system is (k, t). In the limit where $k \neq 0$, (where the polariton description was presented) we only considered the waves *inside* the medium. The limiting cases of finite optical depths were therefore not included in our normal mode analysis. When $k = 0$, the light can leave the medium with a probability given by the optical depth. We now integrate the Maxwell Bloch equations in k-space including the $k = 0$ discontinuity and find the relation

$$\alpha(k,t) = \alpha(k - \eta t, t_s)|\frac{k}{\eta ts}|^{i\beta} \exp(-\beta\pi\delta(k)). \tag{7.17}$$

This expression allows to find how much excitation is left in the medium after k reached 0 which, using conservation of energy arguments, gives us the portion of light leaving the sample. We find it to be $1 - \exp(-\beta\pi)$. The efficiency of the rephasing (after switching the electric field) can also be evaluated in a different way by considering a light field propagating backwards and using auxiliary light pulses [Longdell et al., 2007].

To summarize, the input light is "reflected off" by the first beam splitter by an amount $\epsilon = 1 - \exp(-\beta\pi)$. The created atomic polarisation, is being re-phased after the switching of the electric field, and an amount $1 - \exp(-\beta\pi)$ leaves the medium. The total efficiency is then given by $(1 - \exp(-\beta\pi))^2$. This formula is in agreement with the numerical simulations shown Fig. 7.3.

As noted in the first section, when the optical depth corresponds to an efficiency of about 50%, large atomic excitation is left in the sample after the echo left the medium.

This remaining excitation can be used to reemit light a second time by flipping the electric field again. This procedure can be repeated n times to finally retrieve completely the excitation. The total input pulse energy then leaves the medium but at different times.

Two-level atom CRIB efficiency versus optical depth

The case of a randomly distributed spectral ensemble (the forward CRIB) can in fact be calculated easily from the above picture. The forward CRIB can be modelled like a network of beam splitters, representing arrays of optically thin gradient echo memories as depicted Fig. 7.9-(b). Each beam splitter transmits or reflects a portion of the light according to the GEM parameters calculated above. By cascading j optically thin "beam splitters" with splitting ratios $T = 1 - \pi\beta\frac{z}{j}$, one can show that the first echo amplitude is

$$\mathcal{E}(z) = \lim_{j\to\infty} \left((j+1)(1-T)\sqrt{T}^j\right) = \pi\beta e^{-2\pi\beta} \tag{7.18}$$

Fig. 7.10-(a) shows a plot of the efficiency of forward CRIB as a function of optical depth using the numerical[3] and analytical result from Eq. 7.18. A complete agreement is found between the two models and also with the results of Sangouard et al. [2007]. The efficiency reaches a maximum of 54 % and at high optical depths, the optical information is retained in the medium. Fig. 7.10-(b) shows the same results but with a decay from the excited state γ of $0.04/t_0$ using the numerical model. The no-cloning regime is not reached anymore, showing the sensitivity of this forward CRIB scheme to experimental imperfections.

We note that beam-splitter type picture does not allow one to deal with more complex problems of phase and frequency shifts, and also situations where the input bandwidth lies outside of the absorption bandwidth. Nevertheless, the total efficiency can be calculated easily, and the reason for the lack efficiency at high optical depths appears clearly as the consequence of reabsorption. The beam splitter description also allows one to follow the vacuum terms coming from the initial atomic and light field vacuum modes entering the various empty ports of the beam splitters. As there is are non-linear processes involved during the mixing at the beam splitters, the process does not add excess noise. As for the GEM case, we can use this picture to predict what would happen if the Stark-shift slope was flipped several times. As more excitation is left in the medium, at high optical depth, flipping the field many times allows one to recover all the excitations [Longdell et al., 2008].

We finish by noting that even though the shape of the broadening used in this beam-splitter model differs significantly from the natural distribution of frequency shifts in solid state systems or Doppler broadened media, the physics is qualitatively the same. As confirmed by a comparison with the work of [Sangouard et al., 2007], the maximum efficiencies for the forward CRIB are the same. We therefore expect the multiple echoes behavior to still hold in, for example, the case of Gaussian inhomogeneous broadening.

7.3.2 Optimum storage of two optical modes

One of the attractive features of CRIB quantum memories is that they are frequency encoding memories. In GEM for example, the frequency information is stored spatially as

---

[3] The numerical model of random broadening was presented in the earlier chapter

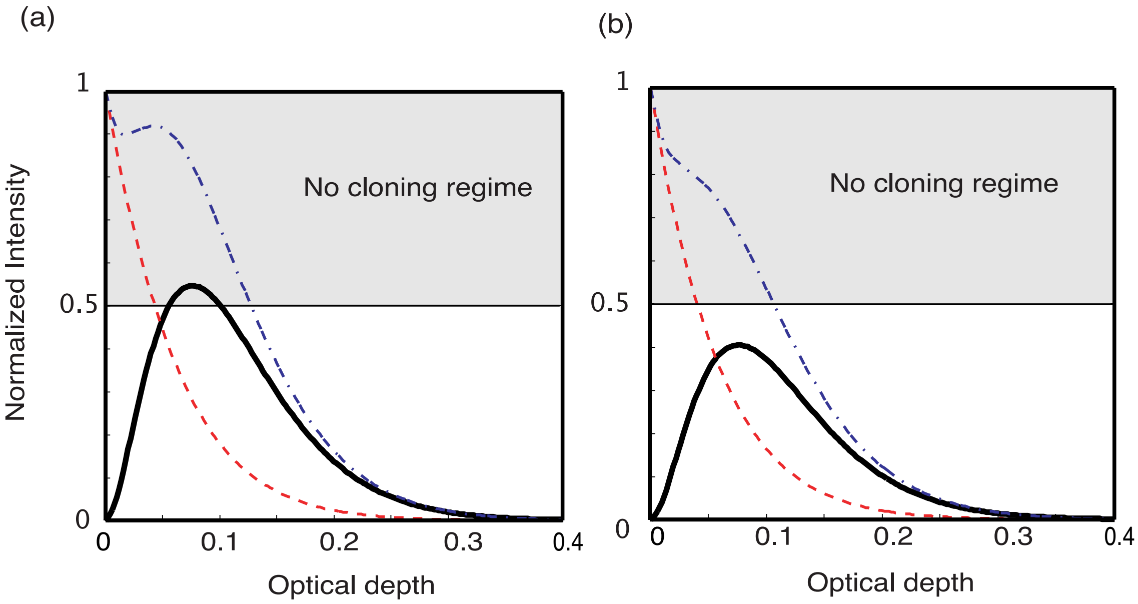

Figure 7.10: Forward-CRIB efficiency as a function of optical depth with (a) no decoherence rate (b) with decoherence. Solid lines represent the efficiency of the memory; dashed lines, the fraction of transmitted light; and dot-dashed lines, the total energy exiting the medium. Shaded regions are the no-cloning regimes.

the Fourier transform of the input pulse, which allows a straightforward processing of the information. To give an example, we consider the storage of the two sidebands of a two mode continuous variable quantum state, in two separate ensembles used in series. These two modes can be classical or quantum correlated sidebands (cf. chapter 1).

The scheme would work as follows : A GEM medium is prepared to be resonant with the upper sideband and transmits the carrier. This is easility achievable experimentally by lifting the Stark shift by an offset that matches the sideband frequency or shifting the frequency of the light field. The second GEM is made resonant with the lower sideband.

In Fig. 7.11-(a), we show numerical simulations of the protocol. We input an amplitude modulated pulse to the first memory and prepare the two media by the appropriate Stark-shift slopes and frequency offsets. We see that part of the input pulse Fourier spectrum is mapped onto the atomic coherence of the first memory. The lower sideband propagates with the carrier to the second memory and is then also mapped in the atoms. The transmitted pulse only comprises the low frequency envelope.

At a time t=40 μs, the electric field is flipped and the two sidebands leave their respective media. The upper sideband recombines with the lower sideband inside the second medium and the signal propagates back into free space. To quantify the process, we plot the Fourier transform of the input and output pulses in Fig. 7.11-(b). The input field is the red signal, which is shown to be comprised of a carrier and the two sidebands we want to store. The output is plotted in black. Its Fourier transform was calculated at $z = 8$ from $t = 40\ \mu s$ to $80\ \mu s$. The output field is only composed of the two sidebands that were stored in the medium[4].

---

[4] A slight frequency shift is seen between the input and output sidebands arise here, because the switching was performed whilst there were still some significant light in the medium. This can be eliminated for example by switching the Stark-shift later as shown in section 7.4

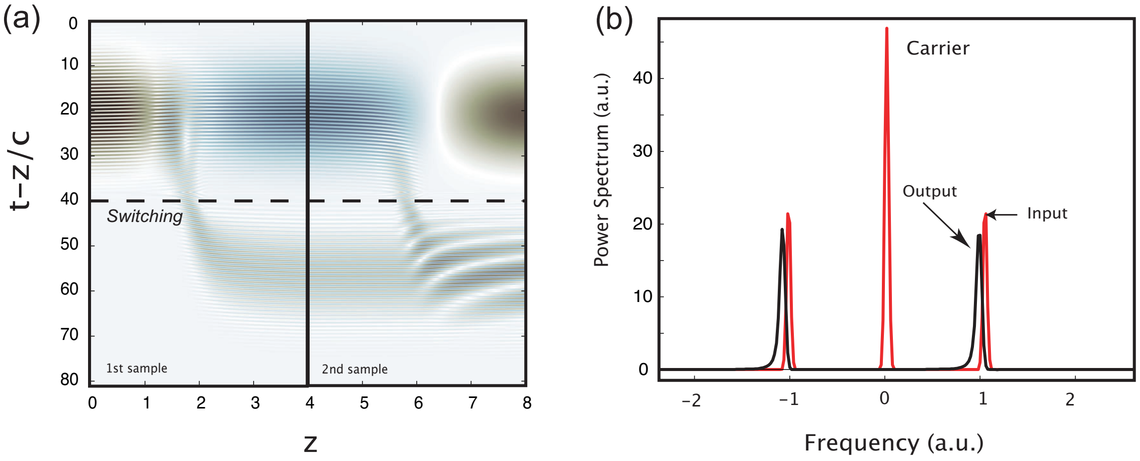

Figure 7.11: Sideband separation scheme. (a) Modulated light field propagation on a time space grid, in two memories. (b) Fourier transform of the input and output probe pulses calculated before and after the switching time respectively. The Stark shift of the first memory matches the upper sideband frequency, thereby storing it. The Stark shift of the second memory matches the lower sideband frequency. The carrier goes straight through the two samples.

This storing procedure is particularly attractive for entanglement of two atomic samples, as it alleviates the initial sideband separation required, for example, for EIT (see section 4.4.1). Also the storage of only two modes, allows one to introduce a small broadening that keeps a large effective optical depth $g\mathcal{N}/\eta$. The storage is then optimized for each mode by introducing the minimum broadening required to match the Fourier width of each sideband (given by the length of the carrier field).

7.3.3 Light amplification

Another interesting prospect for information processing is light amplification. Using GEM, we found that it is possible to amplify the input light field by inverting the medium initially. To perform numerical simulations of the effect, we then included the population terms and used the set of equations 7.1 (without the Langevin noise terms). Fig. 7.12 shows the result of simulations where, an input light field (trace (i), multiplied by 10 for clarity) is sent to an initially inverted Stark-shifted medium. The population inversion used in the simulations is 80%. 50% of the light comes out straight out of the sample. However, upon flipping the electric field, an amplified version of the input field comes out as an echo. This shows that the GEM memory can potentially be used as an efficient phase-insensitive amplifier. Quantum simulations are, however, required to calculate how much noise would be added to such a process. Using the T-V diagram (see chapter 2) would then tell if the memory is still performing better than any classical device and operates within the no-cloning regime.

7.3.4 Stationary light

Let us finish this chapter by pointing out the potential of the Gradient echo memory to generate stationary light fields. We saw in section 7.2.2 that, by turning the gradient to zero a short time after the pulse entered the medium, a combined atom-light superposition is trapped in the medium in the form of a polaritonic excitation. If the Stark-shift slope is turned off shortly after the input pulse entered the medium, a significant portion of light

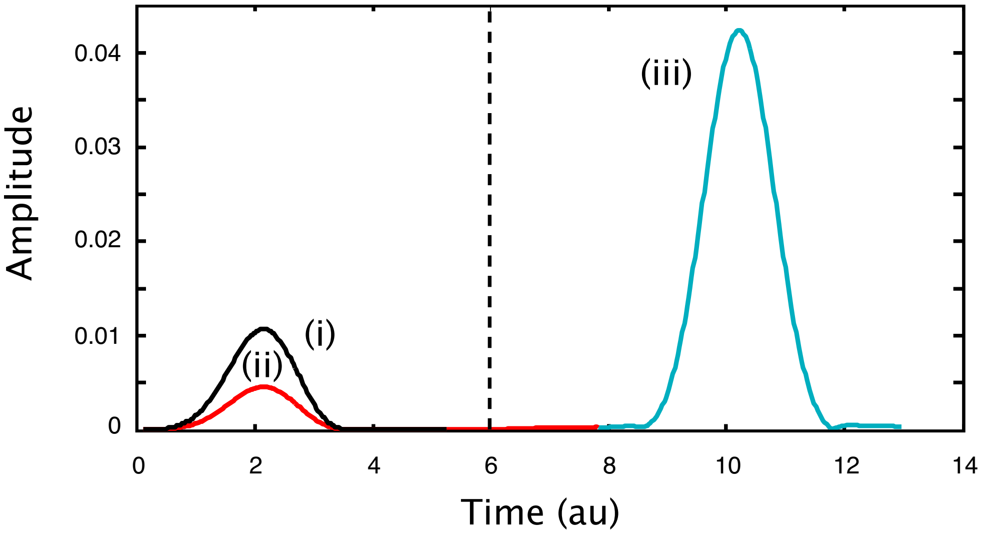

Figure 7.12: Light amplification with an inverted medium. (i) The input pulse amplitude (it was multiplied by a factor of 10 for clarity). (ii) The transmitted light. (iii) The output signal, amplified version of the input by a gain of around a 100, coming out as an echo.

stays in the medium.

The physics behind such a localized electromagnetic energy is similar to the Bragg reflections in photonic crystals or EIT with two counter-propagating control pulses [Bajcsy et al., 2003], where the light field is reflected off the absorption nodes created by the atomic wave. The periodic spatial modulation of the atomic wave creates a vanishing group velocity for the signal beam.

We already calculated the dispersion relation associated with the two level atom, in the limit where $\eta = 0$ in chapter 6. We found that $v_g(\omega) = \omega^2/(g\mathcal{N})$ is extremely small for small frequencies. To allow the control of the light propagation, one can dynamically tune the Stark-shift slope. After the light has entered the medium, turning off the Stark-shift changes the dispersion properties of the medium and stops the light field. This is apparent in Fig. 7.6 which shows the dispersion associated with the presence of a Stark shift. Turning off the Stark-field shrinks the absorption window and stops the light field which remains trapped in the Bragg grating. The light field can be retrieved by turning on the Stark-shift with the opposite slope.

This behavior of the protocol is similar to the stationary light field found in EIT. It was shown that after having stored the light information in the ground states, applying a pair of counter propagating control fields precisely achieves what we described here. The light field is regenerated and subsequently trapped within the stationary pattern created by the two control field in the Λ structure. This method is also dynamical as it allows one to tune the velocity of the light field in the medium by changing the ratio between the control fields. In GEM, we can also tune the group velocity of the trapped light field by tuning the Stark-shift slope.

7.4 Conclusion

To conclude this chapter, we summarize the properties of a new quantum memory scheme, the gradient echo memory (GEM). GEM is an adaptation of the CRIB memories, where the broadening varies linearly with distance. This simple change in the broadening engineering allows the memory to work efficiently with only two-level atoms. We show that the output echo is emitted in the forward direction as an ideal time reversed copy of the input state at large optical depths. An experiment was performed in a solid state system and shows efficiencies of 15%, mostly limited by the lack of optical depth. The results were found in good agreement with theoretical simulations.

In a second section, we investigated the dynamics of the GEM scheme and found collective polaritonic modes that can be created or annihilated by controlling the Stark-shift slope. The polaritons are found in k-space, which highlights the difference with the EIT quantum memory where the polaritons are usually presented in z-space. This difference comes from the Fourier encoding nature of the memory. When information is stored in Fourier Space as opposed to real space for most time-encoded memories, we show that the time-bandwidth product can be made very large.

We finished this chapter by showing that GEM may be used as a tool to describe the properties of the CRIB memories. We then noticed that the Fourier encoding nature of the memory also allows an efficient storage of a single optical mode. We illustrated this by considering the storage of two correlated modes and show that the GEM gradients can be tuned so as to efficiently entangle two atomic ensembles from a single squeezed light source. This contrasts with EIT memories where an initial sideband separation needs to be done. We then show how one can perform amplification of a light field via simple initial inversion of the GEM medium. We conclude by showing that GEM can support stationary light field. By turning the Stark-shift slope to zero after the initial mapping, the polaritonic excitation can be trapped in the medium. The speed of this localized stationary wave can be controlled later on by the Stark shift slope.

Chapter 8

Λ-gradient echo memory

In this chapter, we propose and demonstrate experimentally a technique that allows the storage and retrieval of a light pulse from three level atoms with short excited state lifetime. The quantum memory proposal is similar to the gradient echo memory (GEM) that we studied in the preceding chapter. The main difference is that the information is stored on long lived hyperfine ground states via a coherent Raman absorption. This allows one to achieve a "strong coupling" with the collective atomic state together with an, in principle, long lived storage.

In the first section, we present the ideas and the theory behind this Λ-GEM scheme. We show that, if the control field used in the two photon absorption process is sufficiently strong, and both the probe and control fields far detuned, the system is equivalent to a linearly Zeeman/Stark-shifted two-level atom with long-lived excited state lifetime.

We show proof of principle experiments performed in a rubidium vapour cell. A narrow absorption line was prepared on the rubidium 87 D_1 line. A linear and controllable magnetic field was applied using a set of four coils that Zeeman shifted the atomic ground states. After absorption of the pulse from the Zeeman-shifted medium, the magnetic field slope was flipped, leading to a time-reversal of the absorption process and an echo emerged from the medium.

The chapter is structured as follows : We present the theory behind our proposal and compare it with the inital CRIB memory proposal made in [Moiseev and Kröll, 2001]. We demonstrate narrow Raman absorption lines using rubidium in a buffer gas system, characterize the free induction decay of the broadened and unbroadened line and compare the results with the light storage time.

8.1 Λ-gradient echo memory theory

We start the chapter by deriving the equations of motion for the Λ-Gradient Echo Memory (Λ-GEM). We show that a Λ-system driven off-resonance by a strong control beam and a weak probe is equivalent to a two-level system driven by the weak probe. The lifetime of the equivalent two-level atom is given by the ground state lifetime of the three-level atom and is therefore long lived, in theory. This tailoring of a two-level system with tunable decay constant is a common method that is used for example in laser cooling and cavity QED scenarios.

8.1.1 Equations of motion

We solve the Maxwell-Bloch equations in the weak probe and far detuned regimes. We consider the three-level system depicted Fig. 8.1-(a) with a one photon detuning Δ, a two-photon detuning $\delta(z,t)$ that can be varied in time and be made linear with a magnetic or electric field $\delta(z,t) = \eta(t)z$, a classical control beam Ω_c, and a weak quantum field $\hat{\mathcal{E}}$. The interaction Hamiltonian of the three-level system is

$$\hat{\mathcal{H}} = \hbar(\Delta\sigma_{33} + \delta(z,t)\hat{\sigma}_{22}) + \hbar(g\hat{\mathcal{E}}^\dagger\hat{\sigma}_{13} + \Omega_c\hat{\sigma}_{23} + h.c). \tag{8.1}$$

We solve the Heisenberg equations for the probe quantum field and the atomic dipoles in the weak probe regime. As the system is close to the EIT scenario studied in chapter 4, we give the simplified equations directly here.

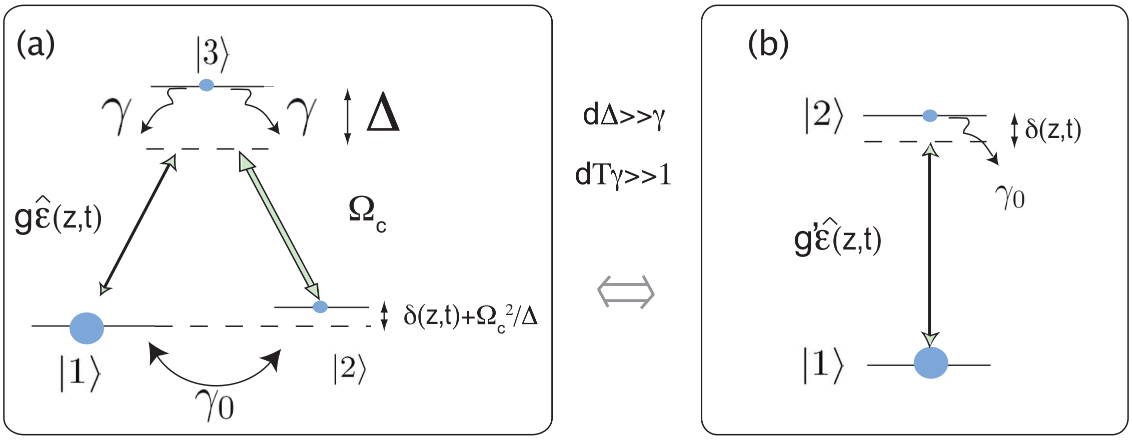

Figure 8.1: (a) Level structure of the three-level atom. (b) Equivalent two-level system.

Weak probe approximation

One difference between the off-resonance scheme and EIT though, is that in steady state, and usual experimental conditions, the atoms are not fully pumped by the control field to the level $|1\rangle$. To ensure that this is the case, an initial pumping step is required. We suppose that this was done, and assume all the population to be in state $|1\rangle$ initially. From the Heisenberg-Langevin equations in the weak probe regime ($\sigma_{11} \simeq 1$) and in a moving frame at the speed of light, we get

$$\begin{aligned}
\dot{\hat{\sigma}}_{13} &= -(\gamma + \gamma_0/2 + i\Delta)\hat{\sigma}_{13} + ig\hat{\mathcal{E}} + i\Omega_c\hat{\sigma}_{12} + \hat{F}_{13}. \\
\dot{\hat{\sigma}}_{12} &= -(\gamma_0 + i\delta(z,t))\hat{\sigma}_{12} + i\Omega_c^*\hat{\sigma}_{13} + \hat{F}_{12} \\
\frac{\partial}{\partial z}\hat{\mathcal{E}} &= i\mathcal{N}\hat{\sigma}_{13}.
\end{aligned} \tag{8.2}$$

where $\mathcal{N}$ is the effective linear atomic density. The Langevin operators $\hat{F}_{13}$ and $\hat{F}_{12}$ account for noise coming from spontaneous emission γ and ground state decoherence γ_0 respectively. As discussed in chapter 4, no excess noise is generated from those processes so we will be ignoring the Langevin terms from now on.

We ignored population redistribution terms for simplicity, in order to ensure that once the atoms are prepared in state $|1\rangle$ they stay there, and also to make sure the output field stays in a vacuum state. The full quantum treatment of noise from this population shuffling term γ_c was done for EIT in chapter 4. Gain in the probe mode due to γ_c was responsible for excess noise. Calculating the excess noise from the Λ-GEM is a little bit more involved because of the other time scale given by Δ, but we expect this noise to be equally, if not more, important here.

We now simplify the equations by performing an adiabatic elimination of the excited state and, a far off-resonance approximation.

Adiabatic elimination and far off-resonance approximation

We adiabatically eliminate fast excited state fluctuations by assuming $\frac{\partial}{\partial t}\hat{\sigma}_{13} \ll \gamma$, or equivalently, $1/T \ll \gamma$, where T is the fastest time-scale of the system. We also assume a large detuning compared to the spontaneous emission rate ($\Delta \gg \gamma$).

In large atomic ensembles, the adiabatic elimination and far detuned approximation are in fact less stringent than for a single atom [Gorshkov et al., 2007b]. By solving the Maxwell equation for the probe field and substituting it back into the equation of motion for $\hat{\sigma}_{13}$ we can show that $1/dT \ll \gamma$ and $\Delta \gg \gamma d$ are sufficient conditions when the density is larger than 1. This is because of the collective coupling between the optical modes and the many atom state. Assuming the control beam to be real, and $\Delta \neq 0$, combining the three equations yields

$$\begin{aligned}
\dot{\hat{\sigma}}_{12} &= (-\gamma_0 + i\delta(z,t) - i\frac{\Omega_c^2}{\Delta})\hat{\sigma}_{12} - i\frac{g\Omega_c}{\Delta}\hat{\mathcal{E}} \\
\frac{\partial}{\partial z}\hat{\mathcal{E}} &= \frac{igN}{\Delta}\hat{\mathcal{E}} + i\frac{gN\Omega_c}{\Delta}\hat{\sigma}_{12}.
\end{aligned} \tag{8.3}$$

We can always choose a frame where the speed of light in the medium is normalized by the refractive index term $i\frac{gN}{\Delta}$ and can also choose the coupling beam frequency to match the light shift term $\frac{\Omega_c^2}{\Delta}$. With those two simplifications, we reach

$$\begin{aligned}
\dot{\hat{\sigma}}_{12} &= -(\gamma_0 + i\delta(z,t))\hat{\sigma}_{12} - i\frac{g\Omega_c}{\Delta}\hat{\mathcal{E}} \\
\frac{\partial}{\partial z}\hat{\mathcal{E}} &= i\frac{gN\Omega_c}{\Delta}\hat{\sigma}_{12}.
\end{aligned} \tag{8.4}$$

We now show that this set of coupled Maxwell-Bloch equations is equivalent to a two-level atomic system.

8.1.2 Analogy with GEM

From the preceding chapters, we know that the equations for the two-level atom are (including the decay γ from the excited state)

$$\begin{aligned}
\dot{\hat{\sigma}}_{12} &= -(\gamma + i\delta'(z,t))\hat{\sigma}_{12} - ig'\hat{\mathcal{E}} \\
\frac{\partial}{\partial z}\hat{\mathcal{E}} &= ig'N\hat{\sigma}_{12},
\end{aligned} \tag{8.5}$$

which are formally equivalent to the above Raman situation, if we set $g' = \frac{g\Omega_c}{\Delta}$ and $\gamma = \gamma_0$. We show the equivalence in Fig. 8.1. The effective interaction Hamiltonian 8.1 can then be rewritten simply as

$$\hat{\mathcal{H}} = \hbar(\delta(z,t)\sigma_{22}) + \hbar\ (g'\hat{\mathcal{E}}^\dagger\hat{\sigma}_{12} + h.c). \tag{8.6}$$

which is the two-level atom Jaynes-Cummings Hamiltonian. The coupling strength between the two-level atom and the probe field is proportional to the ratio between the control field Rabi frequency and the detuning. To enable a strong coupling, the detuning must be sufficiently small whilst still being large enough to minimize spontaneous emission. For large detunings, if light power is available, increasing the control field will give strong coupling.

8.1.3 Protocol

The conclusions of the two-level GEM discussion in the preceding chapter can be translated straight over to this Λ-GEM scheme. In the adiabatic limit and far-off resonance, the Λ-GEM works in nearly the same way as the two-level GEM scheme. The steps are now as follows :

1. Optical pumping to the state $|1\rangle$ is performed. A narrow coherent absorption line is then prepared using a strong off-resonant control field.
2. The absorption line is broadened using a linearly varying Stark or Zeeman shift whose width matches the Fourier spectrum of the quantum state to be stored.
3. The quantum state is absorbed by the medium, off-resonance with the optical transition $|1\rangle - |3\rangle$, but two-photon resonant with the Raman transition. The different frequency components are mapped linearly across the sample, onto the long lived ground state coherences.
4. After flipping the Stark or Zeeman shift, a time-reversal of the absorption process occurs and an echo leaves the medium as a time-reversed copy of the input state.

One advantage of this scheme is that the lifetime of the equivalent two-level atom can be really long. In particular, lifetimes of minutes have been reported in solid state systems [Fraval et al., 2004]. Also, the coherent Raman-absorption allows one to store light in systems with a short excited state lifetime, such as Alkali atoms.

During the whole process, the strong control field can be left on and the mapping to long-lived ground states is performed automatically. In the original CRIB schemes [Moiseev and Kröll, 2001, Kraus et al., 2006, Nilsson and Kröll, 2005], the transfer to long lived coherences was performed dynamically and immediately after the probe was absorbed (in the case of rubidium atoms, this transfer would have to be done within a fraction of nanoseconds, which would be quite a challenge). Another simplification compared to CRIB is that, as the control field is constant and applied in the forward direction, the echo leaves in the forward direction.

Time-bandwidth products

In chapter 7, we showed that the switching of the Stark-shift in GEM can be done smoothly or quickly without changing the storage capabilities. This contrasts with EIT where the adiabatic following into the dark state limits the storage bandwidth at small optical depths. Together with the limitation on the pulse length, that once compressed must fit the sample, EIT and time-encoded memories have a finite time-bandwidth product at small optical depths. We showed that the time-bandwidth limit in the GEM scheme is only limited by the excited state lifetime, for any optical depth. We discussed how this was a consequence of GEM being a frequency encoded memory.

One can then think that using the Λ-GEM scheme, arbitrarily large time-bandwidth product would be obtained because of the long lifetime of the ground state coherence. Long pulses may indeed be stored well in the Λ-GEM. Pulses with large bandwidth, however, present a difficulty that is not present in the two-level scheme. The reason is because of the adiabatic elimination that was performed initially. The necessary conditions for Λ-GEM to be efficient are essentially the same as for EIT, we required $\gamma_0 \ll 1/T$, $d\gamma \ll \Delta$ and $1 \ll T\gamma$. The last equation is the adiabatic elimination of the excited state that prevents any quantity to fluctuate too fast with respect to the excited state[1]. This means that both the probe and the Stark/Zeeman shifts slope are not allowed to vary too quickly. This is the same condition as the EIT adiabatic following. The time-bandwidth product could potentially be improved by shaping the broadening with time but knowledge about the pulse shape would then be required to phase match the quantum state temporal mode with the memory [Gorshkov et al., 2007a, Nunn et al., 2007]. Alternatively, the control field in Λ-GEM could also be turned off so as to decouple the ground states with the excited state after the probe absorption. This will lead to improvements of the efficiency when the one photon detuning is not large enough with respect to the spontaneous emission rate.

8.2 Experimental set-up

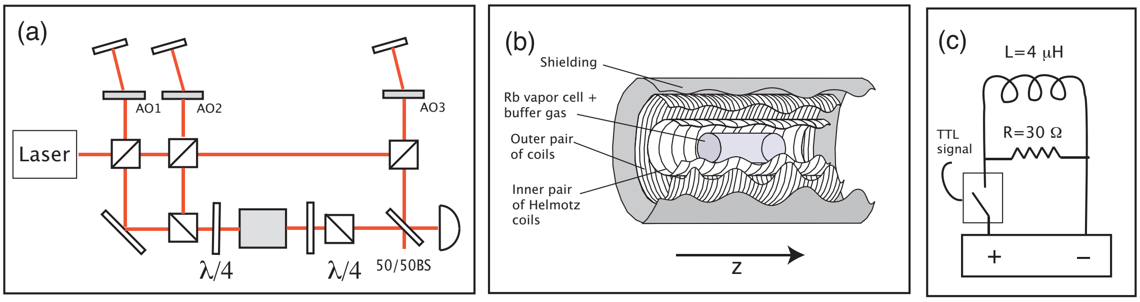

Figure 8.2: (a) Schematic diagram of the experimental set-up. The laser beam is frequency shifted by three AOMs in a double pass configuration and used as probe, control and local oscillator beams respectively. (b) Magnetic coils and μ-metal shielding placed around the rubidium vapour cell. (c) Electronic circuit used to switch the magnetic fields off/on. A power supply delivered about 0.5 A to the coils. The inductance of the coil was about 4 μH. A resistance of 30 Ω was placed across the resistance to improve the time response of the system. A switch was placed in series with the coil and controlled by a TTL signal.

As discussed above, the Λ-GEM scheme allows one to use atoms that have a short lived exited state (thereby giving a strong coupling with the light field) and also to store information on long lived hyperfine or Zeeman coherences. This is particularly attractive for light storage using alkali atoms. The ground state lifetime can be made really long in warm and cold alkali atomic vapours with a large coupling strength.

We present here proof of principle experiments of the Λ-GEM scheme in a warm vapour cell containing rubidium 87 filled with 5 Torr of Helium buffer gas. We generate photon echoes and characterize their decay as a function of storage time.

---

[1] A sufficient but not necessary condition is $1 \ll Td\gamma$ [Gorshkov et al., 2007a].

8.2.1 Control of magnetic field

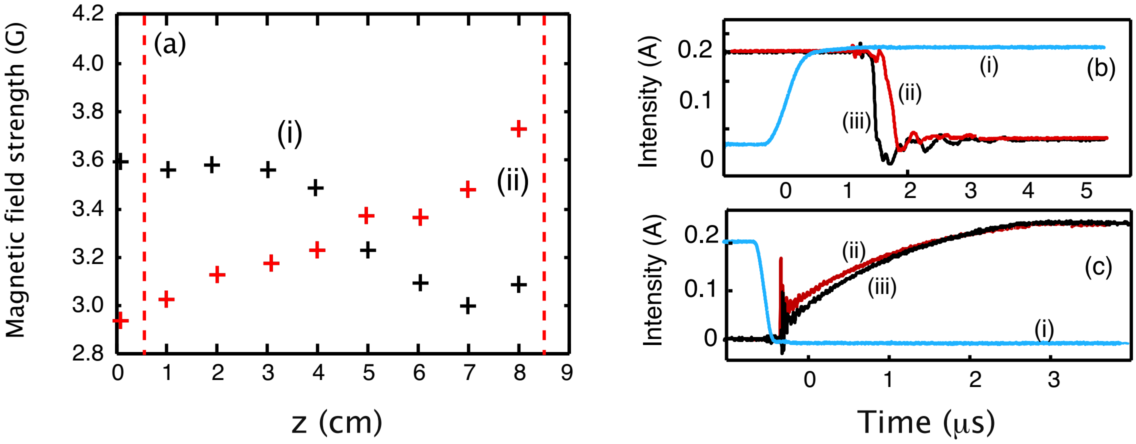

Figure 8.3: Magnetic field preparation. (a) Measurement of the dependence of the magnetic field with propagation distance through the cell, with (i) the inner coils on and (ii) the inner coils off. (b)-(c) current flowing through the inner coils during the switching off/on the control signal applied to the switches. Trace (i) shows the TTL signal used to control the switches. (ii) and (iii) show the current flowing through the inner left and right coils respectively.

To generate the controlled broadening, we used the Zeeman effect. Rubidium atoms have no linear Stark shift, so instead we used a linearly varying magnetic field to create a Zeeman gradient in the cell. We used a set of two outer and two inner magnetic coils, as depicted Fig. 8.2-(b). Fig. 8.3-(a) shows the dependence of the magnetic field with z when (i) the inner coils were off and (ii) when the inner coils were on. The broadening width was about 0.1 Gauss/cm for these measurements which corresponded to about 800 kHz of introduced broadening.

The pair of outer coils generates a linearly varying magnetic field that is kept on at all times. For these measurements, the left coil produces a magnetic field of around 4 Gauss, 4 cm away from its edge, with a current of 0.5 A (the number of turns is about 1/mm). The right coil produces a smaller magnetic field in the same direction but its current is allowed to vary depending on the pulse duration. The net result was a monotonically varying field shown centered at 3.4 G. Fig. 8.3-(a), trace (i).

The inner coils are in a Helmholtz configuration. Both generated a magnetic field of the same strength but in opposite direction, thereby decreasing/increasing the magnetic field generated by the left/right outer coils. The number of turns of the inner coils was ten times smaller than that of the outer coils. The inner coils can then be switched quickly without inducing a large current through the outer pair of coils. A large number of turns would increase the mutual inductance between them and change the current through the outer coils during the switching.

The electronic circuit used to switch the magnetic field is shown Fig. 8.2-(c). The switching of the magnetic field was done using switches driven by TTL signals. When a 5V TTL signal was applied to the switch, it closed and let the current flow through the coil. The inner coils inductance was calculated to be about 4 μH. To allow fast switching, a resistance of 30 Ω was placed in parallel with the coils. We found that the higher the inductance the higher was the resistance we had to place in parallel with the coil to maximize the response time. Fig. 8.3-(b-c) shows the time dependence of the current through the two inner coils when the current was switched on and off respectively. The time it took for the current to reach its steady state value was about 3 μs for turning on and about 300 ns for turning off. We also observed a time lag of about 1 μs between the time the TTL signal was applied to the switch and the response of the current. Ripples of about 5% of the signal depth were also observed due the fast current variations in the circuit. The switching rate and the ripples were reduced by a factor of 2 using a resistance in parallel with the coils. We normally used the "switching on" configuration as the observed ripples were much smaller which provided a cleaner output echo signal.

We now move to the presentation of the optical set-up.

8.2.2 Preparation and detection of narrow absorption features

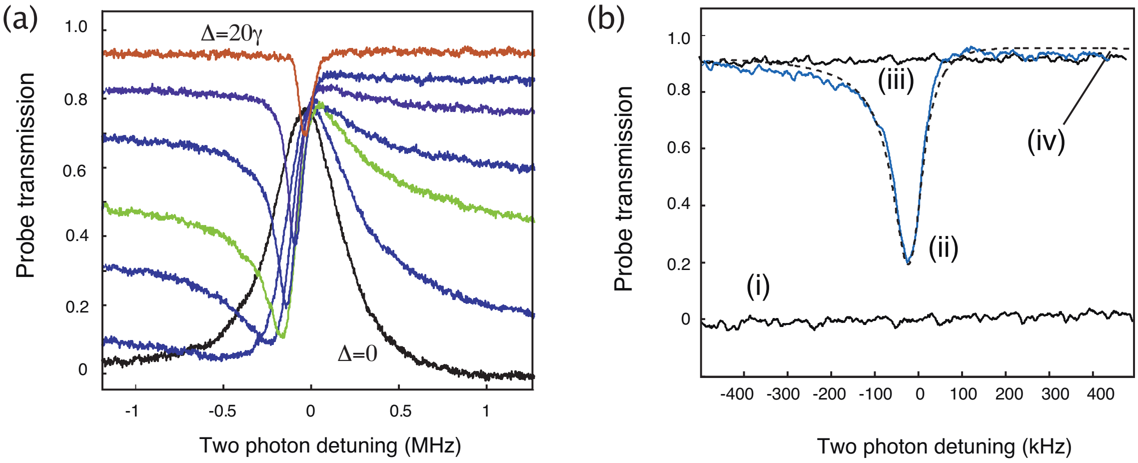

Figure 8.4: (a) Transition from electromagnetically induced transparency to a coherent Raman absorption by changing the one-photon detuning Δ from 0 to 20γ. (b) Optimized Raman absorption line. (i) Level obtained by blocking the probe beam, (ii) absorption feature due the coherent Raman absorption. (iii) Level obtained when blocking the control beam. (iv) Shows the result of numerical simulations using a one-photon detuning Δ of about 10γ, a control beam power of 2γ, and a decoherence rate of 0.001γ.

The Ti:sapph laser was locked to the reference cavity, red detuned by 600 MHz from the F=2 to F=1 line (a description of the laser apparatus was given chapter 3). A total power of 500 mW was used and sent to a set of AOMs in double pass. A small portion was sent through AO_1, which shifted the laser frequency by a total of 160 MHz and was used as the *probe*. Another part of the laser was sent to AO_2 to shift the frequency of the *control beam* by around 154 MHz. The frequency detuning between the control and the probe matched the two-photon detuning introduced by the magnetic field offset (3.4 G) and the light shift. About 50 mW was used to frequency shift the laser by 174 MHz using AO_3, and was used as a local oscillator for a *heterodyne detection*. The local oscillator was mode matched to the probe after the cell and the signal mixed down at 14 MHz using an electronic local oscillator phase locked to the function generators delivering the signals used in $AO_{1,2}$. This allows the stable detection of the *frequency* of the probe. The interferometer was not actively locked to the carrier phase of the probe so the measured probe signal *phase* drifted due to slow thermal and acoustic fluctuations of the mirrors. This heterodyne detection method allows, in principle, shot noise limited detection and accurate measurement of the probe frequency.

The rest of the experiment is similar to the EIT experiment of chapter 5. The control beam is linearly polarized orthogonally to the probe before mixed on a beam splitter and then converted into orthogonal circularly polarized light fields. After the cell, the beams are converted back to linearly polarized light and the control beam filtered by a Glan-Thomson polarizer. The output probe is then detected without large contamination from the control beam. In steady state measurements, residual control field photons are being mixed with the probe due to polarization self-rotation and finite extinction ratios. However, as the control beam frequency is different to the probe, the beating between the beams can be eliminated using low pass filters.

The control field is about 1 cm wide and the probe around 0.4 cm wide. This beam geometry is a compromise between too small beam areas, which would reduce the time-of-flight of the atoms in the beam, and too wide beams, where the contribution from atoms that hit the cell walls could introduce a large exchange of population between the "ground states" and decrease the efficiency. Also, the amount of power and beam quality required are harder to achieve using large beams.

To observe the Raman line, we scan the control beam frequency and monitor the probe absorption. In order to present the transition between the EIT and Raman processes, we show in Fig. 8.4-(a) the evolution of the absorption profile as a function of one-photon detuning (Δ).

When $\Delta = 0$, we find the EIT profile. As the detuning was increased, the EIT became more and more asymmetric and when the detuning is larger then the Doppler width, finally turns into a symmetric absorption profile, albeit with reduced absorption. As no extra parameters other than the laser frequency were changed for this measurement, the absorption efficiency of the Raman process is not optimum. In practice, self-rotation effects depend on the one photon detuning so that for a given laser frequency the power of the control field and the polarizing optics ($\lambda/4$ plates) have to be re-optimized[2].

Figure. 8.4-(b), trace (ii) shows the optimized Raman absorption. Trace (iv) shows the result of the solving of Eq. 8.2 in steady state. The experimental parameters were $\Delta = 600$ MHz and control beam power 40 mW. Traces (i) and (iii) show the detected level when the probe/control are blocked before the medium. The Raman feature was 170 kHz full width at half maximum and 80% absorptive. Such a narrow Raman feature could not be observed in the same experimental conditions using cells that did not not contain buffer gas, as the time-of-flight of the atoms inside the beam is the factor limiting the width of the feature. Increasing the buffer gas concentration would possibly allow even narrower absorption lines to be observed, although collisions with the buffer gas could also introduce undesirable collisional effects.

8.2.3 Free induction decay

One of the first steps towards photon echoes is observing free induction decay (see chapter 6). If the atoms are prepared in the same "way", after exciting them by a short pulse

---

[2] Such a self-rotation mechanism comes from AC-Stark shifts induced by the off-resonant atomic levels. Because the Clebsch-Gordan coefficients for these upper levels change sign from the one side of the manifold, to the other, self-rotation is expected. The magnitude of the self-rotation depends on the amount of population in the two ground states situated in the middle of the manifolds. For EIT, where the control beam pumps most of the atoms to the $m_F = -2$ state, such a population is negligible. As the optical pumping to the $m_F = -2$ state reduces with one photon detuning, the ground state populations becomes evenly distributed across the manifolds. This causes the off-resonant levels to disturb the dark-state preparation and a significant rotation of the light polarisation. See for example : [Novikova et al., 2000].

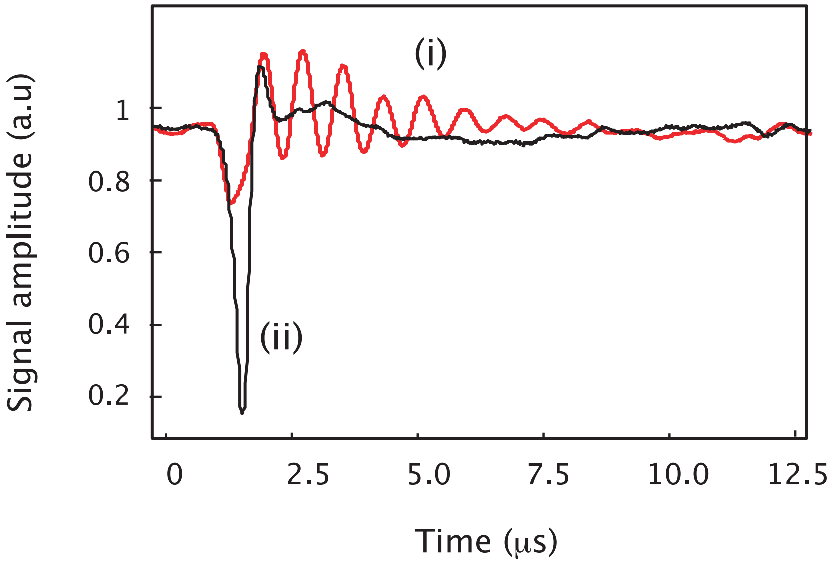

Figure 8.5: Free induction decay measured using heterodyne detection with (i) a collection of identical atoms and (b) with a linear Zeeman-splitting of 0.3 Gauss/cm.

the atomic ensemble will reradiate light for a time given by the inverse of the absorption feature width. This can also be understood as the consequence of the spectral narrowing of the pulse, resulting in a spread of the pulse in time and the necessary phase shifts that preserve causality via Kramers-Krönig's relations. If the atomic ensemble is broadened, the macroscopic coherence decays faster and the FID is much shorter.

The atomic re-radiation duration will give an estimate of the homogeneous ground state decay time we will observe in the echo generation. To observe the FID, we use heterodyne detection and excite the atoms by a short weak pulse of 250 ns. Figure 8.5, trace (i) shows the free induction decay observed without applying the broadening magnetic field. The frequency of the oscillations is determined (mainly) by the optical depth of the medium. The decay time for the oscillations of the amplitude is about 2.5 μs, corresponding to a decay of the intensity of about 1.2 μs, consistent with the width of the unbroadened Raman feature $(1/(2\pi 170\text{ kHz}) \approx 1\ \mu s)$.

Trace (ii) shows the result of the same experiment but with the Raman feature broadened by the linear magnetic field. As the atomic ensemble macroscopic coherence decays, the FID is much faster, and the oscillations are almost completely eliminated.

The FID duration (when the ensemble is not broadened) is not as long as the ground state decay time measured from the EIT light storage experiments of chapter 5. The difference between the two schemes, in warm vapor cells, is that when the laser is detuned away from resonance, moving atoms also contribute to the coherent absorption. As was pointed out in chapter 5, for EIT, atoms that are moving at a $|kv|$ larger than the natural linewidth do not contribute to the ground state coherence and simply do not see the two fields. The situation is different off-resonance, as the only frequency selection comes from the light shift term $\frac{\Omega_c^2}{\Delta}$ and the coupling strength $g\frac{\Omega_c}{\Delta}$ (cf. Eq. 8.5). The dependence of both these terms with one-photon detuning is weak for large detunings, so that most atomic velocity classes contribute with the same weight to the Raman absorption. This means that, on the one hand, the average time-of-flight is smaller for EIT than for Raman memories in a gas cell, on the other hand, the effective optical depth is larger in the Raman scenario for a given cell temperature.

8.3 Experimental observation of a photon echo using Λ-GEM.

The observation of the FID shows that we indeed prepared a narrow absorption line that was broadened in a coherent fashion. We can now in principle time-reverse the absorption process by flipping the magnetic field slope. In this section, we show that when performing such switching, an echo comes out of the medium in the forward direction.

8.3.1 Observation of a photon echo in a vapour cell

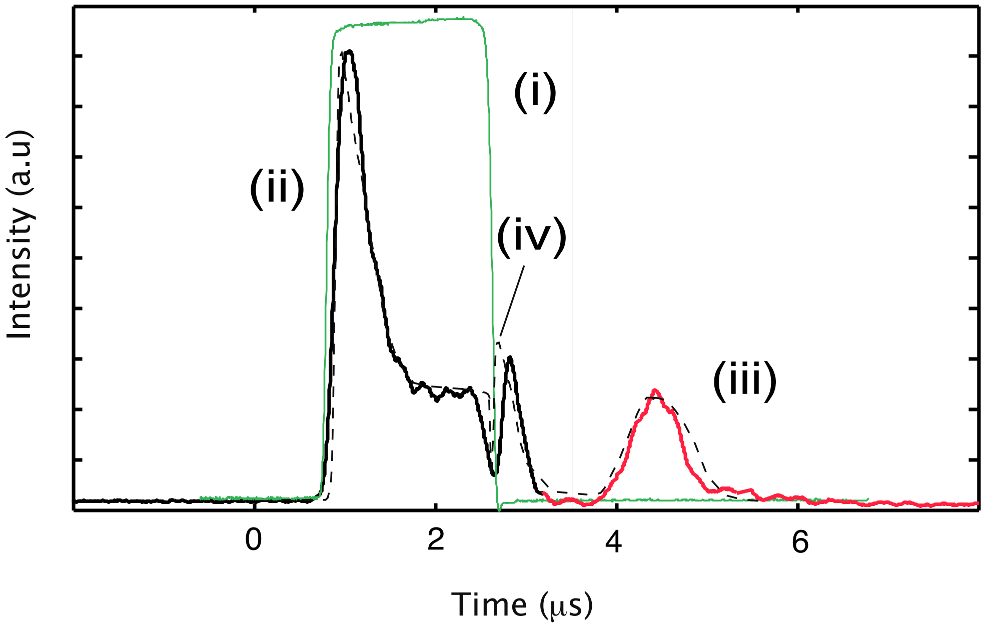

Figure 8.6: Observation of a photon echo produced by switching the magnetic field gradient. (i) signal going through the sample with the control field off. (ii) signal leakage going through the sample when the control field is on. (iii) Recalled light after the magnetic field switching. (iv) Results from the two-level atom numerical simulations. The experimental parameters are $\Delta = 600$ MHz and control beam power 40 mW.

After broadening the medium, the FID shortens. As discussed earlier this absorption process is not irreversible. By flipping the magnetic field to its opposite slope after the pulse absorption, we could indeed observe photon echoes. The first observed echoes were measured using heterodyne detection, for good signal to noise ratios. After some improvements to the set-up (for example by pumping atoms from the $F_g = 1$ to the $F_e = 2$ hyperfine sub-levels using the diode laser[3], see chapter 5), we were able to observe echoes using direct detection. Fig. 8.6 trace (iii) shows such a photon echo.

The experimental parameters used here are $\Delta = 600$ MHz and control beam power 40 mW. Trace (i) shows the input pulse, of around 2 μs long, being measured by blocking

---

[3] The use of the diode laser enhanced the absorption and total efficiency by a factor of two. Good pumping preparation is critical for this off-resonance experiment.

the control field. Trace (ii) shows the amount of light that is being transmitted straight through the cell without being absorbed. The shape of the transmitted pulse is the consequence of the filtering of the low frequency components of the input by the Zeeman-shifted medium. We indeed notice that the fast variations of the pulse are not absorbed as efficiently[4]. After flipping the magnetic field slope at $t = 3.6\ \mu s$ we retrieved part of the stored excitation. About 30% of what was coherently absorbed, was retrieved as an echo. This result is well predicted by numerical simulations using the two-level atom model presented chapter 7. Trace (iv) shows the result of the simulations, using a decay time of 500 ns, an optical depth of 0.4, magnetic field gradient of 0.2G/cm and accounting for the finite switching rate of the current. The main features of the experiment are reproduced by the model.

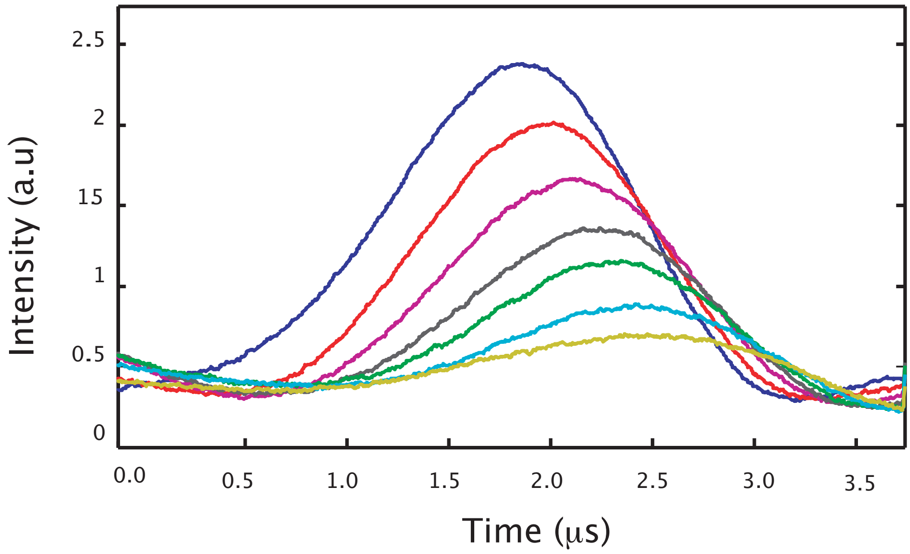

Figure 8.7: Measurement of the echo intensity as a function of storage time. The estimated decay time is 600 ns.

It is important to point out that the efficiency of the whole storage process cannot be assessed from the present results only. As the laser operated rather close to the Doppler profile, the input beam was already absorbed by about 50% when the control beam was off. Trace (i) is the signal going through the cell with the control beam blocked, and not what would be measured with the cell out. Going further off resonance reduced this incoherent absorption (thereby making the Raman feature more symmetric) but also reduced the depth of the Raman absorption. One could think that applying a larger control field would allow to compensate the decreasing coupling efficiency but this was not the case. The reason for such a reduced efficiency is not completely understood. Modelling using population exchange between the ground states and including the extra atomic levels is underway and might explain the extra loss that we observed.

The same experiments were also performed by turning off the control field after the absorption of the pulse and turning it on again after the Zeeman-shift slope was flipped. As expected, about the same results were obtained. Without broadening the absorption

---

[4] Using a broader Zeeman-shift reduced the strength of these fast variations, but also the total efficiency, as the optical depth for each spectral component decreased. Using a Fourier limited pulse, such as a Gaussian pulse, did not help either because the duration was too long for it to be efficiently retrieved.

line however, no echoes were also observed[5]. This demonstration is an important step towards the production of maybe more efficient echoes in warm/cold atomic vapours and solid states.

To characterise the light storage mechanism further we now study the evolution of the efficiency as a function of storage time.

8.3.2 Storage time

Fig. 8.7 shows the echo output as a function of time, as the input pulse was shifted further away from the switching point. The input pulse was moved backwards by steps of 200 ns. The echo emerges further away from the magnetic field switching, as expected from the dipoles time-reversed evolutions. This result is a clear indication that what we observed were photon echoes. The echo, however, did not come out by steps of 200 ns after the switching point but emerges slightly earlier than expected. A shift of about 50 ns is systematically observed. This "too early" rephasing was likely to arise due to a slightly different Zeeman-shift slope used for the recall and writing stages. Indeed when the Zeeman slope used to store is larger than the slope used for the reading stage, the dipole rephasing is performed faster and the echo leaves the medium earlier than it would in the symmetric switching case. Using this method, we found the decay to be around 600 ns a little bit shorter than the free induction decay observations. As we discussed earlier, we believe this decay time corresponds to the mean time-of-flight of the atoms at their respective positions, including all the velocity classes.

8.3.3 Controlled frequency shift

We also investigated the dependence of the output echo frequency in various regimes. Using the heterodyne detection, we found that the output echo frequency depended on the control field frequency. Fig 8.8 shows the echo output measured using heterodyne detection. Trace (i) is the input field and residual, phase shifted, FID. Part (ii) shows the echo being measured when the control field frequency was tuned slightly away from the two-photon absorption condition. Trace (iii) shows the output echo when the control field matched the two-photon absorption. The figure shows that the echo frequency is determined by the control field chosen to retrieve the echo. This observation is in agreement with numerical simulations, using a three-level model of GEM.

This result suggests two possible applications. One could think about applying the same technique as for EIT and retrieve the echo at a different "wavelength" from another transition [Zibrov et al., 2002, Appel et al., 2006] by choosing a different control field frequency after the writing stage. Also, from chapter 7, we know that if the switching was performed whilst there were still some significant amount of light in the medium, the echo would be slightly frequency shifted. The frequency shift can here be controlled by tuning the control field frequency.

---

[5] We also varied the length of the probe pulse and control beam power so that the whole pulse could be absorbed by the unbroadened Raman feature. After switching the control beam off, and back on, we did not observe any output signal. The reason might be that, to allow an efficient writing and retrieval using the plain Raman absorption, the control field has to be mode matched to the input signal, as discussed chapter 4, and shown in [Nunn et al., 2007, Gorshkov et al., 2007a].

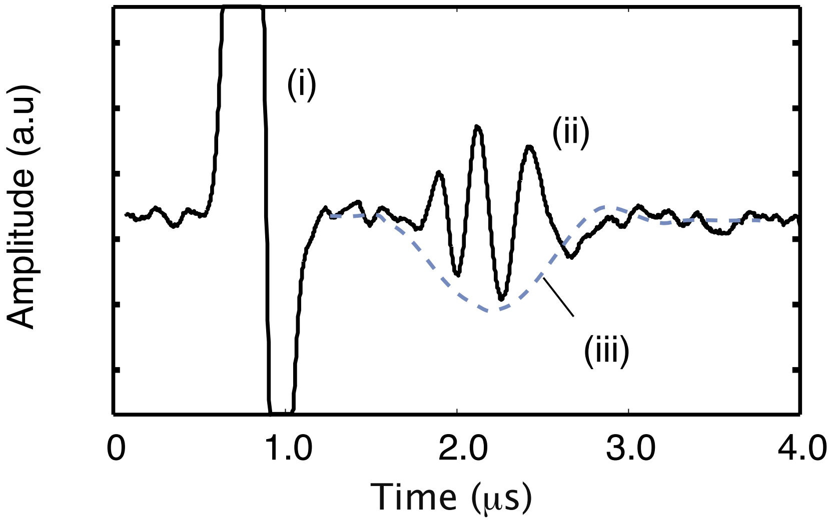

Figure 8.8: Heterodyne detection of the output echo. (i) Light leakage. The peak and dip show the input and residual FID respectively. The ripples at point (ii) show the output echo when the control field is slightly frequency shifted from the two-photon resonance condition. Trace (iii) shows the output echo when the control field frequency matches the two-photon absorption.

8.4 Conclusions and perspectives

In conclusion, we proposed a scheme that extended the two-level atom GEM to a Λ-GEM scheme using three-level atoms with (potentially) long coherence times. The scheme is close in spirit to the initial CRIB proposal but is simpler in the sense that there is only one switching operation and that the output quantum state leaves the medium in the forward direction. The Λ-GEM scheme is closely related to EIT [Fleischhauer and Lukin, 2000] or "plain" Raman memories [Nunn et al., 2007, Gorshkov et al., 2007a] but, like GEM, the scheme uses frequency encoding. The potential of the Λ-GEM in terms of time-bandwidth products was discussed in this chapter. One advantage of the technique as applied to continuous variable atom-light entanglement, is that no initial sideband separation would be required to actually entangle two atomic ensembles from a squeezed light source.

The simplicity of the scheme allowed us to demonstrate proof of principle experiments in a warm vapour cell. A narrow Raman absorption line was prepared and broadened using monotonically varying and reversible magnetic fields. We then observed free induction decays and subsequent photon echoes. We discussed the limits to the efficiency and compared the results with the EIT light storage performed chapter 5. Improvements of the experimental set-up may be possible by switching the current faster, controlling a larger magnetic field and understanding the reduced Raman contrast at large one-photon detunings.

Using cold atomic samples or solid state systems, would allow to reach long storage times and (potentially) larger Raman features. A study of the dependence of ground state decoherence with optical depth (and maybe also including experimental complications) is required to tell which system would be most efficient.

Conclusion and perspectives

To conclude, let us briefly summarize the work presented in this thesis.

We defined benchmarks for quantum memories and then used a quantum model to find the regimes where Electromagnetically Induced transparency (EIT) based memories surpass the Heisenberg limit. We showed from both a Schrödinger and Heisenberg approach of EIT, that population exchange between the ground states generates excess noise on the output probe mode.

We designed a low-sideband frequency source of squeezed light capable of suppressing the vacuum noise by more than 5 dB, and used it to probe the efficacy of EIT based delay lines. Our EIT system was shown to transmit about 2 dB of squeezed light and delay entangled states by 2 μs whilst preserving a degree of inseparability of 0.71. No excess noise was measured on the squeezed field in the presence of buffer gas. We also stored classical light pulses by controlling dynamically the EIT properties.

We then discussed the potential of quantum memories based on photon echo techniques and presented the gradient echo memory (GEM) scheme. We demonstrated the potential of GEM in terms of time-bandwidth product, highlighted its dynamics using a polariton picture and also used our model to fit an experiment performed in a solid state system. Finally we extended the GEM technique to a three-level atomic system, Λ-GEM, and performed proof of principle experiments in a rubidium gas cell that are also in good agreement with theory.

More efficient quantum memories

As discussed in this thesis, efficient memories are required for secure and fast quantum communication. Sources of losses and excess noise have been identified and suppressed from our rubidium-based memories, but other miscellaneous effects remain. Notably, the lack of transmission in the Λ-GEM, when the probe was two-photon detuned from the Raman line was not completely understood. Also, the EIT-delay and the Raman absorption contrast achieved were not optimum in rubidium gas cells at moderate temperatures. At higher optical depths, the efficiency of both memories dropped even more. It seems important to improve on these aspects and, for instance, compare theoretical modelling with experimental evidence for the degradation of efficiency with optical depth. Performing these experiments in cold atomic samples (in magneto-optical traps, for example), seems a next logical step. Without Doppler effects, the storage time of the Λ-GEM can be improved. Also, without significant atomic motion, the EIT and Raman lines contrasts can potentially be increased using cold atoms. The difficulty will lie in preparing a clean magnetic environment and achieving large enough optical depths.

More efficient continuous variable quantum states

On the non-classical light generation side, PPKTP was found an ideal crystal for squeezing experiments at the D1 line. The major bottle-neck for larger degrees of squeezing was the doubling cavity. A long-term and efficient ultra-violet production would be a possible future direction for a better memory characterisation. If first order poled-PPSLT were commercialized at this wavelength, it could potentially allow efficient UV production, as SLT presents a high damage threshold together with a large non-linear coefficient.

Other more compact squeezed light sources using, for example, four-wave-mixing in atoms, may also be used to obtain large degrees of squeezing at the rubidium D1 line [McCormick et al., 2007a].

We note that low-frequency squeezed light might not be critical for efficient memory operation using the Λ-GEM scheme. By tackling the residual "two-photon detuned absorption" mentioned above, the two entangled sideband modes from squeezed light sources can be efficiently stored and retrieved from two spatially separated atomic samples at sideband frequencies on the order of MHz's.

Outlook

The most studied materials for quantum information storage are cold or warm vapours of Alkali atoms, and ion-doped solid state systems.

In solid state systems, the resonant optical depth seems to be limited by the ion doping technology. On the other hand, because the atoms are stationary, the coherence time can be made really long. This was for example demonstrated in [Longdell et al., 2005] where light was stored for seconds but the efficiency limited by the lack of resonant optical depth. Because of the large inhomogeneous broadening, hole burning has to be performed for the CRIB or EIT methods to work, which reduces the total number of available atoms. Techniques that would make use of all the atoms in the sample are therefore promising. A scheme in that direction was recently proposed in [Afzelius et al., 2008]. The protocol is experimentally quite challenging, but the effective optical depth can, in theory, be greater than what would be achieved with the standard hole-burning technique.

We note that, as the two-level GEM technique does not allow arbitrarily long storage times to be reached, it might seem attractive to implement the Λ-GEM in a solid state system. However, because most of the optical transitions that are used are weak, an efficient Raman absorption will require a lot of power on the control field which brings further complication. The full CRIB protocol might then be more advantageous. This contrasts with atomic vapours using Alkali atoms, where the number of atoms and the coupling strength gives a large effective coupling with the light. Achieving large optical depths is also "generally" not an issue. The Λ-GEM technique is then suitable for Alkali systems. However as we discussed in chapter 8, the decay time is rather short in vapour cells to the Doppler broadening. The velocity selection using co-propagating beams in EIT is not present off-resonance which dramatically reduces the time spent by the atoms at their initial position in the sample. The primary limitations to decay time will then be given by this problem in warm vapour cells. Residual magnetic fields are the current limitation in cold atoms [Matsukevich and Kuzmich, 2004, Felinto et al., 2005].

Appendix A

Theory of open quantum systems

The quantum states we use in this thesis are usually manipulated using some form of non-linear interaction with atoms, which is often associated with loss. This loss will be modelled by coupling the system comprising the light modes and the atoms to a Hilbert space containing a larger number of modes, a reservoir. This interaction entangles the system's degrees of freedom with the reservoir's and upon measurement of any of the system observables will eventually lead to their "decay".

The *master equation* for the reduced density matrix of the system "in the reservoir" will be derived in the first part of this Appendix. When a quasi-probability distribution for the system variables is chosen, the master equation can eventually be converted into a Fokker-Planck equation. This is the object of the second part of this appendix. Finally, stochastic differential equations can be found. We will present the mathematical apparatus needed to derive the stochastic differential equations in appendix B.

A.1 Operator form of the master equation

We will derive the master equation modelling the interaction of a system with a reservoir in the *Markov approximation.* In most of this thesis, the system will be a collection of atoms interacting with light, coupled to a reservoir of vacuum radiation modes, but we will keep the derivation general. This description was inspired from [Cohen-Tannoudji et al., 1993, Gardiner, 1985].

A.1.1 Evolution of $\hat{\rho}$ in the interaction picture

We suppose that the fluctuations of the reservoir acting on the system variables occur over a time scale that we will call τ_c, the memory, or correlation time, of the reservoir. The time scale over which the system evolves in the reservoir will be called T_s. We derive a master equation in the limit where $\tau_c \ll T_s$, the Markov limit.

To simplify the notations, the hats will be removed from all the operators in this subsection. The free Hamiltonian of the bath is noted $\mathcal{H}_B$, and the Hamiltonian of the system $\mathcal{H}_\mathrm{S}$. The coupling between the bath and the system can be described quite generally by the Hamiltonian

$$V = X^\dagger \mathcal{B} + h.c. \tag{A.1}$$

where X is an operator of the system and $\mathcal{B}$ an operator of the bath. Any other coupling Hamiltonian can be chosen without changing the reasoning below, however, different system variables will be damped differently depending on the actual form of this coupling.

The total Hamiltonian is

$$\mathcal{H} = \mathcal{H}_\mathrm{B} + \mathcal{H}_\mathrm{S} + V. \tag{A.2}$$

We will write any operator $\tilde{A}$, the operator corresponding to A in the interaction picture. The density matrix, $\tilde{\rho}_{\mathrm{S+B}}(t)$ of the "universe", and the interaction Hamiltonian $\tilde{V}$, are related to $\rho_{\mathrm{S+B}}(t)$ and V via the unitary transformations

$$\tilde{\rho}_{\mathrm{S+B}}(t) = \mathcal{U}^{-1}(t)\rho_{\mathrm{S+B}}(t)\,\mathcal{U}(t) \quad \text{and} \quad \tilde{V}(t) \quad = \quad \mathcal{U}^{-1}(t)V\mathcal{U}(t), \tag{A.3}$$

where $\mathcal{U}(t) = \exp\left(\frac{1}{i\hbar}(\mathcal{H}_\mathrm{B} + \mathcal{H}_\mathrm{S})t\right)$. The Von Neumann equation for $\tilde{\rho}_{\mathrm{S+B}}$ is then

$$\frac{\partial}{\partial t}\tilde{\rho}_{\mathrm{S+B}}(t) = \frac{1}{i\hbar}\Big[\tilde{V}(t), \tilde{\rho}_{\mathrm{S+B}}(t)\Big], \tag{A.4}$$

which integrated two times gives

$$\begin{aligned} \Delta\tilde{\rho}_{\mathrm{S+B}}(t) \quad &= \quad \frac{1}{i\hbar}\int_t^{t+\Delta t} \mathrm{d}t'\Big[\tilde{V}(t'), \tilde{\rho}_{\mathrm{S+B}}(t')\Big] \\ &- \quad \frac{1}{\hbar^2}\int_t^{t+\Delta t} \mathrm{d}t' \int_t^{t'} \mathrm{d}t''\Big[\tilde{V}(t'), \Big[\tilde{V}(t''), \tilde{\rho}_{\mathrm{S+B}}(t'')\Big]\Big], \end{aligned} \tag{A.5}$$

where $\Delta\tilde{\rho}_{\mathrm{S+B}}(t) = \tilde{\rho}_{\mathrm{S+B}}(t+\Delta t) - \tilde{\rho}_{\mathrm{S+B}}(t)$.

This equation describes the evolution of the whole Hilbert space containing the modes of the system, but also all the modes of the reservoir. We will here only be interested in the evolution of the system *within* the bath, that is in the *reduced* density matrix $\tilde{\rho}$ of the system. It is obtained by tracing over the bath variables

$$\tilde{\rho}(t) = \mathrm{Tr}_\mathrm{B}(\tilde{\rho}_{\mathrm{S+B}}(t)). \tag{A.6}$$

Its evolution is then given by the trace with respect to B in Eq. (A.5)

$$\begin{aligned} \Delta\tilde{\rho}(t) \quad &= \quad \frac{1}{i\hbar}\int_t^{t+\Delta t} \mathrm{d}t'\mathrm{Tr}_\mathrm{B}\Big[\tilde{V}(t'), \tilde{\rho}_{\mathrm{S+B}}(t')\Big] \\ &- \quad \frac{1}{\hbar^2}\int_t^{t+\Delta t} \mathrm{d}t' \int_t^{t'} \mathrm{d}t''\mathrm{Tr}_\mathrm{B}\Big[\tilde{V}(t'), \Big[\tilde{V}(t''), \tilde{\rho}_{\mathrm{S+B}}(t'')\Big]\Big]. \end{aligned} \tag{A.7}$$

In general we do not need to keep that much information to model the interaction of the reservoir with the system. As the reservoir is large, it seems natural to assume that it will not be affected too much by the interaction. Some approximations about the bath and its interaction with the system will now be done to simplify Eq. (A.7).

A.1.2 Assumptions about the bath

We write the bath density operator as

$$\tilde{\rho}_\mathrm{B}(t) = \mathrm{Tr}_\mathrm{S}(\tilde{\rho}_{\mathrm{B+S}}(t)). \tag{A.8}$$

We will assume that it contains a number of modes so large that $\tilde{\rho}_\mathrm{B}(t)$ will not change much due to the coupling with the system. Its dependence with time will then be ignored and we will write $\tilde{\rho}_\mathrm{B}(t) = \rho_\mathrm{B}$.

By assuming the reservoir to be in a stationary state, i.e. to commute with the Hamiltonian $\mathcal{H}_{\rm B}$, we can write $\rho_{\rm B}$ as a statistical mixture of the Hamiltonian eigenstates $|\mu\rangle$

$$\rho_{\rm B} = \sum_{\mu} p_\mu |\mu\rangle\langle\mu|, \tag{A.9}$$

p_μ being the probability to find the reservoir in the state $|\mu\rangle$. We can write $|\mu\rangle$ in the number state basis

$$|\mu\rangle = |n_1, ..., n_i, ...\rangle, \tag{A.10}$$

where n_i is the number of excitation quanta in the mode i of the reservoir. The expansion of $\rho_{\rm B}$ in the Fock basis, in a reservoir at temperature T, is given by Eq. (1.24).

We also assume that the first order correlation function $\mathrm{Tr}_{\rm B}(\rho_{\rm B}\tilde{\mathcal{B}}(t))$ is zero. This is saying that the average value of $\mathcal{B}$ in the state $\rho_{\rm B}$ of B, i.e the mean number of photons in the bath, is negligible, which implies that

$$\mathrm{Tr}_{\rm B}(\rho_{\rm B}\tilde{V}(t)) = X^\dagger(t)\mathrm{Tr}_{\rm B}(\rho_{\rm B}\tilde{\mathcal{B}}(t)) = 0. \tag{A.11}$$

The first term of Eq. (A.7) is therefore negligible. We will also soon use the correlation function $g(t,t') = \mathrm{Tr}_{\rm B}(\rho_{\rm B}\tilde{\mathcal{B}}(t)\tilde{\mathcal{B}}(t'))$ of the reservoir variables. Using Eq. (A.9), one can show that the two times averaged correlation function $g(t,t')$ satisfies the two symmetry properties

$$g(t,t') = g(\tau) \text{ and } g(-\tau) = g^*(\tau), \tag{A.12}$$

which will become useful in the following derivations.

A.1.3 The Born-Markov approximation

To proceed further we will need to perform two approximations in Eq. (A.7).

We assume that the Hamiltonian $\tilde{V}$ is treated as a small perturbation to the free evolution of the system so that the time Δt over which the integration is done, is much shorter than the time evolution of the system modes T_s, i.e. $T_s \gg \Delta t$. This is *Born*'s approximation. With this assumption, we can neglect the evolution of $\tilde{\rho}_{\rm S+B}$ between t and t'' in Eq. (A.7).

We also suppose the correlation time τ_c between the reservoir modes and the system to be short so that, after a time $\tau_c \ll \Delta t$, there are no more correlations between them. This is equivalent to assuming that $g(\tau)$ tends to zero faster than the evolution of the system in a time Δt, a *Markov* approximation.

This allows us to approximate $\tilde{\rho}_{\rm S+B}(t)$ by

$$\tilde{\rho}_{\rm S+B}(t) \approx \tilde{\rho}(t) \otimes \rho_{\rm B}. \tag{A.13}$$

We can now write Eq. (A.7) in a simpler form

$$\frac{\Delta\tilde{\rho}}{\Delta t} = \frac{-1}{\hbar^2 \Delta t}\int_t^{t+\Delta t} \mathrm{d}t' \int_t^{t'} \mathrm{d}t'' \mathrm{Tr}_{\rm B}\Big[\tilde{V}(t'), \Big[\tilde{V}(t''), \tilde{\rho}(t'') \otimes \rho_B\Big]\Big]. \tag{A.14}$$

The integrand of the left hand side of this equation contains terms like $\mathrm{Tr}_B(\rho_{\rm B}\tilde{\mathcal{B}}(t')\tilde{\mathcal{B}}(t''))$, which are the functions $g(t',t'')$ introduced earlier. From the symmetry of g shown Eq. (A.12), it seems a good idea to change variables from (t',t'') to (τ,t'), where $\tau = t'-t''$.

Because $\tau_c \ll \Delta t$, we can now rewrite Eq. (A.14) as

$$\frac{d\tilde{\rho}}{dt} = \frac{-1}{\hbar^2 \Delta t}\int_0^\infty \mathrm{d}\tau \int_t^{t+\Delta t} \mathrm{d}t' \mathrm{Tr}_{\mathrm{B}}\Big[\tilde{V}(\tau), \Big[\tilde{V}(t'), \tilde{\rho}(t') \otimes \rho_B\Big]\Big]. \tag{A.15}$$

This is the *master equation.*

Because any quantum system interacts, to a certain degree, with its environment this equation forms the basis of many studies in quantum physics. As we will see, the coupling to the environment leads to irreversible damping of the system variables.

A.2 Unravelling the master equation to a c-number equation

We described the system evolution in the Schrödinger picture. One other method to solve a problem is using the Heisenberg picture, including Langevin noise terms to ensure a canonical evolution of the operators. When the problem to be solved has a complex non-linear dynamics however, one has to use numerical simulations which is not trivial from the Heisenberg picture because of the non-commuting properties of the operators. One possible method is to expand the master equation in a Fock state basis. The equation is then truncated to a certain number of photons to get something computationally manageable. This technique is therefore well adapted to the study of a small number of photons and atoms. We present here another way to extract exact solutions to non-linear problems by means of stochastic simulations in phase space [Gardiner, 1985], in the Schrödinger picture. To simulate a problem using stochastic methods one goes through the following steps

1. Convert the master equation in an equation for the characteristic function, in the appropriate representation, such as the Wigner, P, complex-P, or positive-P representations.

2. Fourier transform the characteristic function equation of motion to obtain a Fokker-Planck equation for the chosen quasi-probability distribution.

3. Convert the Fokker-Planck equation onto a set of stochastic differential equations in the Itô form.

4. Write the Itô stochastic differential equations in the Stratonovitch form, if required.

We describe here how to obtain a Fokker-Planck equation (FPE) from the reduced density matrix equation of motion, that is we present the steps 1 and 2. As they are a bit more involved and rather mathematical, steps 3 and 4 are presented in appendix A.

It can be seen from Eq. (A.15) that a general term in the master equation can be written

$$\frac{\partial}{\partial t}\hat{\rho} = \sum_{R_+,R_-,L_+,L_-} C_{R_+,R_-,L_-,L_+} (\hat{a}^\dagger)^{L_+}(\hat{a})^{L_-}\hat{\rho}(\hat{a}^\dagger)^{R_+}(\hat{a})^{R_-}, \tag{A.16}$$

where C_{R_+,R_-,L_-,L_+} are c-number coefficients and the $\hat{a}$'s are operators of the system, the superscripts refering to the ordering of the operators. We can now obtain an equation of motion for any characteristic function. Irrespective of the representation chosen, we have

$$\frac{\partial}{\partial t}\chi(\underline{\lambda}) = \sum_{R_+,R_-,L_+,L_-} C_{R_+,R_-,L_-,L_+}\langle(\hat{a}^\dagger)^{R_+}(\hat{a})^{R_-}\hat{\Xi}(\underline{\lambda})(\hat{a}^\dagger)^{L_+}(\hat{a})^{L_-}\rangle, \quad (A.17)$$

where we used Eq. (1.17) and the cyclic properties of the trace of a product. This is the first step of the method.

Let us now concentrate on the simpler case of a single bosonic mode $\hat{a}$ and write

$$\hat{\Xi} = e^{i\lambda_+\hat{a}^\dagger}e^{i\lambda_-\hat{a}}, \quad (A.18)$$

in the normally ordered definition. This choice of kernel implies that we are in the P representation. Before carrying on with the calculation, we first have to establish a few relations. It can be shown that

$$\begin{aligned}\hat{a}\hat{\Xi} &= \hat{\Xi}\hat{a} + [\hat{a},\hat{\Xi}] = (-\frac{\partial}{\partial\lambda_-} + i\lambda_+)\hat{\Xi}\\ \hat{\Xi}\hat{a}^\dagger &= \hat{a}^\dagger\hat{\Xi} - [\hat{a}^\dagger,\hat{\Xi}] = (-\frac{\partial}{\partial\lambda_+} + i\lambda_-)\hat{\Xi}\\ \hat{a}^\dagger\hat{\Xi} &= -i\frac{\partial}{\partial\lambda_+}\hat{\Xi} \text{ and } \hat{\Xi}\hat{a} = -i\frac{\partial}{\partial\lambda_-}\hat{\Xi}. \quad (A.19)\end{aligned}$$

From Eq. (A.19) and Eq. (A.17), we can obtain the equation of motion for the normally ordered characteristic function

$$\frac{\partial}{\partial t}\chi_N = (-\frac{\partial}{\partial\lambda_-} + i\lambda_+)^{R_-}(-i\frac{\partial}{\partial\lambda_+})^{R_+}(-\frac{\partial}{\partial\lambda_+} + i\lambda_-)^{L_+}(-i\frac{\partial}{\partial\lambda_-})^{L_-}\chi_N. \quad (A.20)$$

We can write $\underline{\alpha} = \alpha + i\beta$, the fourier conjugate of $\underline{\lambda}$, and, after Fourier transforming this result, obtain

$$\frac{\partial}{\partial t}P(\underline{\alpha}) = (\alpha - \frac{\partial}{\partial\beta})^{R_-}\beta^{R_+}(\beta - \frac{\partial}{\partial\alpha})^{L_-}\alpha^{L_-}P(\underline{\alpha}), \quad (A.21)$$

which is a *Fokker-Planck equation.* Such a FPE describes how the probability distribution P of the system state broadens, or drifts with time.

It is straightforward to generalize the FPE to an n-dimensional variable $\underline{x}$ and get

$$\frac{\partial}{\partial t}P(\underline{x}) = -\sum_i \partial_i[A(\underline{x},t)P(\underline{x})] + \frac{1}{2}\sum_{i,j}\frac{\partial^2}{\partial i\partial j}[\mathbf{B}(\underline{x},t)\mathbf{B}^T(\mathbf{x},t)]_{ij}P(\underline{x})]). \quad (A.22)$$

The first order derivatives correspond to the *deterministic* part, or the *drift velocity.* The second order derivatives correspond to the *diffusion* part of the FPE. We show in appendix A that there is equivalence between the FPE and stochastic partial differential equations.

A.3 Stochastic averages

One can in principle obtain numerical solutions to any non-linear problem by calculating moments from stochastic averages. To output the average of the operator

$\hat{O} = \hat{O}_1^{n_1} \hat{O}_2^{n_2} ... \hat{O}_N^{n_N}$ one calculates

$$\overline{\prod_j \alpha_j^{n_j}} = \int d\underline{\alpha} \prod_{j=1}^{N} \alpha_j^{n_j} P(\underline{\alpha}), \tag{A.23}$$

where P obeys a Fokker-Planck equation. Let us show that the stochastic average (A.23) gives the correct quantum mechanical measurement of $\hat{O}$. As an example, we again choose the normally ordered characteristic function $\chi_N(\underline{\lambda})$, with the normally ordered kernel defined as $\hat{\Xi}(\underline{\lambda}) = \prod_{j=1}^{N} e^{i\lambda_j \hat{O}_j^{n_j}}$. We then have

$$\int d\underline{\alpha} \prod_{j=1}^{N} \alpha_j^{n_j} P(\underline{\alpha}) \;=\; \int d\underline{\alpha} \int d\underline{\lambda} \frac{1}{(2\pi)^N} \mathrm{Tr}\big(e^{-i\underline{\lambda}\underline{\alpha}} \hat{\rho} \prod_{j=1}^{N} \alpha_j^{n_j} e^{-i\lambda_j \hat{O}_j}\big). \tag{A.24}$$

After successive integrations by parts and assuming the boundary terms to be zero, we have

$$\int d\lambda_j e^{-i\lambda_j \alpha_j} \alpha_j^{n_j} e^{-i\lambda_j \hat{O}_j} \;=\; \int d\lambda_j e^{-i\lambda_j \alpha_j} \hat{O}_j^{n_j} e^{-i\lambda_j \hat{O}_j}. \tag{A.25}$$

After some work, we can finally show that

$$\int d\underline{\alpha} \prod_{j=1}^{N} \alpha_j^{n_j} P(\underline{\alpha}) \;=\; \mathrm{Tr}\big(\hat{\rho} \prod_{j=1}^{N} \hat{O}_j^{n_j}\big) = \langle \hat{O}_1^{n_1} \hat{O}_2^{n_2} ... \hat{O}_N^{n_N} \rangle. \tag{A.26}$$

The result shows that expectation values using stochastic averages gives the correct quantum mechanical average. The answer depends on the chosen ordering. The calculation can also be repeated for the symmetrically and anti-normally ordered characteristic functions. It can be shown that the anti-normally/symmetrically ordered moments are also calculated from the anti-normally/symmetrically ordered characteristic functions.

A.4 Langevin correlations

We presented the Heisenberg-Langevin equations in chapter 1. To calculate expectation values of the operators in the Heisenberg picture, the knowledge of the correlations between the Langevin operators $\langle \hat{F}_q \hat{F}_{q'} \rangle$ is required. We derive here the generalized Einstein relations that link the atomic mean variables with the fluctuations. To calculate them, we follow the derivation made in [Cohen-Tannoudji et al., 1993]. For a general system described by an n-dimensional vector $\hat{\underline{\sigma}} = (...\hat{\sigma}_q...)$, a Heisenberg-Langevin equation can always be written

$$\frac{d}{dt}\hat{\underline{\sigma}}(t) \;=\; \mathcal{D}(\hat{\underline{\sigma}}(t)) + \hat{\underline{F}}(t). \tag{A.27}$$

$\mathcal{D}(\hat{\underline{\sigma}}(t))$ is called the *deterministic part*, or the *drift velocity* of the Heisenberg-Langevin equations which contains both the reversible and irreversible mean evolution of the system variables. Let us write

$$\langle \hat{F}_q^{\dagger}(t) \hat{F}_{q'}(t') \rangle = 2D_{qq'} g(t - t'), \tag{A.28}$$

where $D_{qq'}$ is a diffusion coefficient with characteristic dynamic rate γ and $g(t-t')$ a normalized correlation function, with a width on the order of a characteristic time τ_c. The objective of this section is to derive $D_{qq'}$ as a function of the drift velocity coefficients.

Let us first calculate the equation of motion for the averaged operator $\hat{\sigma}_q^\dagger(t)\hat{\sigma}_{q'}(t)$

$$\begin{aligned} \frac{d}{dt}\langle\hat{\sigma}_q^\dagger(t)\hat{\sigma}_{q'}(t)\rangle &= \langle\mathcal{D}(\hat{\sigma}_q^\dagger(t)\hat{\sigma}_{q'}(t))\rangle && \text{(A.29)} \\ &= \langle\mathcal{D}(\hat{\sigma}_q^\dagger(t))\hat{\sigma}_{q'}(t)\rangle + \langle\hat{\sigma}_q^\dagger(t)\mathcal{D}(\hat{\sigma}_{q'}(t))\rangle \\ &+ \langle\hat{F}_q^\dagger(t)\hat{\sigma}_{q'}(t) + \hat{\sigma}_q(t)\hat{F}_{q'}(t)\rangle. && \text{(A.30)} \end{aligned}$$

where we used Eq. (A.27), and the formula for the derivative of a product, to obtain the second equation. We will now integrate Eq. (A.27) from a time $t-\Delta t$ to a time t, assuming Δt much smaller than $1/\gamma$. This allows us to make a linear approximation for the rate of variation of $\hat{\sigma}_{q'}(t)$ and to get

$$\hat{\sigma}_{q'}(t) - \hat{\sigma}_{q'}(t-\Delta t) = \Delta t\mathcal{D}(\hat{\sigma}_{q'}(t-\Delta t)) + \int_{t-\Delta t}^{t} dt'\hat{F}_{q'}(t'). \tag{A.31}$$

As the Langevin forces $\hat{F}_q(t)$ and the atomic operators $\hat{\sigma}_{q'}(t')$ are uncorrelated after a time $\Delta t > \tau_c$, (in the Markov approximation) using Eq. (A.31) and Eq. (A.28), we obtain

$$\begin{aligned} \langle\hat{F}_q^\dagger(t)\hat{\sigma}_{q'}(t) + \hat{\sigma}_q(t)\hat{F}_{q'}(t)\rangle &= \int_{t-\Delta t}^{t} dt'\langle\hat{F}_q^\dagger(t)\hat{F}_{q'}(t) + \hat{F}_q^\dagger(t)\hat{F}_{q'}(t)\rangle \\ &= 2D_{qq'}\int_{-\Delta t}^{\Delta t} d\tau g(\tau) \simeq 2D_{qq'}. && \text{(A.32)} \end{aligned}$$

We can finally insert Eq. (A.32) into Eq. (A.30) to obtain

$$2D_{qq'} = \big\langle\mathcal{D}(\hat{\sigma}_q^\dagger\hat{\sigma}_{q'}) - \mathcal{D}(\hat{\sigma}_q^\dagger)\hat{\sigma}_{q'} - \hat{\sigma}_q^\dagger\mathcal{D}(\hat{\sigma}_{q'})\big\rangle, \tag{A.33}$$

which are the generalized Einstein relations. We recognize the similarity between Eq.(A.33) and the Liouvillian terms in the master equation.

These relations link dissipation with the macroscopic fluctuations $D_{qq'}$, and will be proven useful to gain understanding in the processes giving excess-noise in quantum memories. In a reservoir at zero temperature, the anti-normally ordered correlations $\langle\hat{F}_q\hat{F}_{q'}^\dagger\rangle$, add vacuum noise only. However, the normally ordered correlations $\langle\hat{F}_q^\dagger\hat{F}_{q'}\rangle$ will contribute to excess noise in some regimes.

Unfortunately, for a general situation, no method (even numerical) can yet solve the set of Heisenberg-Langevin equations for a two-level atom with a quantized light field. Approximations always have to be made on the strength of the input beam whilst still keeping the higher order non-linearities[1]. We will show briefly why phase space simulations also fail to get within the full non-linear regime in chapter 4.

---

[1] The equations are often linearized, then a mean field approximation is made to solve the resulting linear set of equations. This precludes the study of non-gaussian states.

Appendix B

From stochastic equations to the Fokker-Planck equation

From the Fokker-Planck equation (FPE) presented chapter 1, stochastic partial differential equations (SPDE) can be obtained. A completely *equivalent* equation to the Fokker-Planck equation is

$$\frac{dx(t)}{dt} = a(x,t) + b(x,t)\xi(t), \tag{B.1}$$

where $\xi(t)$ and $\xi(t')$ are noise terms correlated within a certain time interval τ_c, and have a zero average. Obtaining *a* SPDE (the solution is not unique) from the FPE can be done shown but because there is no unicity the other implication is a bit more involved. We will show here that the FPE can also be obtained from the SPDE.

Each solution of the above "Langevin" equation follows a different path, or trajectory, in phase space because of the random variable $\xi(t)$. When averaged over many of these paths, a physical answer can be obtained. However, because the noise terms are delta correlated they will give rise to a white noise spectrum. This is valid in situations where the time between each measurements is much greater than the correlation time. The mathematical derivation of the Langevin equation was done much later by Itô. The proof relies on defining a stochastic integral obeying specific calculus rules.

A stochastic differential equation for $x(t)$ can be written

$$dx(t) = a[x(t),t]dt + b[x(t),t]dW(t), \tag{B.2}$$

where $dW(t)$ (analogous to $\xi(t)dt$) is a stochastic Wiener process, that is a continuous function with Gaussian probability distribution, whose width is asymptoting to zero with time. By definition, a stochastic variable $x(t)$ obeys a SPDE if

$$x(t) = x(t_0) + \int_{t_0}^{t} dt' \Big[a[x(t'),t'] + b[x(t),t]dW(t')\Big]. \tag{B.3}$$

The Wiener process is not continuous so one has to be careful when doing the integration. The integral used in this expression can be defined rigorously in the manner of Riemann-Stieltjes. The total interval over which the integration is done is divided into discrete segments and the integral defined as the limit of partial sums where local averaging has been done. The value of the mean partial sum can be calculated in different ways but actually changes the value of the integral. Two definitions are normally used in the literature : the Itô and Stratonovitch definitions.

The Itô integral I is defined as :

$$I\int_{t_0}^{t} b(t')dW(t') = \lim_{n\to\infty}\sum b(t_i)\big[W(t_{i+1,t_0}) - W(t_{i,t_0})\big], \tag{B.4}$$

whilst the Stratonovitch integral S is :

$$S\int_{t_0}^{t} b(t')dW(t') = \lim_{n\to\infty}\sum b(\frac{t_i + t_{i+1}}{2})\big[W(t_{i+1,t_0}) - W(t_{i,t_0})\big], \tag{B.5}$$

The conditions for uniqueness and existence of the coefficients in the integral B.3 can be shown [Gardiner, 1985] for both the Itô and Stratonovitch definitions, demonstrating the validity of those expressions.

Change of variables in the Itô algebra

A set of rules can be derived in the Itô calculus. It can be shown that $[dW(t)]^2 = dt$, implying that $dW(t)$ is on the order $\sqrt{dt}$. We then also have $dt^2 \to 0$ and $dtdW \to 0$.

Performing operations in the Itô algebra is not immediate, as the rules of ordinary calculus do not always apply. We will here give the (important) example of the change of variables to illustrate it. To derive a SPDE for a general function f of $x(t)$ one can expand $df[x(t)]$ to second order in $dW(t)$ and get

$$\begin{aligned} df[x(t)] &= f[x(t)+dx(t)] - f[x(t)] \\ &= \partial_x f[x(t)]dx(t) + \frac{1}{2}\partial_x^2 f[x(t)]dx(t)^2 \\ &= \partial_x f[x(t)]\Big(a[x(t),t]dt + b[x(t),t]dW(t)\Big) + \frac{1}{2}b[x(t),t]^2\partial_x^2 f[x(t)][dW(t)]^2 + ... \end{aligned} \tag{B.6}$$

By definition of the Wiener increment $[dW(t)]^2 = dt$, so we obtain

$$\begin{aligned} df[x(t)] &= \Big(a[x(t),t]\partial_x f[x(t)] + \frac{1}{2}b[x(t),t]^2\partial_x^2 f[x(t)]\Big)dt \\ &+ b[x(t),t]\partial_x f[x(t)]dW(t). \end{aligned} \tag{B.7}$$

This is the *Itô formula*. We see that a change of variable does not follow normal calculus because from normal algebra we expect the change of variable to give

$$df[x(t)] = \Big(a[x(t),t]dt + b[x(t),t]dW(t)\Big)\partial_x f[x(t)]. \tag{B.8}$$

Unless $f[x(t)]$ is linear in $x(t)$[1], we cannot use standard algebra to solve the equations. This result can be generalized to an n-dimensional system. For an n-dimensional vector $\mathbf{x(t)}$ satisfying the SPDE

$$d\mathbf{x}(t) = \mathbf{A}[\mathbf{x}(t),t]dt + \mathbf{B}[\mathbf{x}(\mathbf{t}),\mathbf{t}]\mathbf{dW}(\mathbf{t}), \tag{B.9}$$

---

[1] The last term of the first line of Eq. (B.7) would then vanish because $\partial_x^2 f[x(t)] = 0$.

we have

$$
\begin{aligned}
df[x(t)] &= \Big(\sum_i A_i[\mathbf{x},t]\partial_i f(\mathbf{x}) + \frac{1}{2}\sum_{i,j}\big[\mathbf{B}[\mathbf{x},t]\mathbf{B}^T[\mathbf{x},t]_{ij}\partial_i\partial_j f[\mathbf{x},t]\big]\Big)dt \\
&+ \sum_{i,j} B_{i,j}[\mathbf{x},t]\partial_i f(x) dW_j(t). \qquad \text{(B.10)}
\end{aligned}
$$

This is one example for which normal calculus does not apply. The chain rule used in most algorithms for solving partial differential equations also does not hold and using such an equation in numerical simulations is therefore impossible. The Stratonovitch definition of the stochastic integral does not have these issues.

Stratonovitch form of the SPDE

It can be shown, using the Itô formula, that there is a connection between the Itô SPDE and Stratovitch SPDE. The equivalent Stratonovitch equations of the Itô equations is found by doing the change of variable

$$
A_i^s = A_i - \frac{1}{2}\sum_{j,k} B_{kj}\partial_k B_{ij} \text{ and } B_{ij}^s = B_{ij}. \qquad \text{(B.11)}
$$

The new form of the SPDE now obeys normal calculus. It can now be shown, for example, that the rule for a change of variable is the same as in ordinary calculus. We also note that if the diffusion coefficient is a constant, the Itô and Statonovitch forms are equivalent. The linear dependence of the diffusion terms on the system variables has to be checked whenever an Itô SPDE is used in numerical simulations otherwise these corrections have to be made.

From the SPDE to the Fokker-Planck equation

From the Itô SPDE (or Stratonovitvh SPDE) a Fokker-Planck equation can be obtained. Although SPDE are normally derived from the Fokker-Planck equations after unravelling of the master equation, this derivation allows one to present one side of the equivalence simply. We consider the one-dimensional case for simplicity. Let us consider the time evolution of a function $f[x(t)]$

$$
\begin{aligned}
\frac{\langle df[x(t)]\rangle}{dt} &= \langle\frac{df[x(t)]}{dt}\rangle = \frac{d}{dt}\langle f[x(t)]\rangle \\
&= \langle a[x(t),t]\partial_x f + \frac{1}{2}b[x(t),t]^2\partial_x^2 f\rangle \qquad \text{(B.12)}
\end{aligned}
$$

where we used Itô's formula (Eq. B.7) and $\langle dW(t)\rangle = 0$. If we call $p(x(t))$ the probability density of the variable $x(t)$ we have

$$
\begin{aligned}
\frac{d}{dt}\langle f[x(t)]\rangle &= \int dx f(x)\partial_t p(x(t)) \\
&= \int dx\big[a(x,t)\partial_x f + \frac{1}{2}b(x,t)^2\partial_x^2 f\big]p(x(t)). \qquad \text{(B.13)}
\end{aligned}
$$

We can then integrate by parts and show that

$$\int dx f(x) \partial_t p = \int dx f(x) \big(- \partial_x [a(x,t)p] + \frac{1}{2} \partial_x^2 [b(x,t)^2 p] \big). \tag{B.14}$$

Because we chose an arbitrary function f we can obtain

$$\partial_t p = - \big(\partial_x [a(x,t)p] + \frac{1}{2} \partial_x^2 [b(x,t)^2 p] \big). \tag{B.15}$$

We found the one-dimensional version of the *Fokker-Planck* Equation A.22. The result can be generalized to a multidimensional problem easily. Again, there is a perfect equivalence between a diffusion process modeled by this equation and the stochastic equations.

Appendix C

Stochastic equations for EIT

We list here the stochastic equations describing the evolution of the atomic c-numbers in the presence of a quantized probe field and a classical pump for one slice δz of the EIT medium. These equation are solved numerically in chapter 4. The c-numbers α and β represent the operators $\hat{\mathcal{E}}^\dagger(z,t)$ and $\hat{\mathcal{E}}(z,t)$. The atomic variables $(\sigma_{11},\sigma_{10},\sigma_9,\sigma_7,\sigma_6,\sigma_5,\sigma_4,\sigma_3)$ represent the operators $(\hat{\sigma}_{13},\hat{\sigma}_{23},\hat{\sigma}_{12},\hat{\sigma}_{11},\hat{\sigma}_{22},\hat{\sigma}_{21},\hat{\sigma}_{32},\hat{\sigma}_{31})$. The equation for σ_8 linearly depends on σ_6 and σ_7 via the population preservation equation $\sigma_6+\sigma_7+\sigma_8=1$ and is therefore not computed. The noise terms n_j (for $j=1$ to 18) are all delta-correlated and follow a Gaussian distribution, and have been normalized by $\frac{1}{\sqrt{n\mathcal{A}}}$. The variables $\overline{g}, \overline{\gamma_0}$, $\overline{\gamma_c}$ and $\overline{E_c}$ are all normalized to the spontaneous emission rate γ.

The equations for the optical polarisations and the ground state coherences are

$$\begin{aligned}
\dot{\sigma}_3 &= -(1+\overline{\gamma}_0/2+\overline{\gamma}_c/2)\sigma_3+\overline{E}_c\sigma_5-\alpha(1-2\sigma_6-\sigma_7)+\sqrt{\frac{\overline{g}}{2\gamma}}(\alpha/\overline{g}-\sigma_3)n_1\\
&\quad +i\sqrt{\frac{\overline{g}}{2\gamma}}(\alpha/\overline{g}+\sigma_3)n_2-(\alpha\sigma_4+\overline{E}_c\sigma_3)(n_3-in_4)\\
&\quad +\frac{1}{2\sqrt{\gamma}}\sqrt{(\overline{\gamma}_c+\overline{\gamma}_0/2)(1-\sigma_7-\sigma_6)}(in_7+\sqrt{2}n_{10}+in_{12})\\
&\quad +\sqrt{2}(\overline{\gamma}_c+\overline{\gamma}_0/2)\sigma_4(n_{14}-in_{13})\\
\dot{\sigma}_4 &= -(1+\overline{\gamma}_0/2+\overline{\gamma}_c/2)\sigma_4+\alpha\sigma_9+\overline{E}_c(\sigma_6+2\sigma_7-1)+\sqrt{\frac{\overline{g}}{2\gamma}}(\sigma_4-\overline{E}_c/\overline{g})n_1\\
&\quad -i\sqrt{\frac{\overline{g}}{2\gamma}}(\sigma_4+\overline{E}_c/\overline{g})n_2+(n_3+in_4)/\gamma\\
&\quad +(\overline{\gamma}_c+\overline{\gamma}_0/2)(1-\sigma_6-\sigma_7)(in_{15}+n_{16})/4\\
\dot{\sigma}_5 &= -(\overline{\gamma}_c+\overline{\gamma_0})\sigma_5-\alpha\sigma_{10}-\overline{E}_c\sigma_3-\sqrt{\frac{\overline{g}}{2\gamma}}\sigma_5(n_1-in_2)\\
&\quad +(\alpha(\sigma_6-\sigma_7)+(\overline{\gamma}_c+\overline{\gamma}_0/2)\sigma_3)(n_3-in_4)/2+\frac{1}{2\sqrt{2}\gamma}(n_5-in_6)\\
&\quad +\frac{1}{2\sqrt{\gamma}}\sqrt{\alpha\sigma_{11}+\beta\sigma_3+1-\sigma_6-\sigma_7+2\overline{\gamma}_0\sigma_7+\overline{\gamma}_c(\sigma_6+\sigma_7)}(in_8+\sqrt{2}n_9+in_{11})
\end{aligned} \tag{C.1}$$

$$
\begin{aligned}
\dot{\sigma}_9 &= -(\overline{\gamma}_c + \overline{\gamma}_0)\sigma_9 - \beta\sigma_4 - \overline{E}_c\sigma_{11} \\
&\quad + \frac{1}{2\sqrt{\gamma}}\sqrt{\alpha\sigma_{11} + \beta\sigma_3 + 1 - \sigma_6 - \sigma_7 + \overline{\gamma}_c(\sigma_6 + \sigma_7) + 2\overline{\gamma}_0\sigma_7}(-in_8 + \sqrt{2}n_9 - in_{11}) \\
&\quad + \frac{1}{2\sqrt{2}\gamma}(n_{14} + in_{13}) + (\beta(\sigma_6 - \sigma_7) + (\overline{\gamma}_c + \overline{\gamma}_0/2)\sigma_{11})(in_{15} + n_{16})/2 \\
&\quad - \sqrt{\frac{\overline{g}}{2\gamma}}\sigma_9(in_{17} + n_{18}) \\
\dot{\sigma}_{10} &= -(1 + \overline{\gamma}_0/2 + \overline{\gamma}_c/2)\sigma_{10} + \beta\sigma_5 + \overline{E}_c(2\sigma_7 + \sigma_6 - 1) \\
&\quad + (\overline{\gamma}_c + \overline{\gamma}_0/2)(1 - \sigma_6 - \sigma_7)(n_3 - in_4)/4 + (n_{16} - in_{15})/\gamma \\
&\quad + i\sqrt{\frac{\overline{g}}{2\gamma}}(\sigma_{10} + \overline{E}_c/\overline{g})n_{17} + \sqrt{\frac{\overline{g}}{2\gamma}}(\sigma_{10} - \overline{E}_c/\overline{g})n_{18} \\
\dot{\sigma}_{11} &= -(1 + \overline{\gamma}_0/2 + \overline{\gamma}_c/2)\sigma_{11} + \overline{E}_c\sigma_9 - \beta(1 - 2\sigma_6 - \sigma_7) + \sqrt{2}(\overline{\gamma}_0/2 + \overline{\gamma}_c)\sigma_{10}(n_5 + in_6) \\
&\quad + \frac{1}{2\sqrt{\gamma}}\sqrt{(\overline{\gamma}_c + \overline{\gamma}_0/2)(1 - \sigma_6 - \sigma_7)}(-in_7 + \sqrt{2}n_{10} - in_{12}) \\
&\quad - (\beta\sigma_{10} + \overline{E}_c\sigma_{11})(in_{15} + n_{16}) - i\sqrt{\frac{\overline{g}}{2\gamma}}(\beta/\overline{g} + \sigma_{11})n_{17} \\
&\quad + \sqrt{\frac{\overline{g}}{2\gamma}}(\beta/\overline{g} - \sigma_{11})n_{18}. \qquad \text{(C.2)}
\end{aligned}
$$

The equations for the populations are

$$
\begin{aligned}
\dot{\sigma}_6 &= 1 - \sigma_6 - \sigma_7 - \overline{\gamma}_c(\sigma_6 - \sigma_7) - \alpha\sigma_{11} - \beta\sigma_3 - \frac{\overline{\gamma}_c}{\sqrt{2\overline{g}\gamma}}(n_1 + in_2) - \alpha\sigma_9(n_3 - in_4)/2 \\
&\quad + \sqrt{\alpha\sigma_{11} + \beta\sigma_3 + 1 - \sigma_6 - \sigma_7} \times \\
&\quad \sqrt{\alpha\sigma_{11} + \beta\sigma_3 + 1 - \sigma_6 - \sigma_7 + 2\overline{\gamma}_0\sigma_7 + \overline{\gamma}_c(\sigma_6 + \sigma_7)}(n_5 + in_6 + n_{14} - in_{13}) \\
&\quad + \sqrt{\frac{\overline{\gamma_c}}{2\gamma}(\sigma_6 + \sigma_7)}(n_7 - n_{12}) - \frac{1}{\sqrt{\gamma}}\sqrt{\alpha\sigma_{11} + \beta\sigma_3 + 1 - \sigma_6 - \sigma_7}n_9 \\
&\quad - \beta\sigma_5(in_{15} + n_{16})/2 - \frac{\overline{\gamma}_c}{\gamma}(n_{18} - in_{17}) \\
\dot{\sigma}_7 &= 1 - \sigma_6 - \sigma_7 - \overline{\gamma}_c(\sigma_7 - \sigma_6) - \overline{E}_c(\sigma_4 + \sigma_{10}) + \frac{\overline{\gamma}_c}{\sqrt{2\overline{g}\gamma}}(n_1 + in_2) + \alpha\sigma_9(n_3 - in_4)/2 \\
&\quad + \sqrt{2}(\alpha\sigma_{10} + \overline{E}_c\sigma_3)(n_5 + in_6) + \sqrt{\frac{\overline{\gamma}_c}{2\gamma}(\sigma_6 + \sigma_7)}(n_{12} - n_7) \\
&\quad + \frac{1}{\sqrt{2\gamma}}\sqrt{\overline{E}_c(\sigma_4 + \sigma_{10}) + 1 - \sigma_6 - \sigma_7}(n_8 - n_{11}) \\
&\quad + \sqrt{2}(\beta\sigma_4 + \overline{E}_c\sigma_{11})(n_{14} - in_{13}) + \beta\sigma_5(n_{16} + in_{15})/2 + \frac{\overline{\gamma}_c}{\sqrt{2\overline{g}\gamma}}(n_{18} - in_{17}). \qquad \text{(C.3)}
\end{aligned}
$$

The Stratonovitch corrections to the Ito-SDE $(\partial_t\sigma_3, \partial_t\sigma_4, \partial_t\sigma_5, \partial_t\sigma_6, \partial_t\sigma_7, \partial_t\sigma_9, \partial_t\sigma_{10}, \partial_t\sigma_{11})$ are

$$
\begin{aligned}
&(\frac{3\alpha}{2\gamma}, \frac{\overline{E}_c}{2\gamma}, \frac{(\overline{\gamma_c}-1)\sqrt{1-\alpha_6-\alpha_7+\alpha\sigma_{11}+\beta\sigma_3}}{4\gamma\sqrt{2}\sqrt{1-(1-\overline{\gamma_c}\alpha_6-(1-\overline{\gamma_c}-\overline{\gamma_0})\alpha_7+\alpha\sigma_{11}+\beta\sigma_3}}, \frac{1}{4\gamma} \\
&, \frac{1}{4\gamma}, \frac{(\overline{\gamma_c}-1)\sqrt{1-\alpha_6-\alpha_7+\alpha\sigma_{11}+\beta\sigma_3}}{4\gamma\sqrt{2}\sqrt{1-(1-\overline{\gamma_c})\alpha_6-(1-\overline{\gamma_c}-\overline{\gamma_0})\alpha_7+\alpha\sigma_{11}+\beta\sigma_3}}, \frac{\overline{E}_c}{2\gamma}, \frac{3\beta}{2\gamma}). \qquad \text{(C.4)}
\end{aligned}
$$

They are negligibly small compared to the other variables of the Ito-SDE equations and are not used in the simulations.

Appendix D

Storage of a continuous wave signal using GEM

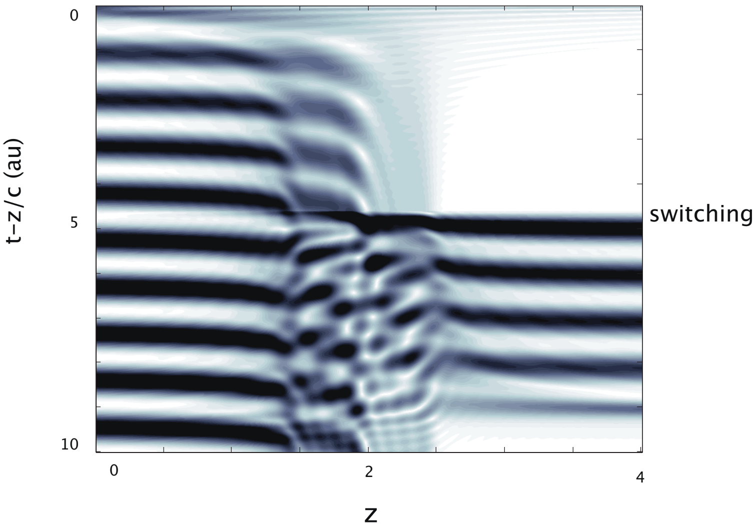

Figure D.1: Storage of a continuous wave signal.

We saw in chapter 7, that the Fourier encoding nature of the GEM system allows large time bandwidth products to be reached. This is again only true, provided the pulse does not saturate the medium and that decoherence effects are negligible. The consequence is that storing a really long Gaussian pulse is not an issue, it is in fact easier, as less broadening is required. During the storage time the information concerning the pulse length is stored in the width of the atomic spatial profile. The spatial atomic profile narrows as the pulse comes in the medium.

A natural question to ask is then, what would happen if one decided to leave the signal field continuously on and to flip the electric field whilst there is still light input to the system ? We show here that, provided the frequency of the information carried by light is large enough, the medium stores and recalls the signal that was input before the flipping stage, without interfering with the light that is still coming.

Simulations of such a scheme are presented Fig. D.1, where a long modulated pulse is input to the medium. The Stark shift is flipped at a time $t = t_{\text{switch}}$. The first part of the pulse (at $t < t_{\text{switch}}$) interacts when the medium has a positive Stark shift slope. The second part of the pulse (at $t < t_{\text{switch}}$) interacts with the medium when the Stark shift slope is negative. When the first part of the field is stored, we can see again the frequency decomposition of the GEM system. Because of the flipping of the Stark shift, the information stored leaves the medium whilst the last part of the pulse is still entering. The surprising result here is that the modulation from the first part of the pulse leaves the medium without interfering with the second incoming wave.

Let us concentrate on the evolution of the upper sideband of the modulated pulse. The upper sideband information was stored in the second part of the medium (because the Stark-shift slope is positive). After flipping, it is sent to the first part of the medium. When the second half of the pulse comes after a time $t > t_{\text{switch}}$, its upper sideband will now be stored at the beginning of the sample. When the time taken for this information to reach the atoms they are resonant with, is much larger than the time it takes for the initial upper sideband that was stored to leave, they do not interact with each other. The same arguments can be used for the lower sideband.

The beating seen in Fig. D.1 indeed happens for low frequency information, therefore the light at high frequency can leave the sample without problems. A quantitative study of the amount of phase shift and the actual cut-off frequency for which this continuous wave storage works was not done in details.

The conclusion of this appendix is that, a continuous wave signal carrying information can be input to the Stark shifted medium, and when the information needs to be retrieved, the signal does not need to be turned off. Provided the sideband frequency of the information is large enough, the Stark-shift slope can be simply flipped and the whole input signal can leave the medium without interfering with what is still coming in.

Bibliography

D. S. Abrams and S. Lloyd. Simulation of Many-Body Fermi Systems on a Universal Quantum Computer. *Phys. Rev. Lett.*, 79:2586–2589, September 1997.

M. Afzelius, C. Simon, H. de Riedmatten, and N. Gisin. Multi-Mode Quantum Memory based on Atomic Frequency Combs. *arXiv:0805.4164v1*, May 2008.

D. Akamatsu, K. Akiba, and M. Kozuma. Electromagnetically Induced Transparency with Squeezed Vacuum. *Phys. Rev. Lett.*, 92(20):203602, May 2004.

D. Akamatsu, Y. Yokoi, T. Tanimura, A. Furusawa, and M. Kozuma. Ultraslow Propagation of a Squeezed Vacuum with Electromagnetically Induced Transparency. *ArXiv Quantum Physics e-prints*, November 2006.

E. B. Aleksandrov and V. S. Zapasskii. A fairy tale of stopped light. *Physics-Uspekhi*, 47 (10):1033, 2004.

A. L. Alexander, J. J. Longdell, M. J. Sellars, and N. B. Manson. Photon Echoes Produced by Switching Electric Fields. *Phys. Rev. Lett.*, 96(4):043602, February 2006.

A. L. Alexander, J. J. Longdell, M. J. Sellars, and N. B. Manson. Coherent information storage with photon echoes produced by switching electric fields. *Journal of Luminescence*, 127:94–97, 2007.

J. Appel, E. Figueroa, D. Korystov, M. Lobino, and A. I. Lvovsky. Quantum Memory for Squeezed Light. *Phys. Rev. Lett.*, 100(9):093602, March 2008.

J. Appel, D. Hoffman, E. Figueroa, and A. I. Lvovsky. Electronic noise in optical homodyne tomography. *Phys. Rev. A*, 75(3):035802, March 2007.

J. Appel, K.-P. Marzlin, and A. I. Lvovsky. Raman adiabatic transfer of optical states in multilevel atoms. *Phys. Rev. A*, 73(1):013804, January 2006.

M. Arikawa, K. Honda, D. Akamatsu, Y. Yokoil, K. Akiba, S. Nagatsuka, A. Furusawa, and M. Kozuma. Observation of electromagnetically induced transparency for a squeezed vacuum with the time domain method. *Optics Express*, 15:11849, 2007.

E. Arimondo. Relaxation processes in coherent-population trapping. *Phys. Rev. A*, 54: 2216–2223, September 1996.

E. Arimondo, M. Inguscio, and P. Violino. Experimental determinations of the hyperfine structure in the alkali atoms. *Reviews of Modern Physics*, 49:31–76, January 1977.

D. K. Armani, T. J. Kippenberg, S. M. Spillane, and K. J. Vahala. Ultra-high-Q toroid microcavity on a chip. *Nature*, 421:925–928, February 2003.

A. Aspect, E. Arimondo, R. Kaiser, N. Vansteenkiste, and C. Cohen-Tannoudji. Laser cooling below the one-photon recoil by velocity-selective coherent population trapping. *Phys. Rev. Lett.*, 61:826–829, August 1988.

M. Bajcsy, A. S. Zibrov, and M. D. Lukin. Stationary pulses of light in an atomic medium. *Nature*, 426:638–641, December 2003.

P. Barberis-Blostein and M. Bienert. Opacity of Electromagnetically Induced Transparency for Quantum Fluctuations. *Phys. Rev. Lett.*, 98(3):033602, January 2007.

P. Barberis-Blostein and N. Zagury. Field correlations in electromagnetically induced transparency. *Phys. Rev. A*, 70(5):053827, November 2004.

M. D. Barrett, J. Chiaverini, T. Schaetz, J. Britton, W. M. Itano, J. D. Jost, E. Knill, C. Langer, D. Leibfried, R. Ozeri, and D. J. Wineland. Deterministic quantum teleportation of atomic qubits. *Nature*, 429:737–739, June 2004.

C. H. Bennett, G. Brassard, C. Crepeau, R. Jozsa, A. Peres, and W. K. Wootters. Teleporting an unknown quantum state via dual classical and Einstein-Podolsky-Rosen channels. *Phys. Rev. Lett.*, 70:1895–1899, March 1993.

C. H. Bennett, G. Brassard, S. Popescu, B. Schumacher, J. A. Smolin, and W. K. Wootters. Purification of Noisy Entanglement and Faithful Teleportation via Noisy Channels. *Phys. Rev. Lett.*, 76:722–725, January 1996.

C.C.H. Bennett and G Brassard. Quantum Cryptography: Public Key Distribution and Coin Tossing. *Proceedings of IEEE International Conference on Computers, Systems, and Signal Processing*, 175, 1984.

T. Böttger, Y. Sun, C. W. Thiel, and R. L. Cone. Spectroscopy and dynamics of Er^{3+} : Y_2SiO_5 at 1.5μm. *Phys. Rev. B*, 74(7):075107, August 2006.

B. Boulanger, J. Rousseau, J P. Fève, B. Maglione, M. Ménaert , and G. Marnier. Optical studies of laser-induced gray-tracking in KTP. *IEEE J. Quant. Electron.*, 35:281, January 1999.

W. P. Bowen. *'Experiments towards a quantum information network with squeezed light and entanglement'.* PhD thesis, Australian National University, Canberra, ACT, Australia, 2003.

W. P. Bowen, P. K. Lam, and T. C. Ralph. Biased EPR entanglement and its application to teleportation. *Journal of Modern Optics*, 50:801, 2003a.

W. P. Bowen, R. Schnabel, P. K. Lam, and T. C. Ralph. 'experimental investigation of criteria for continuous variable entanglement'. *Phys. Rev. Lett.*, 90:043601, 2003b.

W. P. Bowen, R. Schnabel, N. Treps, H.-A. Bachor, and P. K. Lam. Recovery of continuous wave squeezing at low frequencies. *Journal of Optics B: Quantum and Semiclassical Optics*, 4:421–424, December 2002.

W. P. Bowen, N. Treps, B. C. Buchler, R. Schnabel, T. C. Ralph, H.-A. Bachor, T. Symul, and P. K. Lam. Experimental investigation of continuous-variable quantum teleportation. *Phys. Rev. A*, 67(3):032302, March 2003.

G. D. Boyd and D. A. Kleinman. Parametric Interaction of Focused Gaussian Light Beams. *Journal of Applied Physics*, 39:3597–3639, July 1968.

D. A. Braje, V. Balić, G. Y. Yin, and S. E. Harris. Low-light-level nonlinear optics with slow light. *Phys. Rev. A*, 68(4):041801, Oct 2003.

S. L. Braunstein, C. A. Fuchs, and H. J. Kimble. Criteria for continuous-variable quantum teleportation. *Journal of Modern Optics*, 47:267–278, February 2000.

H.-J. Briegel, W. Dür, J. I. Cirac, and P. Zoller. Quantum Repeaters: The Role of Imperfect Local Operations in Quantum Communication. *Phys. Rev. Lett.*, 81:5932–5935, December 1998.

B. C. Buchler. *'Electro-optic control of quantum measurements'*. PhD thesis, Australian National University, Canberra, ACT, Australia, 2001.

N. W. Carlson, L. J. Rothberg, A. G. Yodh, W. R. Babbitt, and T. W. Mossberg. Storage and time reversal of light pulses using photon echoes. *Optics Letters*, 8:483–485, September 1983.

C. M. Caves. Quantum limits on noise in linear amplifiers. *Phys. Rev. D*, 26:1817–1839, October 1982.

T. Chanelière, D. N. Matsukevich, S. D. Jenkins, S.-Y. Lan, T. A. B. Kennedy, and A. Kuzmich. Storage and retrieval of single photons transmitted between remote quantum memories. *Nature*, 438:833–836, December 2005.

S. Chaturvedi, K. Dechoum, and P. D. Drummond. Limits to squeezing in the degenerate optical parametric oscillator. *Phys. Rev. A*, 65(3):033805, March 2002.

S. Chu. Nobel Lecture: The manipulation of neutral particles. *Reviews of Modern Physics*, 70:685–706, July 1998.

C. Cohen-Tannoudji. Manipulating Atoms with Photons. *Physica Scripta Volume T*, 76: 33–40, 1998.

C. Cohen-Tannoudji, J. Dupont-Roc, G. Grynberg, and T. A. B. Kennedy. Atom-Photon Interactions: Basic Processes and Applications. *American Journal of Physics*, 61:572–572, June 1993.

M. J. Collett and C. W. Gardiner. Squeezing of intracavity and traveling-wave light fields produced in parametric amplification. *Phys. Rev. A*, 30:1386–1391, September 1984.

J. F. Corney, P. D. Drummond, J. Heersink, V. Josse, G. Leuchs, and U. L. Andersen. Many-Body Quantum Dynamics of Polarization Squeezing in Optical Fibers. *Phys. Rev. Lett.*, 97(2):023606, July 2006.

M. D. Crisp. Propagation of Small-Area Pulses of Coherent Light through a Resonant Medium. *Phys. Rev. A*, 1:1604–1611, June 1970.

J. Cviklinski, J. Ortalo, A. Bramati, M. Pinard, and E. Giacobino. Reversible Quantum Interface for Tunable Single-sideband Modulation. *ArXiv e-prints*, 711, November 2007.

A. Dantan, J. Cviklinski, M. Pinard, and P. Grangier. Dynamics of a pulsed continuous-variable quantum memory. *Phys. Rev. A*, 73(3):032338, March 2006.

A. Dantan and M. Pinard. Quantum-state transfer between fields and atoms in electromagnetically induced transparency. *Phys. Rev. A*, 69(4):043810, April 2004.

A. Dantan, M. Pinard, V. Josse, N. Nayak, and P. R. Berman. Atomic spin squeezing in a Λ system. *Phys. Rev. A*, 67(4):045801, April 2003.

V. Delaubert. *'Quantum imaging with a small number of transverse modes'*. PhD thesis, Australian National University-Universite Pierre et Marie Curie, Canberra, ACT, Australia, 2007.

L. Deng, E. W. Hagley, M. Kozuma, and M. G. Payne. Optical-wave group-velocity reduction without electromagnetically induced transparency. *Phys. Rev. A*, 65(5):051805, May 2002.

D. Deutsch. Quantum theory, the Church-Turing principle and the universal quantum computer. *Royal Society of London Proceedings Series A*, 400:97–117, July 1985.

R. W. P. Drever, J. L. Hall, F. V. Kowalski, J. Hough, G. M. Ford, A. J. Munley, and H. Ward. Laser phase and frequency stabilization using an optical resonator. *Applied Physics B: Lasers and Optics*, 31:97–105, June 1983.

P. D. Drummond and C. W. Gardiner. Generalised P-representations in quantum optics. *Journal of Physics A Mathematical General*, 13:2353–2368, July 1980.

L.-M. Duan, G. Giedke, J. I. Cirac, and P. Zoller. Inseparability Criterion for Continuous Variable Systems. *Phys. Rev. Lett.*, 84:2722–2725, March 2000.

L.-M. Duan, M. D. Lukin, J. I. Cirac, and P. Zoller. Long-distance quantum communication with atomic ensembles and linear optics. *Nature*, 414:413–418, November 2001.

M. D. Eisaman, A. André, F. Massou, M. Fleischhauer, A. S. Zibrov, and M. D. Lukin. Electromagnetically induced transparency with tunable single-photon pulses. *Nature*, 438:837–841, December 2005.

D. Felinto, C. W. Chou, H. de Riedmatten, S. V. Polyakov, and H. J. Kimble. Control of decoherence in the generation of photon pairs from atomic ensembles. *Phys. Rev. A*, 72 (5):053809, November 2005.

D. Felinto, C. W. Chou, J. Laurat, E. W. Schomburg, H. de Riedmatten, and H. J. Kimble. Conditional control of the quantum states of remote atomic memories for quantum networking. *Nature Physics*, 2:844–848, December 2006.

J. P. Fève, B. Boulanger, G. Marnier, and H. Albrecht. Repetition rate dependence of gray-tracking in $KTiOPO_4$ during second-harmonic generation at 532 nm. *Applied Physics Letters*, 70:277–279, January 1997.

E. Figueroa, F. Vewinger, J. Appel, and A. I. Lvovsky. Decoherence of electromagnetically induced transparency in atomic vapor. *Optics Letters*, 31:2625–2627, September 2006.

M. Fleischhauer. Correlation of high-frequency phase fluctuations in electromagnetically induced transparency. *Phys. Rev. Lett.*, 72:989–992, February 1994.

M. Fleischhauer and M. D. Lukin. Dark-state polaritons in electromagnetically induced transparency. *Phys. Rev. Lett.*, 84(22):5094–5097, May 2000.

M. Fleischhauer and A. S. Manka. Propagation of laser pulses and coherent population transfer in dissipative three-level systems: An adiabatic dressed-state picture. *Phys. Rev. A*, 54:794–803, July 1996.

E. Fraval, M. J. Sellars, and J. J. Longdell. Method of Extending Hyperfine Coherence Times in $Pr^{3+} : Y_2SiO_5$. *Phys. Rev. Lett.*, 92(7):077601, February 2004.

E. Fraval, M. J. Sellars, and J. J. Longdell. Dynamic Decoherence Control of a Solid-State Nuclear-Quadrupole Qubit. *Physical Review Letters*, 95(3):030506, July 2005.

E. S. Fry, X. Li, D. Nikonov, G. G. Padmabandu, M. O. Scully, A. V. Smith, F. K. Tittel, C. Wang, S. R. Wilkinson, and S.-Y. Zhu. Atomic coherence effects within the sodium D_1 line: Lasing without inversion via population trapping. *Phys. Rev. Lett.*, 70: 3235–3238, May 1993.

A. L. Gaeta, R. W. Boyd, and G. S. Agarwal. Quantum-noise limit on optical amplification by two-beam coupling in an atomic vapor. *Phys. Rev. A*, 46:4271–4275, October 1992.

C. W. Gardiner. Handbook of Stochastic methods, 2nd ed. *Springer, Berlin*, 1985.

A. Gilchrist, C. W. Gardiner, and P. D. Drummond. Positive P representation: Application and validity. *Phys. Rev. A*, 55:3014–3032, April 1997.

R. J. Glauber. Coherent and Incoherent States of the Radiation Field. *Phys. Rev.*, 131: 2766–2788, September 1963.

A. V. Gorshkov, A. André, M. Fleischhauer, A. S. Sørensen, and M. D. Lukin. Universal Approach to Optimal Photon Storage in Atomic Media. *Phys. Rev. Lett.*, 98(12):123601, March 2007a.

A. V. Gorshkov, A. André, M. D. Lukin, and A. S. Sørensen. Photon storage in Λ -type optically dense atomic media. I. Cavity model. *Phys. Rev. A*, 76(3):033804, September 2007b.

A. V. Gorshkov, A. André, M. D. Lukin, and A. S. Sørensen. Photon storage in Λ -type optically dense atomic media. II. Free-space model. *Phys. Rev. A*, 76(3):033805, September 2007c.

A. V. Gorshkov, A. André, M. D. Lukin, and A. S. Sørensen. Photon storage in Λ -type optically dense atomic media. III. Effects of inhomogeneous broadening. *Phys. Rev. A*, 76(3):033806, September 2007d.

P. Grangier, J. A. Levenson, and J.-P. Poizat. Quantum non-demolition measurements in optics. *Nature*, 396, December 1998.

N. B. Grosse, W. P. Bowen, K. McKenzie, and P. K. Lam. Harmonic Entanglement with Second-Order Nonlinearity. *Phys. Rev. Lett.*, 96(6):063601, February 2006.

F. Grosshans and P. Grangier. Quantum cloning and teleportation criteria for continuous quantum variables. *Phys. Rev. A*, 64(1):010301, July 2001.

F. Grosshans and P. Grangier. Continuous Variable Quantum Cryptography Using Coherent States. *Phys. Rev. Lett.*, 88(5):057902, February 2002a.

F. Grosshans and P. Grangier. Reverse reconciliation protocols for quantum cryptography with continuous variables. *ArXiv Quantum Physics e-prints*, April 2002b.

L. K. Grover. Quantum Mechanics Helps in Searching for a Needle in a Haystack. *Phys. Rev. Lett.*, 79:325–328, July 1997.

E. L. Hahn. Spin Echoes. *Phys. Rev.*, 80:580–594, November 1950.

S. A. Haine, M. K. Olsen, and J. J. Hope. Generating Controllable Atom-Light Entanglement with a Raman Atom Laser System. *Phys. Rev. Lett.*, 96(13):133601, April 2006.

B. S. Ham, S. M. Shahriar, and P. R. Hemmer. Electromagnetically induced transparency over spectral hole-burning temperature in a rare-earthdoped solid. *Journal of the Optical Society of America B Optical Physics*, 16:801–804, May 1999.

K. Hammerer, K. Mølmer, E. S. Polzik, and J. I. Cirac. Light-matter quantum interface. *Phys. Rev. A*, 70:044304, 2004.

W. Happer. Optical pumping. *Reviews of Modern Physics*, 44:169–249, 1972.

S. E. Harris. Electromagnetically induced transparency with matched pulses. *Phys. Rev. Lett.*, 70:552–555, February 1993.

S. E. Harris. Normal modes for electromagnetically induced transparency. *Phys. Rev. Lett.*, 72:52–55, January 1994.

J. Heersink, V. Josse, G. Leuchs, and U. L. Andersen. Efficient polarization squeezing in optical fibers. *Optics Letters*, 30:1192–1194, May 2005.

G. Hétet, B. C. Buchler, O. Glöckl, M. T. L. Hsu, and H.-A. Lam P.K. Akulshin, A. M. Bachor. Delay of squeezing and entanglement using electromagnetically induced transparency in a vapour cell. *Optics Express*, 16:7369–7394, May 2008a.

G. Hétet, O. Glöckl, K. Pilypas, C. C. Harb, B. C. Buchler, H.-A. Bachor, and P. K. Lam. Squeezed light for bandwidth limited atom optics experiments at the Rubidium D1 line. *Journal of Physics B: Atomic, Molecular and Optical Physics*, 40:221, January 2007.

G. Hétet, J. J Longdell, A. L. Alexander, P. K. Lam, and M. J. Sellars. Electro-Optic Quantum Memory for Light Using Two-Level Atoms. *Phys. Rev. Lett.*, 100:23601, January 2008b.

G. Hétet, A. Peng, M. T. Johnsson, J. J. Hope, and P. K. Lam. Characterization of EIT-based continuous variable quantum memories. *Phys. Rev. A*, 77:012323, January 2008.

G. Hétet, A. Peng, M. T. Johnsson, M. T. L. Hsu, O. Glöckl, P. K. Lam, H. A. Bachor, and J. J. Hope. Erratum: Squeezing and entanglement delay using slow light [Phys. Rev. A 71, 033809 (2005)]. *Phys. Rev. A*, 74(5):059902, November 2006.

R. Holzlöhner, V. S. Grigoryan, C. R. Menyuk, and W. L. Kath. Accurate Calculation of Eye Diagrams and Bit Error Rates in Optical Transmission Systems Using Linearization. *Journal of Lightwave Technology*, 20:389, March 2002.

K. Honda, D. Akamatsu, M. Arikawa, Y. Yokoi, K. Akiba, S. Nagatsuka, T. Tanimura, A. Furusawa, and M. Kozuma. Storage and Retrieval of a Squeezed Vacuum. *Phys. Rev. Lett.*, 100(9):093601, March 2008.

D. M. Hope, H.-A. Bachor, P. J. Manson, D. E. McClelland, and P. T. H. Fisk. Observation of quadrature squeezing in a cavity-atom system. *Phys. Rev. A*, 46:1181, August 1992.

M. T. L Hsu. *'On multi-mode optical imaging and light-atom ensemble interactions'*. PhD thesis, Australian National University, Canberra, ACT, Australia, 2008.

M. T. L. Hsu, G. Hétet, O. Glöckl, J. J. Longdell, B. C. Buchler, H.-A. Bachor, and P. K. Lam. Quantum study of information delay in electromagnetically induced transparency. *Phys. Rev. Lett.*, 97(18):183601, Nov 2006a.

M. T. L. Hsu, G. Hétet, A. Peng, C. C. Harb, H.-A. Bachor, M. T. Johnsson, J. J. Hope, P. K. Lam, A. Dantan, J. Cviklinski, A. Bramati, and M. Pinard. Effect of atomic noise on optical squeezing via polarization self-rotation in a thermal vapor cell. *Phys. Rev. A*, 73(2):023806, Feb 2006b.

E. H. Huntington, G. N. Milford, C. Robilliard, T. C. Ralph, O. Glöckl, U. L. Andersen, S. Lorenz, and G. Leuchs. Demonstration of the spatial separation of the entangled quantum sidebands of an optical field. *Phys. Rev. A Rapid*, 71(4):041802, April 2005.

J. C. Jacco, D. R. Rockafellow, and E. A. Teppo. Bulk-darkening threshold of flux-grown KTiOPO4. *Optics Letters*, 16:1307–1309, September 1991.

B. C. Jacobs and J. D. Franson. Quantum cryptography in free space. *Optics Letters*, 21: 1854–1856, November 1996.

J. R. Jeffers, N. Imoto, and R. Loudon. Quantum optics of traveling-wave attenuators and amplifiers. *Phys. Rev. A*, 47:3346–3359, April 1993.

H. Jeong, T. C. Ralph, and W. P. Bowen. Quantum and classical fidelities for Gaussian states. *ArXiv Quantum Physics e-prints*, September 2004.

V. Josse, A. Dantan, A. Bramati, M. Pinard, and E. Giacobino. Continuous Variable Entanglement using Cold Atoms. *Phys. Rev. Lett.*, 92(12):123601, March 2004.

B. Julsgaard, J. Sherson, J. I. Cirac, J. Fiurášek, and E. S. Polzik. Experimental demonstration of quantum memory for light. *Nature*, 432:482–486, November 2004.

E. Knill, R. Laflamme, and G. J. Milburn. A scheme for efficient quantum computation with linear optics. *Nature*, 409:46–52, January 2001.

A. E. Kozhekin, K. Mølmer, and E. Polzik. 'quantum memory for light'. *Phys. Rev. A*, 62:033809, 2000.

A. E. Kozhekin, K. Mølmer, and E. Polzik. Quantum memory for light. *Phys. Rev. A*, 62 (3):033809, September 2000.

B. Kraus, W. Tittel, N. Gisin, M. Nilsson, S. Kröll, and J. I. Cirac. Quantum memory for nonstationary light fields based on controlled reversible inhomogeneous broadening. *Phys. Rev. A*, 73(2):020302, February 2006.

S. Kuhr, S. Gleyzes, C. Guerlin, J. Bernu, U. B. Hoff, S. Deléglise, S. Osnaghi, M. Brune, J.-M. Raimond, S. Haroche, E. Jacques, P. Bosland, and B. Visentin. Ultrahigh finesse Fabry-Pérot superconducting resonator. *Applied Physics Letters*, 90:4101, April 2007.

N. A. Kurnit, I. D. Abella, and S. R. Hartmann. Observation of a Photon Echo. *Phys. Rev. Lett.*, 13:567–568, November 1964.

A. Kuzmich, W. P. Bowen, A. D. Boozer, A. Boca, C. W. Chou, L.-M. Duan, and H. J. Kimble. Generation of nonclassical photon pairs for scalable quantum communication with atomic ensembles. *Nature*, 423:731–734, June 2003.

P. K. Lam. *'Application of quantum electro-optic control and squeezed light'*. PhD thesis, Australian National University, Canberra, ACT, Australia, 1998.

P. K. Lam, T. C. Ralph, B. C. Buchler, D. E. McClelland, H.-A. Bachor, and J. Gao. Optimization and transfer of vacuum squeezing from an optical parametric oscillator . *Journal of Optics B: Quantum and Semiclassical Optics*, 1:469–474, August 1999.

A. Lambrecht, T. Coudreau, A. M. Steinberg, and E. Giacobino. Squeezing with cold atoms. *Europhysics Letters*, 36:93–98, October 1996.

A. M. Lance, T. Symul, V. Sharma, C. Weedbrook, T. C. Ralph, and P. K. Lam. No-Switching Quantum Key Distribution Using Broadband Modulated Coherent Light. *Phys. Rev. Lett.*, 95(18):180503, October 2005.

J. Laurat, H. de Riedmatten, D. Felinto, C.-W. Chou, E. W. Schomburg, and H. J. Kimble. Efficient retrieval of a single excitation stored in an atomic ensemble. *Optics Express*, 14:6912–6918, July 2006.

A. Lezama, A. M. Akulshin, A. I. Sidorov, and P. Hannaford. Storage and retrieval of light pulses in atomic media with "slow" and "fast" light. *Phys. Rev. A*, 73(3):033806, March 2006.

A. Lezama, S. Barreiro, and A. M. Akulshin. Electromagnetically induced absorption. *Phys. Rev. A*, 59:4732–4735, June 1999.

C. Liu, Z. Dutton, C. H. Behroozi, and L. V. Hau. Observation of coherent optical information storage in an atomic medium using halted light pulses. *Nature*, 409:490–493, January 2001.

J. J. Longdell, A. L. Alexander, and M. J. Sellars. Characterization of the hyperfine interaction in europium-doped yttrium orthosilicate and europium chloride hexahydrate. *Phys. Rev. B*, 74(19):195101, November 2006.

J. J. Longdell, E. Fraval, M. J. Sellars, and N. B. Manson. Stopped Light with Storage Times Greater than One Second Using Electromagnetically Induced Transparency in a Solid. *Phys. Rev. Lett.*, 95(6):063601, August 2005.

J. J. Longdell, G. Hétet, A. L. Alexander, P.K. Lam, and M. J. Sellars. Gradient echo quantum memory for light using two-level atoms. *Proc. SPIE 6710, 67100X*, 92, September 2007.

J. J. Longdell, G. Hétet, P. K. Lam, and M. J. Sellars. Analytical treatment of the gradient echo memory, in preparation. 2008.

J.J. Longdell. *'Quantum Information Processing in Rare Earth Ion Doped Insulators '*. PhD thesis, Australian National University, Canberra, ACT, Australia, 2003.

A. Mair, J. Hager, D. F. Phillips, R. L. Walsworth, and M. D. Lukin. Phase coherence and control of stored photonic information. *Phys. Rev. Lett.*, 65(3):031802, March 2002.

M. Martinelli, P. Valente, H. Failache, D. Felinto, L. S. Cruz, P. Nussenzveig, and A. Lezama. Noise spectroscopy of nonlinear magneto-optical resonances in Rb vapor. *Phys. Rev. A*, 69(4):043809, April 2004.

A. B. Matsko, I. Novikova, M. O. Scully, and G. R. Welch. Radiation trapping in coherent media. *Phys. Rev. Lett.*, 87(13):133601, Sep 2001a.

A. B. Matsko, I. Novikova, G. R. Welch, D. Budker, D. F. Kimball, and S. M. Rochester. Vacuum squeezing in atomic media via self-rotation. *Phys. Rev. A*, 66(4):043815, October 2002.

A. B. Matsko, Y. V. Rostovtsev, O. Kocharovskaya, A. S. Zibrov, and M. O. Scully. Nonadiabatic approach to quantum optical information storage. *Phys. Rev. A*, 64(4): 043809, Sep 2001b.

A. B. Matsko, D. V. Strekalov, and L. Maleki. On the dynamic range of optical delay lines based on coherent atomic media. *Optics Express*, 13:2210, March 2005.

D. N. Matsukevich and A. Kuzmich. 'quantum state transfer between matter and light'. *Science*, 306:663, 2004.

C. F. McCormick, V. Boyer, E. Arimondo, and P. D. Lett. Strong relative intensity squeezing by four-wave mixing in rubidium vapor. *Optics Letters*, 32:178–180, January 2007a.

C. F. McCormick, A. M. Marino, V. Boyer, and P. D. Lett. Strong low-frequency quantum correlations from a four-wave mixing amplifier. *ArXiv Quantum Physics e-prints*, March 2007b.

K. McKenzie. Private communication. 2007.

K. McKenzie, N. Grosse, W. P. Bowen, S. E. Whitcomb, M. B. Gray, D. E. McClelland, and P. K. Lam. Squeezing in the Audio Gravitational-Wave Detection Band. *Phys. Rev. Lett.*, 93(16):161105, October 2004.

K. McKenzie, E. E. Mikhailov, K. Goda, P. K. Lam, N. Grosse, M. B. Gray, N. Mavalvala, and D. E. McClelland. Quantum noise locking. *Journal of Optics B: Quantum and Semiclassical Optics*, 7:421, October 2005.

S. A. Moiseev and S. Kröll. Complete Reconstruction of the Quantum State of a Single-Photon Wave Packet Absorbed by a Doppler-Broadened Transition. *Phys. Rev. Lett.*, 87(17):173601, October 2001.

C. Monroe, D. M. Meekhof, B. E. King, W. M. Itano, and D. J. Wineland. Demonstration of a fundamental quantum logic gate. *Phys. Rev. Lett.*, 75:4714–4717, December 1995.

T. W. Mossberg. Time-domain frequency-selective optical data storage. *Optics Letters*, 7:77–79, February 1982.

T. W. Mossberg, R. Kachru, S. R. Hartmann, and A. M. Flusberg. Echoes in gaseous media: A generalized theory of rephasing phenomena. *Phys. Rev. A*, 20:1976–1996, November 1979.

A. N. Nesmeyanov. Vapor pressure of the chemical elements. *Elsevier, Amsterdam*, 2007.

M.A. Nielsen and I.L. Chuang. Quantum Computation and Quantum Information. *Cambridge Univ. Press.*, 2000.

M. Nilsson and S. Kröll. Solid state quantum memory using complete absorption and re-emission of photons by tailored and externally controlled inhomogeneous absorption profiles. *Optics Communications*, 247:393–403, March 2005.

I. Novikova, A. B. Matsko, V. A. Sautenkov, V. L. Velichansky, G. R. Welch, and M. O. Scully. Ac-Stark shifts in the nonlinear Faraday effect. *Optics Letters*, 25:1651–1653, November 2000.

I. Novikova, D. F. Phillips, and R. L. Walsworth. Slow Light with Integrated Gain and Large Pulse Delay. *Phys. Rev. Lett.*, 99(17):173604, October 2007.

J. Nunn, I. A. Walmsley, M. G. Raymer, K. Surmacz, F. C. Waldermann, Z. Wang, and D. Jaksch. Mapping broadband single-photon wave packets into an atomic memory. *Phys. Rev. A*, 75(1):011401, January 2007.

M. Oberst, F. Vewinger, and A. I. Lvovsky. Time-resolved probing of the ground state coherence in rubidium. *Optics Letters*, 32:1755–1757, June 2007.

Z. Y. Ou, S. F. Pereira, H. J. Kimble, and K. C. Peng. Realization of the Einstein-Podolsky-Rosen paradox for continuous variables. *Phys. Rev. Lett.*, 68:3663–3666, June 1992.

A. S. Parkins, P. Marte, P. Zoller, and H. J. Kimble. Synthesis of arbitrary quantum states via adiabatic transfer of Zeeman coherence. *Phys. Rev. Lett.*, 71:3095–3098, November 1993.

C. K. Patel and R. E. Slusher. Photon Echoes in Gases. *Phys. Rev. Lett.*, 20:1087–1089, May 1968.

A. Peng, M. Johnsson, W. P. Bowen, P. K. Lam, H.-A. Bachor, and J. J. Hope. Squeezing and entanglement delay using slow light. *Phys. Rev. A*, 71(3):033809, Mar 2005.

D. F. Phillips, A. Fleischhauer, A. Mair, R. L. Walsworth, and M. D. Lukin. Storage of light in atomic vapor. *Phys. Rev. Lett.*, 86(5):783–786, Jan 2001.

W. D. Phillips. Nobel lecture: Laser cooling and trapping of neutral atoms. *Rev. Mod. Phys.*, 70(3):721–741, Jul 1998.

K. A. Pilypas. UV pump source for the production of squeezed light at the ^{87}Rb D1 line. Master's thesis, Australian National University, Canberra, ACT, Australia, 2006.

G. J. Pryde, M. J. Sellars, and N. B. Manson. Solid State Coherent Transient Measurements Using Hard Optical Pulses. *Phys. Rev. Lett.*, 84:1152–1155, February 2000.

T. C. Ralph and P. K. Lam. Teleportation with Bright Squeezed Light. *Phys. Rev. Lett.*, 81:5668–5671, December 1998.

T. C. Ralph, P. K. Lam, and R. E. S. Polkinghorne. Characterizing teleportation in optics. *Journal of Optics B: Quantum and Semiclassical Optics*, 1:483–489, August 1999.

M. D. Reid and P. D. Drummond. 'quantum correlations of phase in nondegenerate parametric oscillaton'. *Phys. Rev. Lett.*, 60:2731, 1988.

M. Riebe, H. Häffner, C. F. Roos, W. Hänsel, J. Benhelm, G. P. T. Lancaster, T. W. Körber, C. Becher, F. Schmidt-Kaler, D. F. V. James, and R. Blatt. Deterministic quantum teleportation with atoms. *Nature*, 429:734–737, June 2004.

J. Ries, B. Brezger, and A. I. Lvovsky. Experimental vacuum squeezing in rubidium vapor via self-rotation. *Phys. Rev. A*, 68(2):025801, August 2003.

N. Sangouard, C. Simon, M. Afzelius, and N. Gisin. Analysis of a quantum memory for photons based on controlled reversible inhomogeneous broadening. *Phys. Rev. A*, 75(3): 032327, March 2007.

V. A. Sautenkov, Y. V. Rostovtsev, and M. O. Scully. Switching between photon-photon correlations and Raman anticorrelations in a coherently prepared Rb vapor. *Phys. Rev. A*, 72(6):065801, December 2005.

R. Schnabel, H. Vahlbruch, A. Franzen, S. Chelkowski, N. Grosse, H.-A. Bachor, W. P. Bowen, P. K. Lam, and K. Danzmann. Squeezed light at sideband frequencies below 100 kHz from a single OPA. *Optics Communications*, 240:185–190, October 2004.

C. Schori, B. Julsgaard, J. L. Sørensen, and E. S. Polzik. Recording Quantum Properties of Light in a Long-Lived Atomic Spin State: Towards Quantum Memory. *Phys. Rev. Lett.*, 89(5):057903, July 2002.

M. Scully, M. J. Stephen, and D. C. Burnham. Photon Echo in Gaseous Media. *Phys. Rev.*, 171:213–214, July 1968.

Peter W. Shor. Algorithms for quantum computation: Discrete logarithms and factoring. In *IEEE Symposium on Foundations of Computer Science*, pages 124–134, 1994. URL `citeseer.ist.psu.edu/14533.html`.

C. Simon, H. de Riedmatten, M. Afzelius, N. Sangouard, H. Zbinden, and N. Gisin. Quantum Repeaters with Photon Pair Sources and Multimode Memories. *Phys. Rev. Lett.*, 98(19):190503, May 2007.

C. Sjaarda Cornish, W. R. Babbitt, and L. Tsang. Demonstration of highly efficient photon echoes. *Optics Letters*, 25:1276–1278, September 2000.

R. E. Slusher, B. Yurke, J. C. Mertz, J. F. Valley, and L. W. Hollberg. Observation of squeezed states generated by four-wave mixing in an optical cavity. *Phys. Rev. Lett.*, 55:2409–2412, November 1985.

J. L. Sørensen, J. Hald, and E. S. Polzik. Quantum Noise of an Atomic Spin Polarization Measurement. *Phys. Rev. Lett.*, 80:3487–3490, April 1998.

D. Stucki, N. Gisin, O. Guinnard, G. Ribordy, and H. Zbinden. Quantum key distribution over 67 km with a plug and play system. *New J. Phys.*, 4(41), 2002.

E. C. Sudarshan. Equivalence of Semiclassical and Quantum Mechanical Descriptions of Statistical Light Beams. *Phys. Rev. Lett.*, 10:277–279, April 1963.

Q. Sun, Y. V. Rostovtsev, J. P. Dowling, M. O. Scully, and M. S. Zubairy. Optically controlled delays for broadband pulses. *Phys. Rev. A*, 72(3):031802, September 2005.

Y. Sun, C. W. Thiel, R. L. Cone, R. W. Equall, and R. L. Hutcheson. 'recent progress in developing new rare earth materials for hole burning and coherent transient applications'. *Journal of luminescence*, 98:281, 2002.

S. Suzuki, H. Yonezawa, F. Kannari, M. Sasaki, and A. Furusawa. 7 dB quadrature squeezing at 860 nm with periodically poled $KTiOPO_4$. *Applied Physics Letters*, 89: 1116, August 2006.

A. V. Taichenachev, A. M. Tumaikin, and V. I. Yudin. Electromagnetically induced absorption in a four-state system. *Phys. Rev. A*, 61(1):011802, January 2000.

Y. Takeno, M. Yukawa, H. Yonezawa, and A. Furusawa. Observation of -9 dB quadrature squeezing with improvement of phase stability in homodyne measurement. *Optics Express*, 15:4321–4327, April 2007.

T. Tanimura, D. Akamatsu, Y. Yokoi, A. Furusawa, and M. Kozuma. Generation of a squeezed vacuum resonant on a rubidium D1 line with periodically poled KTiOPO4. *Optics Letters*, 31:2344–2346, August 2006.

H. C. Torrey. Transient Nutations in Nuclear Magnetic Resonance. *Phys. Rev.*, 76:1059–1068, October 1949.

N. Treps, V. Delaubert, A. Maître, J. M. Courty, and C. Fabre. Quantum noise in multipixel image processing. *Phys. Rev. A*, 71(1):013820, January 2005.

H. Vahlbruch, S. Chelkowski, B. Hage, A. Franzen, K. Danzmann, and R. Schnabel. Coherent Control of Vacuum Squeezing in the Gravitational-Wave Detection Band. *Phys. Rev. Lett.*, 97(1):011101, July 2006.

H. Vahlbruch, M. Mehmet, S. Chelkowski, B. Hage, A. Franzen, N. Lastzka, S. Goßler, K. Danzmann, and R. Schnabel. Observation of Squeezed Light with 10-dB Quantum-Noise Reduction. *Phys. Rev. Lett.*, 100(3):033602, January 2008.

L. Vestergaard Hau, S. E. Harris, Z. Dutton, and C. H. Behroozi. Light speed reduction to 17 metres per second in an ultracold atomic gas. *Nature*, 397:594, February 1999.

D. F. Walls and G. J. Milburn. Effect of dissipation on quantum coherence. *Phys. Rev. A*, 31(4):2403–2408, Apr 1985.

A. G. White, T. C. Ralph, and H.-A. Bachor. Active versus passive squeezing by second-harmonic generation. *Journal of the Optical Society of America B Optical Physics*, 13: 1337–1346, July 1996.

A.G White. *Classical and quantum dynamics of optical frequency conversion.* PhD thesis, Australian National University, Canberra, ACT, Australia, 1997.

W. K. Wootters and W. H. Zurek. A single quantum cannot be cloned. *Nature*, 299:802, October 1982.

Q. Xu, P. Dong, and M. Lipson. Breaking the delay-bandwidth limit in a photonic structure. *Nature Physics*, 3:406–410, June 2007.

Z. Zhu, D. J. Gauthier, and R. W. Boyd. Stored Light in an Optical Fiber via Stimulated Brillouin Scattering. *Science*, 318:1748–, December 2007.

A. S. Zibrov, A. B. Matsko, O. Kocharovskaya, Y. V. Rostovtsev, G. R. Welch, and M. O. Scully. Transporting and Time Reversing Light via Atomic Coherence. *Phys. Rev. Lett.*, 88(10):103601, March 2002.

A. S. Zibrov and I. Novikova. Observation of quantum noise in the polarization of laser light in a Rubidium-vapor cell. *JETP Letters*, 82:110, 2005.